MEASURING, CHARACTERISATION AND MODELLING OF LOAD DYNAMIC BEHAVIOUR IN A WET OVERFLOW-DISCHARGE BALL MILL

Augustine Barasa Makokha

MSc Eng (Wits)

A thesis submitted to the Faculty of Engineering and the Built Environment, University of the Witwatersrand, Johannesburg, in fulfilment of the requirements for the degree of Doctor of Philosophy in Engineering

Johannesburg, June 2011

Declaration

I declare that this thesis is, to the best of my knowledge and belief, my own unaided work. It is being submitted for the degree of Doctor of Philosophy in Engineering in the University of the Witwatersrand, Johannesburg. It has never been submitted either in part or in whole for a degree in this or any other University.

……..

Augustine B. Makokha

…….....day of ……

Abstract

Overflow ball mills have found popular application in the ore dressing process for post-primary grinding firstly owing to their ability to produce finer grinds, necessary for efficient mineral liberation and better flotation recovery and secondly due to lower initial capital outlay. However they are inefficient and intensive energy consumers. This trend has been exacerbated in the wake of increased installation of large diameter ball mills to benefit from economies of scale, coupled with diminishing ore quality currently being experienced by mines worldwide. To fully utilise the available mill capacity and achieve optimal performance whilst maintaining energy efficiency for these large devices, closer and more effective control is needed. Satisfaction of this need would result in stability of the entire mineral processing circuit, thereby reducing the overall cost in mineral extraction. Clear and deeper understanding of the in-mill behaviour is fundamental to the realisation of the above objective.

This thesis explores several experimental and modelling techniques to obtain deeper understanding of the internal behaviour of an overflow ball mill. A direct load sensor comprising an inductive proximity probe and a conductivity probe installed through the mill shell has been utilised to collect information of the media and slurry dynamic positions inside a laboratory ball mill while a commercial on-line ball and pulp sensor was employed to collect similar information on an industrial overflow ball mill. Useful insights were acquired that can help the design of control strategies for optimal mill performance. Four feature variables, i.e. dynamic media angle, slurry pool angle, conductivity signal amplitude and the slurry pool depth, derived from the sensor signals data were characteristically influenced by changes in mill operational conditions. Therefore the possibility of using these features to predict the associated mill operational variables is feasible. In view of the findings, two multivariate models, one based on the concept of data projection to latent space (PLS) and the other combining PLS and radial basis functions neural networks (RBF) were built and applied to predict the in-mill slurry density and ball load volume. Both models yielded adequate predictions, albeit the hybrid PLS-RBF model displayed marginally better prediction performance. The results are indicative of the available potential

for mill on-line monitoring and control by multivariate techniques based on relevant features contained in the media and slurry sensor signals data.

In another endeavour, a gamma camera was successfully employed to study the flow and mixing behaviour of slurry inside a laboratory mill using Technetium-Tc^{99m} radiotracer as a flow follower. The effects of slurry viscosity and mill rotational speed on slurry mixing rate within the ball charge and slurry exchange rate between the pool and the ball charge were assessed, yielding insightful data. However, the results remain inconclusive as only qualitative information could be obtained owing to the radiation attenuation effects by the steel ball charge.

In the quest to improve the understanding of material transport inside the mill, the data acquired on an industrial mill through salt tracer tests was adequately analysed to assess the variation of slurry residence time distribution (RTD) and volumetric holdup inside the mill as affected by changes in slurry concentration and ball load volume. A model based on the concept of serial stirred mixers with a plug flow component produced fairly accurate predictions of the RTD data. Also, equations derived from a mathematical description of the dynamic load profile produced good estimates of the in-mill slurry volumetric holdup.

Further, an improved mixing-cell model was developed and applied to characterise the in-mill slurry hydrodynamic transport based on the measured RTD data. The model was able to account for the effects of non-ideal flow conditions such as slurry back-mixing, slurry exchange between the pool and ball charge and bypass flows on the main flow of slurry thus giving correct description of the inherent in-mill slurry transport dynamics. Note that failure to tune the mill appropriately to achieve desirable in-mill slurry transport behaviour may result in poor milling performance and corresponding high energy expenditure.

Thus, the results obtained in this thesis clearly demonstrate that, a combination of experimental techniques and mathematical models is a viable route to enhance understanding of mill internal behaviour, which in turn enables development of better control schemes for optimal mill performance.

Publications

The papers published by the author on the contents of this thesis are as follows:

Makokha, A.B., Moys, H.M., Bwalya, M.M., 2011. Modelling the RTD of an industrial overflow ball mill as a function of load volume and slurry concentration, *Minerals. Engineering,* **24** (3-4) 335-340

Makokha, A.B., Moys, H.M., Bwalya, M.M., 2011. Application of gamma emission imaging in mineral processing industry: Case study of slurry transport in a wet laboratory ball mill, *Measurement Science & Technology*, **22** (4) 045706

Makokha, A.B., Moys, H.M., 2011. Characterizing slurry hydrodynamic transport in a large overflow tubular ball mill by an improved mixing cell model based on tracer response data, *Powder Technology***, 211** (2-3), 207-214.

The paper submitted for publication on the contents of this thesis:

Makokha, A.B., Moys, H.M., 2011. Application of multivariate techniques to predict in-mill slurry density and ball load volume based on load behaviour signals, *Minerals Engineering*, (Under review)

Other publications:

Makokha, A.B., Moys, H.M., Cousta, C., Muumbo, A., 2009. Steady state inferential modelling of temperature and pressure in an air-swept coal pulverizing ball mill, *Powder Technol.*, **192**: 260 – 267.

Makokha, A. B., Moys H. M., Bwalya M. M., Kiangi, K., 2007. A new approach to optimising the life and performance of worn liners in ball mills: Experimental study and DEM simulation, *Int. J. Miner. Process,* **84**: 221-227.

Makokha, A. B., Moys H. M., 2007. Effect of cone-lifters on the discharge capacity of the mill product: case study of a dry laboratory scale air-swept ball mill, *Miner. Eng.*, **20** (2) 124 -131.

Makokha, A. B., Moys H. M., 2006. Towards optimising ball-milling capacity: Effect of lifter design, *Miner. Eng.*, **19** (14) 1439 - 1445.

This work is dedicated to all my family members: My wife, son, father, mother, brothers and sisters.

Acknowledgements

I would like to express my utmost appreciation to the following, who in one way or another, facilitated the completion of this work:

My supervisor, Prof. Michael, H. Moys for his guidance, encouragement and support throughout the execution of this work.

My colleagues including Dr. Murray Bwalya, Mr. Francois Katubilwa, Mr. Pheneas Chikerema, Mr. Clayton Bhondayi and Mr. Pascal Simba for their help with experimental work and for providing many useful suggestions which helped to enhance the quality of this work.

Mr. Theo Prassinos and the entire workshop staff for the many stimulating discussions and timely advice. Their critical suggestions and helping hand during equipment modifications and set-up enabled the experimental process to be successful and safety compliant.

Mr. Pratish Keshav, Process metallurgist and the entire staff of Metallurgical laboratory for their invaluable assistance during the industrial plant surveys.

Prof. Vangu, Head of Nuclear Medicine at Johannesburg Hospital for his insight and suggestions on gamma emission imaging experiments. Radiographers, Tau and Pitso for their invaluable service during the course of experiments.

I am deeply indebted to my family and friends for their understanding and moral support during the span of this work.

The funding from Anglo-Platinum, NRF, COMPS and University of the Witwatersrand (PMA bursary) enabled the execution of this research work.

Finally, to the Almighty for availing me the opportunity and ability to pursue this research work.

Table of Contents

List of Figures

List of Tables

CHAPTER 1

Introduction

1.1 Background and motivation

The increasing focus by industrialists in the mineral processing industry on expanding production capacities and minimising costs has steered a strong impetus to research on better and effective methods for monitoring, control and optimisation of mineral processing plants. Milling has been identified as a pivotal unit operation in the mineral processing circuit whose performance defines the performance of all the downstream processes and thus it has been accorded more research attention. Surprisingly, the researches into the milling process continue to lay emphasis on the acquisition of information that can help in understanding the mill power consumption pattern. This is on account of a widely held belief that the pattern of mill power draw correlates with mill capacity. However, with increasing installation of large diameter mills, which have to operate under characteristically multivariate milling environments, it is feared that this rule of thumb can present a control drawback where small changes in mill capacity cannot be detected through variation in a power draw pattern or the observed power draw pattern is due to changes in load behaviour associated with individual influences such as change in ore characteristics, ball loading or slurry properties. Therefore, it is imperative that the in-mill dynamics are properly understood and correctly characterised in order to successfully control and optimise the performance of milling circuits.

Generally, the mill internal dynamics are dependent on design and operational factors such as the mill filling level, mill rotational speed, grinding media size, liner characteristics and slurry properties. Accordingly, by monitoring mill internal behaviour, the individual effect of these factors and their nature of interaction can be studied and clarified, leading to effective control and optimisation of the milling circuit. For instance, understanding the interactions of the ball media and slurry (by closely monitoring the media and slurry angular positions) would allow for just on-time detection of the load expansion and appropriately tuning the mill to operate with grinding zones properly saturated with slurry. Equally, the degree of mill filling and the proportion of grinding media relative to the ore could be well controlled within the established desirable range to reduce the operating costs

while maintaining the grinding performance at optimum level. Also, the solids concentration in slurry could be set at a level that yields favourable conditions of slurry viscosity and density required to achieve optimal mill product size distribution and energy efficient grinding. Note that slurry viscosity and density are generally considered to have significant influence on the flow and entrainment of slurry within the grinding media and its discharge from the mill as well as the motion and behaviour of the grinding media. These events impact heavily on the mill power draw and grinding efficiency.

Furthermore, having good knowledge of in-mill slurry transport behaviour, mixing pattern, holdup volume and residence time distribution (RTD) for any set of operating conditions enables better control of the milling process, which in turn leads to improved milling efficiency.

While the advances in instrument technology and computer capabilities have enabled the development of special instruments and measuring techniques to monitor the in-mill dynamics, some challenges still remain posed. Firstly, the target data captured by the measuring instruments is more often presented to the mill operators in an ambiguous format which requires further interpretation before necessary mill control actions can be implemented. This creates a possible scenario for inadequate interpretation of data as well as data misinterpretation. Secondly, in some cases the features which may carry information related to the process remain concealed in the raw measured data presumably due to lack of valid interpretation schemes. As one possible means to address the above shortfalls, the raw measured data could be linked to mathematical models which relate the measured parameters that define the in-mill dynamics to key variables involved to give an intelligent interpretation of the data. This approach, due to reduced interpretational uncertainties, would assist in easily identifying the sources of concerns, and allow confident implementation of mill control actions.

1.2 Research objectives

This thesis seeks to obtain clear and deeper understanding of the dynamic behaviour of media and slurry inside an overflow-discharge ball mill and transform the data obtained into valuable information that would aid mill operators and process engineers in timely decision making with regard to mill control and performance optimisation. One way would be to use the experimental data generated to develop mathematical models that relate various measurable aspects of media and slurry behaviour inside the mill such as media and slurry dynamic positions or slurry residence time distribution to key operational variables such as mill load volume or slurry properties and performance indices such as mill energy efficiency. These models may serve as predictive tools for providing insights of the process and thus they would lay ground on which sound control schemes can be created for improved mill product quality and process performance.

1.3 Thesis outline

The work presented in this thesis is organised into 10 chapters based on both laboratory and industrial investigations. The current chapter has presented the background, motivation and scope for the research work to follow.

Chapter 2 presents a review of literature on measurement and modelling of mill load behaviour. The progress made to date and the areas where information is still lacking are highlighted. Hence, this chapter provides a context for the research work to follow.

Chapter 3 describes the experimental equipment and the measuring system components used in the work undertaken for this thesis as well as the programs involved and the methodology applied.

Chapter 4 presents both the laboratory and the industrial data obtained from measurements of media and slurry dynamic behaviour using direct load sensors

and the subsequent analysis and discussion. Analysis of sensor response data revealed some useful information that is related to mill operational parameters and performance indices. As it shall be seen, this information can be potentially utilised for process control.

Chapter 5 uses the characteristic features extracted from the media and slurry sensor signals data discussed in chapter 4 to predict the in-mill slurry density and load volume by multivariate modelling. Two multivariate modelling approaches are considered: the partial least squares (PLS) and a hybrid combining PLS and radial basis functions neural network (RBF). The results indicate adequate predictions of ball load volume and slurry density. This is a clear demonstration that the characteristic features contained in media and slurry sensor signals data in combination with multivariate modelling could provide a promising means to improve the mill control, through effective monitoring of changes in mill operational conditions.

Chapter 6 is dedicated to the study of the in-mill slurry flow pattern and mixing rate in a laboratory ball mill using gamma emission imaging technique. Fundamental information relating to in-mill slurry transport behaviour is generated that might be resourceful in diagnosis and control of ball milling process. But despite this progress, some challenges still remain posed with regard to the extension of the technique to full scale mills.

Chapter 7 deals with the analysis of slurry residence time distribution (RTD) data obtained on an industrial overflow ball mill through salt tracer tests. A novel method is proposed to estimate slurry feed rate and volumetric holdup inside the mill by tracer balance technique based on measured RTD data.

Chapter 8 presents two models describing the data discussed in chapter 7. The first model describes the in-mill slurry residence time distribution (RTD) while the second describes the in-mill slurry volumetric holdup. Once accurately calibrated, the two models could provide a simple means of estimating slurry residence time

and holdup volume inside the mill without necessarily having to perform tracer tests providing the values of measurable variables in the models are known. This would save on both cost and time associated with experimentation.

Chapter 9 presents an improved mixing-cell model that is able to account for the effects of non-ideal processes such as axial mixing, cross-flows and short-circuit flows on the main flow of slurry inside an overflow-discharge ball mill. The model is successfully applied to characterise the in-mill slurry hydrodynamic transport based on the RTD data discussed in chapter 7. Considering the strong influence of slurry hydrodynamic transport on milling efficiency of an overflow discharge mill, correct knowledge of in-mill slurry transport characteristics would allow the mill to be appropriately tuned to achieve desirable in-mill behaviour that corresponds to optimum mill performance.

Chapter 10 presents the main conclusions drawn from the work described in this thesis and offers suggestions for future work, completing the thesis.

This thesis thus provides invaluable information relating to media and slurry dynamic behaviour inside an overflow-discharge ball mill that has hitherto been veiled but which is critical towards developing best strategies for effective mill control and performance optimisation.

CHAPTER 2

Literature Review

2.1 Introduction

The work done in fracturing of mineral bearing ore particles in a grinding mill is proportional to the energy applied (Fuerstenau and Han, 2003). Thus, for maximum efficiency in ore breakage, the energy delivered to the mill should be efficiently transferred to the mill grinding zones. In general practice the liner characteristics, mill filling, media size and mill rotational speed are considered to be the most important variables in the quest to meet this objective. This is due to their strong influence on the load lifting capacity inside the mill which in turn defines the energy distribution within the mill load. However, it should be borne in mind that for mills operated at constant speed and filling level typical of conventional ball mills, factors such as slurry properties and its complex hydrodynamic interaction with the grinding media are the principal sources of concern. Comprehensive understanding of these dynamics is vital for establishing an effective mill control scheme and optimising the milling process so as to achieve desired throughputs efficiently and economically.

This chapter presents a review of some of the studies accomplished to date which make available information on the mill internal behaviour, both at laboratory and full scale levels. Also included is a brief discussion on the previous efforts by other researchers, aimed at modelling the mill load behaviour. Hence this chapter provides *a priori* knowledge and understanding on whose base the research work to follow is built.

2.2 Description of mill load behaviour

The mechanism of media and slurry motion inside a wet overflow ball mill and the subsequent behaviour of the mill have only been superficially explored in literature. This is owing to the various limitations ranging from experimental costs to technological difficulty. The focus has largely been on measuring the dynamics inside dry grinding mills. The use of direct and indirect measurement techniques has been reported with their various levels of success and shortfalls.

White (1905) was notably among the early researchers who reported some work on mill load motion. He studied the ball paths in a laboratory tube mill in an effort to establish the most efficient milling speed for any given case. Others include Rose and Sullivan (1958) who observed the load position inside a laboratory scale mill having transparent glass windows and attempted to develop a dynamic theory called surging. They described it as the pendulum-like oscillation of the whole charge about the mill centre. Although their work was confined to dry mills it laid a good foundation for further explorations in both dry and wet mills.

Generally, the dynamic position of the load inside the mill at low speeds can be represented by the profile shown in Figure 2.1(a) that resembles a kidney. However at high mill speeds, the load dilates and part of the media starts to cataract (i.e. a portion of the load is thrown from the shoulder into free flight, clear of the *en masse* load) with the load assuming a different shape characterised by four distinct regions as illustrated in Figure 2.1(b), redrawn after Liddel and Moys (1988). In region 1, the balls are rising in circular paths; region 2, the balls are rising in non-circular paths and having relative motion to each other and to the mill; region 3, the balls are falling in parabolic (cataracting) or rolling (cascading) paths while region 4, is the bed toe position where balls are in random and turbulent motion.

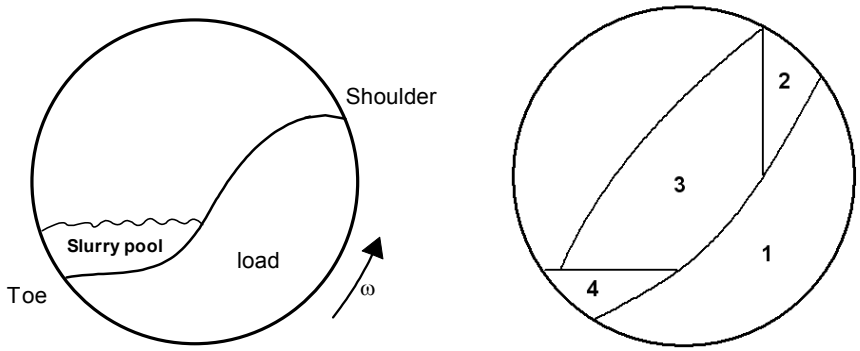

(a) (b)

Figure 2.1: **(a)** Load position at low mill speeds **(b)** Various regions within the load at high mill speeds.

With a continuous increase in mill speed, a point is reached when the cataracting load would start to impact directly on the descending side of the rotating mill shell away from the toe of the load. This behaviour causes excessive wear of liners and a reduction in mill power draw. With further increase in mill speed, beyond the critical speed, the load may start to centrifuge. This is a phenomenon where a layer of the balls adheres on the mill shell and continuously rotates with it thereby reducing the load effective mass and mill effective diameter. Premature centrifuging may also set in under mill overload conditions as reported by Van Nierop and Moys (1998).

In the wet milling process, the slurry is normally entrained in the load taking up the voids volume and hence directly influences the motion of fine particles out of the mill and the distribution of coarse particles to the breakage fields. If the volume of slurry exceeds the voids volume (i.e. if the fractional voids filling exceeds unity) then a pool of slurry forms at the load toe position. This tends to be located on the opposite side of the load as shown in Figure 1(a), thus aiding in the mill rotation, which consequently lowers the mill power draw. However, with correct knowledge of the load motion and behaviour under the given mill design and operating conditions, the mill can be tuned to operate with the correct level of slurry that would enhance efficient grinding. In overflow mills, a certain constant level of pool has to be maintained to facilitate the discharge of fine material from the mill.

2.3 Factors influencing load behaviour in a wet ball mill

2.3.1 Slurry properties

Mineral slurry is a mixture of fine ore particles and water where the latter serves as a carrier fluid. The properties of slurry are crucial in achieving efficient flow and distribution of slurry within the load and subsequent transport out of the mill. Slurry viscosity and density are generally considered to be the main properties which significantly influence the flow behaviour of mineral slurry.

2.3.1.1 Slurry Viscosity

Viscosity of a fluid can be generally defined as a measure of its resistance to flow. Therefore it is a function of shear stress, which acts between two layers of fluid lying adjacent to each other. Mathematically, the gradient of the flow curve (i.e. shear stress versus shear rate), for "Newtonian" flows gives the viscosity of a fluid but where the flow curve is non-linear, the fluid can be regarded as "non-Newtonian". Mineral slurries generally display non-Newtonian behaviour due to heterogeneous nature of the slurry composition.

Klimpel (1982) characterised the viscosity of mineral slurries into three regimes based on the rheological properties: Dilatent (low slurry density), Newtonian pseudo-plastic (slurry density near to maximum breakage rate) and pseudo-plastic with high yield stress (high slurry density), illustrated in Figure 2.2.

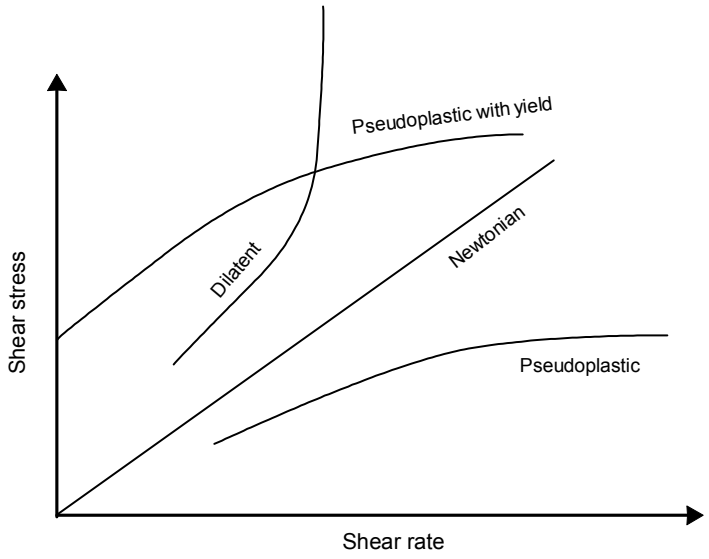

Figure 2.2: Rheological behaviour of slurry (Klimpel, R.R, 1982)

They noted that slurry viscosity should be sufficiently high to give matching higher breakage rates. However, excessively high viscosity would result in very thick slurry, which cushions the impacts thus reducing the stressing force which is

necessary for breakage action. Similarly, highly viscous slurry would cause bridging of grinding media on mill liner wall which may assist the load to centrifuge prematurely. On the other hand, low viscosity (dilute slurry) implies that the cohesive particles behave like a fluid thus flowing away from the grinding zones and allowing direct contact between grinding media which results in media wear. Hence an optimum value of slurry viscosity that corresponds to maximum breakage rate must exist.

Kawatra and Bakshi (1996) reported a decreased breakage of media sized ore and an increased production of critical sized material with increasing viscosity. However a decrease in grinding rate was observed after reaching a certain level, which was attributed to excessively thick slurry in the mill. Similar observations were reported by Tangsathitkulchai (1989) who noted a slowing down effect in a laboratory wet grinding mill with quartz slurry. In his conclusions, he pointed out that slowing down of grinding may occur at any particles size depending on the level of slurry viscosity.

According to Smit (2000), slurry viscosity determines the interaction between slurry and media and has a significant effect on mill load behaviour. He observed that slurry entrainment and flow within the grinding media and its discharge heavily depends on its rheology and subsequent behaviour of the load. This is in-line with the findings by Songfack (1996) who further observed an effect of slurry properties on the slurry build-up in the mill (i.e. slurry hold-up). Highly viscous slurry would offer greater resistance to flow in the pool and within the grinding media leading to a reduction in slurry discharge rate and subsequent build-up of slurry in the mill. The mill will then “go off the grind” (Austin *et al,* 1984). The mill ‘overload’ point is then reached which is characterised by excessive appearance of grinding media in discharge slurry, mill choking and slurry spillage from feed end (Moys 1986). Therefore, rheology may be the key to more effective mill control as reiterated by Moys (*Op cit*).

Slurry viscosity is a strong function of solids concentration and is affected by other properties such as particle size distribution and temperature inside the mill, which makes it a difficult property to measure. Presented in Table 2.1 are some of the models that have been proposed in literature which show an exponential dependence of slurry viscosity on solids concentration (% solids) in slurry.

Table 2.1: Viscosity as a function of solids volume (C_v), (Nicholas, 1986).

$\frac{\mu}{\mu_f} = Exp\left(\frac{2.5C_v}{1-kC_v}\right)$	$0.75 \le k \le 1.5$	Mooney (1951)
$\frac{\mu}{\mu_f} \approx Exp(4.58C_v)$	$C_v \le 0.30$	Happel (1957)
$\frac{\mu}{\mu_f} = 1 + 2.5C_v + 10.05C_v^2 + 0.00273Exp(16.6C_v)$		Thomas (1965)

in which μ/μ_f is the relative viscosity while C_v is the fraction of solids, by volume, which is related to % solids by weight in the feed as shown by equation 2.1:

$$C_v = \frac{(w_s/\rho_s)}{w_s/\rho_s + [(1-w_s)/\rho_l]} \qquad [2.1]$$

Where

w_s : Weight fraction of solids in the mixture.

ρ_s : Specific gravity or density of the solid.

ρ_l : Specific gravity or density of the liquid (dilution water).

In essence, clear information about slurry viscosity and its influence on mill internal dynamics would help characterise and control the milling process for efficient operation.

2.3.1.2 Slurry density

Slurry density is closely related to slurry viscosity and hence it is an important parameter in ore grinding process. A change in slurry density might greatly

influence the movement pattern of the balls and the flowability of slurry within the ball charge during mill tumbling process. This would be accompanied by a change in grinding performance which should be traditionally reflected by a change in mill power. For a mixture of media and slurry, the slurry density is defined by the percentage by weight of solids in the mixture and hence is closely related to slurry viscosity. Slurry density can be calculated using the following expression based on elementary physics.

$$\rho_{sl} = \frac{1}{\left(w_s / \rho_{solids} + (1-w_s)/\rho_{water}\right)} \qquad [2.2]$$

Where

w_s	:	Weight fraction of solids in the mixture.
ρ_{solids}	:	Specific gravity or density of the solid.
ρ_{sl}	:	Slurry density/specific gravity
ρ_{water}	:	Specific gravity or density of the liquid (dilution water).

Slurry density increases gradually with percent solids which directly effects the distribution and mass hold-up of slurry charge within the mill (Songfack and Rajamani, 1999; Nasr-EL-Din *et al,* 1992). This in turn affects the moving path of the balls and thus the interaction between the particles and the grinding media. The slurry density is related to its mass hold-up in the mill as follows:

$$M_{sl} = \rho_{sl} U \varepsilon_v J_L V_m \qquad [2.3]$$

Where

U	:	Fractional filling of voids with slurry.
ε_V	:	Voidage in the load (voids volume fraction).
J_L	:	Load volume as a fraction of the mill volume.
V_m	:	Volume of the mill.

Hogg and Rogovin (1982) found out that the level of solids concentration in slurry has a significant influence on the slurry flow and holdup inside the mill. They showed that the residence time of solids inside the mill is higher than that of the fluid. However, only low levels of solids concentration were tested (24 – 46%). Further, they proposed a mill model which predicts the optimum grinding at the interstitial filling of slurry (U) slightly higher than 1 (load with a small pool of slurry). Under this condition, the charge motion through the slurry pool is governed by the slurry density, which is directly affected by its viscosity. At high slurry viscosity and hence high slurry density, the media encounters some drag and buoyancy forces, which reduces the impact forces between the media and the ore rocks. This information is useful in determining the mill torque and power draw under the varying slurry properties.

Tangsathitkulchai and Austin (1989) using quartz as the test material in a batch ball mill and with the aid of photographic techniques observed that slurry density (related to viscosity) affects the distribution of solid charge in the mill and the circulation paths of balls. Various grinding characteristics were noted which were attributed to the change in behaviour of the balls and slurry under changing levels of slurry levels.

2.3.2 Mill liner and lifter design

In tumbling mills, the load motion and power draft are largely influenced by the type of liners and the configuration of lifters where present. McIvor, (1984) revealed that for a given mill speed and filling, the trajectories of the ball charge depend on the lifter profile and leading line face angle which may have a profound effect on the mill performance. He noted that the point at which the balls depart for parabolic flight and the point where they impact on the mill shell at the end of their parabolic flight are sensitive to the leading angle. He further observed that an increase in height of lifters causes the balls to follow higher trajectories. His analysis is suggestive of the fact that the entire load motion is dependent on the behaviour of the outer layer of balls in contact with the mill liners.

The design of lifter profiles (height and face angle) goes in tandem with the mill operating conditions and performance requirements. It is well understood by mill operators that liners having lifter bars with gradual profiles would retain their profiles a bit longer compared to those with sharp edged profiles; but to achieve more cataracting, sharper edged profiles are preferred. However, other researchers (Powell and Vermeulen, 1994; Hlungwani *et al*, 2003) have acknowledged that no single liner design exists which would give optimum performance in all mill types. Different liner profiles give varying performance levels in different mills, which imply that any small change in operating parameters is bound to have a profound effect on the liner performance. Therefore, in milling practice an optimum design has to be sought or the existing one modified or optimised to yield the required results under given conditions.

Fuerstenau and Abouzeid (1985) studied the effect of lifters on the grinding kinetics and energy consumption in a tube mill. They found out that the specific energy consumption (Kwh/t of product) was higher in a mill with smooth liners i.e. in absence of lifters. This was presumably due to the load slippage, which is in line with the experimental observations by McIvor (1984).

Liddell and Moys (1988) using a laboratory mill with smooth liners established that slip was predominant for mill fillings below 30%. However, for mill filling beyond 30%, slip reduced with increase in mill speed. They concluded that, at high mill filling, the load exerts more dynamic pressure on the mill liner wall, which helps to 'key in' the load to the mill rotary motion thus reducing slip. Liddell's observations further underscore the significance of the liner/lifter effect on the accuracy and consistency of the mill power models.

Moys (1993), investigated the influence of four different liner designs on the mill load behaviour and power draw, in an effort to develop a semi-empirical mill power model. The effect of speed and mill filling was similarly assessed. The experimental work was accomplished on a laboratory mill of 530mm diameter (inside liners) and 300mm long using steel balls having size distribution of 12mm,

18mm and 25mm. The Grid and Shiplap liners exhibited excessive slippage at low mill fill levels (less than 20%) up to the speeds of 100% and 120% of the critical respectively. Above this range, the load assumed the behaviour similar to cases with liners having lifter bars. The smooth liner with half the number of lifter bars yielded more power at sub-critical speeds. This observation was similarly reported by Powell (1991).

Moys (1993) further reported the occurrence of centrifuging at lower speed in a mill fitted with lifter bars than the one without the lifters. This behaviour serves to explain the ultimate reduction in mill power draw that follows the insertion of lifters in high-speed mills. The high lifter profile assists in locking the load to the rotary motion of the mill which may aid in centrifuging at higher mill speeds. This observation once more confirms the theory of 'critical lifter height' which is dependent on the mill operating speed.

Powell and Nurick (1996 b, c) studied the load motion in a small Perspex mill (190mm diameter by 97mm long) using both X-ray and Gamma video cameras. They reported a phenomenon of radial segregation in the load, which was governed by the mass and size of the balls, radial location of the balls and the liner geometry. Larger balls concentrated progressively to the centre of charge at high mill speeds (above 82% of critical) but segregated to the periphery of the charge at low mill speeds. At speeds beyond 90% of critical, the effect of mass and size operated in opposite directions. The ratio of their distributions would determine the direction of segregation. They found that lifter height influenced the ball trajectories, and that the optimal lifter face angle was a strong function of mill speed. Their study gives a significant contribution to the knowledge of load dynamics and the influence of lifters.

The radial segregation of the load has an influence on the mill grinding behaviour. Where the larger ore rocks are found at the periphery, breakage would predominantly be by impact while at the centre of the load attrition breakage would

dominate. The heaviest balls force their way down through the cascading load and concentrate near the centre of the mill to attain a low energy state in the load.

Therefore clear understanding of the load motion and the interaction behaviour with the liners/lifters is of significance to mill operators and designers. With this information the mills can be tuned to achieve appropriate flow pattern of the charge that ensures effective grinding.

2.3.3 Mill rotational speed and media filling level

The load motion inside the mill is sensitive to mill rotational speed and level of ball filling inside the mill. Ball mills typically operate at a constant speed in the range of 70 – 80% of critical speed depending on the level of mill filling. At speeds above 80% of critical, the load motion would assume a predominantly cataracting regime. Some of the impact energy of the cataracting media is converted into a turning moment contributing to the mill rotation hence lowering the mill torque. At speeds above 100% of critical, the balls on the outer layers would start to centrifuge, reducing the mill active load, thus contributing to the loss of mill power (Moys, 1993). At higher mill fillings, this phenomenon may be experienced at speeds slightly below 100% of critical. Therefore the choice of mill operating speed and load filling should be optimized to ensure the mill operates with maximum throughput at minimum costs (i.e. decrease energy consumption and reduce wear of liners and grinding media).

2.4 Overview of mill load behaviour measurements

Literature presents several methods of load behaviour measurement that have been explored by researchers to date. The methods can be classified into two categories; non-intrusive and intrusive. Non-intrusive methods include the use of acoustics such as microphones mounted close to the mill shell to record the sound signal emanating from the mill. In this case, changes in load position inside the mill are

detected by relating the sound power of the microphone(s) with mill operational variables (Watson, 1985). Other examples of non-intrusive techniques which are progressively developing include Positron Emission Particle Tracking system (PEPT) and Gamma Emission Imaging technology both of which involve the use of radioisotope tracers. One merit of the radiotracer techniques is that they can be applied in harsh environments where conventional methods have been infeasible. This might help to unravel some hitherto veiled information about the internal flows in such systems. Following the establishment of International Atomic Energy Agency, 1945 to regulate the licensing and use of radioactive materials, a range of radiotracers have been developed that can be applied for research as well as diagnostic examination in various industrial processes.

The PEPT technique involves irradiation of a particle within a system and as the particle decays, nuclear reactions cause a pair of coincident X-rays to be emitted which are detected by the PEPT camera. By using a reconstructive algorithm the position and hence trajectory of the particle can be computed (Conway-Baker *et al*, 2002). This is demonstrated in the work presented by Barley *et al* (2004) which describes the motion of the grinding beads within the stirred mill under different operating conditions. While this approach appears feasible, the inability to track multiple particles simultaneously presents a major limitation to its accuracy especially in systems involving complex multiphase flow, typical of wet ball mills.

Gamma emission imaging technique on the other hand can provide continuous tracking of the radiotracer in space and time (Ziock, 1995; Ivanov *et al* 2004). Although the technique was specifically developed to be used for medical tomography, increased interest from researchers and industrialists have led to the development of portable compact gamma imaging systems which can be applied to harsh industrial environments for process diagnosis and control, (IAEA, 2008). The relatively high energies of γ-rays enable imaging of processes that are hidden behind thick vessel walls, which makes this technique preferable to other methods like positron emission tomography (PET), for industrial process tomography. Also

it is suitable for multiphase flow systems where information on a specific phase needs to be obtained in time and space.

Previous work by (Kantzas *et al*, 2000 and Jonkers *et al*, 1990) demonstrated that the application of gamma ray emission imaging technique could be extended to research in industrial processes such as fluidized beds where direct visual observation is infeasible. Separately, they applied γ-ray imaging technique to study multiphase flow in porous media with ascertainable level of success. Using radiotracers the dynamics of fluid distribution and saturation were recorded and analysed. However, due to inadequacy of their data acquisition and processing system, their results were only qualitative in nature. Surprisingly nothing has been reported with reference to the hydrodynamics of the wet ball mills, presumably due to lack of laboratory calibration and characterisation data related to ball mills.

Residence time distribution (RTD) methods provide another non-intrusive approach to studying the in-mill slurry behaviour. Typically, measuring of RTD involves introduction of a tracer at the feed and continuously or discretely monitoring the response at the discharge in terms of conductivity or concentration (Gardner, *et al*, 1975). The shape of RTD curves depends on the combined effect of the flow behaviour and mixing performance inside the process equipment, which is usually related to the RTD function parameters i.e. mean residence time and variance. This information is important for diagnostics as well as control purposes. Process malfunctions such as bypassing, channelling or existence of dead volumes can easily be detected. Studies by Kelsall *et al* (1970), Hogg (1984), Kinneberg and Herbst (1983), Austin *et al* (1984) and King (2001) have shown that residence time distribution function is a key component of the breakage behaviour model for continuous mills. The residence time distribution function describes the flow through the mill while grinding equations describe the breakage behaviour as a function of time. Although the residence time distribution methods can be applicable to opaque systems they can only provide Eulerian type data (local instantaneous information on the flow field) which limits their applications.

Unlike non-intrusive methods, intrusive techniques involve the use of contact sensors to directly probe the load behaviour inside the mill. Direct interaction of the load with the sensor, instils some level of accuracy which certainly renders this approach appealing. One such technique that is quickly gathering popularity in mineral processing research industry is the use of electro-mechanical sensors. Nevertheless, its application remains confined to laboratory and pilot scale mills seemingly due to exceedingly rough conditions inside an industrial mill. However, with the current advances in instrumentation technology, improvements can be made on these sensors that would allow for direct measurement of the load behaviour inside industrial mills; a consideration that constituted part of the motivation for this research work.

Moys (1985) and Vermeulen *et al* (1985) were notably the first ones to explore load behaviour inside a mill using direct contact sensors. Moys (*op cit*) used an electrical conductivity sensor installed on a pilot mill to measure the variables that characterise the load behaviour inside the mill. The effects of, mill speed, load volume and slurry properties on load behaviour were explored. The same measurement principle was applied by Vermeulen *et al* (*op cit*) on an industrial mill using both conductivity and piezo-electric sensors. Some useful information was obtained about the level of cataracting inside the mill and the angular distribution of the impacts. This information could be useful in establishing the regions or fields within the load where grinding is more effective so that mills can be appropriately tuned to achieve that flow pattern.

Other similar studies reported in literature include Moys and Montini (1987) who used an electrical conductivity sensor to probe the load dynamic orientation in a pilot scale ball mill. They studied the effect of design and operating variables on load shoulder and toe positions and determined the height to which the charge was lifted with increase in mill filling. At the same time, they explored the effect of slurry % solids on load shoulder angle at fixed mill speed and filling. It was possible to estimate the slurry viscosity in the mill based on the slurry thickness on the probe and its rate of drainage from the probe at the shoulder position. Slurry

viscosity is a pertinent parameter in mill control process and the success of this technique though simple could be a great step towards realizing effective control of wet grinding mills, considering the complexities associated with direct measurement of slurry properties.

Moys *et al* (1996) investigated the load behaviour in a wet pilot scale mill using both conductivity and force probes to acquire information of the load position inside the mill. The dynamic orientation of the load and slurry hold-up in the pilot mill were determined for both overflow and grate discharge arrangements. The presence of a slurry pool for overflow discharge arrangement as indicated by the conductivity probe data was in line with the expectations and is consistent with the observations by other researchers such as Morrell (1993). Their studies further indicated a strong effect of slurry viscosity on mill load behaviour and power draw. In further investigations, Van Nierop (2001) used conductivity and movement probes to measure the load behaviour of an industrial autogenous mill. The experimental variables were; mill rotational speed, load volume/mass, slurry viscosity and slurry density. He determined the load toe and shoulder positions which he used to calculate the load angle of repose (α), an important variable in mill power modelling. The load shoulder position was a strong function of mill speed, mill filling and percent solids while the toe position was invariant at low mill speeds and filling. From the conductivity data, it was possible to detect the onset of premature centrifuging of the load with highly viscous slurry. This observation was a clear indication that an optimum level of slurry viscosity exists where grinding would proceed efficiently.

Tano *et al* (2005) used a strain-gauge sensor embedded in a rubber lifter to measure the flow resistance of slurry and the load inside the mill in response to change in slurry percent solids. The toe and shoulder positions of the load as recorded by the sensor, varied in a systematic way from which the load flow regime could easily be deduced. Nonetheless, the respective positions of slurry and media could not be distinguished which constitutes the main shortfall of this technique.

From the studies described in the foregoing, it is apparent that both electrical conductivity and strain-gauge sensors can give useful information about the media and slurry angular positions inside the mill. However information about the relative position of the grinding media and slurry cannot be accurately obtained; especially in cases where a substantial proportion of the grinding media is cataracting or the slurry is so thick that it saturates the probe. This surely indicates the challenge that faces a single sensor in an effort to detect all the phenomena occurring in a multivariate process typical of wet ball milling.

Kiangi and Moys (2006) implemented a new technique for detecting the angular position of ball media inside the mill using an inductive proximity probe. A series of tests were performed on a dry pilot mill of diameter 0.54m and length 0.2m using steel balls as grinding media and dry quartz powder to simulate the ore. The probe data were used to calculate the toe and shoulder positions for the ball media. This technique could be adapted easily to a wet ball mill in combination with a conductivity probe to yield clear information about the media and slurry positions inside the mill, which forms part of the motivation for our research.

In further quest for information on mill internal dynamics, Behera *et al* (2007) studied the mill vibration signals using an accelerometer mounted on the mill shaft. The vibration signals were analysed as a function of mill speed, load (media and ore) filling and grinding time using Fast Fourier Transform (FFT) technique and correlated with mill internal behaviour. Mill conditions such as overload and surging were reliably detected from the interpretation of the vibration signal peaks. However, other facets of load behaviour which are useful for mill control purpose such as the flow pattern of powder (or slurry for wet mill) within the media and the proportion of media to powder (or slurry) cannot be detected by this technique which poses a challenge.

More recently, Clermont *et al* (2008) presented a new method of measuring the load position inside an industrial mill using the SENSOMAG® sensor, which is basically a combination of an electrochemical probe and a proximity probe. They

obtained information about the angular positions of the ball media and slurry inside an industrial mill. They suggested that this information could be used together with mill power data to determine the level of mill filling and slurry loading via relevant mathematical models. However, further tests are required both at laboratory and industrial scale levels to assess the viability of the sensors and acquire more data for their calibration.

In this study, new techniques for measuring the dynamic behaviour of the media and slurry inside an overflow ball mill are explored both at laboratory and full scale levels. On a laboratory scale, a hybrid sensor comprising of a conductivity probe and an inductive proximity probe has been used to measure the dynamic positions of the media and slurry while a non-contact technique that utilises a Gamma ray camera was employed to study the slurry flow path and mixing profile inside the mill. In the latter case, Technetium (^{99m} Tc) radioisotope in an aqueous form was used as a radiotracer. On industrial scale, an online ball and pulp sensor was employed to monitor the angular position of balls and slurry while salt tracer tests were applied to study the mill internal flows and residence time distribution.

2.5 Load behaviour modelling

While researchers and industrialists generally agree that accurate models of mill load behaviour could be the key to accurate design and effective control of grinding mills, it is surprising to note that the subject has only been moderately addressed over the past years. The focus has been on studying the effects of mill design and operating factors in efforts to obtain information that would help in calibration of mill power models. Developing models for load behaviour could be the way forward since mill power is derived from load behaviour. Upon recognizing this challenge, Mishra and Rajamani (1990, 1992, and 1994) adapted and applied a numerical scheme called Discrete Element Method (DEM) to study the in-mill behaviour. In 1996, they successfully implemented DEM to simulate a dry SAG mill and obtained information on load motion and power draw. Since

then, other researchers have come up with efforts to further validate and apply DEM in milling. Prominent among them include Cleary (1998), Hlungwani *et al* (2003) and Radziszewski (1999).

One inherent success with DEM is that balls can be allowed to cascade, interpenetrate between layers, and also cataract. The balls can bounce off the lifters and mill shell and balls of different sizes can collide with each other obliquely. Therefore fairly accurate information of the load dynamics inside the mill can be generated by this numerical method as it allows the balls to take their paths depending on their collisions with other balls and the mill wall. Hence, DEM becomes a potentially useful tool for mill control and optimisation. Cleary (*op cit*) used DEM to predict the charge motion and liner wear in tumbling mills with success. He maintains that the use of numerical techniques is the surest and cheapest way to study the in-mill dynamics considering the nature of mill internal environment which is hostile to electronic sensors.

In modelling of wet mills, DEM suffers from one major shortfall in that it assumes a soft contact approach in a Lagrangian computational domain and models particles as distinct but interacting elements whose dynamics are determined by Newton's equations of motion. This limits its ability to delineate the true effect of slurry in the load. Therefore information about the slurry position, its flow pattern within the load relative to the grinding media may not be clearly obtained.

In an attempt to adapt DEM to wet milling, Cleary *et al* (2006) presented a sequential numerical scheme that combines DEM and SPH (Smoothed Particle Hydrodynamics) models to simulate the load behaviour in a SAG mill. Smoothed particle hydrodynamics (SPH) is a basically a computational method used for simulating fluid flows. It works by dividing the fluid into a set of discrete elements, referred to as particles. These particles have a spatial distance (known as the "smoothing length"), over which their properties are "smoothed" by a kernel function. This means that any physical quantity of any particle can be obtained by

summing the relevant properties of all the particles which lie within the range of the kernel.

In a combined DEM-SPH model, DEM simulation is first performed to characterise the load as a dynamic porous media through which the slurry can be able to flow. This information is then transferred into the SPH model through Darcy drag laws and Kozeny-Carmen permeability relationship to predict slurry motion within the media. In view of the challenges presented by this method as reported by Cleary (*Op cit*), it is clear that more experimental data is required to correctly validate the model in order to reliably predict the behaviour of the grinding media and slurry inside the mill as a function of key mill operational variables. However, their efforts serve as a source of impetus and a good starting point for further investigations.

2.6 Conclusions

From the information presented in this chapter, it is apparent that a major impediment to successful control and optimisation of wet milling systems is lack of precise knowledge of media and slurry dynamics inside the mill. Therefore, it is expected that future research in the mineral processing industry will continue to focus on efforts aimed at filling the above knowledge gap. Simulation models such as Discrete Element Method and Computational Fluid Dynamics (DEM-CFD) are emerging strongly as useful tools that might provide some insight into this obscure phenomenon. However, this requires accurate calibration of the models against accurate experimental data; but unavailability of appropriate techniques and instrumentation for experimental tests remains a major setback to achieving this objective. As a contribution towards countering the aforementioned challenges, this thesis seeks to make available comprehensive information of media and slurry dynamic behaviour inside the mill by employing a combination of experimental techniques and mathematical modelling.

CHAPTER 3

Experimental Equipment, Measuring System, Programs and Methods

3.1 Introduction

This chapter presents detailed description of the experimental work undertaken for this thesis. The experimental equipment and measuring system components including instrumentation system are described first followed by discussions of experimental programs, measuring techniques, materials and procedures. Both the industrial and the laboratory programs are considered. Difficulties and challenges encountered during the course of experimental planning and execution and the success achieved are also noted here. The data obtained from the experimental programs discussed in this chapter is analysed in subsequent chapters.

3.2 Laboratory mill - 1

3.2.1 Description of the mill rig

Part of the experimental work carried out for this thesis was accomplished using a 3 dimensional laboratory scale mill constructed from steel and mounted on a mill rig. The mill is driven by a 2.5KW motor via a chain drive. The motor speed is controlled electronically using a speed controller (tachometer), which regulates the power supply to the motor by varying the current frequency. The milling chamber measures 550 mm in diameter by 400 mm long (inside liners) and is fixed to the mill axle on which the load beams are connected for torque measurements. The mill is lined with 18 pieces lifters that were suitably scaled down from industrial size. A 10 mm thick PVC disc is used to close the front side of the mill with a provision for feeding and discharging the mill contents during batch tests. The torque yielded by the load beam as a result of the tumbling load is transmitted to the computer as a voltage signal for processing and storage. A desk top computer which is interfaced to the data acquisition system is utilised for real time data processing using the Waveview© program from Eagles Technology. The signals from both the proximity and conductivity sensors are transmitted off the mill to the computer by means of slip rings mounted on the mill axle. Schematics of the experimental set-up can be reviewed in Figure 3.1.

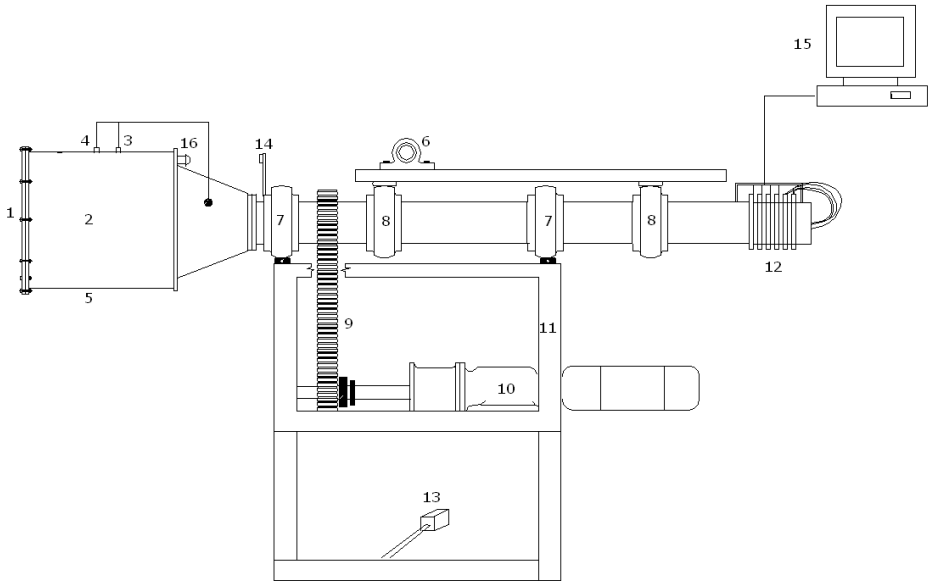

Figure 3.1: Schematic representation of the setup of the experimental equipment and measuring facilities.

Table 3.1 Summary of the important features and test facilities in the experimental laboratory mill setup (mill-1)

1	Front plate (PVC)	9	Chain drive
2	Milling chamber	10	Motor and Gear box
3	Conductivity sensor	11	Support frame
4	Inductive proximity sensor	12	Slip rings
5	Mill shell	13	Axial load beam
6	Pivot load beam	14	Glass mirror
7	Motor gage bearings	15	Computer for data acquisition
8	Axle bearings	16	Phototransistor (PT) and LED

3.2.2 Model Lifters

The size of the lifters used in the laboratory experiments was appropriately scaled down from the industrial scale. The lifters were machined to a face angle of 20^0, tangent to the mill shell. They were installed at radial centre to centre distance of 95mm with lifter spacing to height ratio of 2.91 which lies within the conventional range of 2.5 – 4.5 as reported in literature by Bigg and Raabe (1996). Steel bolts of 8mm in diameter were used to secure the lifters onto the mill shell.

3.2.3 Measurement system components

3.2.3.1 Inductive proximity sensor

The inductive proximity sensor (probe) installed on our laboratory mill measures 30mm x 60mm (diameter x length). The probe is mounted through the mill shell in an inline configuration with the conductivity sensor and secured in position by a special housing. The probe is designed to detect the proximity or presence of any metal object that moves into the operating zone situated immediately in front of its sensing face. This sensing face comprises of a coil and the winding which is fed from an oscillator, the whole creating an alternating magnetic field in front of the coil. Whenever a metal target moves into this field, the resulting induced eddy currents form an additional load, which dampens the oscillations, triggering the output circuit response. Figure 3.2 shows the sensor assembly and installation details while Figure 3.3 schematically illustrates the core features and operating principle of the inductive proximity sensor (probe).

For the purpose of our investigations, the probe sensing surface was shielded from direct abrasive and impact contacts with the tumbling load using a 3 mm PVC plate. It should be noted that this did not hamper the functionality of the sensor since its sensitivity to the metal targets is within the range of 0 mm to 8 mm. The output signal from the sensor was calibrated and attenuated to the range of -5V to +5V for transmission to the computer. For each experimental run a threshold voltage value was established at which the load position could be determined. According to our analysis, the load toe position corresponds to the point where the signal begins to drop continuously to the lowest level while the shoulder position is

estimated at the point where the signal begins to rise steadily. This rule can however be modified on the basis of the observed load behaviour. Details of the analysis of proximity sensor data are discussed in the next chapter.

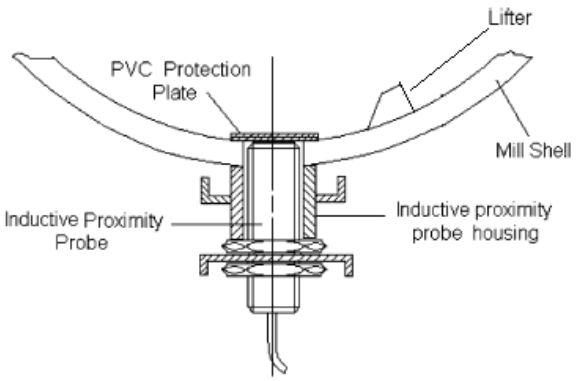

(a)

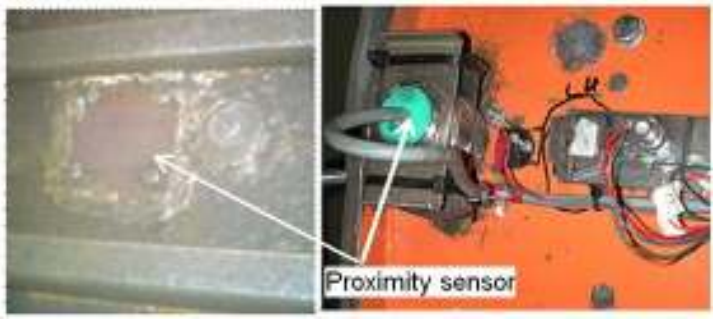

(b)

Figure 3.2: (a) Inductive proximity sensor assembly and (b) installation details.

Figure 3.3: The schematic representation of the salient components and operating principle of the inductive proximity sensor.

Figure 3.4 illustrates the dynamic response analysis of the proximity sensor to the step test. This analysis was deemed necessary and appropriate in understanding the rate of response of the sensor to the excitations, considering further that the sensing surface had been embedded by a PVC plate.

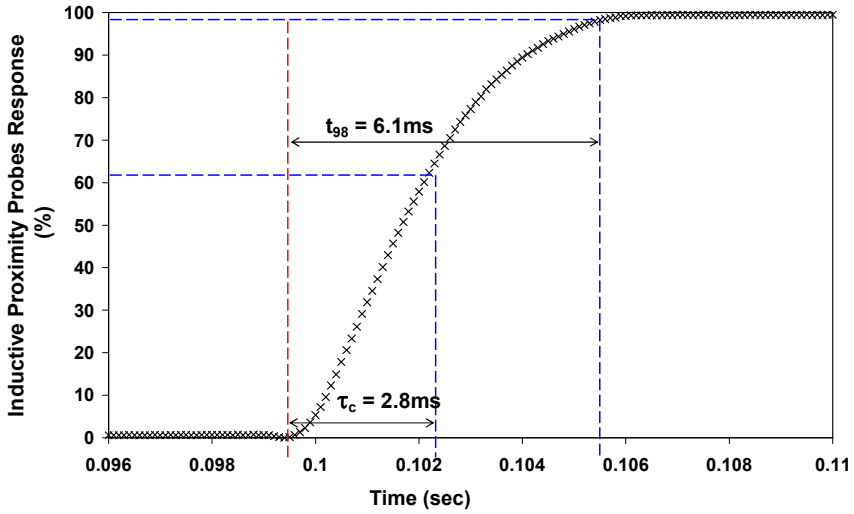

Figure 3.4: Response curve showing the sensitivity of the inductive proximity sensor to a step input.

The test was accomplished by placing a target (piece of metal) on the surface of the sensor as an input or excitation then moving it away in the fastest way possible. The error incurred in the test is estimated to be less than 1% which is within the range of experimental error. The output signal from the sensor was recorded online by a computer, which runs the 'Waveview' program that facilitates the real time data recording and processing.

From Figure 3.4, the response time (t_p) refers to the time taken for the sensor to react to the input or excitation while the rise time (t_r) refers to the delay or time taken before the output (voltage) rises from 10% to 90% of the peak value, as it responds to the instantaneous change in input. The settling time (t_s) on the other hand is the time taken for the sensor output to reach 98% of the final value.

3.2.3.2 Conductivity sensor

The conductivity sensor used in our tests was constructed out of an ordinary mild steel bolt of diameter 6 mm and 20mm long with a flat face. The diameter is small enough to measure slurry position over a small volume in space. The sensor was mounted through the mill shell and secured in position using a locknut as

illustrated in Figure 3.5. The PVC bush and washer insulated the sensor from the mill shell.

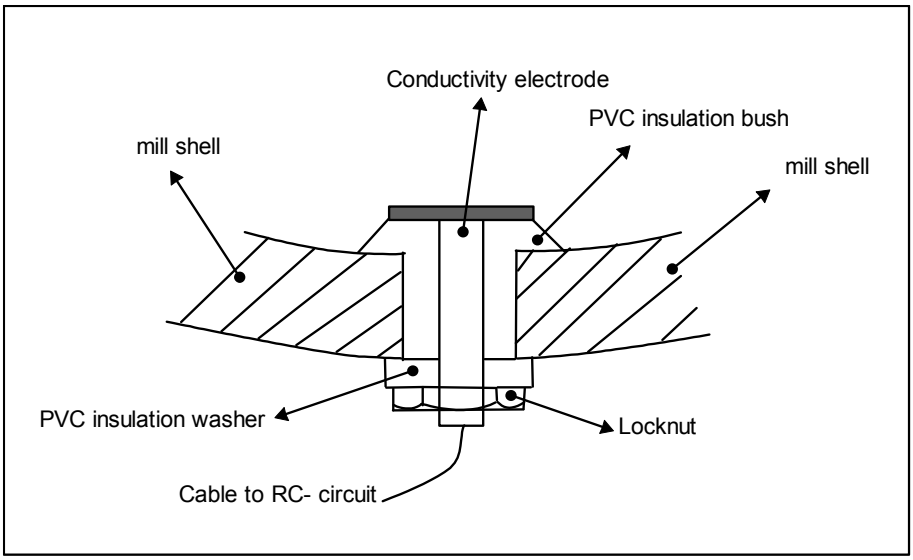

Figure 3.5: Illustration of the conductivity sensor installation details

The conductivity sensor is designed to detect the position of slurry inside the mill relative to the grinding media. It was installed at the same angular position as the inductive proximity probe to allow for comparative analysis of the output signals. A comparison of the two signals would provide some information about the media and slurry interactions inside the mill.

The operation of the conductivity sensor relies on slurry conductance of electrical current. Submersion of the conductivity sensor in slurry results in a lower resistance between the mill shell and the sensor. This in effect causes the shunt-capacitor in the RC-filter circuit to charge leading to an instant rise in the voltage signal. On the other hand, when the conductivity sensor emerges from the slurry, it creates an open circuit with the mill shell causing an instant drop in the voltage signal as the capacitor begins to discharge. The magnitude of the change in voltage is dependent on slurry conductance. Higher solids concentration in slurry results in

higher resistance hence poor conductivity and vice versa. In this study, the conductivity sensor output signal ranges from 0 to -3V. This voltage level lies within the acceptable limit for direct recording to the computer.

Figure 3.6 shows the dynamic response of the conductivity sensor to a step input. This was accomplished by connecting the conductivity sensor to an RC-filter circuit powered by 12V DC power supply. Two conductivity sensor electrodes, one connected to the circuit output and the other to the circuit ground, were placed in a container of tap water. This created a short circuit between the two electrodes hence charging up the shunt- capacitor. The sensor was then withdrawn quickly from the water to create an open circuit hence discharging the shunt-capacitor. The sequence was repeated several times to establish the margin of error (i.e. estimated in the margin of 0.1 – 0.5%). The sensor response pattern is as shown in Figure 3.6. During the discharging circle, it takes 0.012 seconds for the sensor output signal to decay by 98% while on the charging circle it takes only 0.008 seconds for the sensor output signal to reach 98% of its peak value.

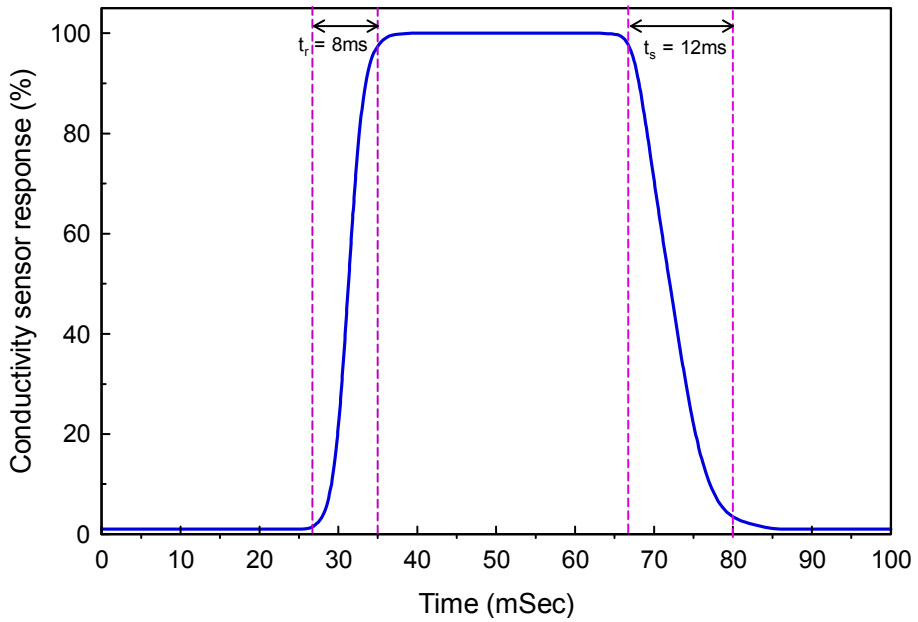

Figure 3.6: Conductivity response curve showing the sensitivity to a step input.

3.2.3.3 Reference probe

This consisted of a phototransistor (PT), a light emitting diode (LED) and a glass mirror. In operation the LED emits light, which is reflected by the glass mirror mounted on the outer surface of the mill in-line with the LED. The reflected light is sensed by the PT which records a signal each time it gets energised. The PT signal indicates the start and end of a mill revolution; hence this serves as a reference point from which the proximity sensor position in the rotating mill can be tracked. The displacement of the proximity sensor signal from the reference signal is recorded at a time interval, which represents a given angular position of the proximity sensor in the mill. The toe and shoulder positions are derived from the position of the proximity sensor relative to the reference signal.

3.2.4 Mill Calibration

3.2.4.1 Torque calibration

The torque was calibrated using a series of known weights suspended vertically at one end of the steel rod. The other end of the rod was connected to the load beam that is mounted to the frame of the mill rig and connected to the mill axle. The value of torque was then obtained from the lever arm principle. According to the principle, the applied torque that counters the rotational motion of the mill maintains the steel rod horizontal. Therefore, the product of the weight of the load and the arm length of the steel rod gives the value of the torque. The exercise was repeated for different masses while the mill was rotated at a low speed of 40% of critical. The calibration curve was obtained by relating the mill torque to the output voltage (from the load beam) to obtain a functional relationship. The losses from the chain drive and bearings were eliminated by subtracting the zero-load torque from the total mill torque. The zero load torque was obtained by running the empty mill over the range of speeds tested. Details of the calibration results can be reviewed in appendix A.

3.2.4.2 Mill speed calibration

The mill used for our experimental studies utilises a tachometer (speed controller) that required calibration. The speed calibration was achieved by setting the

controller to a certain value then measuring the mill speed by taking the mill revolutions for a time period of 60 seconds. This process was accomplished using an online data acquisition system, which is interfaced to the mill rig. The measurements were taken repeatedly at various speed settings to obtain a fairly accurate and representative calibration curve. The mill rotational speed was represented as a percentage of the critical speed where the latter is derived from the balance between gravitational and centrifugal forces acting on the mill load as presented in equation 3.1.

$$N_c = \sqrt{\frac{3600 * g}{4 * \pi^2 * \bar{R}}} \qquad [3.1]$$

Where, N_c : the critical speed
g : the gravity constant
$\bar{R}$: $(R - r_b)$
R, r_b : radius of the mill, radius of the largest ball.

Substituting for all the known constants in equation 3.1 and solving yields a more simplified equation which is a function of only the mill diameter and ball size. The resultant expression is presented as follows:

$$N_c = 42.3 / \sqrt{(D - d)} \qquad [3.2]$$

In which D is the mill diameter (m) and d is the ball diameter (m). The largest ball radius in our experiments was 5 mm while the mill radius was 275 mm (inside liners), which yields the critical speed of 57.6 revolutions per minute. Details of the speed calibration and the associated data can be reviewed in appendix A. Note that the 5 mm radius balls were scaled to mill diameter down from the industrial scale balls of 20 mm radius. However, it is understood that the motion of smaller balls in laboratory mills is more likely to be influenced by slurry viscosity than that of bigger balls in full scale mills; hence the grinding efficiency would be different.

3.3 Laboratory mill –2

3.3.1 Description of the mill rig

In order to investigate radial transport and mixing of slurry inside the mill, a model mill was constructed from Perspex. The mill drum had an inner diameter of 550 mm and a length of 200 mm and was fitted with 18 equally spaced radial lifters (20^0 face angle), made of Perspex. The lifters were fitted on the mill drum using special contact glue and reinforced with specially machined PVC plugs. The mill was appropriately designed to allow for slurry flow visualisation using a gamma camera as well as a video camera. It was mounted on two horizontal rubber rollers which are driven by a constant speed motor via the belt and pulley system; but the mill speed can simply be varied by adjusting the pulley diameter. The central opening on the mill front plate allows for loading and unloading of media while a small opening at the bottom of the front plate provides for draining the slurry from the mill at the end of each experimental run. Figure 3.7 shows the components of the mill rig and the setup.

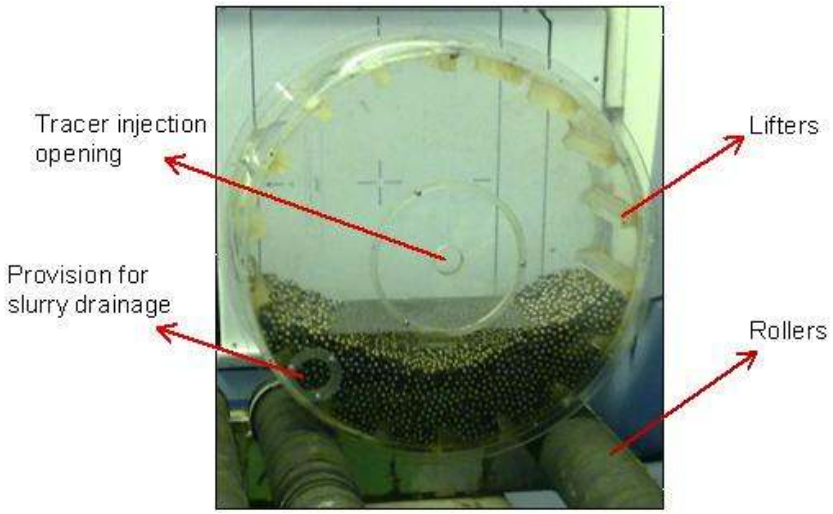

Figure 3.7: Components of the experimental mill rig and the setup

3.3.2 Model lifters

The model lifters installed in laboratory mill-2 were constructed from Perspex material. The lifters had the same height and profile as those in mill-1, and equally spaced around the mill circumference.

3.4 Industrial ball mill

The overflow ball mill utilised in the sampling survey has an inside diameter of 7.312m and length of 9.6m and is run in open circuit. It is used in secondary grinding of UG2 Platinum ore at Anglo Platinum Waterval concentrator, situated in Rustenburg in the North West Province of South Africa. The mill is equipped with 44 rubber lifter bars with height 100mm. Forged Chromium steel balls of diameter 30-40mm are used as grinding media. Under normal operating conditions, the mill ball filling is 30% of total mill volume, mill speed is 75% of critical speed, solids concentration in slurry is 75%, solids feed rate is 330 tph and rated power draw is 9500 KW. The mill has an installed power of 11000kW.

Figure 3.8 illustrates the on-line balls and slurry position sensor system components (SENSOMAG) mounted on the mill. The SENSOMAG system consists of a proximity switch and an electrochemical sensor both assembled into a single unit and installed on the mill through a liner referred to as sensor liner. The electrochemical sensor detects the slurry angular position while the proximity switch detects the angular position of the grinding media. Other system components are the CPU for digitizing the signals before storage and Zinc-air cells for DC power. The signals are conveyed off the mill to the control room via a radio system. Details of the operating principle of the SENSOMAG can be reviewed in the work by Clermont *et al,* (2008) hence will not be discussed here.

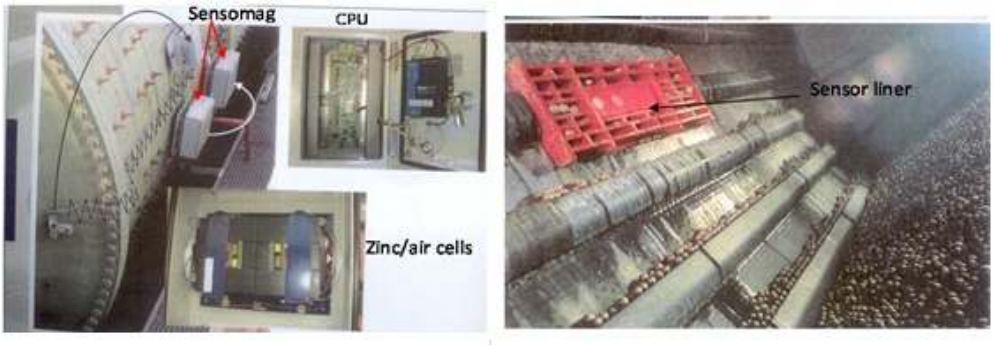

Figure 3.8: The industrial mill with mounted SENSOMAG© system components

3.5 Experimental programs

3.5.1 Laboratory scale experiments on mill-1

3.5.1.1 Experimental design and materials

The first experimental program was undertaken on mill-1 (see section 3.2 for description of mill rig and setup). The focus of this experimental program was to assess the effect of individual variables, ball load volume and slurry % solids on the load behaviour and mill product size distribution by isolating the effect of one on each other. This was accomplished by treating one variable as independent for different test runs as presented in Table 3.2. The mill speed was kept constant during the tests.

Table 3.2: Summary of the experimental tests performed on mill-1

Independent Variables (IVs)				Parameters measured
Ball load volume (%)	Slurry Load (U)	% Solids	Mill speed (% critical)	
20 25 30 35	2.6 2.1 1.8 1.5	50 - 70	75	Sensor signal response, Product size distribution, Mill power draw, Media and slurry positions.

A sample from the underflow of the primary cyclones at Anglo-Platinum UG2 Waterval Concentrator was used as feed material. The size distribution of the feed material is presented in Table 3.3. All experimental tests were performed at constant slurry holdup volume to simulate an overflow mill. The volume of slurry was measured as 20 litres, a level that was carefully chosen to ensure that the pool angles lie in the same range with those measured on the industrial mill. Steel balls measuring 10 mm in diameter were used as grinding media.

Table 3.3: Size distribution of the feed material used in the laboratory experiments

Size (μm)	Cum. % passing	Size (μm)	Cum. % passing
38	2.62	212	58.75
53	4.77	300	76.76
75	9.33	425	91.42
106	19.57	600	97.11
150	37.09	850	99.89

3.5.1.2 Measuring techniques and procedures

The dynamic positions of media and slurry inside the mill were measured using proximity and conductivity sensors respectively, installed through the mill walls. The data captured by the sensors was passed through the amplifying circuit to enhance their readability before being conveyed to the computer by means of slip rings. The 'Waveview' software installed on our laboratory computer was utilised in the continuous acquisition and processing of the data. The raw data from the mill was sampled at a frequency of 500 Hz which is sufficiently high to capture at least one data point per one degree of mill revolution. For each test run, a total of 5000 data samples were generated over a sampling period of 30 seconds. The start and end of each mill revolution was indicated by a signal from the revolution reference probe. By analysis of the load position signals, the variation in load behaviour with mill operating variables can be detected and linked to mill performance, thus enabling the mill to be properly controlled.

The mill torque was recorded during all the tests to assess its dependence on load behaviour. The power drawn by the mill was derived from the torque measured using the load beam as described in section (3.2). The net power which represents the true energy expended in tumbling the load was obtained by subtracting the zero-load power from the total mill power (P_{tot}). These can be mathematically presented as follows.

$$P_{tot} = (2\pi N / 60)T \quad [3.3]$$

$$P_{net} = P_{tot} - P_{no-load} \quad [3.4]$$

Samples were also collected from the mill after each test run for size distribution analysis. A small sample of about 400 g was removed from the mill and split to obtain a sample that is representative of the properties of both coarser and finer materials in the mill. A representative sample of about 80 g to 90 g was then wet washed on the screen size (-38μm) to remove the fines. The wet samples were dried in an oven for 20 minutes at a temperature setting of 110^0. This was followed by the sieving of each sample in separate runs but using the same sieves on the shaker machine. The screens were nested (stacked) in decreasing order of size from 850μm to 38μm at an interval of $\sqrt{2}$. The reason for maintaining the same sieves in all the test runs is to ensure consistency in the results. This is given the fact that different sieves have different reliabilities despite having same nominal aperture size. During the successive sieving intervals, the screens were cleaned with compressed air to avoid the 'blinding' effect that would lower the reliability of the sieves. The duration of sieving in all the tests was 20 minutes which was considered sufficient for all the undersize to be separated. At the end of each sieving test, the material retained in each screen interval was weighed and its mass expressed as a percentage of the total mass after screening, including the mass washed out. Similar procedures were followed in all experimental runs. The data obtained here was utilised in assessing the mass specific energy consumption in production of particles finer than 75 microns for a set of operating conditions.

The results from the laboratory measurements performed in this program together with their analysis and discussions are presented in chapter 4.

3.5.2 Laboratory scale experiments on mill-2

3.5.2.1 Experimental design and materials

The second experimental program was undertaken on mill-2 described in section 3.3. The aim of this experimental program was to understand the slurry radial transport behaviour and mixing pattern inside the mill. A gamma camera was employed to monitor the flow of slurry as a function of time. Aqueous ^{99m}Tc radioisotope that emits 140 keV photons with a short half-life of 6.02h was used as a flow follower while steel balls of 10 mm in diameter were used as grinding media. Glycerol-water mixture was used to mimic the motion of actual slurry as found in full scale systems. The choice of glycerol was motivated by the need to maintain a fairly constant level of viscosity inside the mill for each experimental run (glycerol displays Newtonian behaviour). The physical properties of the glycerol-water mixture used in this study are summarised in Table 3.4.

Table 3.4: Physical properties of glycerol –water mixtures used in the batch tests

Percent glycerol (%wt)	Density at 20^0C (kg/m^3)	Viscosity at 20^0C (cp)
70	1.181×10^3	22.5
75	1.194×10^3	35.5
80	1.208×10^3	60.1
85	1.221×10^3	109
90	1.235×10^3	219

The experiments were designed and performed in line with the objectives of this study. It was designed as a factorial of 2 x 2 independent factors and 3 variables to be assessed. The independent factors were 2 levels of slurry viscosity and 2 level of mill speed while the response variables were: slurry radial transport rate, the mixing behaviour within the ball charge and the volumetric rate of slurry transfer from the pool to the ball charge. Mill speed is varied because it results in different intensities. In real systems, a reduction in mill speed would be a proxy for

increasingly worn liners. The load volume was kept constant during the tests at 25% of mill volume. Table 3.5 presents a summary of the experimental design.

Table 3.5: Summary of experimental tests performed on Wits mill-2

Tests	Viscosity of glycerol - water mixture (cp)	Mill speed (%Nc)	Radiotracer activity
Set 1	10	28	10 mCi
	70	28	10 mCi
Set 2	70	60	10 mCi

The first set of tests aimed at assessing the effect of viscosity while the second assessed the effect of mill speed. Generally, slurry viscosity for secondary ball mill discharge would range between 140 and 250 cp, due to a higher concentration of finer progenies (<25microns). Therefore, in order to achieve a realistic motion of media relative to the slurry, the level of slurry viscosity in the laboratory mill had to be judiciously chosen. The governing rule was that the terminal settling velocity of balls in the laboratory mill has to match that in the full scale mill. In view of this consideration, only 2 viscosity levels, 10 and 70cp were investigated representing low and high viscosity respectively.

3.5.2.2 Gamma camera system

The General Electric gamma camera utilised in this study is located in the Department of Nuclear Medicine at Johannesburg General Hospital. The camera has the capability to operate both in static and dynamic modes. Figure 3.9 shows the gamma camera system in one of our experimental setups. The main components of the gamma camera are a collimator, an array of electron multiplier phototubes (PMTs) and a detector crystal. A low energy (< 200 keV) parallel hole collimator, with a series of PMTs was employed in all our studies.

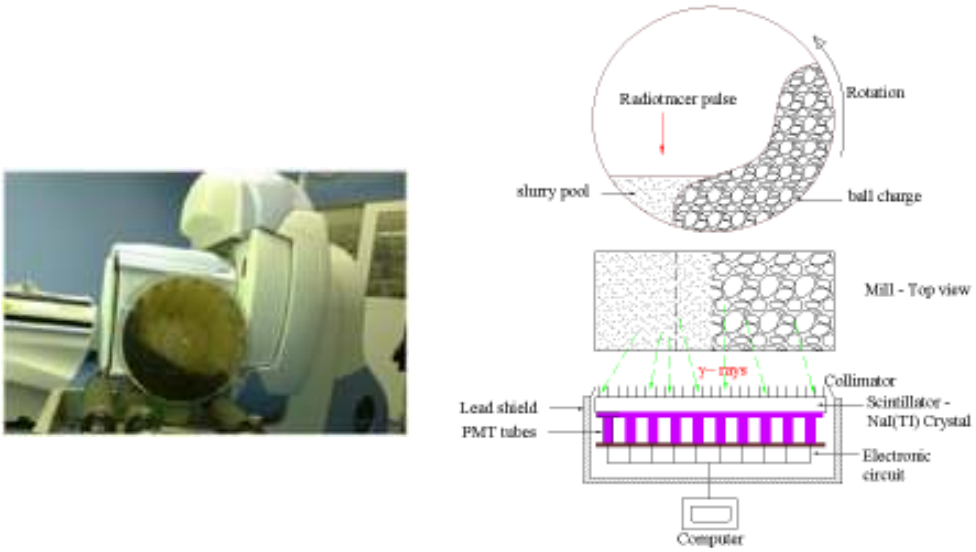

Figure 3.9: View of experimental setup and schematics of the operating principle of the GE gamma camera system.

In operation, the gamma rays emitted by the radioisotope are projected by a collimator onto the detector crystal. The collimator consists of a series of holes in a lead plate. The holes are normally parallel to suppress ray scatter by focusing only rays from a chosen direction onto the detector crystal, while the rest is attenuated by lead shield. The commonly used scintillating material for detecting gamma rays is Sodium iodide with thallium doping (NaI(Tl)). The detector crystal absorbs the radiations and converts the photon energy into light i.e. scintillates. The fluorescent flashes of light are detected by the PMTs located behind the detector crystal which determines the source of each radiation. The intensity of each flash is proportional to the energy of the incoming gamma rays.

3.5.2.3 Measuring techniques and procedures

For each experimental run, 2ml of aqueous ^{99m}Tc, with 10 mCi of activity was premixed with 4ml of glycerol-water mixture to a uniform density then injected as a pulse into the slurry pool inside the mill while the mill was stationary. The mill drive was then switched on and the motion of the radiotracer was tracked using the gamma camera. The gamma radiations that originated from the radiotracer as it flowed inside the mill were detected by the gamma camera and the detected photons were projected by the collimator onto the detector crystal creating a

pattern of scintillations that correlate with the point of origin of the incident radiations. The data acquisition and recording was accomplished in real time where by the scintillation intensity distribution was recorded as frames over a period of time. During each test run, the Camera was programmed to continuously acquire the frames until the desired number of frames was reached. Images were separated in time frames of 0.1sec. The digitized images were recorded in size of either 64 x 64 or 128 x 128 bit matrix and stored in DICOM format (Digital Imaging and Communication in Medicine) for analysis. For consistence, a similar procedure was followed for all the three batch tests.

By studying the time history of the scintillation intensity (related to radiotracer concentration) within the pool, it may be possible to determine the volumetric rate of transfer of slurry between the pool and the ball charge region. Further, a study of the scintillation pattern at various regions of interest (ROIs) within the load would give an idea of the slurry distribution map (mixing). The results from the measurements undertaken in this program and subsequent analysis and discussions are presented in chapter 6.

3.5.3 Industrial mill sampling survey

3.5.3.1 Experimental design and materials

Operational data was collected from an overflow ball mill at the Anglo Platinum UG2 Waterval plant in Rustenburg during normal operation at selected conditions for analysis and interpretation and for possible comparison with the laboratory data. The tests included sampling of the load position signals, measuring the residence time distribution (RTD) and mill power draw at different mill operating conditions as presented in Table 3.6. The literature (Kelsall *et al*, *op cit*; Gardner, 1975) presents several types of tracers that have been used for RTD measurement in tumbling mills ranging from soluble salts to radioisotopes. After careful evaluation of possible tracers, common salt, sodium chloride was adopted for RTD measurements.

Table 3.6: Summary of the mill industrial sampling survey program

Independent Variables		Response variables
Mill filling (%)	Wt. % Solids	
25	67.3 75.6	Residence time distribution (RTD), Product size distribution (PSD), Mill power draw, Media and slurry dynamic position
30	73.4 75.1	
33	65.1 72.1	

3.5.3.2 Experimental methods and procedures

Concurrent tests were performed to determine the media and slurry positions as well as the slurry residence time distribution (RTD) inside the mill. Six sets of salt tests were performed on the mill to determine the slurry residence time and the RTD. In each test run 250kg of salt (NaCl) was dumped into the cyclone underflow almost instantaneously (within 5sec) and the response was monitored at the discharge. Figure 3.10 is a schematic representation of the flowsheet of the secondary milling circuit illustrating the sampling points. Timed samples were collected manually into 250 ml plastic bottles over the duration of 90 minutes for conductivity analysis. The sampling period of 90 minutes was considered sufficient for the salt to completely disappear from the mill. The sampling process was accomplished using a specially designed sampling manifold installed at the mill discharge just before the discharge sump. It should be mentioned that the beginning of sample collection was synchronized with the salt impulse event and that prior to each test run, the mill was allowed to stabilize at a set feed flow rate and percent solids for about 1.5 hours. A summary of the experimental program can be reviewed in Table 3.6.

Solids feed rate to the mill was measured at the densifier cyclone underflow as depicted in Figure 3.10. Samples were collected from each of the 5 densifier cyclones into sampling bags for a period of 2-3 seconds and then weighed to

determine the mass flow rate. The sampling process was repeated for 1 hour with a total of 3 runs per cyclone from which an average flow rate was determined. In order to obtain accurate time duration of each sampling sequence, the sampling process was videoed using a Panasonic NV-GS180 camera with a shutter rate of 25 frames per second.

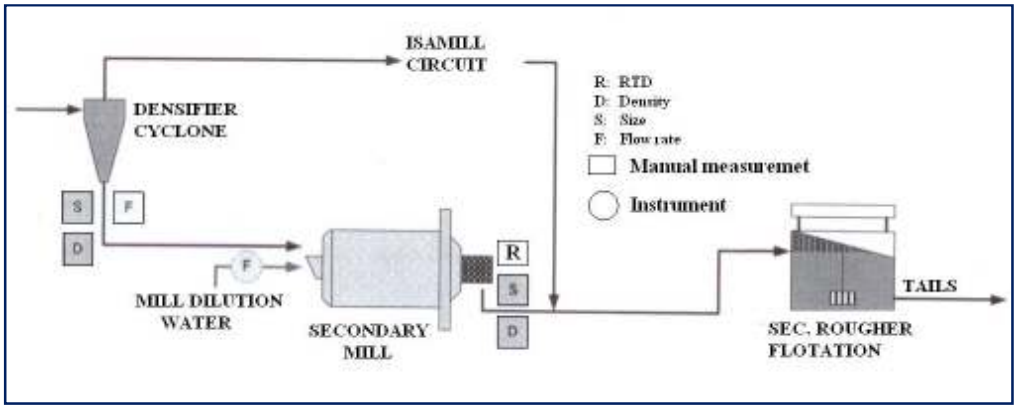

Figure 3.10: Flow-sheet illustrating the sampling points during RTD and Flow rate measurement on the industrial overflow ball mill circuit.

All the data measured by the on-line instruments around the mill circuit including mill power, media and slurry dynamic positions were recorded by the supervisory control and data acquisition (SCADA) system. The results from the industrial surveys and subsequent analysis and discussion are presented in chapter 7.

3.6 Difficulties encountered

The main problem encountered during laboratory experimental set-up was to get the milling chamber to be slurry 'leak proof'. Substantial amount of time was spent on sealing the mill with an epoxy resin and silicone sealant before experiments could commence. Also, in line with the occupational safety and health act, it was required that the experimental rig attains the set safety standards, and in which respect, a significant amount of time and resources were expended to get the equipment rectified.

3.7 Conclusions

Despite the minor challenges experienced during the laboratory experimental process, all the experimental tests were completed successfully using the equipment and techniques described in the foregoing. Data on various aspects relating to mill dynamic load behaviour, power draw and energy efficiency was suitably collected and analysed.

The industrial surveys were accomplished as planned with a wide range of plant data collected, both manually and by plant instruments. The data collected during the test works was of good quality. The measurement of feed flow rates was identified as a potential source of errors and where inconsistencies were noted in the measured flow rates, such data was excluded from the analysis.

CHAPTER 4

Media and Slurry Dynamic Behaviour Measured by Direct Load Sensors

4.1 Introduction

Sensors are extensively used in industrial processes to capture information that is required for real-time process control, monitoring and diagnosis. Currently, the mineral processing industry is witnessing a marked increase in utilization of direct load sensors in milling circuits for on-line monitoring of in-mill behaviour. This has been stimulated partly by the ongoing developments in computer and instrumentation technologies. Direct load sensors can aid in establishing regimes of mass motion inside the mill and detection of process changes during continuous state of mill operation on the basis of which mills can be appropriately tuned to maximize on energy and milling efficiencies as well as reduce liner and grinding media wear rates.

Direct contact of the sensor with the load boosts reliability and accuracy of the measurements. In process control application, the significant features of the sensor output signals which are related to the process behaviour are continuously monitored. If undesirable characteristics are exhibited in the sensor signals, either it implies that the mill is operating improperly or the load sensors have failed; consequently, necessary control measures would be implemented to restore optimal conditions. But in order to avoid improper or untimely decisions, correct and adequate interpretation of sensor response signals is a prerequisite. This challenge necessitates the need for comprehensive studies, firstly to determine how well the load sensors can detect variations of in-mill dynamics and secondly to understand how the significant process parameters vary during the continuous state of mill operation and how these variations are reflected in the load sensor signals data.

This chapter presents results, analysis and discussion of measurements of media and slurry behaviour inside a laboratory ball mill as well as an industrial ball mill based on signals obtained by conductivity and proximity sensors (direct load sensors) for different conditions of ball load volume and slurry concentration. The proximity sensor gives a response related to the dynamics of media while the

conductivity responds to slurry behaviour. Analysis of response signals from the two sensors corresponding to different in-mill process conditions is performed giving an idea of the continuous interaction and general behaviour of media and slurry inside the mill. This could unveil useful information that can be related to mill operational and performance indices and hence can be utilised for process control. Lastly, an analysis of the mill power draw and mass specific energy consumption in relation to measured load behaviour is also presented here.

4.2 Description of Media and Slurry sensor signals

The media and slurry sensor system employed in our study comprises two probes: a proximity probe for detecting ball media and a conductivity probe for sensing slurry. Details of the sensor system and the measurement process are given in Chapter 3 (c.f. section 3.2.3). The sensor signals possess specific features that are related to important dynamic events during the passage of the sensors underneath the load as well as distinct load parameters such as media and slurry dynamic position, slurry properties and ball load volume. Correct and adequate interpretation of the signals will lead to proper understanding of the mill internal dynamics which is paramount to effective control of the milling process.

Figure 4.1(a) is an illustrative example of the output signals from the media and slurry sensor system for the laboratory mill as the sensors periodically enter and leave the load. The corresponding physical representation of the load behaviour within the mill is shown in Figure 4.1 (b). The denotations in Figures 4.1 (a, b) indicate important and clearly identifiable features that define the dynamic load behaviour. Interpretation of these features (see Table 4.1a, b) was guided by our knowledge of milling and by data inspection. It should be noted that the sensor signals presented here provide only measurements of the load at the mill axial centre. Therefore any load interactions at the mill front and back end are not fully represented.

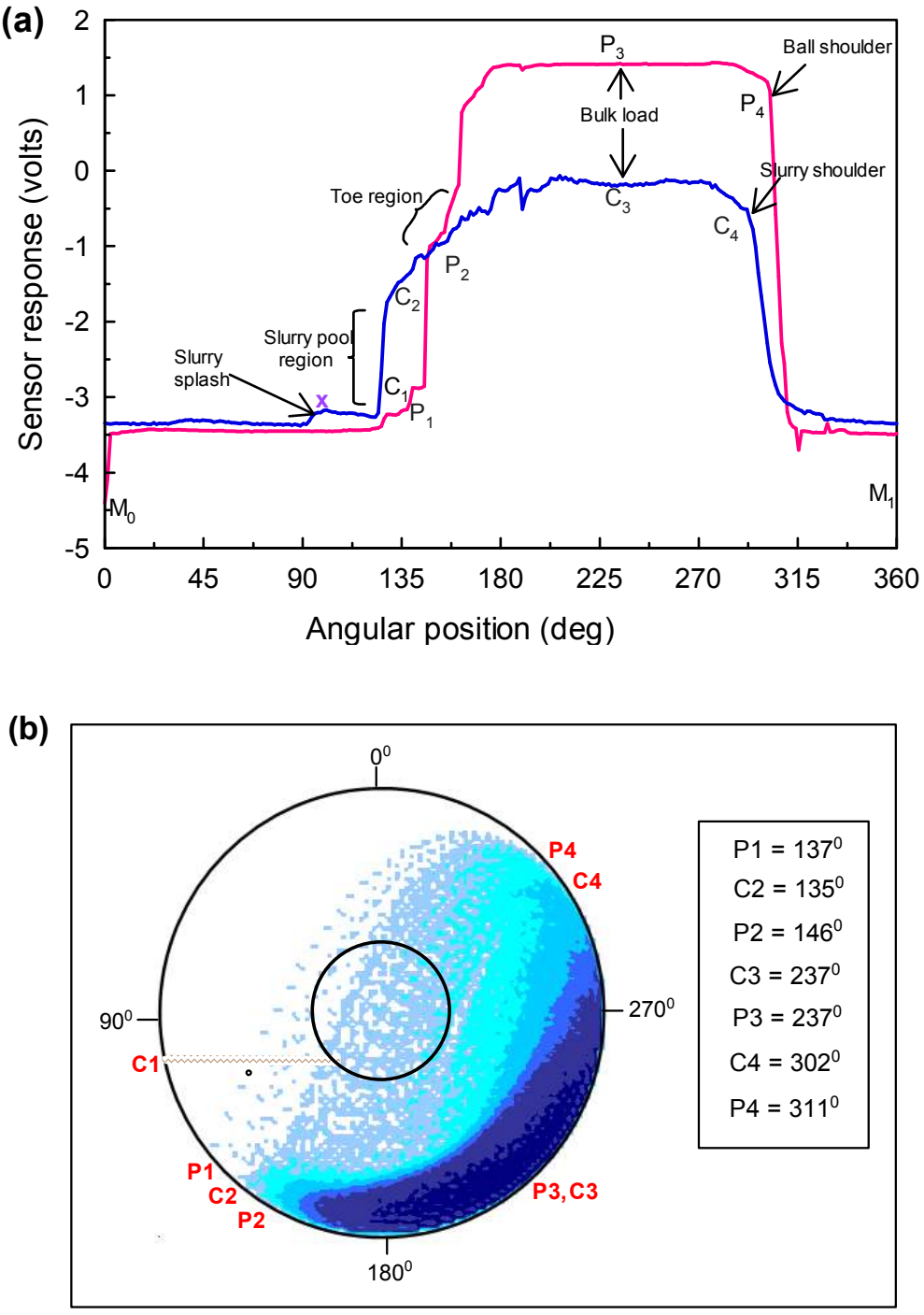

Figure 4.1: (a) Typical signals by the sensor system at J=30% and N=75% **(b)** key positions of the load inside the mill corresponding to the sensor signals.

Table 4.1: Interpretation of sensor signal features

(a) Conductivity sensor:

Feature	Description
X	The sensor is yet to reach the slurry pool but gets intermittently splashed with slurry from the pool due to pool turbulence.
C_1	The sensor strikes the slurry pool and starts to get submerged in slurry.
C_2	The sensor exits the slurry pool and enters the ball charge where conductivity increases gradually. This is due to the balls getting more closely packed as you move away from the toe towards the bulk load.
C_3	The sensor is within the bulk load where the balls are in a fully locked-in position. Conductivity is constant and high being a contribution of both the slurry and the balls.
C_4	Slurry starts to drain away from the dilated ball shoulder region partly due to gravity as well as the effect of mill rotation. Conductivity drops gradually initially due to a layer of slurry adhered to its surface and then sharply as the adherent slurry layer gets stripped by the balls.

(b) Proximity sensor:

Feature	Description
P_1	A few balls bouncing off the ball bed and the liners at the toe region and falling on the sensor causing early onset in signal rise coupled with some noisy behaviour in the signal profile.
P_2	The sensor enters the ball charge at the toe region and the signal begins to rise steadily. The balls are not yet efficiently packed on the sensor surface instead they continuously rearrange themselves due to characteristic turbulence at the toe region.
P_3	The sensor is within the bulk load where the balls are in a fully locked-in position and the signal remains constant.
P_4	The sensor begins to emerge from the ball charge at the shoulder region. The signal drops drastically to the lowest level as the balls fall off the sensor.

It should be mentioned that due to characteristic turbulence of the proximity sensor signal profile at the toe region, finding the exact location of the media toe position was not trivial. In recognition of this problem and on understanding that no explicit rule exists for analysis of load sensor signals, a simple policy was adopted to help determine the media toe and shoulder positions more consistently and realistically. The media toe was defined as the lowest turning point of the bulk load. This is the point where the descending balls in the cascading profile turn and re-enter the *en masse* load that is moving upwards along the mill shell. From the profiles of the proximity sensor data, the media toe is established at the point where the signal begins to rise steadily (denoted by P_2 in Figure 4.1). This coincides closely to the point where the conductivity sensor exits the slurry pool (denoted by C_2 in Figure 4.1). But when there is an early onset in signal rise coupled with noisy behaviour in the signal profile, it would simply be interpreted as effect of cataracting balls at the toe region where some balls bounce off the ball bed or liner walls, colliding with other balls and falling onto the sensor surface. The media shoulder position on the other hand was defined at the point where the balls depart from the mill shell. Therefore, it is the highest point at which the balls on the outermost layer make the last contact with the mill shell (denoted by P_4 in Figure 4.1). In effect the media shoulder position can be estimated more reliably than the toe position using the proximity sensor alone.

The slurry toe and shoulder positions were derived from the conductivity sensor signature. It was relatively easy to obtain the slurry toe (slurry pool level) and slurry shoulder since the conductivity signal displayed some definite features that were repeated in every mill revolution. This allowed for a threshold value to be set to discriminate between the ‘slurry only’, ‘slurry and balls’ and ‘balls only’ conductivities. Based on this rule, the slurry angular location inside the mill could easily be detected. The slurry toe corresponded to the point where the signal began to rise sharply and continuously while the slurry shoulder was detected at the point before a rapid drop in conductivity signal to its lowest level. To facilitate as well as simplify the analysis of the signals data, a MATLAB program was developed which automatically computed the media and slurry angles (cf. Appendix D).

Figure 4.2 presents a sample of the output signals recorded by the on-line media and slurry sensor system (SENSOMAG) on the industrial mill during the passage of sensors through the load. The data corresponds to the ball load volume of 30% and mill rotational speed of 75% of critical, for 3 mill revolutions. Unlike the laboratory case, notice here that the inductive proximity sensor operates in a switch mode registering a Boolean signal, 1 upon intercepting the ball charge and 0 on exit from the ball charge. However, the industrial conductivity sensor operates in a similar version to the laboratory scale sensor. The media and slurry positions are derived from the signal profiles as indicated in the figure using a computer program that is linked to the mill supervisory control and data acquisition system.

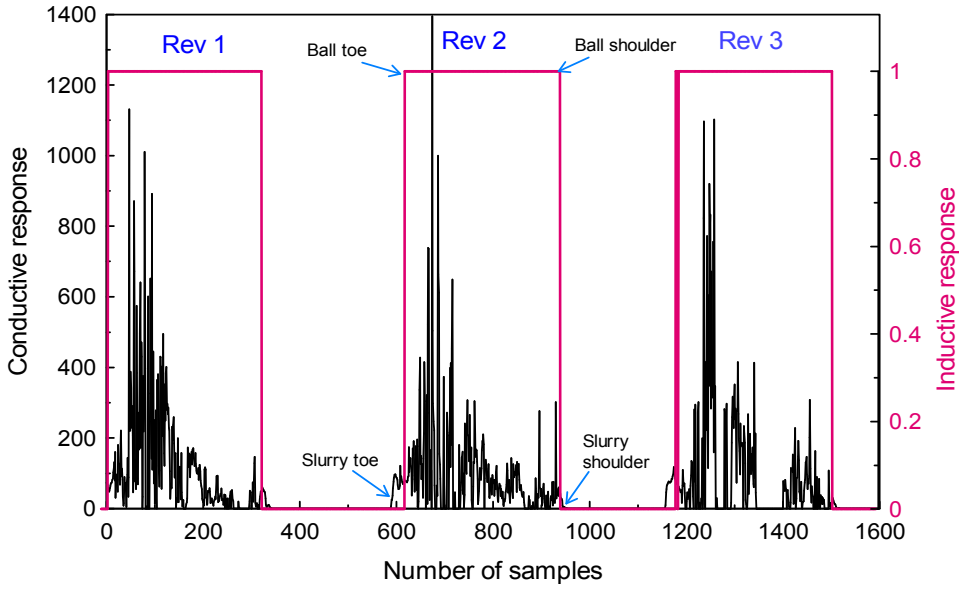

Figure 4.2: Sample signals from the on-line media and slurry sensor system on industrial mill at J= 30%, N= 75% of critical and slurry wt. % solids = 75.

4.3 Analysis of laboratory data

4.3.1 Conductivity sensor signal profiles

To get an idea of the variation of the conductivity sensor signal pattern with changes in slurry concentration and ball load volume inside the mill, average signals were obtained over ten mill revolutions as illustrated in Figures 4.3 and 4.4.

The key feature of our observation in Figure 4.3 is the distinctive pattern of the signal profiles when the sensor is fully out of the load. The magnitude of drop in conductivity (denoted by V) clearly appears to decrease with increase in slurry concentration. It was thought that this behaviour could be due to an adherent layer of slurry on the sensor surface providing a conducting medium. In this case the sensor does not fully de-energise to the no-load voltage (V_o) due to residual conductivity by the adhered slurry layer whose thickness tends to increase with increasing slurry concentration. This information can be useful in determining slurry density and subsequently slurry viscosity, which are vital control parameters in milling but whose on-line measurement remains a challenge. Early work by Van Nierop and Moys (2001) showed that slurry viscosity is related to the rate of slurry drainage from the conductivity sensor upon exiting the load. This trend is however dependent on design and installation configuration of the conductivity sensor. Indeed in the present work, no discernible signal pattern related to slurry drainage from the probe at the load shoulder region could be detected.

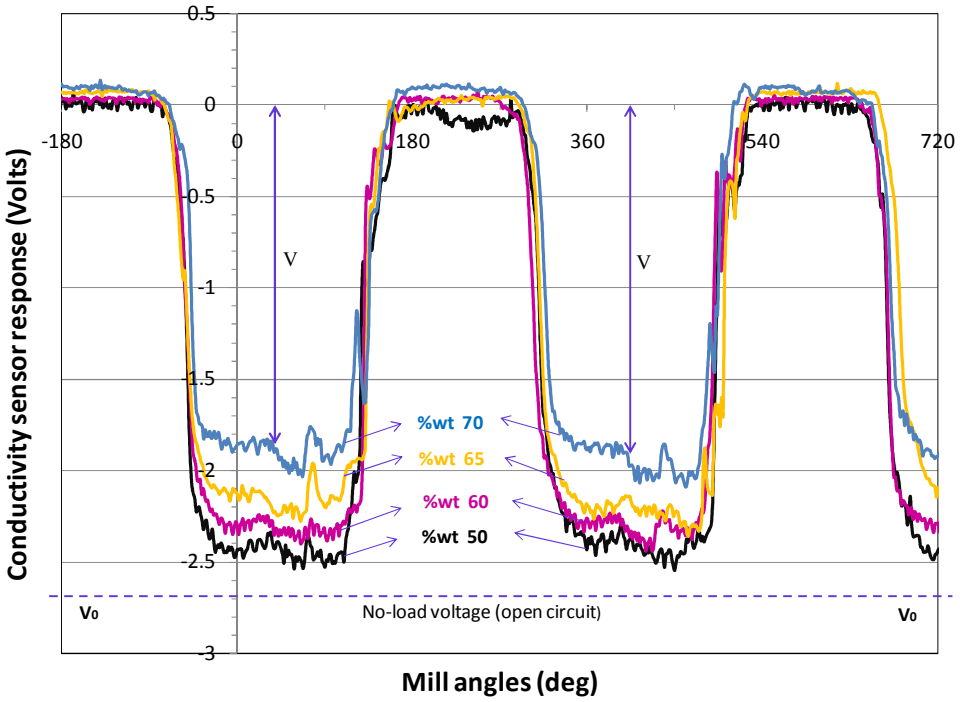

Figure 4.3: Effect of slurry concentration on conductivity sensor signal profiles at mill speed of 75% of critical and ball load volume of J= 30%.

Further notice the characteristic turbulence in the signal when the sensor is fully out of the load. This is believably due to ball collisions at the pool toe region which results in pool turbulence thereby causing slurry to splash intermittently onto the sensor surface. The noise-like features on the signal profiles when the sensor is fully submerged in the load could be attributed to the action of balls continuously interacting with the conductivity sensor surface during the mill tumbling process.

Figure 4.4 shows the conductivity sensor output signals for different ball load volumes and constant slurry concentration of 60% solids by weight. The main feature in this result is the shift between the signal curves at the shoulder position. The signal associated with higher ball load volume (J=35%) begins to drop later than others while the signal associated with lower ball loading (J=20%) drops much earlier which is expected. An increased ball load volume would entrain a larger volume of slurry, consequently leading to higher slurry shoulder position. No distinguishable signal feature is observed at the toe position.

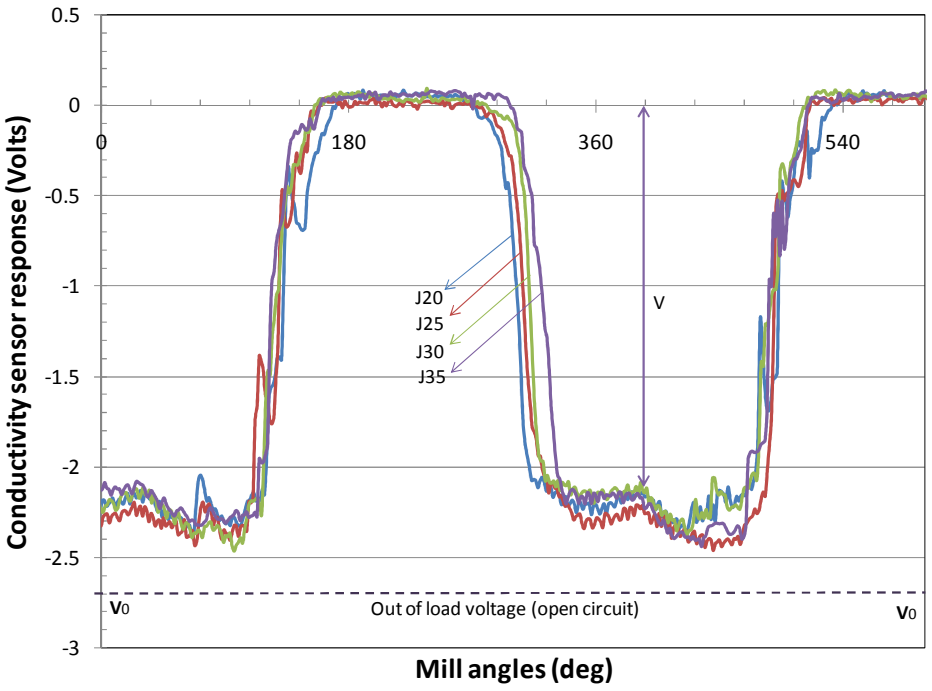

Figure 4.4: Effect of ball load volume on conductivity sensor signal profiles at mill speed of 75% of critical and 60%wt solids

The extent of drop in out-of-load voltage (V) with change in ball load volume and slurry concentration was quantitatively analysed and the results are presented in a surface plot (Figure 4.5). It is worthwhile to mention that since conductivity would generally vary with ore type, a prudent measure would be to express the out-of-load voltage (V) relative to the open circuit voltage (V_0) i.e. , in order to facilitate easier use of this data for mill control.

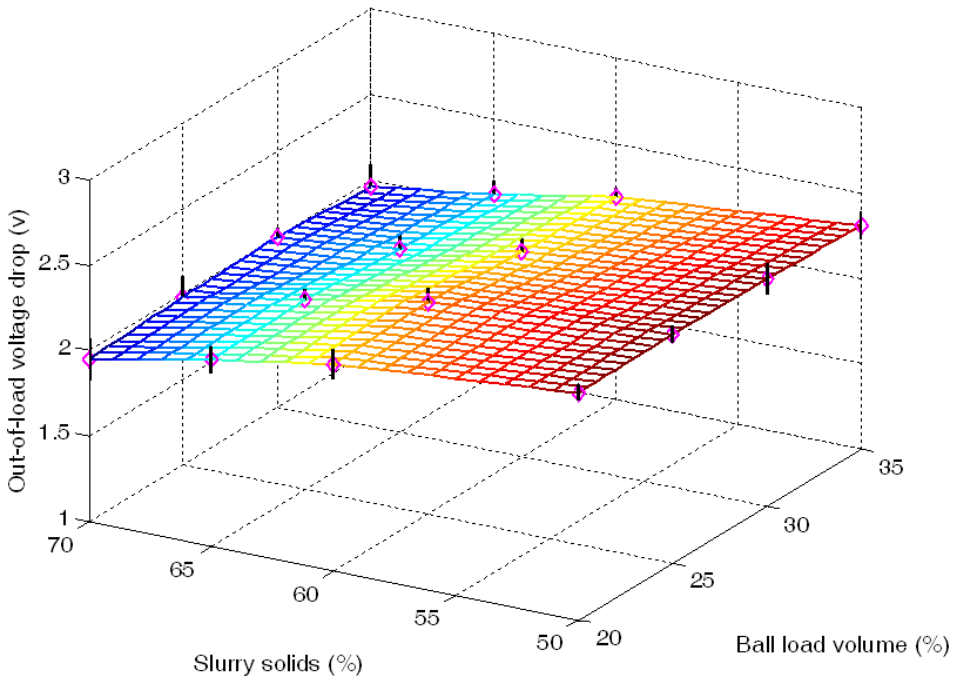

Figure 4.5: Surface plot showing the effect of slurry concentration and ball load volume on the extent of drop in the out-of-load voltage as recorded by the conductivity sensor at mill speed of 75% of critical.

4.3.2 Proximity sensor signal profiles

Figures 4.6 and 4.7 are respective examples showing the effects of ball load volume and slurry concentration on the signal profiles of the proximity sensor output data. From the results in Figure 4.6, a marked shift between the signal curves is evident indicating a change in ball toe and shoulder positions. An earlier

rise and late drop in signal is experienced at higher ball load volume of 35% and vice versa at low ball load volume of 20%. Further, the signals at the toe region become notably noisier with increase in volume of the ball load, which could be related to the amount of cataracting inside the mill, which induces turbulence and ball collisions. Increased cataracting is expected at higher ball load volume owing to enhanced lifting action while at lower ball load volume, the load would flow in a largely cascading manner with less turbulence.

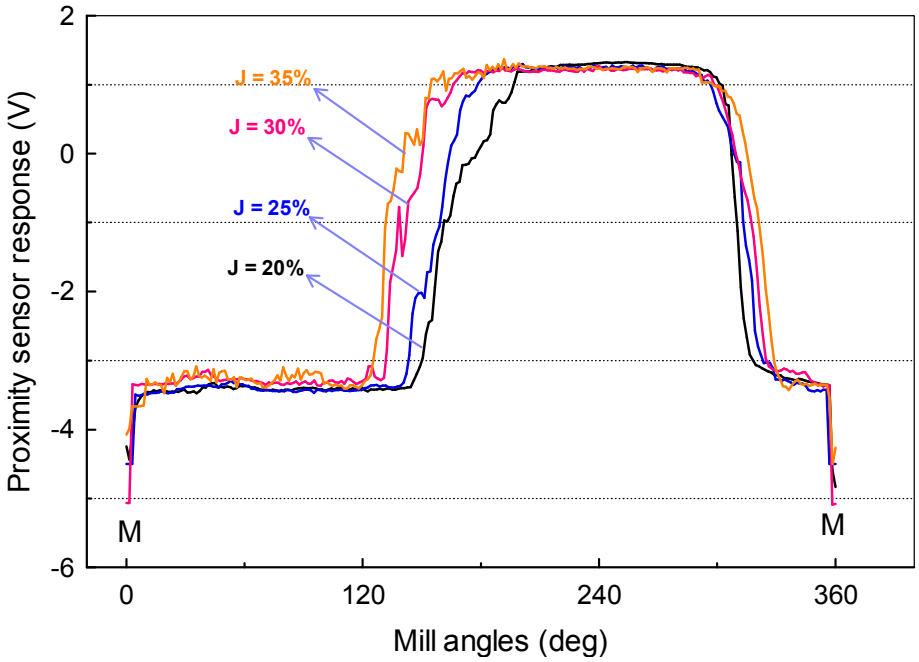

Figure 4.6: Effect of ball load volume on proximity sensor signal profiles at mill speed of 75% of critical and 60%wt solids.

In the event where the signal profile at the shoulder position drops slowly firstly then followed by a sharp and definite drop could be interpreted as the presence of a few balls on the sensor surface. Practically, this would occur when some balls get packed or delayed from leaving the liner with others upon reaching the shoulder position. However, since the lifters were spaced out at 5 balls diameter, the possibility of balls getting packed in spaces between the lifters is ruled out. Therefore it was suspected that this momentary behaviour could be attributed to

the action of a few balls getting shortly trapped in a layer of slurry formed on sensor protection plate thereby delaying the signal drop.

Figure 4.7 presents averaged signals obtained over ten mill revolutions giving a qualitative idea of the effect of slurry concentration on proximity sensor signal pattern. A close examination of the results reveals no definitive pattern both at the toe position and the shoulder position as solids concentration in slurry changes between 50 and 65%. One intriguing observation though is the drastic shift of the signal towards the 9 o'clock position as slurry concentration is increased from 65 to 75% solids. Without photographic evidence, no substantive explanation could be availed, but it is understood from literature (Liddel, 1988; Smit, 2000), that the presence of slurry inside the mill would induce some lubricating effect. This influences the internal friction coefficient within the ball charge and between the ball charge and the mill walls. Very dilute slurry would suppress the lifting effect causing the load to slump while very thick slurry would tend to coat the balls reducing their mobility and causing the load to expand. The unsystematic trend exhibited in the proximity signal in Figure 4.7 precluded any further analysis.

The amplitude of the output signal when the proximity sensor is fully underneath the load is another interesting feature that was closely monitored. Considering that the strength of proximity sensor signal depends on the volume of metallic material presented to the sensing surface (Kiangi and Moys, 2006), it was expected that the signal level would vary commensurate with slurry concentration since slurry interferes with the balls packing pattern and packing efficiency. However, hardly any discernible difference was observed in the results presumably due to the fact that solid particles in slurry were significantly finer (80% below 300μm). This result reinforces the findings by Kiangi and Moys (2008) who used course silica particles (50% passing 1102μm) for one case and fine particles (50% passing 173μm) for another case in a dry ball mill and found that the proximity signal level remains unvaried for finer particles but decreases in proportion to the amount of material for course particles.

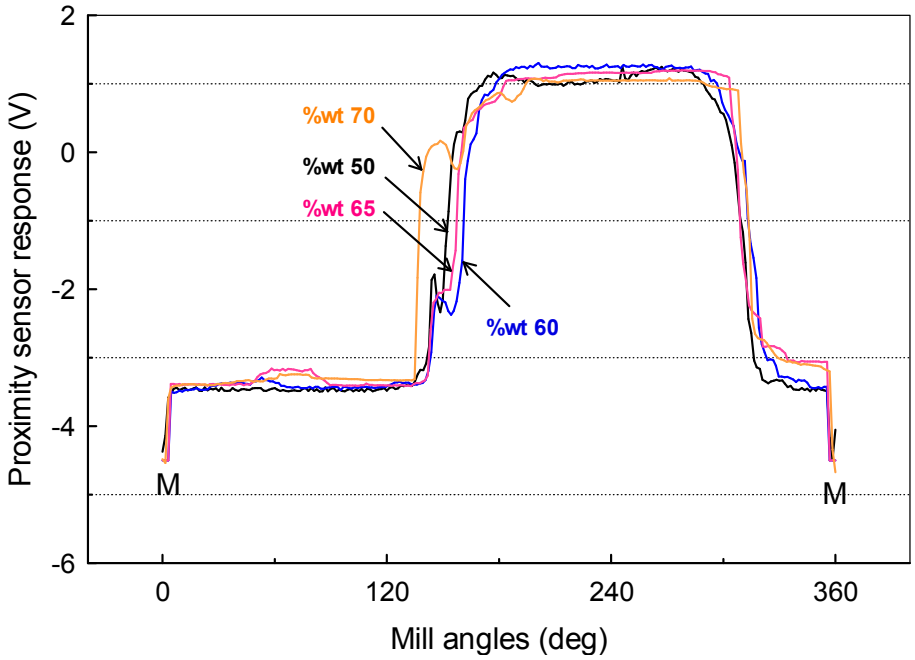

Figure 4.7: Effect of slurry concentration on proximity sensor signal profiles at mill speed of 75% of critical and ball load volume of J= 30%.

4.3.3 Media and slurry dynamic positions

The focus of our analysis in this section is to assess how the compounded influence of ball load volume and slurry concentration (% solids) would affect the load dynamic position. The dynamic shape of the load inside an overflow ball mill and the associated load angles can be represented schematically as shown in Figure 4.8. From the figure, the angle subtended by the slurry pool is the difference between the media toe angle and the slurry toe angle (i.e. $\theta_{Pool} = \theta_{T(Media)} - \theta_{T(Slurry)}$). Other load angles depicted in Figure 4.8 are total slurry angle and total media angle where the former is defined as the difference between the slurry shoulder angle and slurry toe angle, (i.e. $\theta_{D(Slurry)} = \theta_{S(Slurry)} - \theta_{T(Slurry)}$). The total media angle on the other hand is the angle subtended at the mill centre by the ball charge when the mill is rotating. It is obtained as a difference between the shoulder and toe angles of the dynamic media, mathematically expressed as, $\theta_{D(Media)} = \theta_{S(Media)} - \theta_{T(Media)}$. Analysis of the evolution of total media angle would provide an indication of the

mill internal dynamics and ball charge level. This information might help the operator to adapt the mill accordingly so as to optimise the milling efficiency. Equally, the information would be valuable in planning for liner replacement and media replenishment.

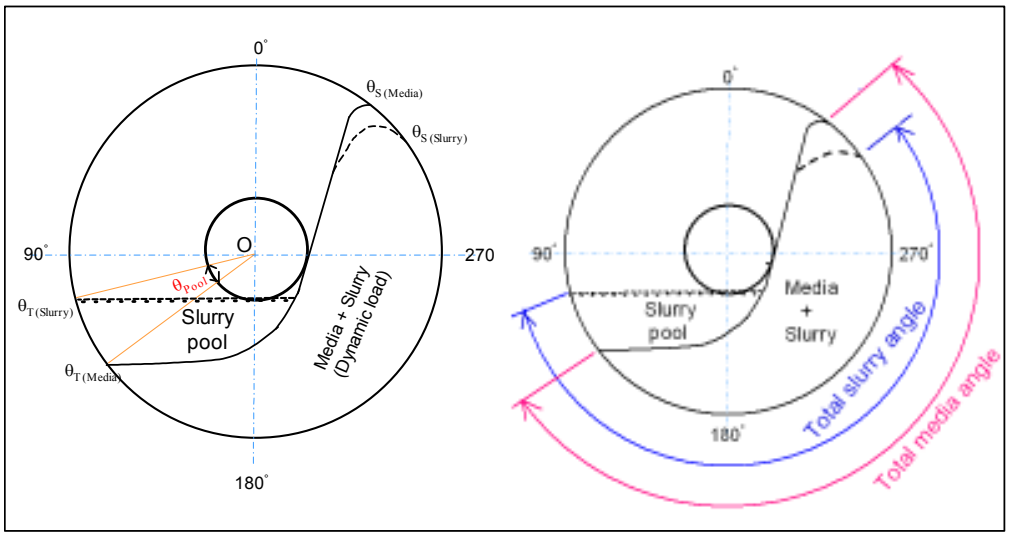

Figure 4.8: Representation of important dynamic load angles in an overflow mill.

Presented in Figures 4.9 and 4.10 are results showing the variation of media toe position and media shoulder position respectively, with slurry concentration and ball load volume. The mill speed was kept constant at 75% of critical during experimentation. From Figure 4.9, it is quite visible that over the range of slurry concentration between 50 and 65% solids, the media toe position is only marginally variable; a trend that was conserved at all levels of ball load volume investigated. However, as the slurry concentration increases from 65 to 70% solids, a clear variation starts to emerge. The toe position begins to occur earlier which could be a pointer to the onset of centrifuging albeit the change is only by a margin of about 5^0. Considering the fineness of our material, it is thought that at this high level of solids concentration in slurry, the viscosity of slurry is significantly higher (cf. Mooney viscosity equation, Table 2.1) thus dragging the media higher up the mill wall. Some of the media on the outermost layer rotate

with the mill only to drop further from the toe and piling up before re-entering the bulk load. This in effect shifts the toe position towards the 9 o'clock (90^0) position, which consequently cancels out the 'lift' effect on the toe position. This observation is consistent with the findings from photographic data by Tangsathitkulchai (1989) who further reiterated that slurry properties affect the moving paths of balls and consequently the interaction between the particles and the balls. The general practice in the industry is to operate ball mills with some desirable proportion of cataracting so as to facilitate rapid reduction of coarse particles by impact breakage. However, while keeping in-line with this practice, care is always taken to ensure that the cataracting balls are not projected far away to intercept the mill liner wall. This behaviour would lead to excessive wear of liners and the grinding media with the resultant decrease in mill throughput and increase in operating costs.

Figure 4.10 shows the trends in media shoulder position with slurry concentration for four cases of ball load volume tested. It is apparent that the level of solids concentration in slurry has an appreciable effect on media shoulder position. All cases display an increasing trend in media shoulder angle with increasing slurry concentration which conforms to our expectations. A closer inspection of the results further reveals that the increases in the shoulder positions are by higher magnitudes than the case of the toe positions. Another interesting observation is recorded at 50% solids in slurry and 20% ball load volume. Here the media shoulder position is significantly lower than all other cases. This is a clear indication that significant slippage was taking place inside the mill which prevented the load from 'locking in' to the rotary motion of the mill. The motion of the load is largely in cascading mode with a few cataracting media which assume lower paths and fall just on the belly of the charge away from the slurry pool before rolling down to the toe. From 60 to 70% solids in slurry, the shoulder position rises steadily for all cases except 35% of ball load volume. It is speculated that at ball load volume of 35%, the centrifuging effects might have slowly ensued. Indeed one should bear in mind that at higher ball load volume, the balls are

closely packed and exert higher dynamic pressure on the mill wall which mitigates the slipping action.

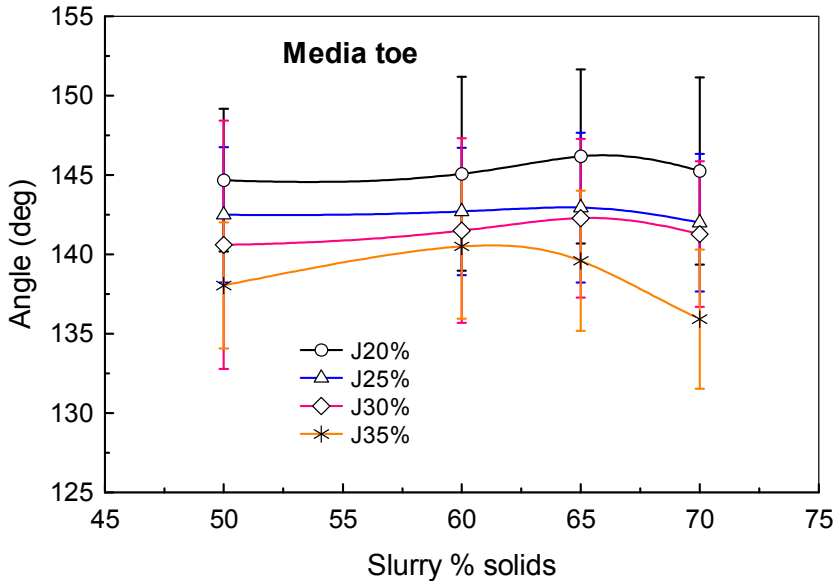

Figure 4.9: Variation of media toe angle with slurry concentration for four different levels of ball load volume at constant mill speed of 75% of critical.

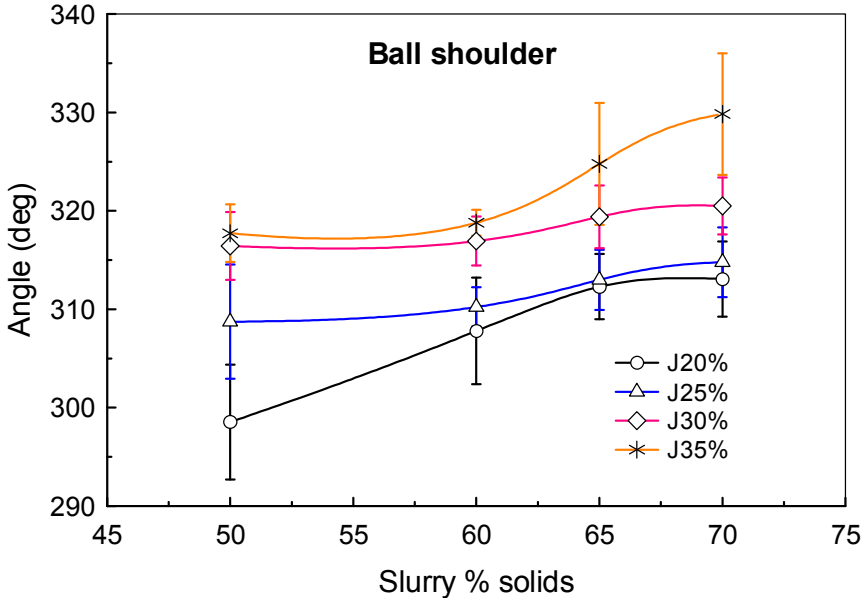

Figure 4.10: Variation of media shoulder angle with slurry concentration for four different levels of ball load volume at constant mill speed of 75% of critical.

The results showing the variation of total media angle with slurry concentration for four cases of ball load volume are presented Figure 4.11. As expected the total media angle increases with increase in ball load volume. Also the total media angle displays an increasing trend with slurry concentration. In a similar pattern to the media shoulder angle, the total media angle ascends drastically when slurry concentration is increased from 65 to 70% solids at ball load volume of 35% which is a clear indication of load expansion. This behaviour is reflected in the power draw pattern which is discussed later in section (4.3.4) and has a direct bearing on the mill energy efficiency. Based on the observed trends in the total media angle, a correlation must exist with ball load volume and slurry concentration. Accordingly, by monitoring the evolution of total media angle, it could be possible to obtain an indicative idea of the level of ball loading and slurry concentration inside the mill for purpose of milling process optimisation.

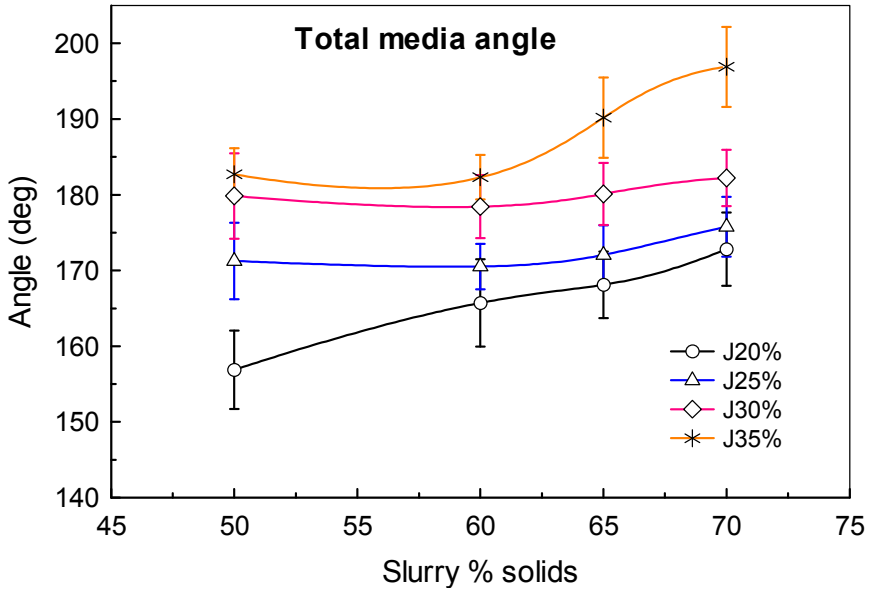

Figure 4.11: Variation of total media angle with slurry concentration for four different levels of ball load volume at constant mill speed of 75% of critical.

The effects of slurry concentration and ball load volume on slurry toe, slurry shoulder and slurry pool angles are depicted in the results shown in Figures (4.12 - 4.14). At ball load volume of 20%, the load continues to be lifted with increase in slurry concentration, shifting the media toe towards the 6 o'clock position, and since the slurry holdup volume is kept constant, the slurry toe will shift in tandem with the media toe. For the ball load volumes of 25, 30 and 35%, the slurry toe angle appears to be unvaried with slurry concentration over the range between 50 and 65% solids but begins to drop steadily afterwards. The observed sudden drop (shift towards 9 o'clock position) in slurry toe angle after 65% solids could be associated with the stronger lift experienced by the load which causes the cataracting media to assume higher paths, falling far inside the slurry pool and displacing part of the pool thereby causing the slurry toe to shift towards 9 o'clock position. The situation with ball load volume of 35% consistently yields higher slurry toes (low pool level) and shoulder angles than the other cases over the entire range of slurry concentrations tested.

On the other hand, the variation of slurry pool angle with slurry concentration and ball load volume appears to take a more definitive trend as described by the results in Figure 4.14. The slurry pool angle exhibits a decreasing trend with slurry concentration, registering a marginal decrease initially before dropping steadily after 65% solids for all cases of ball load volume assessed. This steady drop coincides with the point when a significant rise in total media angle is recorded. Obviously a stronger lift dilates the load substantially enabling more slurry to be entrained in and consequently lowering the pool angle. Over the entire range of slurry concentration tested (50 to 70 wt% solids) the pool angles were observed to decrease with increase in ball load volume. The reason for this behaviour can be explained in twofold: The additional media introduce extra voids in which slurry gets entrained contributing to the reduction in slurry pool volume. It is also possible that the enhanced lift exerted on the load due to increased weight of the load causes the media to cataract further away inside the pool thereby shifting the media toe position and hence reducing the pool angle.

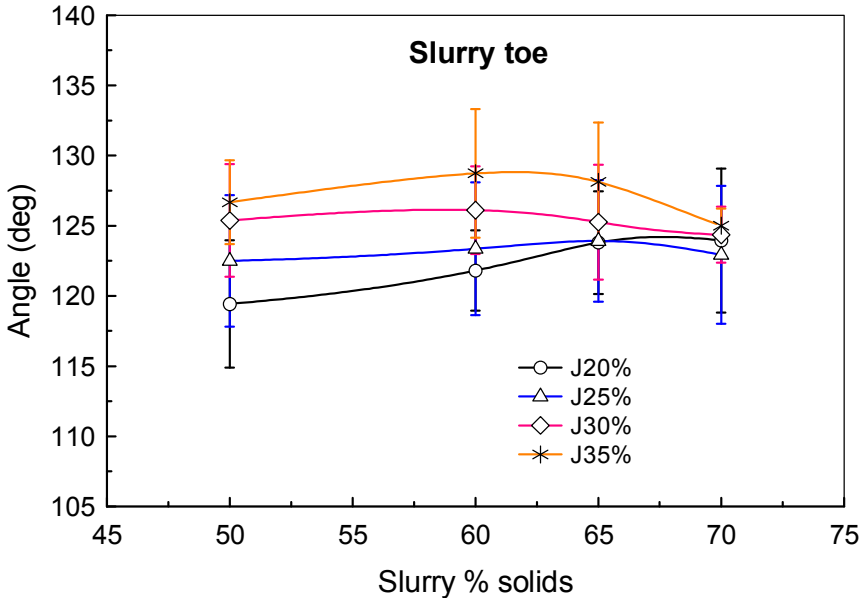

Figure 4.12: Variation of slurry toe angle with slurry concentration for four different levels of ball load volume at constant mill speed of 75% of critical.

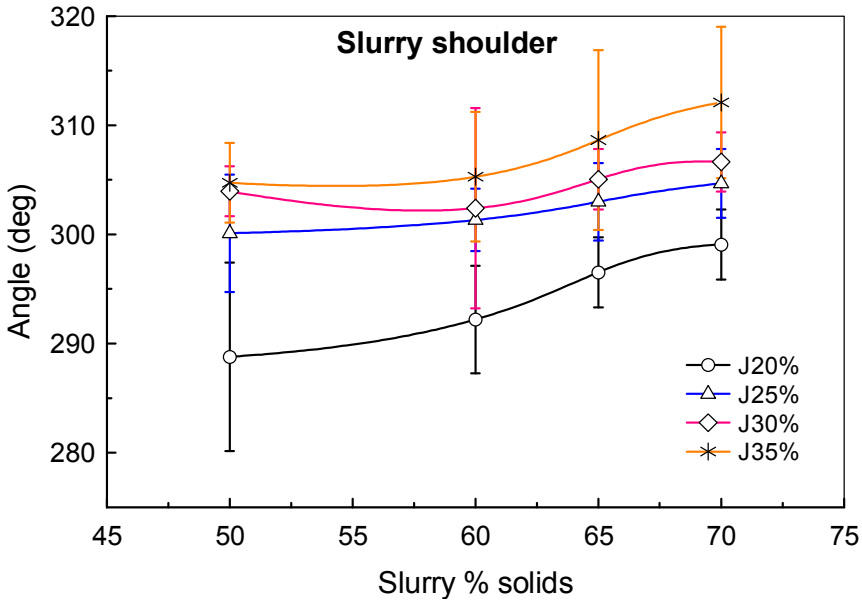

Figure 4.13: Variation of slurry shoulder angle with slurry concentration for four different levels of ball load volume at constant mill speed of 75% of critical.

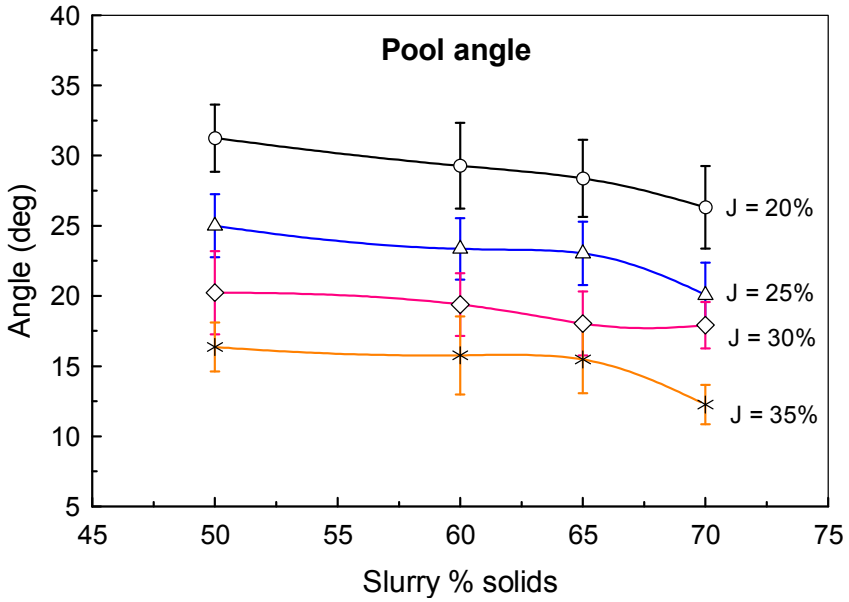

Figure 4.14: Variation of slurry pool angle with slurry concentration for four different levels of ball load volume at constant mill speed of 75% of critical.

Under normal operating conditions, slurry toe position in an industrial overflow mill remains more or less constant, defined by the size of the discharge opening while slurry shoulder position is dependent on the media shoulder angle (cf. Figure 4.15). The media at the shoulder tend to provide support for slurry in contact with the liner until it drains away (Moys *et al*, 1996). The slurry pool angle would vary in tandem with the media toe position. Therefore with regard to mill control, slurry pool angle seems to be a better parameter whose on-line measurement may provide real-time information of the level of solids concentration in slurry.

The foregoing analysis has shown that both slurry concentration and ball load volume have a marked effect on load dynamic position. In overall, higher slurry concentration gave a higher lifting capacity in the mill over the entire range of ball load volume investigated, which is a salient facet of our results. Also, at constant slurry concentration, the effect of changing the ball load volume on load behaviour was clearly visible. Nevertheless, given that the current results were obtained on a laboratory scale batch mill with no consideration of the mass transport effects,

there is no guarantee that the same results can be achieved on a full scale mill, which depicts the intricate nature of load behaviour. But at the very least the results have given us some insight on the possible options for controlling and optimising the mill using load behaviour data. Indeed the load position signals can be used as indicators to detect whether the mill is running on undesirable level of slurry density or ball load volume.

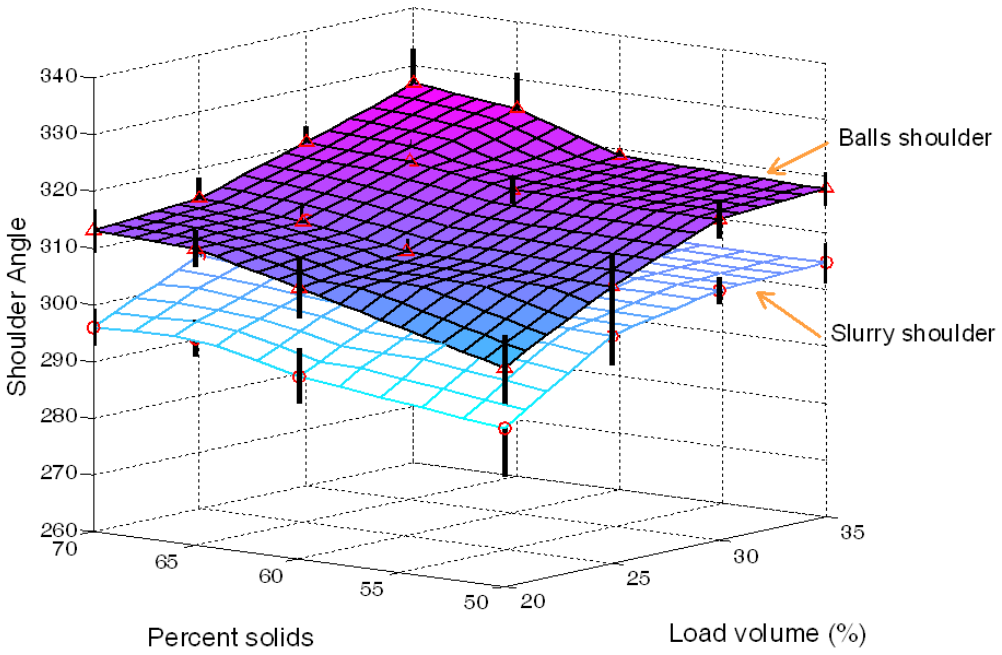

Figure 4.15: Surface plot showing a comparison of variation of media and slurry shoulder positions with slurry concentration (% solids) and ball load volume at a constant mill speed of 75% of critical.

4.3.4 Effect of media and slurry behaviour on mill power draw and specific energy consumption

4.3.4.1Mill power

It is generally accepted that the power required to grind material in a ball mill to the desired product size is an indication of the mill capacity and that mill power

varies intimately with load behaviour. In that respect any change in mill operational variables that directly impact on load behaviour would ultimately affect the mill power and subsequently the mill capacity. In this study, the mill power (excluding zero-load power) was obtained as a product of mill rotational speed and mill torque where the latter was measured using a load beam (cf. Chapter 3 for details). The measured torque relates to the energy required to maintain the load in its offset position as the mill rotates. It is derived from the product of the weight of the load and the horizontal distance between the load centre of gravity and the mill centre (i.e. torque-arm).

Figure 4.16 shows the trends in mill power draw with varying concentration of solids in slurry for four levels of ball load volume. For cases with 20, 25 and 30% ball loading, the trend in power draw appears much the same, increasing steadily as slurry concentration is increased before peaking at 65% solids while for the case of 35% ball loading, power starts to peak just after 60% solids. The steady increase in power draw is believed to come about due to the continuous lift being experienced by the load as slurry concentration increases, an act that would result in the load centre of gravity shifting upwards and away from the mill centre thereby increasing the torque arm, which would in turn increase the mill torque. This phenomenon is illustrated schematically in Figure 4.17. With further increase in proportion of solids in slurry from 65 to 70% wt, the slurry viscosity and particle packing increase which enhances the friction within the load and between the load and the mill wall. As a result, the load moves higher up the mill wall to a point where part of the cataracting media impinge directly on the mill shell, as characterised by a gradual drop in mill power. Also it is possible that the observed drop in power on increasing slurry concentration from 65 to 75% solids is owed to entrapment of the media in a slurry layer formed around the mill wall that reduces the effective mill volume (Moys and Van Nierop, 2001). However, this phenomenon was not reflected in the pattern of load signals, hence it is postulated that a few balls may have temporarily been stuck in the slurry layer and falling off later under the effect of gravity as portrayed by the fluctuations in the load sensor signals at the media toe region.

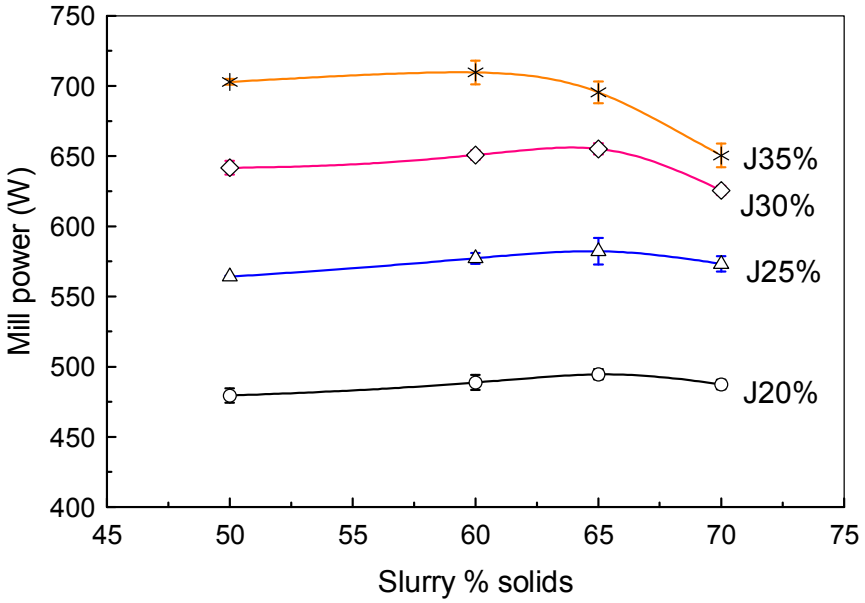

Figure 4.16: Trends in power draw as ball load volume and slurry concentration change at constant mill speed of 75% of critical.

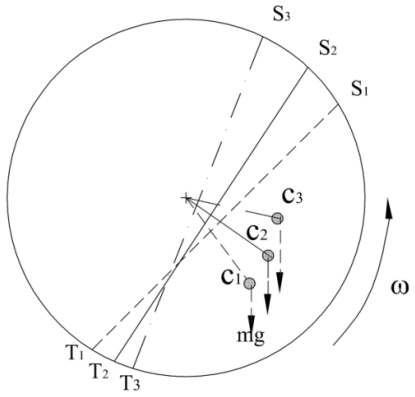

Figure 4.17: Schematic illustration of the shift in the load centre of gravity (c.o.g) with increasing load lift and the effect on the length of the torque-arm.

From the results, it is further noted that, the mill draws proportionally higher power at a higher ball loading, which is consistent with the experience in milling practice. It may sound logical that the additional media would tend to shift the centre of gravity of the now increased load volume towards the mill centre which reduces

the length of the torque-arm. However, the torque does not reduce since this effect is counteracted by the increased mass of the load. Equally, increased volume of the load results in high dynamic pressure exerted by the load on the mill walls. This helps to lock the load to the mill rotary motion subsequent to which a higher lifting action is experienced and the mill torque increases accordingly. But, it should be borne in mind that as further lifting continues a point is eventually reached when the cataracting balls start to fall directly on the mill wall introducing a counter torque to the mill rotation. This accounts for the decline in mill power and partly explains for the early witnessed peak at ball load volume of 35% as compared to other cases of lower ball loading.

Based on the analysis presented in the foregoing, it can be deduced that at a constant mill speed, the maximum power drawn by the mill simply depends on those factors that influence the 'lifting action' on the load such as ball load volume and slurry properties. Similar conclusions were advanced by Clermont *et al* (2008) following a series of tests on a 4.8 m diameter, wet pilot mill using UG2 Platinum tailings as feed material.

4.3.4.2 Specific energy consumption

To understand the relationship between the load behaviour and energy utilisation inside the mill, it was essential to analyse the mass specific energy consumption in producing particles finer than 75 µm over a set period of grinding time. Since experimental tests were performed on a batch mill, then an index used to define specific energy consumption was calculated as in equation 4.1.

$$E_{75\mu m} = \frac{\left(P - P_o\right) t}{60 \left(S_t^{<75\mu m} - S_o^{<75\mu m}\right) C_w m_s} \qquad [4.1]$$

Where,

$E_{75\mu m}$: Specific energy consumption [kWh/t]
P : Mill power [kW]
P_o : No-load power [kW]

m_s	:	mass of slurry inside the mill [tons]
C_w	:	weight fraction of solids in slurry
t	:	Grinding time [mins]
$S_o^{<75\mu m}$	:	Fraction of in-mill material < 75µm at time t = 0.
$S_t^{<75\mu m}$	:	Fraction of in-mill material < 75µm after grinding time, t

Figure 4.18 illustrates the observed trends in mass specific energy consumption in production of particles below 75µm for the milling conditions tested. The particle size distributions (PSD) were obtained by standard wet-dry sieving procedures using a vibratory sieve shaker. The PSD data can be reviewed in appendix B.

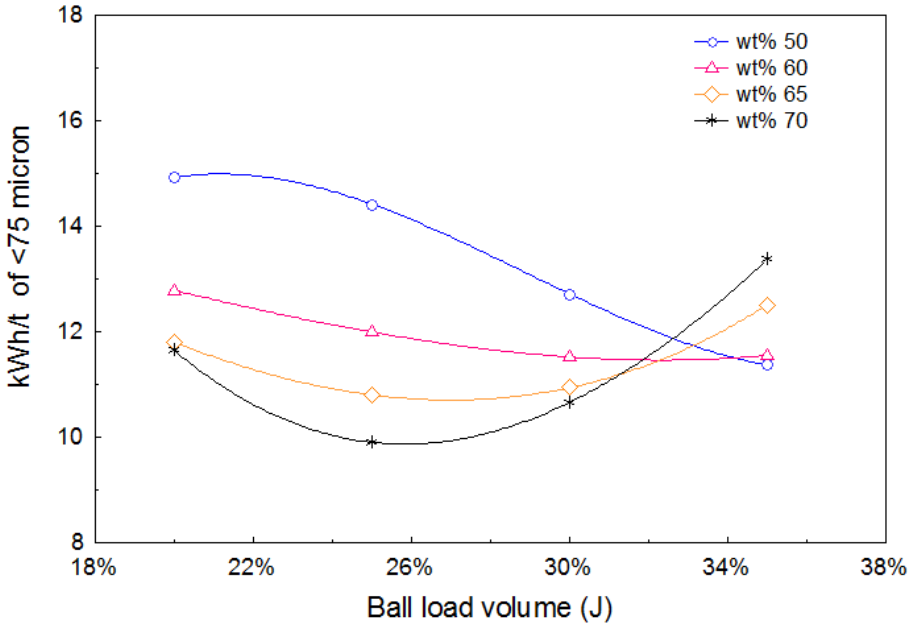

Figure 4.18: Variation of mass specific mill energy consumption with slurry solids concentration for four levels of ball load at mill speed of 75% of critical.

From Figure 4.18, the specific energy consumption appears to be greater at lower slurry concentration for the range of ball loading between 20 and 30%, but the converse becomes true as the ball load volume is increased from 30 to 35%. This trend partly agrees with the observations by Clermont *et al* (2008). Again, for the

range of slurry concentration between 60 and 70%, the results indicate first a gradual decline followed by a gradual rise in specific energy consumption as the ball load is increased. But for the situation of 50% solids, the specific energy consumption drops continuously with increase in ball loading. This unsteady trend in specific energy consumption clearly demonstrates the complex nature of the relationship between mill energy efficiency and operational factors whose understanding hitherto remains obscure.

From the analysis, one can intuitively note that, both the ball load volume and the slurry concentration hold an appreciable influence on specific energy consumption by the mill. The observed non-linear trend in variation of specific energy consumption with ball load volume and slurry concentration attests to the fact that in a multivariable milling environment, better energy efficiency can only be attained with correct tuning of operational factors to the desired optimum point. The results in Figure 4.18 suggest that for a constant mill speed, grinding is likely to proceed more efficiently at lower ball loading of 25% and high slurry concentration of 70% solids or higher ball loading of 35% and lower slurry concentration of 50 to 60% solids. However, one would argue that the cost associated with capacity losses at lower ball load volume or media wear at lower slurry concentration will offset the potential gain in grinding efficiency. Premised on this result, it is expected that studies related to mill control and optimisation strategies will receive greater attention in future and this research work serves as an added impetus to such developments.

4.4 Analysis of industrial data

4.4.1 Media and slurry dynamic positions

Presented in Figures 4.19 (a-d) are the results of the measured load position in an industrial mill using the on-line media and slurry sensor system (SENSOMAG®). Details of the experimental program are described in Chapter 3. Unlike the trend observed in laboratory data, the results in Figure 4.19a show that the media shoulder angle is insensitive to changes in slurry concentration. This unanticipated

trend was perhaps due to the fact that the motion of large balls used in the industrial mill was inappreciably influenced by the slurry behaviour contrary to the situation in the laboratory mill where the motion of the media, owing to their relatively smaller size may have been strongly influenced by slurry behaviour once the slurry got sufficiently viscous. The variation in media shoulder in relation to changes in ball load volume went in-line with our expectations being greater at higher ball load volume.

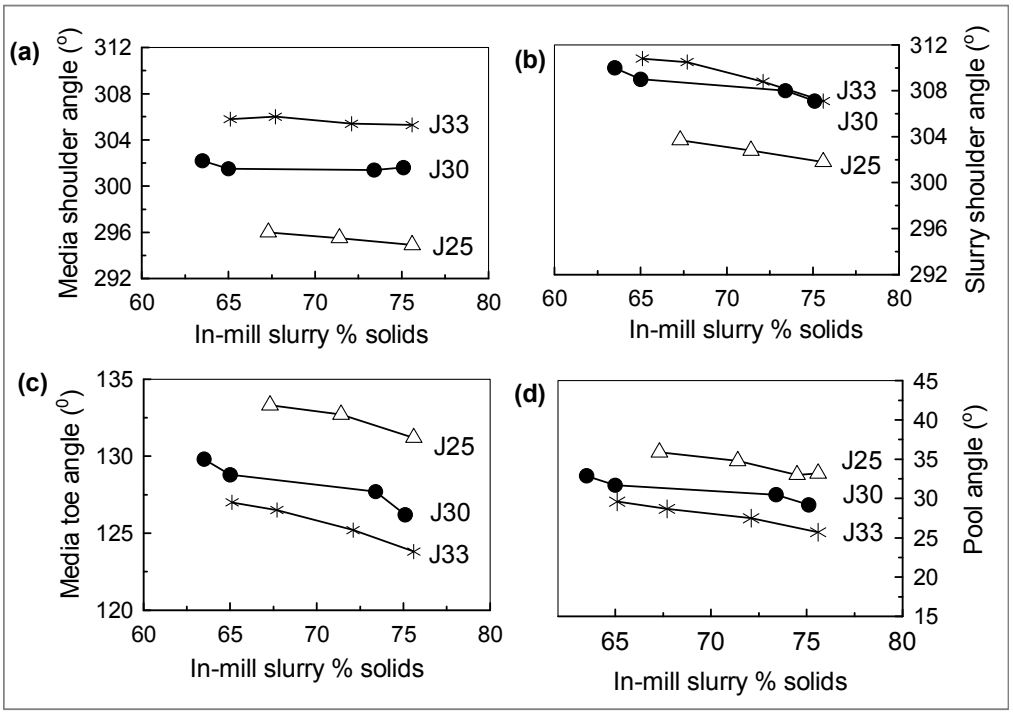

Figure 4.19: Media and slurry dynamic positions as measured by on-line load sensor (SENSOMAG) on industrial mill (N = 75% critical).

On the other hand, the slurry shoulder is typically above the media shoulder as depicted in the results shown in Figure 4.19b, which is counter-intuitive. This intriguing observation is probably a result of relatively slow drainage of the layer of slurry that will adhere to the sensor liner as it rises out of the load. Also, it is suspected that since the in-mill slurry concentration was regulated by varying the

flow rate of mill dilution water, then at the same ball loading, the steady decline in slurry shoulder angle with increase in percentage of solids in slurry could very well have been caused by the combined effects of gravity and cohesive forces which set in as slurry becomes denser.

The trends in media toe signal are given in Figure 4.19c. The results suggest that as slurry concentration increases, the media avalanching down the load's free surface at a faster rate leading to a media toe which moves up the descending mill wall (towards 9 o'clock position). Presumably as slurry concentration increases, the slurry entrapped within the media begins to behave like a lubricant. Now as the media toe shifts towards the 9 o'clock position, part of the space that would have otherwise been occupied by the slurry pool is taken up by the media, thus reducing the pool angle as exhibited by the results in Figure 4.19d. Note that the size of slurry pool has an impact on slurry residence time and consequently on slurry holdup volume.

4.4.2 Pool depth

The depth of slurry pool from the pool free surface to the minimum overflow level at the discharge end is another useful parameter that is related to slurry density and which is easily measurable by the 'SENSOMAG' system. Figure 4.20 graphically illustrates the pool depth and the associated parameters. Depending on slurry properties and mill operational factors, two cases are possible in computation of the slurry pool depth:

Case I:

If $\theta_{T(Slurry)} < 90^0$ then $h = R_T + R_M \text{ Sin } \{90 - \theta_{T(Slurry)}\}$

Case II:

If $\theta_{T(Slurry)} > 90^0$ then $h = R_T - R_M \text{ Sin } \{\theta_{T(Slurry)} - 90\}$

The mill radius (R_m) and discharge opening radius (R_T) were given as 3.636m and 0.84m respectively. The slurry toe angle ($\theta_{T(Slurry)}$) was measured by the 'SENSOMAG' system and the values obtained can be reviewed in Appendix C.

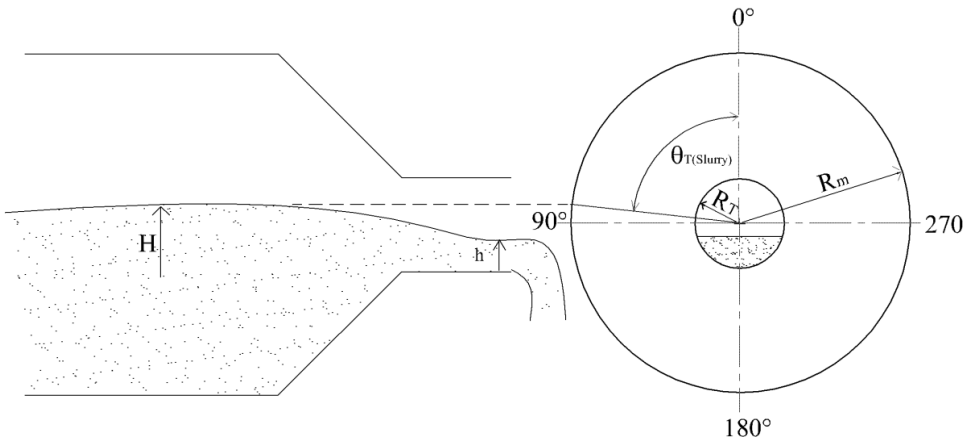

Figure 4.20: Schematic illustration of slurry pool depth at the discharge opening and the associated measureable parameters.

Presented in Figure 4.21 are the results obtained from 12 industrial surveys using the SENSOMAG system showing the variation of the normalized pool depth with slurry concentration and ball load volume. The values of the pool depth were normalized with respect to the volumetric feed flow rate (F), i.e. to neutralize the effect of feed flow rate so that any variations in pool depth can only be associated with ball loadings and slurry % solids. At ball load volume of 30 and 33%, the normalized pool depth increases steadily with increase in percentage of solids in slurry as shown by the results in Figure 4.21. The increasing trend of h^* with increase in slurry concentration could be attributed to the continuous reduction in slurry mobility as a result of increasing slurry viscosity. But notice that at ball load volume of 25%, the normalized pool depth stays unchanged up to 74% solids before it starts to increase. This inconsistent pattern depicts the effect of load behaviour on in-mill slurry transport.

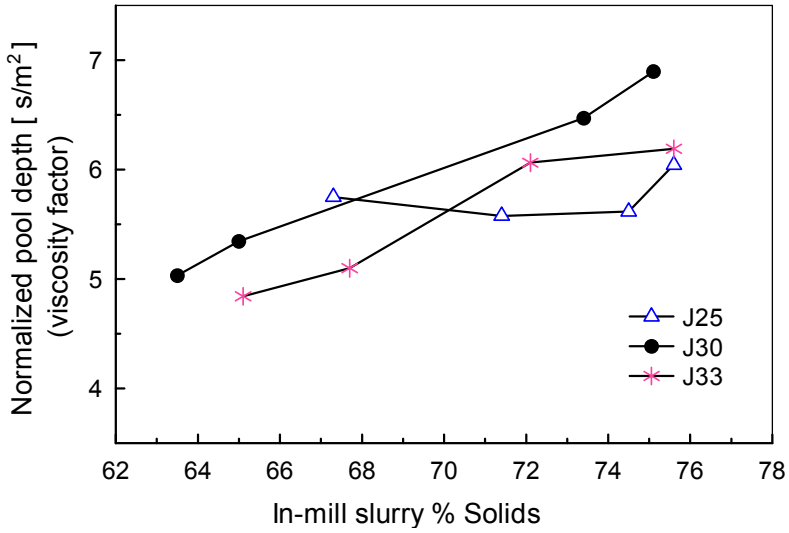

Figure 4.21: A plot of industrial data showing the variation of the normalized pool depth (viscosity factor) with slurry % solids for three different ball load volumes at a constant mill speed of 75% of critical.

In overall, the data obtained from the SENSOMAG® system indicate some possible correlation of dynamic media angle, slurry pool angle and normalized slurry pool depth with slurry % solids and ball load volume. This data if accurately measured and correctly processed could be utilised for mill online monitoring and control as well as characterising the changes in mill operating parameters.

4.4.3 Mill load and power draw

Analysis of the variation of the mill load and power draw with changes in mill operating conditions was performed to gain further understanding of the milling process. Figure 4.22a shows the variation of mill load with changes in slurry concentration for different cases of ball load volume. The mill load increases as the percentage of solids in slurry increases in accordance with the increase in the mass of slurry in the mill. In Figure 4.22b, the mill power decreases systematically with increase in percentage of solids in slurry which is expected. This trend can be

explained in relation to the effect of pool weight on the torque that counters the mill rotation. At same conditions of ball load volume, high percentage of solids in slurry increases the slurry holdup weight in the pool. This in effect displaces the centre of mass of the mill load (media and slurry) towards the mill centre which consequently shortens the torque arm and hence reduces the component of torque that opposes the mill rotation. Accordingly, the mill power is expected to decrease.

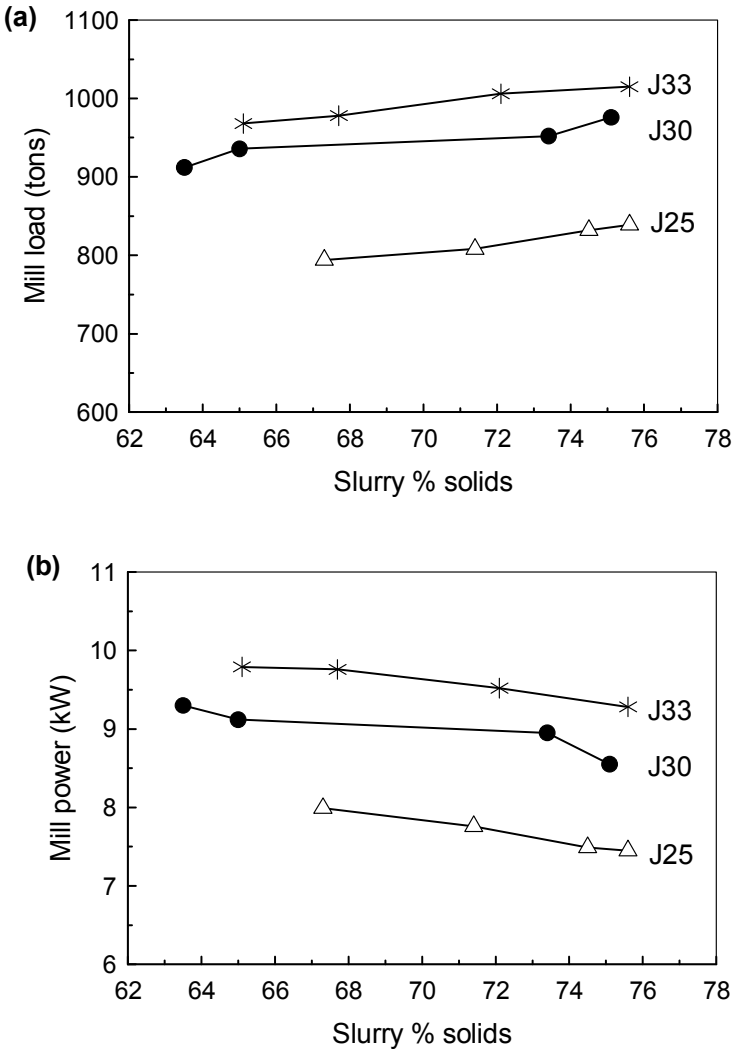

Figure 4.22: Industrial mill data showing the variation of mill load and power draw with slurry concentration for three different levels of ball load volume at constant mill speed, N = 75% of critical.

4.5 Conclusions

The data obtained from both the laboratory mill and the industrial mill using direct load sensors was successfully analysed in this chapter. Through deep analysis of the laboratory sensor signals data, it was possible to characterise the mill internal load behaviour for the set of mill operating conditions tested. Further, the ability of the load sensors to detect changes in mill operating conditions has been clearly demonstrated. Different operating conditions were well distinguishable from each other and by that it would be possible to identify the desired mill operating region. The changes in slurry solids concentration were reflected in the variations of the pool angle for the industrial case and the conductivity signal amplitude for the laboratory case while the media shoulder and media toe angles exhibited observable responses to changes in ball load volume for both laboratory and industrial cases. On this basis, it is believed that by correctly measuring and interpreting the media and slurry sensor signals data, it should be possible to monitor the mill behaviour and characterise changes in mill operating conditions for better mill control and performance optimisation. This is an attractive option due to the simplicity of the data involved and the interpretational ease.

In view of the findings of this chapter, an attempt is made in chapter 5 to explore the feasibility of using the characteristic features extracted from the load sensor signals data to predict the variation of two important mill operating parameters: slurry solids concentration and ball load volume, by multivariate analysis.

CHAPTER 5

Using Media and Slurry Sensor Signals Data to Predict In-mill Slurry Density and Load Volume by Multivariate Modelling

5.1 Introduction

On-line monitoring and control of mill load volume and slurry density is desirable for achieving stable operation of the milling circuit with optimum production capacity and energy efficiency. In this context, several techniques have been proposed by researchers in the drive towards real-time accurate estimation of mill load volume and slurry properties based on measurable mill parameters. Traditionally, the ball load volume was controlled by measuring mill power draw, but this method cannot reliably identify the optimum ball loading due to interactions arising from other factors such as changing liner profile, ore characteristics and feed size distribution on power draw.

Kolacz (1997) proposed a method that uses piezoelectric strain traducers to study the variations in mill charge volume. The strain changes in the mill shell during mill rotation were related to the charge volume inside the mill. Acoustics have also been utilised recently in measurement and control of mill load volume (Xing, 2004, Sha *et al*, 2006a). The acoustic technique is however subject to disturbances from other noise around the mill.

Analysis of vibration signals extracted from the bearing housing by accelerometers is another recent method that is quickly gaining popularity as a means to estimation of mill load volume. Behera *et al* (2007) found that the amplitude of the vibration signal in frequency domain picked up by accelerometers mounted directly on the mill shaft was correlated with mill load volume. Su *et al* (2008) analysed the vibrations picked up on the bearing house of a tubular ball mill and related them to the variations of mill load volume using a multivariate technique, non-linear partial least square (NLPLS). Huang *et al* (2009) established a relationship between the angular position of the maximum vibration point on the mill shell and the mill load volume. Si *et al* (2009) used a microphone and an accelerometer to pick up the mill noise and vibration signals of the inlet trunion respectively. They obtained the characteristic power spectra energy of both mill noise and vibration, the centroid frequency and frequency domain variance of mill noise which they reckon could be used in combination to estimate the mill load. More recently, Tang *et al*

(2010a) analysed the differences in power spectral density of mill shell vibration signals under different wet grinding conditions. They developed a correlation of charge volume and pulp density with mill shell vibration signal using genetic algorithm- partial least squares (GA-PLS) method. As an extension of their work they developed a soft-sensor model based on principal component analysis (PCA), support vector machines (SVM) and fast Fourier transform (FFT) to predict mill load volume using the measured mill vibration signal.

All these researches focus on measurement of mill load volume while attempts to measure slurry density remain scarce, possibly due to absence of a definitive relationship between slurry properties and vibration signals. Also it is appreciated that other factors around the mill circuit other than the mill load may affect the vibration signal resulting in false predictions. To overcome this challenge, Tano *et al* (2005), applied a direct contact technique to estimate both slurry viscosity and mill load volume. They measured the deflection characteristics of a rubber lifter embedded with a strain gauge sensor, as it passed through the charge. A signal profile obtained was related to slurry viscosity and mill load volume by a multivariate method that combined wavelet analysis and linear partial least square (PLS) regression. The results showed good prediction of mill load volume but deviated significantly in estimation of slurry viscosity. The large prediction error for slurry viscosity is believed to be due to non-linear relationship between slurry viscosity and lifter deflection characteristics which could not be addressed by linear PLS approach. However, their approach lays the ground for further work.

The interpretations of the media and slurry sensor signals data in Chapter 4 of this thesis have shown that the key features that define the dynamic behaviour of the media and slurry inside the mill are strongly influenced by both the slurry density and ball load volume. As such, it is strongly believed that if correctly measured, these direct features could provide the most reliable data for estimation of slurry density and mill load volume. As a contribution of this chapter, the data extracted from direct load sensor signals depicting the dynamic behaviour of media and slurry inside the mill is analysed using two multivariate methods: (i) Partial least

squares (PLS) and (ii) combination of PLS and radial basis functions neural networks (RBF-PLS), to predict in-mill slurry density and ball load volume. The RBF neural network is incorporated in the PLS model to handle any possible nonlinearity between the predictor and response datasets.

5.2 Multivariate modelling

Multivariate modelling techniques are increasingly gaining popularity in the mineral processing industry as appropriate tools for extracting from datasets information that may be useful for process monitoring, control and optimisation. One apparent advantage of multivariate based models is the ability to handle conditions in which there are many process variables controlled and uncontrolled, all correlated with one another to varying degrees. The common multivariate techniques that have been useful in building soft sensors in the mineral processing industry include, artificial neural nets (Stange, 1993), partial least squares (Tano *et al*, 2005), principal component analysis (Jemwa and Aldrich, 2006; McElroy *et al*, 2008), support vector machines (Tang *et al*, 2010b), genetic algorithms (Karr and Yeager, 1995), canonical variable analysis (Kourti, 2005) and Fisher discriminant analysis (McElroy *et al*, *op cit*). Three such techniques considered in our study are principal component analysis (PCA), partial least squares (PLS) and radial basis functions neural networks (RBFNN).

5.2.1 Principal component analysis (PCA)

PCA is a method of transforming high dimensional data into low-dimensional subspace by replacing linear combinations of correlated variables with new uncorrelated variables while retaining most of the variations present in the original data (McElroy *et al*, 2008). Therefore, by summarising the pattern of inter-correlation among variables, it reduces the large number of variables to a small number of clusters. The first principal component can thus be defined as an axis along which data is projected with maximum variance whilst the second principal component maximizes variance subject to first axis orthogonality and so forth, the last axis having the least variance of all possible ones. The number of principal

components can be determined based on the amount of variance in the loading vectors to which it is desired that the selected PCs should contribute. The maximum number of possible PCs should equal the rank of input data matrix, *X*.

Given a data matrix, $X \in \Re^{n \times m}$, scaled and centred to zero mean and unit variance with *n* rows (samples) and *m* columns (variables), PCA decomposes the data into outer products of scores, t_i and loadings, p_i plus a residual matrix, E, mathematically represented as,

$$X = TP^T + E \quad \Rightarrow \quad \sum_{i=1}^{k} t_i p_i^T + E_k \qquad [5.1]$$

Where *T* is *n x k* matrix representing the projections of sample points along the principal component direction (stores information on relationship between samples), while *P* is *m x k* matrix that represents the angle cosines of the direction of the principal component (stores information on relationship between variables). The main disadvantage of PCA technique is that sometimes those directions with maximum input data variance do not necessarily contain the most useful information. In essence, one might be analysing the noise signal and rejecting the valid data signal.

5.2.2 Partial least squares method (PLS)

PLS models are based on principal components of both the independent data (predictors) and the dependent data (responses). PLS transforms the predictor variables from high dimensionality to low dimensionality by extracting factors or latent variables which are correlated with responses while capturing a large amount of variation in the predictors (Lee *et al*, 2006). Therefore, PLS maximizes the covariance between input and output variables. The main advantage of PLS is the ability to handle the problem of multi-collinearity and sparse sample data set in regression (Li *et al*, 2007; Wold, *et al*, 2001; Geladi and Kowalski, 1986). Given standardized data matrices *X* and *Y* of predictors and responses respectively, PLS

decomposes X into score vectors, t_i, loading vectors, p_i and residuals matrix, E while Y is decomposed into score vectors, u_i, loading vectors, q_i and residuals matrix, F. This procedure is referred to as the "outer relations" mathematically expressed as,

$$X = TP^T + E \quad \Rightarrow \quad \sum_{i=1}^{a} t_i p_i^T + E \qquad [5.2]$$

$$Y = UQ^T + F \quad \Rightarrow \quad \sum_{i=1}^{a} u_i q_i^T + F \qquad [5.3]$$

In which a is the number of latent variables determined by cross-validation. The common cross-validation method is the leave-out-one (LOO) method (Tinsley and Brown, 2000). X and Y are indirectly related through their scores by an "inner relation" which is a functional mapping model from T to U. If the relation is linear, then $U = BT + H$, where B is a diagonal matrix of regression coefficients, which is determined by minimizing the residual, H. Figure 5.1 shows the architecture of the PLS model.

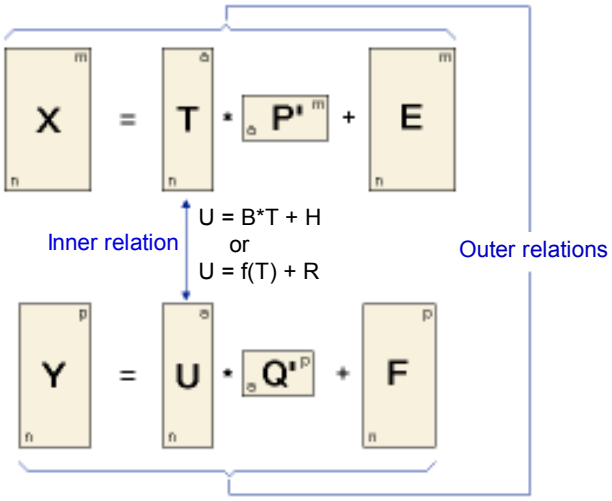

Figure 5.1: Architecture of the PLS model illustrating the outer and inner relations

To handle non-linearity that characterises real industrial processes, the inner relation can be expressed as, $U= f(T)+R$, where $f(.)$ is a mapping function between U and T that can take quadratic form (Tang and Li, 2003; Wold *et al*, 1989) or Neural Network based kernel functions (Baffi *et al*, 2000; Li *et al*, 2007; Su *et al*, 2008).

The often used algorithm for PLS regression is the non-linear iterative partial least squares (NIPALS), presented in a summary in Table 5.1. However, other modified NIPALS algorithms exist which include Kernels algorithms (Lindgren *et al*, 1994, Dayal and MacGregor, 1997, Baffi *et at*, 1999). The goal of PLS algorithm is to minimize the norm of F while keeping the correlation between X and Y by the inner relation between U and T.

Table 5.1: NIPALS algorithm for linear PLS

Step	Summary of steps	
0	Mean centre and scale X and Y	
1	Set the output scores **u** equal to a column of **Y**	
2	Compute input weights **w** by regressing **X** on **u**	$w^T = (u^T.X)/(u^T.u)$
3	Normalize **w** to unit length	$w = w/\|w\|$
4	Calculate input scores, **t**	$t = (X.w)/(w^T.w)$
5	Compute the output loadings **q** by regressing **Y** on **t**	$q^T = (t^T.Y)/(t^T.t)$
6	Normalize **q** to unit length	$q = q/\|q\|$
7	Calculate new output scores **u**	$u = (Y.q)/(q^T.q)$
8	Check convergence on **u:** if YES goto 9 ELSE goto 2	
9	Calculate the input loadings **p** by regressing **X** on **t**	$p^T = (t^T.X)/(t^T.t)$
10	Calculate inner model regression coefficient, **b**	$b = (t^T.u)/(t^T.t)$
11	Calculate input residual matrix	$E = X - t.p^T$
12	Calculate output residual matrix	$F = Y - b.t.q^T$
13	If additional PLS dimensions are necessary, replace **X** and **Y** by **E** and **F** respectively and repeat steps 1 to 13	

5.2.3 Radial basis functions neural networks (RBF)

A radial basis function network can be considered as a 3-layer neural net comprising the input, hidden and output layers. The input layer is a set of source

nodes which basically serves as inputs distributer while the hidden layer contains radial functions each represented by a node and having same dimensionality as the input data. The hidden layer is connected to the output layer by connections of weights. Each node in the hidden layer operates by summing up all its input values, transforming the summed value using an activation function and transmitting the summed and transformed value to the output node. The transformation from input space to the hidden–unit space is non-linear while transformation from hidden space to output space is linear. The typical non-linear transformation functions used in RBF networks are a set of Gaussian kernel (Zheng and Billings, 1996). But it is widely held that the choice of RBF centres and not nonlinearity function is critical to the performance of the RBF networks (Chen *et al*, 1991). The architecture of RBF network can be depicted as shown in Figure 5.2.

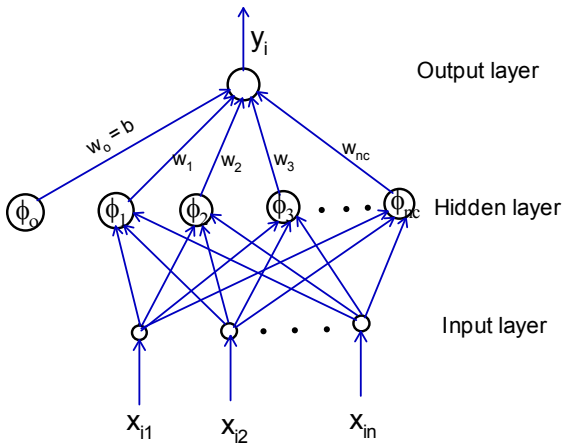

Figure 5.2: Generalized radial basis function architecture for single output

The response *y(x)* of the output layer node for the input objects *x* is calculated using an approximating function, $y^*(x)$, equation 5.4 which represents a linear combination of multidimensional radial activation functions.

$$y^*(x) = w_o + \sum_{j=1}^{n_c} w_j \phi \left\| c_j - x \right\| \qquad [5.4]$$

The norm, $\|\bullet\|$ is the Euclidean distance, n_c is the number of RBF centres, c_j (j = 1, 2,..n_c) is the j^{th} centre chosen from the data sample x while w_j represents the weights associated with j^{th} RBF centre which are found by minimizing the error between $y^*(x)$ and unknown function $y(x)$ during network training. The parameter w_o (bias weight) is a constant that acts as a shift in output level. A set of multi-dimensional Gaussian kernel, ϕ_j is a popular choice for radial basis functions written as shown in equation 5.5 in which σ_j is the centre width for the j^{th} centre in the hidden layer .

$$\phi_j = \exp\left(-\frac{\|c_j - x\|^2}{\sigma_j^2}\right) \qquad [5.5]$$

Due to the capabilities of RBF neural networks to form predictive relationships between inputs (sources) and outputs (Targets), they have found applications in various fields such as image processing, (Sahin, 1997), process fault detection (Jemwa and Aldrich, 2006), predictive maintenance (Zemouri *et al*, 2010), and pattern recognition (Wan and Harrington, 1999). The present study aims at assessing the possible extension of RBF application to estimation of key milling process variables that are hitherto difficult or expensive to measure.

5.2.4 Combined RBF-PLS method

The radial basis functions network is integrated into the regression framework of PLS to model nonlinearities in the process. Figure 5.3 illustrates the RBF-PLS network architecture for a single output. The RBF neural network is trained to capture nonlinearities between the input and output variables in the projected latent space. The RBF network inputs and outputs are the scores, t and u respectively.

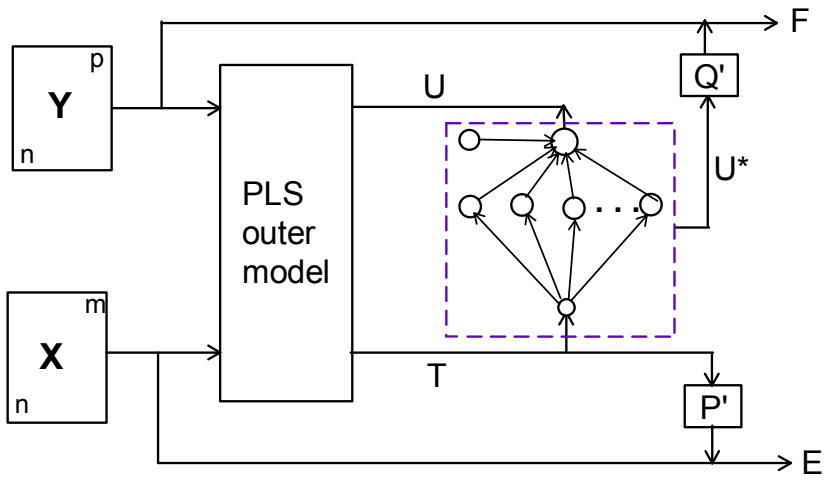

Figure 5.3: Graphical illustration of the RBF-PLS method

Nonlinear mapping between t and u provided by the RBF model can be expressed in the form of equation 5.6 in which all symbols retain their previous definitions.

$$u^* = w_o + \sum_{j=1}^{n_c} w_j . \exp\left(-\frac{\left\| c_j - x \right\|}{\sigma_j^2} \right) \qquad [5.6]$$

For strongly nonlinear data, Baffi *et al* (1999) proposed a modified NIPALS algorithm that utilizes the error between u and u^* to update the outer input weight factor as an improvement to the earlier algorithms presented by Wilson *et al*, (1997) and Qin and McAvoy (1992). The algorithm by Baffi *et al*, (*op cit*), given summarily in Table 5.2 was considered in this study and was implemented in MATLAB environment. The associated MATLAB programs are presented in Appendix D. The theoretical equations illustrating the error based weight updating procedure, as indicated by steps 10 and 11 in Table 5.2 are presented in Appendix E together with other miscellaneous calculations.

Table 5.2: Modified NIPALS algorithm for RBF-PLS (Baffi *et al*, 2000).

Step	Summary of steps	
0	Mean centre and scale X and Y	
1	Set the output scores **u** equal to a column of **Y**	
2	Compute input weights **w** by regressing **X** on **u**	$w^T = \left(u^T.X\right)/\left(u^T.u\right)$
3	Normalize **w** to unit length	$w = w/\|w\|$
4	Calculate input scores, **t**	$t = (X.w)/(w^T.w)$
5	Train RBF neural network between **t** and **u**	$\left(c_j, \sigma_j, \omega_j\right) \leftarrow (t,u)$
6	Calculate non-linear prediction of **u**	$u^* = \sum_{j=1}^{n_c} \omega_j.\exp\left[\left(-\|c_j - t\|\right)/\sigma_j^2\right] + \omega_o$
7	Compute output loadings **q** by regressing columns of **Y** on $\mathbf{u}^*$	$q^T = \left(u^{*T}.Y\right)/\left(u^{*T}.u\right)$
8	Normalize **q** to unit length	$q = q/\|q\|$
9	Calculate new output scores **u**	$u = \left(Y.q\right)/\left(q^T.q\right)$
10	Compute input weights updating parameter **Δ w**	$\Delta w = \left(Z^T.Z\right)^-.Z^T.e$
11	Compute new input weights **w**	$w = w + \Delta w$
12	Normalize **w** to unit length	$w = w/\|w\|$
13	Calculate new input scores **t**	$t = (X.w)/(w^T.w)$
14	Check convergence on **t:** if YES goto 15 ELSE goto 5	
15	Calculate the input loadings **p** by regressing **X** on **t**	$p^T = \left(t^T.X\right)/\left(t^T.t\right)$
16	Repeat steps 5 and 6 and obtain non-linear prediction of **u**	$u^* = \sum_{j=1}^{n_c} \omega_j.\exp\left[\left(-\|c_j - t\|\right)/\sigma_j^2\right] + \omega_o$
17	Calculate input residual matrix	$E = X - t.p^T$
18	Calculate output residual matrix	$F = Y - u^*.q^T$
19	If additional PLS dimensions are necessary, replace **X** and **Y** by **E** and **F** respectively and repeat steps 1 to 19	

5.3 Application case study 1: Laboratory data

5.3.1 Introduction

The predictive performances by two multivariate models discussed in section 5.2; PLS and RBF-PLS were comparatively evaluated. The data obtained during 16 laboratory experiments consisting of 96 samples was considered in the study. The data was divided into two parts: the first 48 samples were used for model training while the rest were utilised for model testing. The root mean square error (RMSE) and the cross-validation correlation coefficient (Q^2) were applied to assess the performance of the two models. The RMSE is given as follows:

$$RMSE = \sqrt{\sum_{i=1}^{n} (y_i - y_i^*)^2 / n} \qquad [5.7]$$

Where y and y^* represent the measured and predicted values respectively while n is the number of samples or observations. The RMSE can be evaluated for the training/calibration set ($RMSE^C$) and for the test/validation set ($RMSE^V$). The cross-validation correlation coefficient (Q^2) which indicates the model prediction accuracy and the coefficient of determination (R^2) which defines data fitting quality are obtained as follows:

$$Q^2 = 1 - \left(PRESS/ss_Y\right) \quad ; \quad R^2 = 1 - \left(ss_R/ss_T\right) \qquad [5.8]$$

Where SS_R and SS_T are the residual and total sum of squares respectively, SS_Y is the sum of squares of response variables while PRESS is the predicted residual sum of squares.

5.3.2 Prediction of slurry density and ball load volume

5.3.2.1 Selection of latent variables

From the media and slurry sensor signals data described in Chapter 4, four factors: slurry pool angle (= media toe - slurry toe), dynamic media angle (= media shoulder - media toe), total slurry angle (= slurry shoulder - slurry toe) and conductivity signal amplitude, displayed characteristic responses to changes in ball load volume and slurry density as depicted in the patterns of the load sensor signals. Therefore, as a starting point for latent variables (LVs) search, all the four factors were considered as candidate feature variables from which the LVs or principal components (PCs) would be extracted. The ball load volume and in-mill slurry density (specific gravity) were treated as response variables.

The cross-validation technique of leave-one-out (LOO-CV) also known as 'jack-knife' was applied within the PLS model framework to extract the latent variables (LVs) out of the four factors. Three factors (slurry pool angle, dynamic media angle and conductivity voltage) cumulatively explained for > 99% of variance in the dataset with PRESS value of < 2 (See Figure 5.4). Therefore, the three factors

were considered as LVs as the benefit of the fourth variable was insignificant. Also, by examining the correlation matrix the three factors were found to be strongly related to the response variables. All programs utilised in the analysis were implemented in MATLAB. The conceptual PLS model is given as,

$$Y = f(Media\ angle,\ Pool\ angle,\ Slurry\ conductivity) + residuals \qquad [5.9]$$

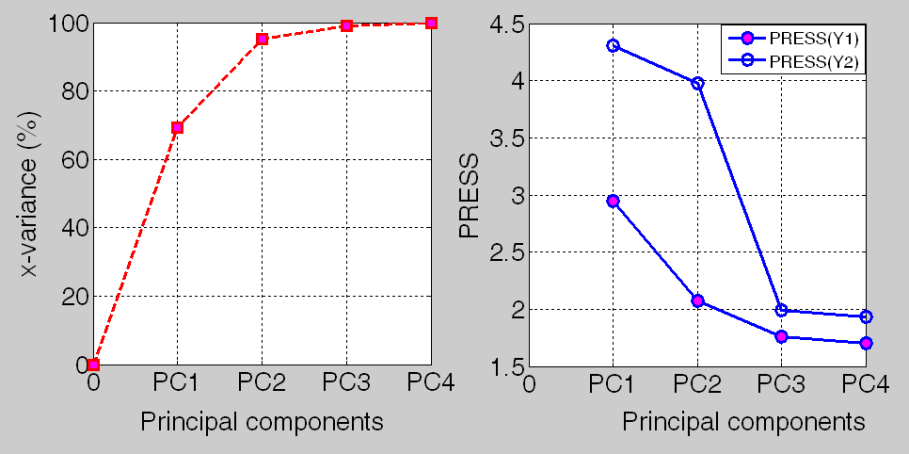

Figure 5.4: The plot of x-variance and PRESS values illustrating the cumulative contribution of the principal components (PCs) to the model performance.

Table 5.3 presents a summary of the dataset used for training and testing the models. It is important to point out that, the mean values and standard deviations presented in Table 5.3 were computed over the entire data generated during each experimental run, simply to illustrate the quality of the data. But to facilitate training and testing of the models, an average sample was computed for every 3 mill revolutions over 20 mill revolutions. This yielded a total of 96 samples for the 16 experimental runs considered. The data recorded in the first and last 10 revolutions were utilised for model training testing respectively. Note that prior to model training and testing, the data was standardised by centring to zero mean and scaling to unit variance to avoid parameter dimension effects on the model outputs.

Table 5.3: Mean values and standard deviations of the laboratory dataset

Exp. #	Predictor variables (X)						Responses (Y)	
	$\theta_{(Pool)}$ [deg]		$\theta_{D\,(media)}$ [deg]		V/V_O [-]		J [%]	S.G [-]
	$\bar{x}_1$	σ	$\bar{x}_2$	σ	$\bar{x}_3$	σ		
1	31.3	1.40	156.9	3.17	0.857	0.008	20	1.55
2	29.3	2.06	165.7	3.72	0.813	0.013	20	1.73
3	28.4	1.75	168.1	2.40	0.768	0.019	20	1.85
4	24.3	1.94	172.8	2.86	0.717	0.024	20	1.98
5	25.0	1.24	171.3	3.04	0.860	0.009	25	1.55
6	23.4	1.19	170.5	1.01	0.829	0.020	25	1.73
7	23.0	1.27	172.1	1.90	0.776	0.012	25	1.85
8	20.1	1.31	175.8	1.94	0.728	0.021	25	1.98
9	20.2	1.96	179.8	3.64	0.857	0.013	30	1.55
10	19.4	1.24	178.4	2.16	0.809	0.020	30	1.73
11	18.0	1.28	180.1	2.09	0.761	0.023	30	1.85
12	17.9	1.65	182.2	1.74	0.735	0.009	30	1.98
13	16.4	1.74	182.7	2.45	0.849	0.021	35	1.55
14	15.8	1.78	182.3	1.93	0.805	0.008	35	1.73
15	15.5	1.41	190.2	1.30	0.757	0.020	35	1.85
16	12.3	1.40	192.9	3.29	0.721	0.028	35	1.98

5.3.2.2 PLS Model training and testing

A linear PLS model between the selected predictors and the responses was built aimed at assessing the predictive ability of the linear model in comparison with the non-linear model, RBF-PLS. Figures 5.5 and 5.6 present the training results by the PLS model over the load volume and slurry density (specific gravity) data respectively while Figures 5.7 and 5.8 depict the testing of the PLS model on the test dataset. The results indicate that the PLS model predicted both the load volume and the slurry density successfully. A closer inspection of the results in Figures (5.5 – 5.8) reveals that the PLS model gives better prediction of ball load volume than slurry density. This is thought to be due to the ability of PLS model to provide good approximation of the underlying linear structure between the ball load volume and the predictors than the non-linear structure between the slurry density and the predictors. As required from PLS theory, the model coefficients estimated

during model training were utilised in the prediction of the response variables during model testing.

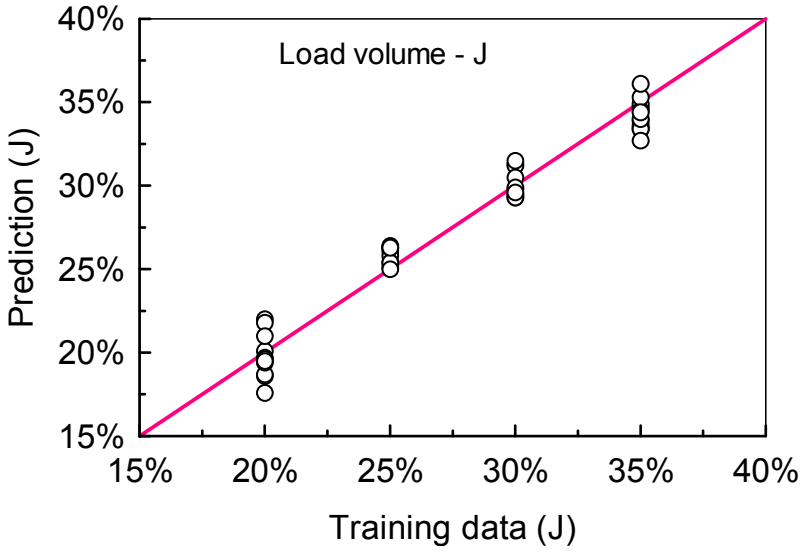

Figure 5.5: Plot of laboratory training data for mill load volume versus predictions by the PLS model

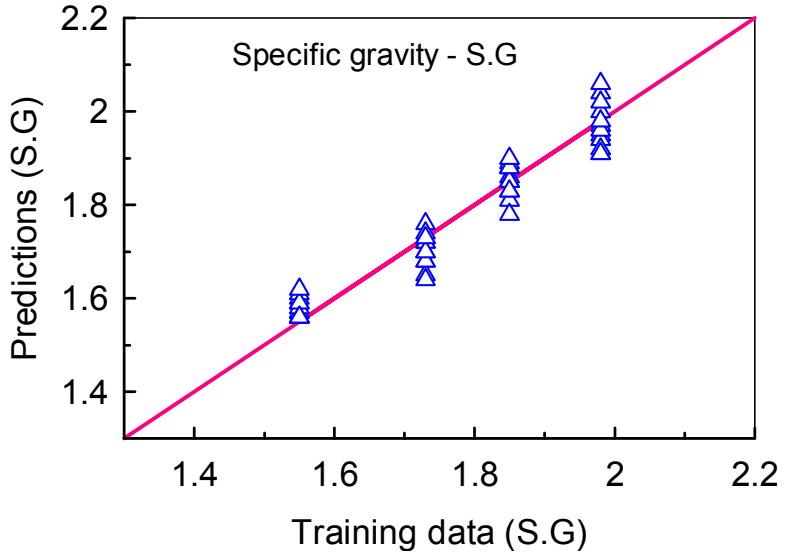

Figure 5.6: Plot of laboratory training data of in-mill slurry density versus predictions by the PLS model.

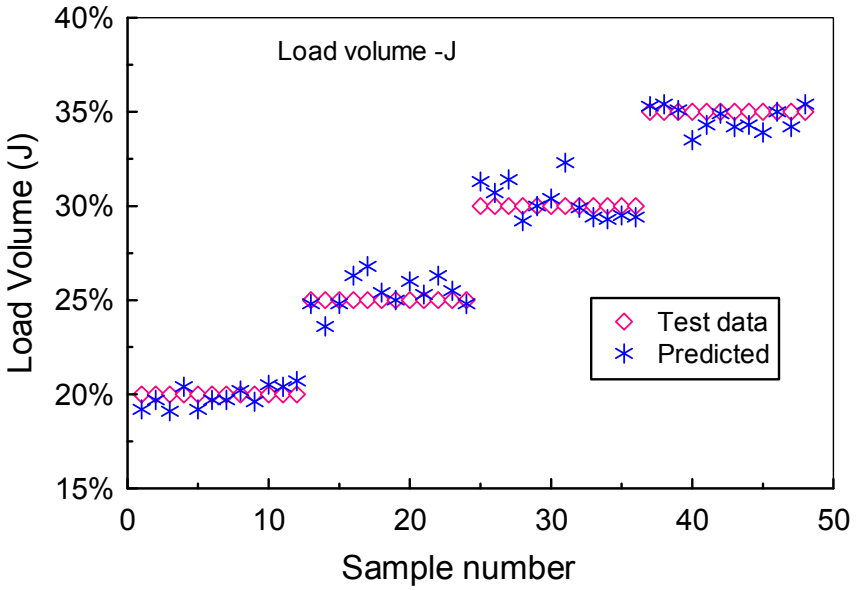

Figure 5.7: Plot of PLS model predictions of mill load volume over laboratory testing data for each observation.

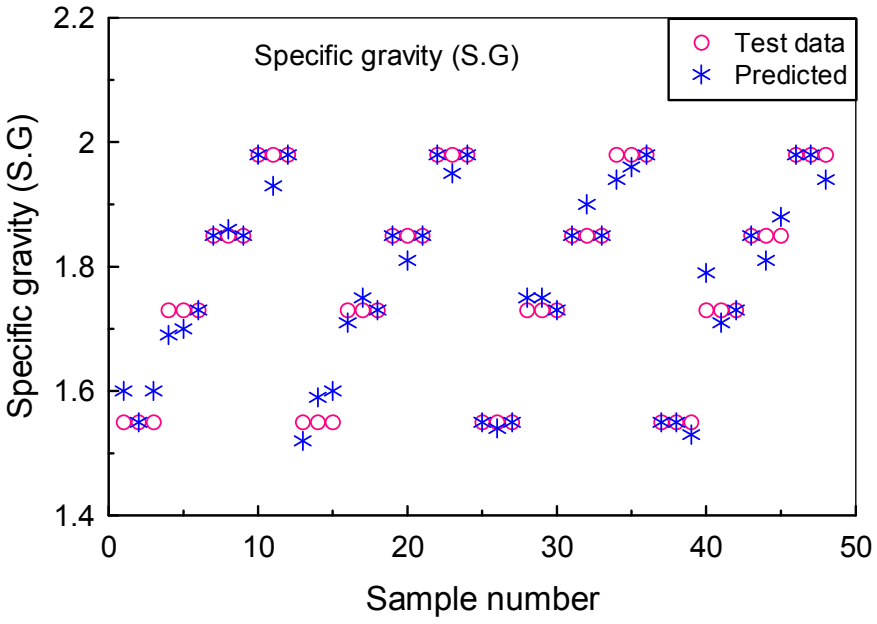

Figure 5.8: Plot of PLS model predictions of in-mill slurry specific gravity over laboratory testing data for each observation

The scaled PLS regression coefficients, denoted as B_{PLS} and the inner relation coefficients denoted as B are shown.

$$B_{PLS} = \begin{array}{c} \\ x_1 \\ x_2 \\ x_3 \end{array} \begin{array}{c} \begin{array}{cc} Y_1 & Y_2 \end{array} \\ \begin{bmatrix} -0.8112 & 0.2597 \\ 0.2357 & 0.2374 \\ 0.3129 & -0.9614 \end{bmatrix} \end{array} ; \quad B = \begin{array}{c} \\ t_1 \\ t_2 \\ t_3 \end{array} \begin{array}{c} \begin{array}{ccc} u_1 & u_2 & u_3 \end{array} \\ \begin{bmatrix} 0.666 & 0.000 & 0.000 \\ 0.000 & 1.089 & 0.000 \\ 0.000 & 0.000 & 0.514 \end{bmatrix} \end{array}$$

The magnitudes of the regression coefficients, B_{PLS} suggest that x_1 (pool angle) reflects better the changes in mill load volume (Y_1) than other predictors while x_3 (conductivity signal amplitude) reflects better the changes in slurry density (Y_2). The two variables x_1 and x_3 can thus be considered as the principal feature variables in the model. The coefficients show that x_1 and x_3 have negative correlations with ball load volume and slurry density respectively.

Given a new dataset of predictors (X-block) that has not been involved in the training process, the new values of response variables (Y-block) can be estimated from equation 5.10, providing the data is mean centred and variance scaled.

$$Y = X * B_{PLS} + \text{Residuals} \qquad [5.10]$$

The amount of explained variance in the predictors, R^2X and responses, R^2Y using the PLS model are presented in Table 5.4. The testing results indicate that 99.08% variance of predictors matrix is required to explain 92.1 and 90.31% variation of Y_1 and Y_2 respectively. Notice that the first two LVs account for most variation of Y_1 while most of the variation of Y_2 can be explained by the third LV. Interestingly, the third LV only explains little variance of the X-block. This interesting observation is contrary to the generally held assumption in multivariate statistics that those variables which contribute maximum input data variance always afford most information. By further inspection of the data, one can observe

that all the predictors display better ability to explain most of the variance in the training dataset than the testing dataset, though only by a marginal difference.

Table 5.4: Variance explained in the X and Y blocks for the PLS model (Laboratory case study)

L Vs	Predictors (X-Block)	Responses (Y-Block)			
	Cumulative % variance explained				
	X	Y1 (Training)	Y1 (Testing)	Y2 (Training)	Y2 (Testing)
X_1	69.14	53.06	50.43	7.45	6.99
X_2	96.53	93.04	90.99	17.61	16.52
X_3	99.08	93.28	92.10	92.08	90.31

Key: Y1 – load volume; Y2 - Specific gravity

5.3.2.3 RBF-PLS Model training and testing

The RBF-PLS model was trained and tested on the same dataset as the PLS model. To help improve the RBF network performance and minimize possibilities of numerical ill-conditioning during parameter estimation, the number of RBF centres was simply set equal to the number of objects in the input data with equal width between the centres. This was made possible by the small size of the dataset. The results in Figures 5.9 and 5.10 demonstrate the ability of RBF-PLS model to predict the training data of load volume and in-mill slurry density. On the other hand, Figures 5.11 and 5.12 are the results of the RBF-PLS predictions of the testing data. One can quickly observe that the specific gravity is modelled with better accuracy than the load volume. This result confirms the ability of RBF inner mapping to capture non-linearity in the dataset.

Table 5.5 presents a summary of the explained variance of the predictors, R^2X and responses, R^2Y using the hybrid RBF-PLS model. In a similar version to the PLS model, the first LV accounts for most variation in Y_1 while most of the variation in Y_2 is explained by the third LV.

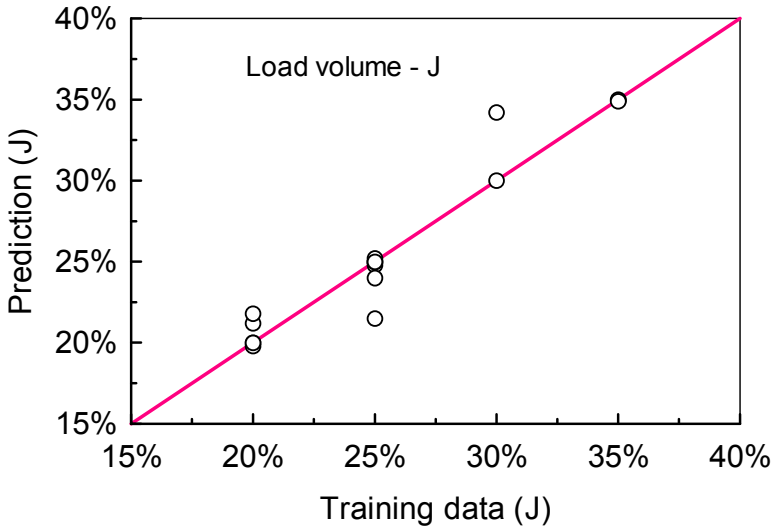

Figure 5.9: Plot of laboratory training data of mill load volume versus predictions by RBF-PLS model.

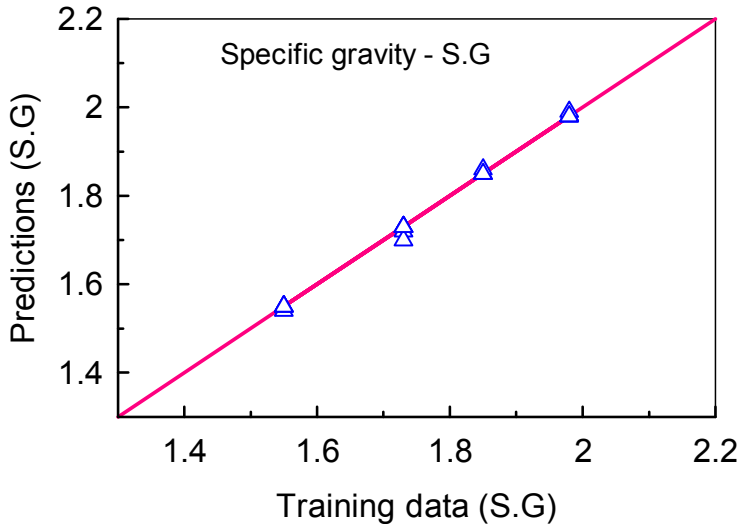

Figure 5.10: Plot of laboratory training data of in-mill slurry specific gravity versus predictions by RBF-PLS model.

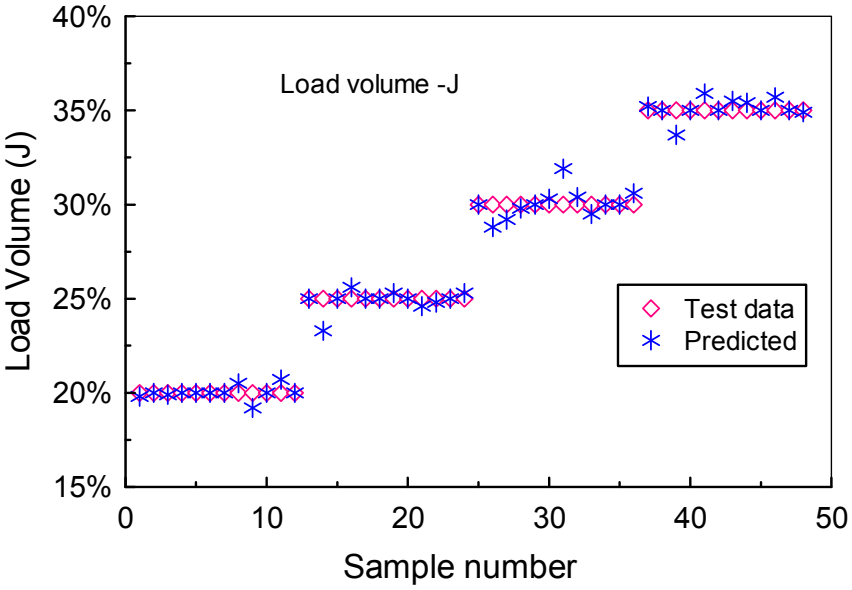

Figure 5.11: Plot of RBF-PLS model predictions of mill load volume over laboratory testing data for each observation

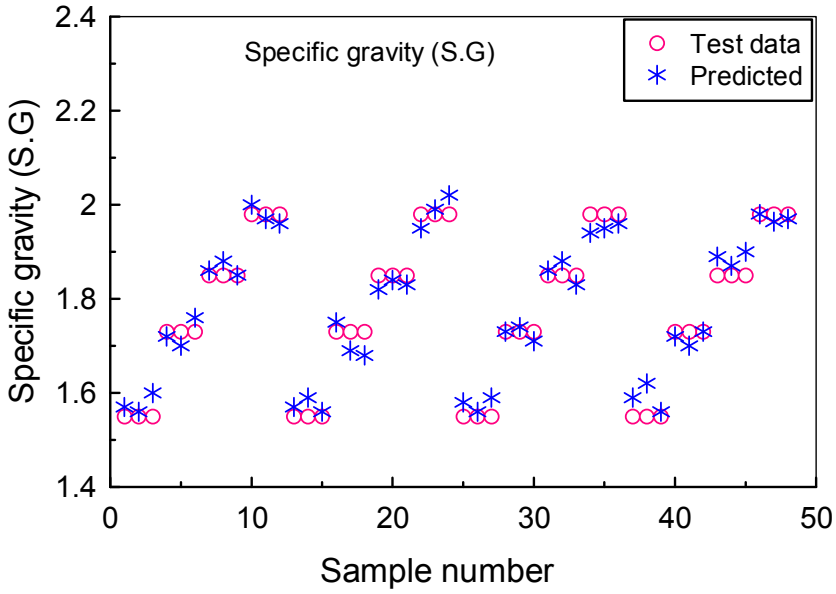

Figure 5.12: Plot of RBF-PLS model predictions of in-mill slurry specific gravity over laboratory testing data for each observation

Table 5.5: Variance explained in the X and Y blocks for the RBF-PLS model (Laboratory case study).

L Vs	Predictors (X-Block)	Responses (Y-Block)			
	Cumulative % variance explained				
	X	Y1 (Training)	Y1 (Testing)	Y2 (Training)	Y2 (Testing)
X_1	72.35	48.85	47.23	8.10	7.81
X_2	95.22	94.79	93.59	17.95	17.32
X_3	99.33	95.38	94.15	96.16	94.77

Key: Y1 – load volume; Y2 - Specific gravity

5.3.2.4 Comparison of PLS and RBF-PLS Models

The values of root mean square error (RMSE), cross-validation correlation coefficient (Q^2) and coefficient of determination (R^2) for the two models are summarised in Table 5.6. Both the PLS model and the RBF-PLS model achieved good predictions of the testing data. However, the RBF-PLS model demonstrated slightly superior predictive ability as indicated by higher values of Q^2 and lower values of RMSE. Further, notice that the RBF-PLS model displays better prediction accuracy on Y2 data than Y1 data while the converse is true for the PLS model. This result may point to the possible existence of only weak nonlinearity in the relation between the predictor variables and response variables.

Table 5.6: Comparison of the prediction ability of the PLS and RBF-PLS models

Model	Y1 (Load volume)			Y2 (Specific gravity)		
	R^2	Q^2	$RMSE^V$	R^2	Q^2	$RMSE^V$
PLS	0.921	0.884	0.0475	0.903	0.870	0.1907
RBF-PLS	0.942	0.911	0.0438	0.947	0.923	0.1118

5.4 Application case study 2: Industrial data

5.4.1 Introduction

In this case study, only the hybrid model (RBF-PLS) was considered for analysis. Based on the industrial data discussed in chapter 4, the dynamic media angle, the slurry pool angle and the depth of the slurry pool from the free surface to the minimum overflow level at the discharge end were selected as latent variables (LVs) to predict slurry density and ball load volume. The identification of LVs was accomplished in a similar manner to the laboratory case by two methods: Principal component analysis (PCA) and leave-out-one cross-validation (LOO-CV). The predictive ability of the model has been assessed through the values of cross-validation correlation coefficient (Q^2) and the root mean square error (RMSE).

5.4.2 Prediction of slurry density and ball load volume

5.4.2.1 Industrial dataset

The industrial dataset consisted of only 36 averaged samples obtained from 12 industrial experiments. The mean values of the predictors obtained for each experimental run and the corresponding standard deviations as well as the values of the response variables are presented in Table 5.7. Due to high costs associated with the industrial surveys, it was considered infeasible to perform repeat experiments to obtain the test data instead the dataset for model-testing was simply generated by adding random noise in the range of $\pm 2\sigma$ to all the samples of each variable in the training dataset. In a similar version to the laboratory case, the data was first centred to zero mean and scaled to unit variance prior to model training and testing to avoid the parameter dimension effects on the model outputs.

Table 5.7: Mean values and standard deviations of the training dataset

Exp. #	Predictor variables (X)						Responses (Y)	
	$\theta_{(Pool)}$ [deg]		$\theta_{D\,(media)}$ [deg]		h^* [s/m^2]		J [%]	S.G [ ]
	$\bar{x}$	σ	$\bar{x}$	σ	$\bar{x}$	σ		
1	35.9	0.692	162.7	0.591	5.75	0.0064	25	1.90
2	34.8	0.645	162.8	0.615	5.58	0.0055	25	2.02
3	33.0	0.597	164.3	0.687	5.62	0.0041	25	2.11
4	33.2	0.616	163.7	0.606	6.05	0.0050	25	2.14
5	33.0	0.537	172.3	0.632	5.03	0.0039	30	1.81
6	31.7	0.631	172.7	0.578	5.35	0.0052	30	1.85
7	30.5	0.693	173.7	0.708	6.47	0.0045	30	2.08
8	29.2	0.658	175.4	0.599	6.90	0.0054	30	2.13
9	29.6	0.559	178.8	0.493	4.84	0.0058	33	1.85
10	28.7	0.617	179.5	0.698	5.10	0.0050	33	1.92
11	27.5	0.569	180.2	0.555	6.06	0.0059	33	2.04
12	25.7	0.525	181.3	0.552	6.19	0.0046	33	2.14

5.4.2.2 Model training and testing

Figures 5.13 and 5.14 are plots of model predictions of training data versus experimental observations for ball load volume and slurry density respectively while Figures 5.15 and 5.16 depict the model testing results. Table 5.8 is a summary of the percentage of explained variance of the X and Y blocks. Similar to the laboratory case, the first LV accounts for most variation in Y1 while most of the variation in Y2 is explained by the third LV. Also it can be seen in Table 5.9 that the RBF-PLS model is able to predict the ball load volume with almost same accuracy as the laboratory case. However, the model predictions of slurry density both on the training and testing data have lower accuracy than the laboratory case. This result may imply that only part of the variation of the third LV (in the industrial case) is related to slurry density. Further, the result suggests that the conductivity signal amplitude (the third LV in the laboratory case) is a better feature variable than the pool depth (the third LV in the industrial case) in describing the slurry density.

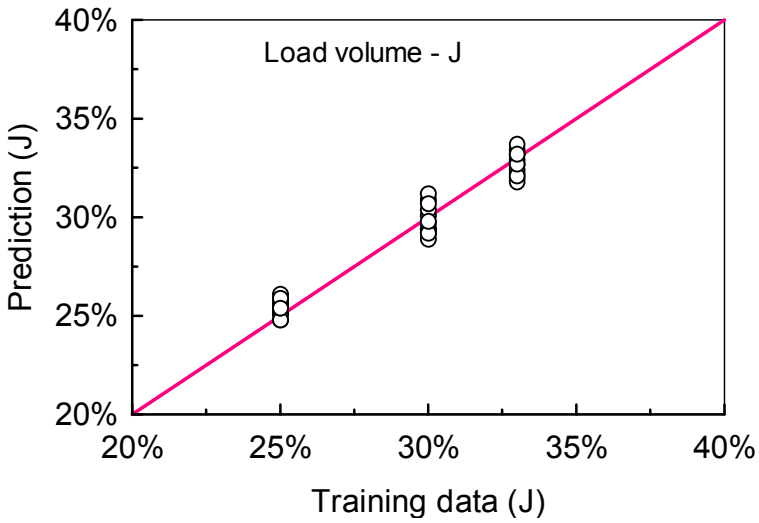

Figure 5.13: Plot of industrial training data of mill load volume versus predictions by RBF-PLS model.

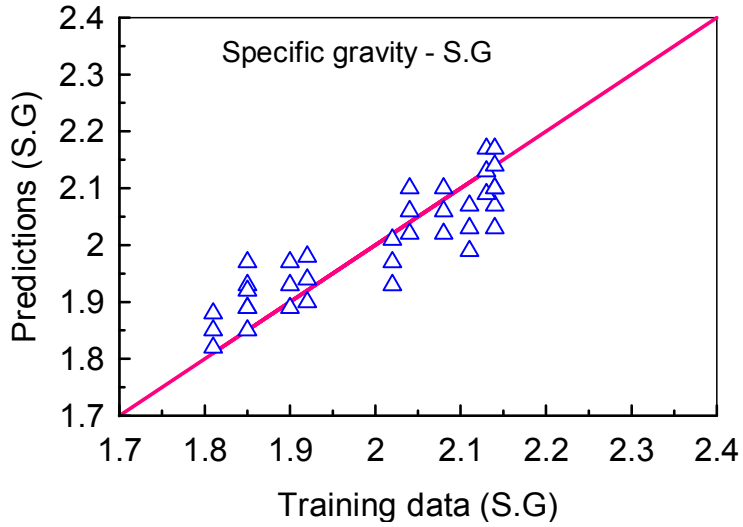

Figure 5.14: Plot of industrial training data of in-mill slurry specific gravity versus predictions by RBF-PLS model.

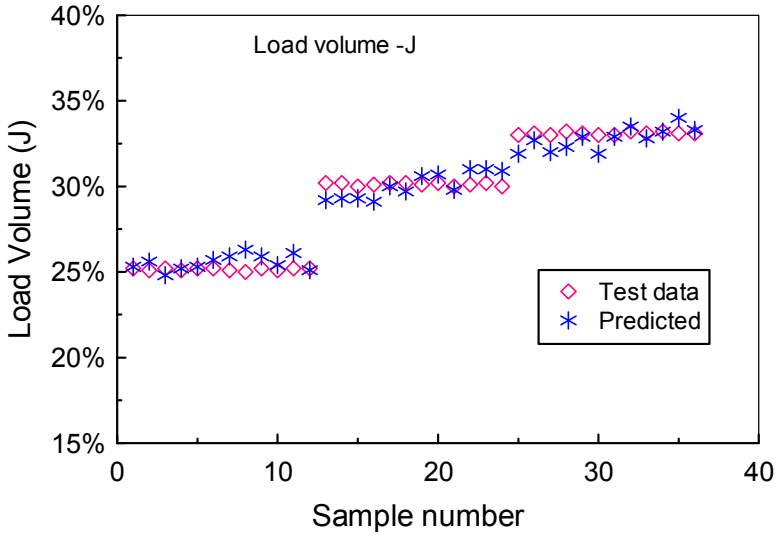

Figure 5.15: Plot of RBF-PLS model predictions of mill load volume over industrial testing data for each observation

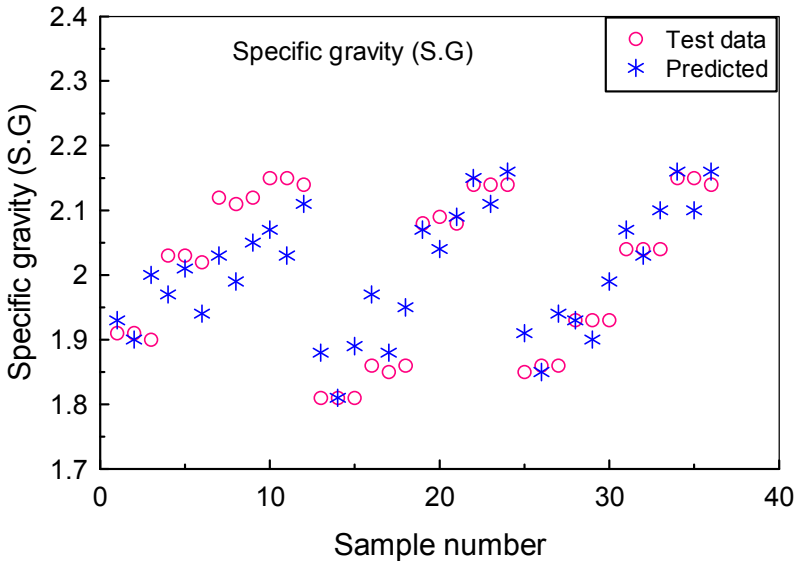

Figure 5.16: Plot of RBF-PLS model predictions of in-mill slurry specific gravity over industrial testing data for each observation

Table 5.8: Variance explained in the X and Y blocks for the RBF-PLS model (Industrial case study).

L Vs	Predictors (X-Block)	Responses (Y-Block)			
	Cumulative % variance explained				
	X	Y1 (Training)	Y1 (Testing)	Y2 (Training)	Y2 (Testing)
X_1	64.47	43.67	43.41	19.44	18.83
X_2	97.69	96.07	95.50	20.52	19.87
X_3	99.91	96.19	95.62	78.51	76.07

Key: Y1 – load volume; Y2 - Specific gravity

Table 5.9: The prediction ability of the RBF-PLS model (Industrial case study)

Model	Y1 (Load volume)			Y2 (Specific gravity)		
	R^2	Q^2	$RMSE^V$	R^2	Q^2	$RMSE^V$
RBF-PLS	0.951	0.920	0.674	0.761	0.752	0.059

5.5 Conclusions

The partial least squares model (PLS) and a hybrid model combining PLS with radial basis functions neural networks (RBF-PLS) have been built to predict two important mill operational parameters i.e. in-mill slurry density and ball load volume. The models were trained and tested against both the laboratory and the industrial data extracted from the load sensor signals to establish possible relationships between the sensor signals data and the mill operational parameters. The dynamic media angle and the slurry pool angle were identified as characteristic features in the load signals data whose variances were largely related to the in-mill ball load volume while the conductivity signal amplitude was

established as the characteristic feature that best described the variation of the in-mill slurry density. The variation of normalized slurry pool depth did not correspond well to the changes in slurry density, but this could partly be attributed to experimental errors in measurements. These observations point to the available possibilities for monitoring and characterising changes in mill operational parameters using information contained in the media and slurry sensor signals data.

The cross-validation correlation coefficient (Q^2) and the root mean square error (RMSE) were employed to assess the prediction performance of the proposed models. For the two case studies considered, both models predicted the in-mill slurry density and the ball load volume with commendable accuracy. However, the hybrid model (RBF-PLS) showed better ability to capture the underlying non-linearity between the slurry density and its predictors.

The close matches between the estimated and measured mill operational parameters suffice to demonstrate the ability of multivariate modelling as a reliable means for on-line mill monitoring and control. Therefore, once accurately trained against mill historical data, the proposed multivariate models have a potential to serve as on-line shadows to provide inferential measurements of slurry density (related to viscosity) and ball load volume during continuous state of mill operation, which is helpful in milling circuit control, diagnosis as well as optimisation.

Lastly, it is important to point out that, other measurement techniques should be explored in combination with direct load sensors to obtain further information on media and slurry behaviour that could be used to improve the mill performance through better control. In light of that consideration, the gamma emission imaging technique is applied in chapter 6 to study slurry transport behaviour in a laboratory ball mill while salt tracer tests are applied in chapter 7 to study the slurry residence time distribution and volumetric holdup in an industrial overflow ball mill.

CHAPTER 6

Radial Transport and Mixing of Slurry Measured by Gamma Emission Imaging

6.1 Introduction

Size reduction in wet ball mills is a highly complex process which involves the dynamics of media and slurry transport inside the mill (Hogg, 1984, Rogovin, 1987). The regime of media and slurry transport further affects the effectiveness of slurry flow and mixing within the ball charge which directly impacts on the grinding performance. Although considerable progress has been made in the recent past in understanding the dynamics of media motion (Morrell, 1993; Rajamani and Mishra, 1996; Van Nierop, 2001; Dong and Moys, 2003), knowledge of slurry flow and its interaction with the media is still far less advanced. An explicit understanding of slurry hydrodynamic transport and mixing is a vital element in the quest for efficient control and optimisation of wet milling circuits.

This chapter presents results and discussions of the application of gamma emission imaging technique for determination of slurry radial flow pattern and mixing profile within the ball charge in a model overflow ball mill. To our knowledge this is the first reported application of gamma camera in ball milling research. The primary aim of the study is to obtain comprehensive understanding of slurry radial flow and mixing behaviour in an overflow ball mill so as to enable better mill control. Further, the information generated would serve as a fundamental resource for validation of particle and slurry flow simulation models such as CFD/DEM.

6.2 Review of mass transport in overflow ball mills

Transport of media and slurry inside the mill is driven by a combination of three factors: gravity, friction and mechanical energy of the rotating mill. The relative contribution of each factor depends on the mill discharge mechanism, the liner profile, the mill speed and the prevailing operating conditions. Basically, the rotating mill imparts mechanical energy into the load via frictional force at the interfacial surface of the load and mill wall, which results in radial flow of the media and slurry. This is accompanied by continuous exchange of slurry between the pool and ball charge region which promotes the transfer of ore particles into the breakage zones and the flow of fine progenies out of the ball charge into the pool

for discharge as illustrated in Figure 6.1. Also, the rate of slurry exchange defines the residence time of ore particles in the breakage zones which subsequently impacts on the effectiveness of the grinding process (Songfack and Rajamani, 1999). High flow rates of slurry through the load would result in under-grinding while low flow rates would result in over-grinding. On the other hand, a poorly mixed load would lead to inefficient grinding and high media wear rate due to increased ball-ball interaction. In essence, the efficiency of material breakage inside the mill would undoubtedly be influenced both by the flow regime and the rate of transport of material through the mill besides other operational parameters.

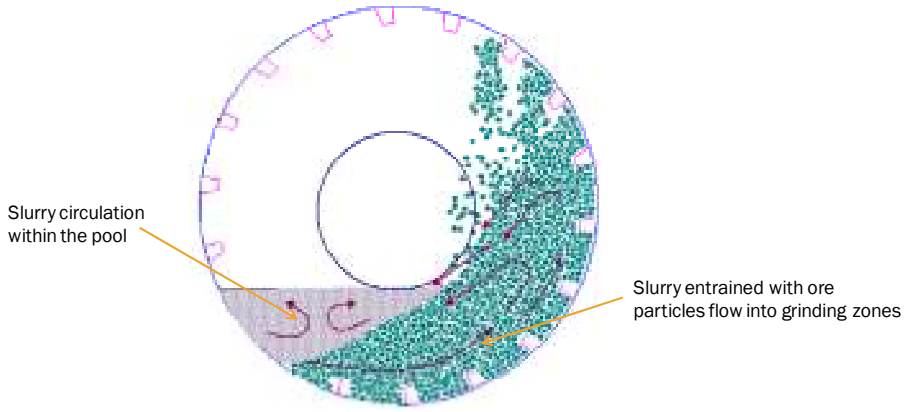

Figure 6.1: Illustration of the radial transport of slurry inside the mill

Overflow ball mills are depicted by an intrinsic pool of slurry at the toe, which facilitates the discharge of fine progenies (finished product) from the mill. To ensure that adequate slurry removal capacity is achieved while keeping the load well saturated with slurry at all times (for efficient grinding), knowledge of slurry mixing behaviour within the ball charge and its rate of transfer from the pool is essential. Although a reasonable number of studies on slurry transport have been reported in literature (Kelsall *et al*, 1970; Fuerstenau *et al*, 1986; Klimpel *et al*, 1989a), the focus has been largely on axial flow studies using black-box principle of residence time distributions, aimed at delineating the effect of important operating variables on slurry hold-up, breakage kinetics and discharge rate. Quantitative information on radial transport and mixing of slurry, which indeed influences both the grind quality and the mill discharge rate, is still deficient

presumably due to inadequacy of the measurement techniques. This presents a need for special techniques to monitor the complex behaviour of slurry and grinding media inside the mill for purpose of mill control and optimisation.

In this study, a gamma ray imaging technique has been applied to provide a detailed analysis of the radial transport of slurry in a laboratory overflow ball mill. The gamma camera detector and aqueous Technetium, ^{99m}Tc radiotracer were utilised. Details of the experimental setup have been described in Chapter 3 together with the measuring techniques and materials.

6.3 Experimental results, analysis and discussion

6.3.1 Data processing technique

From literature (Perret *et al*, 2000; Huang *et al*, 2002; Tugrul and Altinsoy, 2002; Bridge *et al*, 2006), it is clear that, if a radiotracer is mixed with a soluble fluid, the intensity of the emitted radiations or count rate is directly proportional to the concentration of the radiotracer in the fluid. The general mathematical relationship is expressed in the form:

$$\frac{C_m}{C_s} = \lambda \frac{I_m}{I_s}, \text{ where } \lambda = \frac{-\ln\left(I_{\mathrm{m}}(\max)/I_s\right)}{1-\left(I_{\mathrm{m}}(\max)/I_s\right)} \qquad [6.1]$$

In which,

I_m : intensity of the radiations (scintillation counts) as measured

I_s : standard intensity of the radiations (scintillation counts)

C_m : concentration of the radiotracer as measured

C_m : concentration of the radiotracer as measured

λ : calibration factor that accounts for intensity losses due to attenuation, out-scattering and self absorption effects.

Standard intensities are normally obtained via tests on standard phantoms using a pure tracer of known concentration.

In this study, both qualitative and quantitative analyses have been performed on the gamma camera data to determine the rate of slurry transfer between the pool and ball charge and the mixing behaviour within the ball charge. It should be emphasized that, due to the nature of configuration of our mill rig it was not possible to operate the camera in 360^0 mode, instead only the front side of the mill was sampled by the camera (i.e. 2D, 1^{st} generation projection). In essence, some of the radiations out scattered. It is expected that this in effect would introduce a margin of error in the result. To minimize any possible errors and maintain consistence in analysis of gamma camera data, it was considered necessary to first perform a calibration of the scintillation intensity. This was accomplished by measuring the scintillation intensity at no-flow conditions for each test run shortly after injection of the radiotracer into the pool prior to mill rotation. The absolute value of intensity obtained in each calibration test serves as a reference value against which subsequent measurements are normalized. Once the mill is rotational, there would be a continuous flow of the radiotracer between the pool and ball charge region. Consequently, the intensity of the scintillations detected from the pool would drop commensurate with the slurry exchange rate. Relating the measured scintillation intensity to the reference intensity could give some indication of the rate of transfer of the radiotracer from the pool to the ball charge. It is worthwhile to note that the calibration described here is specific to the current experimental configuration.

One potential demerit of the above criterion is that, the accuracy of the analysis is very dependent on the accuracy of the intensity calibration process. For the reference intensity value to be representative of the entire pool volume, the tracer must be uniformly dispersed in the slurry pool at the beginning of each test run. In that respect, injecting the radiotracer pulse while the mill is rotational would highly likely result in biased data, dependent on the location of tracer injection within the pool. To ascertain the reliability of the calibration, an assessment has been undertaken on our measured data to establish the quality of mixing of the radiotracer in the pool. The scintillation intensity profile defining the radiotracer dispersion in a region of interest within the pool was obtained during the first 5 seconds while the mill was still stationary. An algorithm was developed in

MATLAB environment to facilitate the analysis of data. Presented in Figure 6.2 are the results, showing the local scintillation intensity profiles of the radiotracer within the selected region of interest (ROI) in the pool.

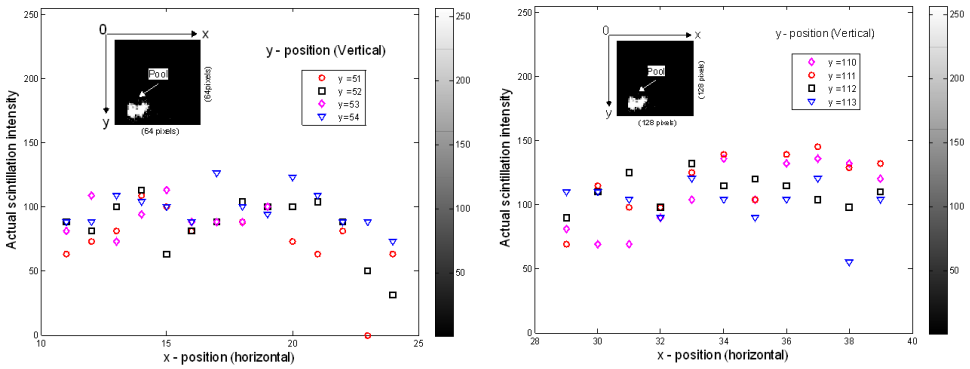

(a) (b)

Figure 6.2: The local scintillation intensity map in the ROI within the slurry pool (prior to mill rotation), for slurry viscosity of (a) 10 cp and (b) 70 cp.

The data presented in Figure 6.2 is 2D in nature since only one gamma camera was used in the experiment. The arbitrary selected region of interest within the pool, designated as ROI-1, spans 12 - 15 pixel elements horizontally and 4 pixels vertically. The x-y coordinates are expected to vary for different test runs depending on the orientation of the ball bed and the pool size at the beginning of the test. From the intensity profiles, a marginal variation in concentration of the radiotracer in the region of interest (ROI) within the slurry pool is expectedly evident. Therefore, to enhance the accuracy of our quantitative analysis, we apply spatial smoothing on intensity data over the region of interest (ROI) as follows:

$$I_o^* = \frac{1}{A_p}\int_A I_o(x,y)\,dA_p \quad \Rightarrow \quad \frac{1}{nm}\sum_{x=0}^{n-1}\sum_{y=0}^{m-1} I_o(x,y) \qquad [6.2]$$

Where,

I_o : is the count rate at a local point within the ROI

x, y : coordinates defining the ROI whose limits are *n* and *m* respectively. In the present case *n* and *m* lie in a domain of 64 x 64 or 128 x 128 pixel elements

Equation 6.2 can be rewritten in terms of concentration as defined in equation 6.3, in which I_o is the average scintillation intensity while C_{ss} is the steady state radiotracer concentration. In the present case, C_{ss} is obtained as a ratio of the total volume of the radiotracer impulse to the total slurry holdup volume inside the mill.

$$C_o^* = \lambda C_{ss}\left(\frac{I_o^*}{I_{ss}}\right) \qquad [6.3]$$

The parameter I_{ss} is the steady state scintillation intensity (count rate) that corresponds to C_{ss}. The steady state is assumed to have been attained once the scintillation intensity becomes invariable with time during mill rotation.

6.3.2 Analysis of slurry flow path and distribution pattern

Figures (6.3 - 6.5) present the gamma ray images of the slurry flow path and distribution profile within the ball charge for different levels of slurry viscosity and mill rotational speed. The results were obtained at regular time intervals over a span of 0 (mill stationary) to 20 seconds (when the dynamic steady state was assumed to have been reached). The data clearly indicates the variation of scintillation intensity detected from different positions within the mill regions. The scintillation intensity is described by the colour map where each colour represents a given level of intensity corresponding to a certain concentration of the radiotracer. A similar procedure was applied in all the tests in order to allow a comparative analysis of the results.

Figures 6.3(a), 6.4(a) and 6.5(a) illustrate the gamma camera imaging region during experimental test. Since the mill was slightly larger than the collimator (i.e. the collimator measures 60 x 40 cm) it was not possible to capture the events over

the entire mill diameter of 55cm. Thus it was ensured that the events in our main regions of interest were fully captured.

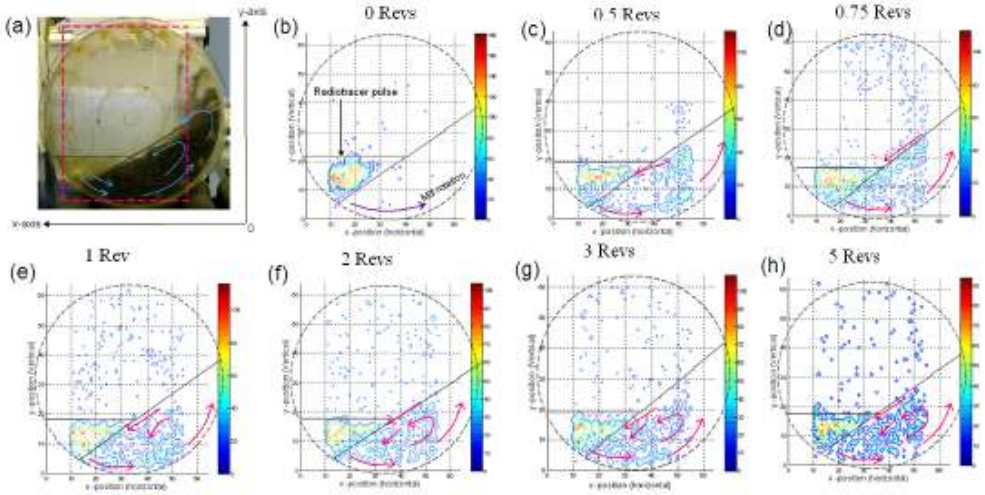

Figures 6.3(a-h): Slurry flow path and distribution map at slurry viscosity, 10cp and mill speed, 28% of critical.

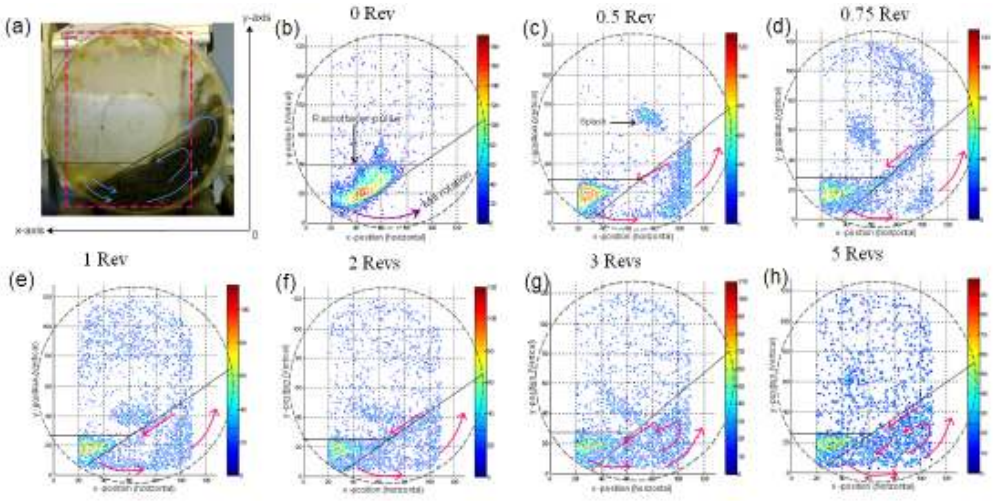

Figures 6.4(a-h): Slurry flow path and distribution map at slurry viscosity, 70cp and mill speed, 28% of critical.

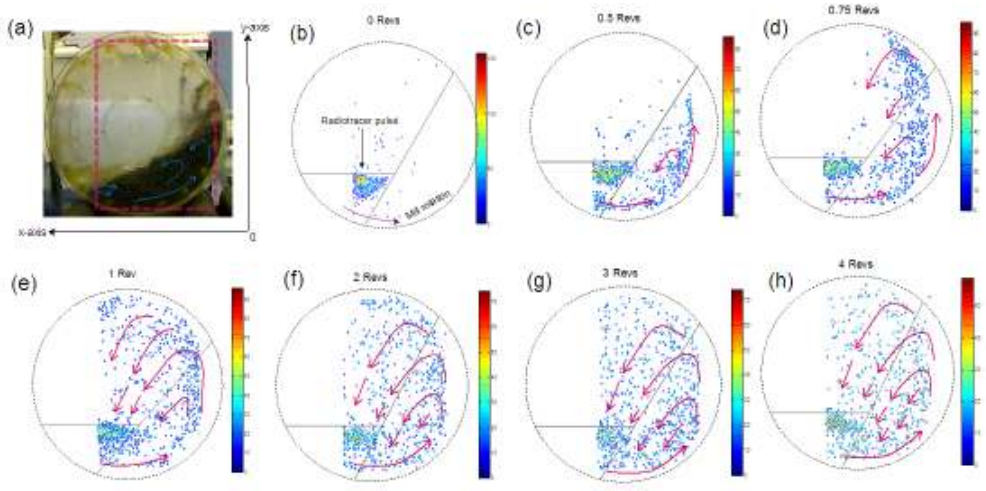

Figures 6.5(a-h): Slurry flow path and distribution map at slurry viscosity, 70cp and mill speed, 60% of critical.

Case I: Viscosity of 10 cp, speed of 28% of critical

The tracer is injected into the pool as a pulse as shown in Figure 6.3b. Once the mill is rotating, the tracer gets swept by the lifters into the ball charge and flows predominantly along the mill wall as depicted in Figure 6.3c. The portion of slurry entrained into the ball charge along the inner ball layers follows the balls' circulation path and regurgitates into the pool without reaching the shoulder as shown by Figure 6.3d. The portion of slurry swept along the mill wall is dragged up to the shoulder before draining back into the pool. During flow back, a part of the slurry flows with avalanching ball layers along the free surface while the rest seeps through the porous ball charge under the effect of gravity. The slurry exhibits high mobility due to its lower viscosity and it is able to percolate easily through the pores of the ball charge. After 2 revolutions, the load starts to get saturated with slurry but still there is higher concentration of slurry within the peripheral ball layers and along the load free surface as compared to the inner regions of the ball charge. Between 3 and 5 revolutions, there is no discernible change in radiation intensity within the pool which indicates that a dynamic steady state would have been reached. Equally, the slurry appears to be well dispersed within the ball charge. At this point, the pool outflow is balanced by the inflow from the ball charge, keeping the pool volume constant.

Case II: Viscosity of 70cp, speed of 28% of critical

In Figure 6.4b, the tracer is similarly introduced into the pool as a pulse. Some little splashing of slurry occurs as depicted in Figure 6.4c. Due to higher viscosity, the slurry has less mobility to move independently hence is dragged all the way to the shoulder and flows back into the pool along the free surface as shown in Figure 6.4d. The slurry takes longer to report back to the pool as compared to the case of dilute slurry (i.e. 10cp). This observation concurs with the findings from the DEM-SPH simulation by Cleary *et al* (2006). It is interesting to observe that after 3 revolutions, the inner region of the ball charge is yet to be fully saturated. In this region, the balls are densely packed which limits the ability of viscous slurry to entrain in. The slurry is relatively concentrated along the mill wall and along the load free surface. At 5 revolutions, the load appears to be saturated with slurry. At this point, a large proportion of slurry is trapped in the ball charge which causes the charge to expand as evidenced by a smaller pool at the toe.

The foregoing observations may lead to the conclusion that increasingly dilute slurry could lead to under-grinding since the slurry spends a shorter time within the ball charge while increased slurry viscosity could lead to over-grinding since the slurry takes longer to drain from the load. However, it is worthwhile to note that under excessively high viscosity conditions, the mill might go "off the grind" hence a desirable level of slurry viscosity must be established which optimizes both breakage and transport of ore progenies inside the mill.

Case III: Viscosity of 70cp, speed of 60% of critical

Figures 6.5(a-h) depict the slurry flow pattern and mixing behavior at mill speed of 60% of critical and slurry viscosity of 70 cp. The radiotracer impulse is introduced into the pool of slurry as shown in Figure 6.5b. Immediately the mill is switched on, the slurry gets swept into the ball charge by the lifters and dragged higher up along the mill wall to the shoulder as shown in Figures 6.5(c, d). Compared to case II, the slurry takes a shorter time to report back to the pool which is expected. It can be observed that after only 3 revolutions (Figure 6.5g) the slurry is already entrained into the inner region of the ball charge. After 4 revolutions, the ball charge appears to be well saturated with slurry.

6.3.3 Analysis of slurry radial mixing behaviour

Mill performance is sensitive to internal mixing behaviour, hence there must exist mixing conditions that are beneficial to mill performance. In light of that, a quantitative analysis was performed here to determine the rate of slurry saturation in the inner region of the ball charge which is related to the mixing dynamics within the ball charge. The region of interest (ROI) was selected such that the vertices (also known as child points) form an irregular shaped polygon which closely describes the profile of the inner region around the load's centre of circulation. Majority of the methods presented in literature for quantifying the extent of mixing are statistical due to stochastic nature of the mixing process and among them the mixing index and variance are commonly used. In this study, the variance method (Fan and Wang, 1975) was applied due to randomness of the process. The saturation index (S) which characterises the degree of mixing within the ball charge was obtained by comparing the tracer concentration in the ROI at any given time (t) to its initial value (t = 0). The saturation index, S is defined mathematically as:

$$S(t) = \sqrt{\frac{1}{N-1}\sum_{i=1}^{N}\left(C_i(t) - \bar{C}(0)\right)^2} \qquad [6.4]$$

where,

N : is the number of pixels in the ROI,

$C_i(t)$: is the normalised concentration in pixel cell i at time t

$\overline{C}(0)$: is the average normalised concentration in the ROI at time, t = 0.

Higher values of S mean less variability in the slurry saturation pattern within the ball charge which implies better mixing.

Figure 6.6 presents the profiles of the evolving tracer concentration distribution within the inner region of the ball load (related to the mixing pattern) for the two viscosity levels tested at a constant mill speed of 28% of critical. Note that the

signals were pre-processed and filtered using MATLAB software for background noise correction and trended with a polynomial fit. From the results in Figure 6.6, one can quickly observe that the inner region of the ball charge wets faster for the case of lower viscosity slurry than for higher viscosity slurry and that it stays relatively wetter for the case of higher viscosity slurry. This result could be explained as follows: The reduced mobility of slurry at higher viscosity (low diffusivity) causes the slurry to remain trapped in the inner circulating layers for longer thereby keeping the region relatively laden with slurry (i.e. higher saturation index). At reduced viscosity, the slurry tends to drain from the ball charge much faster. The transients in our data might be due to constant displacement of slurry by balls and occasional migration of balls into and out of the inner ball charge region, a phenomena previously reported by Hogg and Fuerstenau (1972).

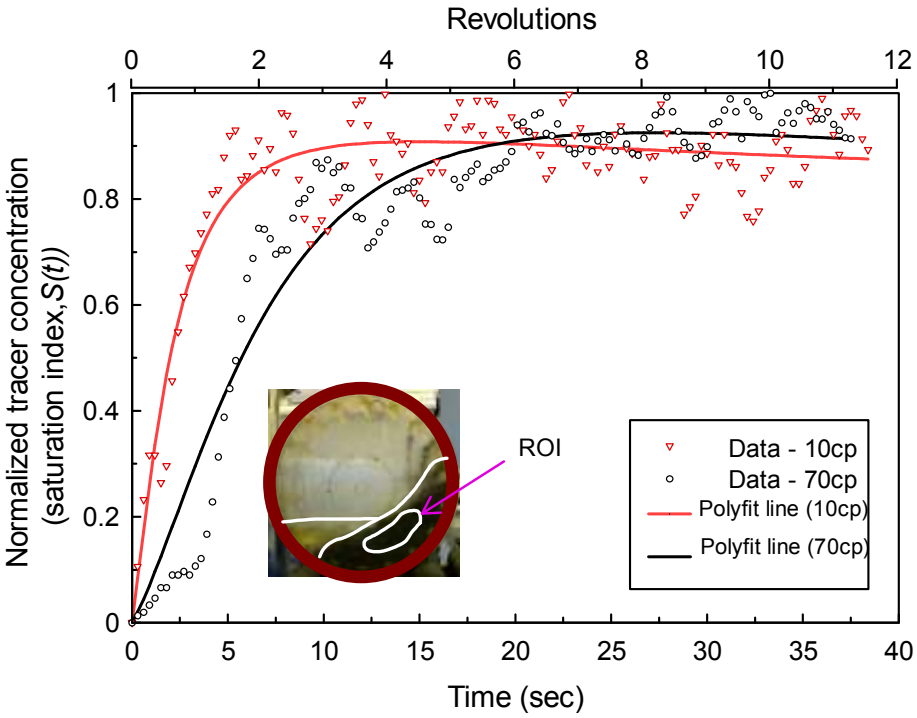

Figure 6.6: Effect of slurry viscosity on the rate of mixing and saturation pattern of the inner region of the ball charge at constant mill speed of 28% of critical.

The effect of varying mill rotational speed on the mixing behaviour of slurry is demonstrated in the results presented in Figure 6.7. Two different mill speeds, 28 and 60% of critical were assessed at a constant slurry viscosity of 70 centipoises. The results in Figure 6.7 reveal a noticeable influence of mill speed on the degree of slurry dispersion within the ball charge. The rate of convective flow of slurry into the ball charge is relatively faster at mill speed of 60% of critical. This is reflected in the signal profiles in Figure 6.7 during the first 10 seconds before diffusive mixing sets in. Here, the signal profile for 60% of critical speed is steeper than that for 28% of critical speed. The partial drop in radiotracer concentration after the peak as portrayed in Figure 6.7 could be attributed to continuous dispersion of the tracer within the ball charge as the mill rotates. Note that at high rotational speed, the charge bed gets dilated (Mellmann, 2001), thereby presenting more voids for slurry entrainment.

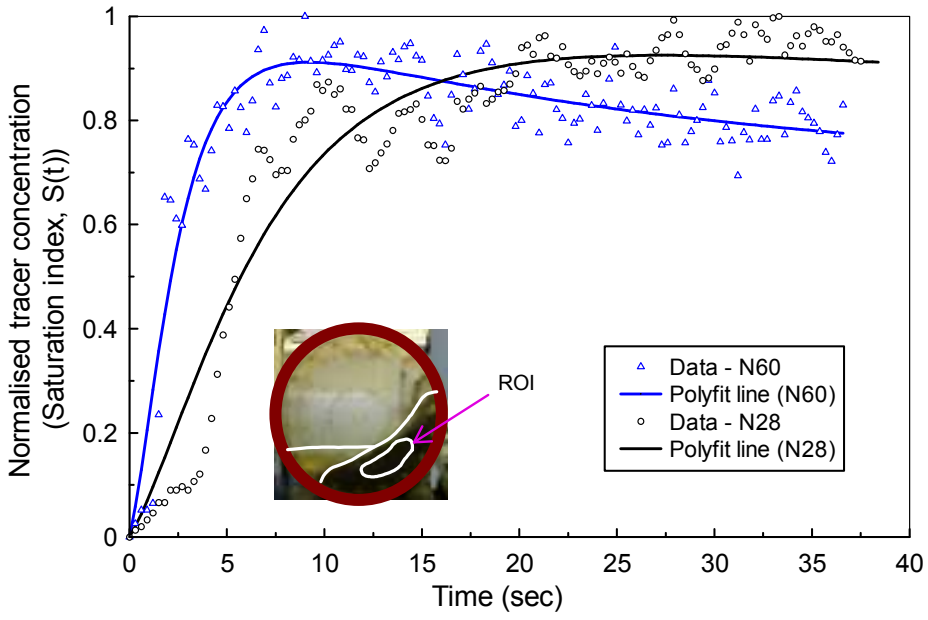

Figure 6.7: Effect of mill rotational speed on the rate of mixing and saturation pattern of the inner region of the ball charge at constant slurry viscosity of 70cp.

In order to establish the mixing time of slurry within the ball charge a comparison of the tracer concentration profiles in two regions of the ball charge, one near the mill wall and the other at the eye was undertaken. It can be observed in Figure 6.8 that mixing time within the ball charge is markedly affected by mill speed. For mill speeds of 60 and 28% of critical, mixing appears to have reached a steady state after 10 and 16 seconds respectively. This result further implies that mixing is a rapid process which backs up the findings by Chibwana and Moys (2006).

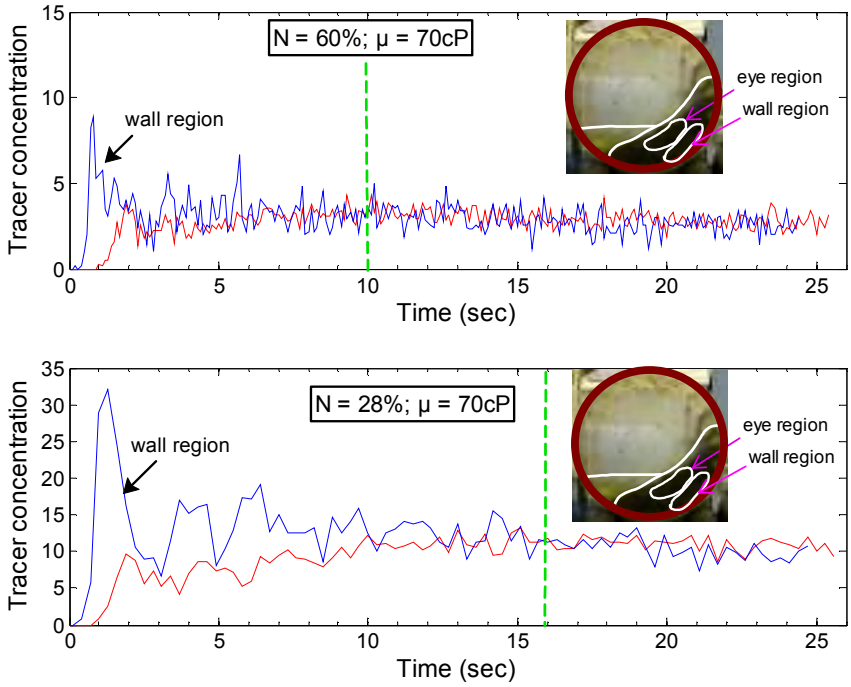

Figure 6.8: Comparison of slurry mixing time within the ball charge at a constant viscosity of 70cp.

6.3.4 Analysis of slurry transfer from the pool to the ball charge

Presented in Figures 6.9(a, b) are experimental results of the slurry transfer rate from the pool to the ball charge, from which both qualitative and quantitative observations can be made. Two levels of slurry viscosity and two mill speeds were

assessed. From the results in Figures 6.9, it can be deduced that the volumetric interchange of slurry between the pool and ball charge is dependent both on mill speed and slurry viscosity. In the duration designated as A, in Figure 6.9, slurry radial transport is dominated by convection due to the lifter effect while viscosity effect is largely unnoticeable. In the duration designated as B, a substantial amount of slurry has been swept into the ball charge. The slurry disperses continuously to fill up the voids within the ball charge (by diffusion and percolation) while part of slurry flows back into the pool due to gravity effect. Due to slurry recirculation between the pool and ball charge, the rate of change of pool tracer concentration in this duration is characteristically low. Here viscosity plays a significant role by influencing the rate of diffusion and percolation.

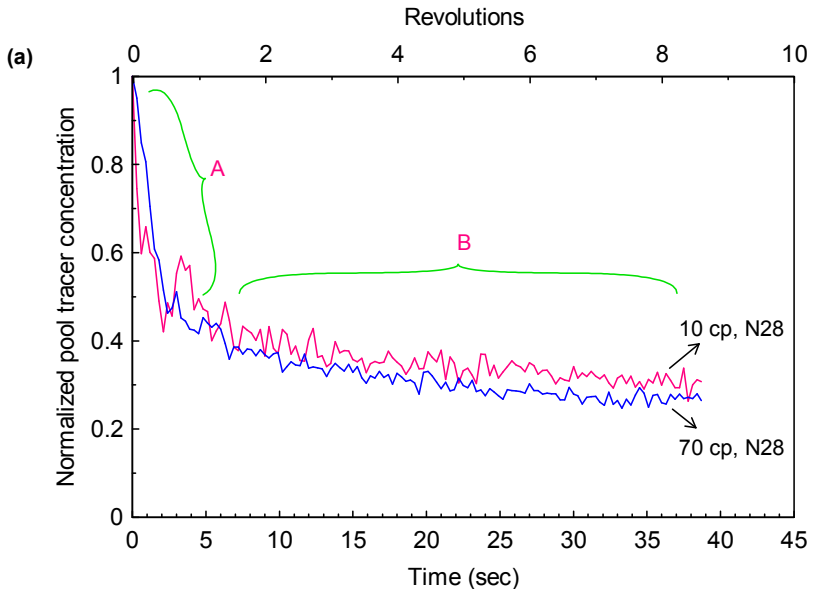

Figure 6.9(a): Effect of slurry viscosity on the rate of slurry transfer from the pool to the ball charge.

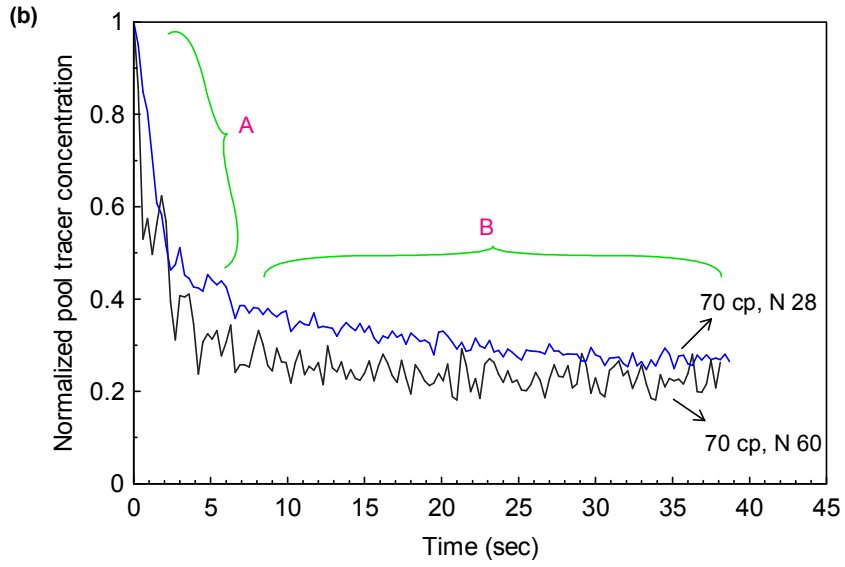

Figure 6.9(b): Effect of mill rotational speed on the rate of slurry transfer from the pool to the ball charge.

The slight variation of steady state pool tracer concentration between the two signals in Figures 6.9 (a, b) indicates the difference in the volume of slurry transported out of the pool into the ball charge while the periodic oscillation of signals (though not obvious) appears to correspond to the slurry turnover time. The superimposed transients on the signals may result from the pool turbulence upon interaction with lifters and with the avalanching balls. Further analysis of the signal features reveals that at low viscosity, the slurry has a shorter turnover time; a part of the slurry does not reach the shoulder instead it circulates along the inner ball layers. However, the reproducibility of this trend cannot be ascertained since only a limited number of tests were performed.

6.4 Modelling of slurry radial exchange

6.4.1 Relationship between tracer concentration and slurry flow

Figure 6.10(a) physically describes the anticipated flow path of the radiotracer inside the mill, while Figure 6.10(b) shows an equivalent model for slurry

exchange between the pool and ball charge region. The general assumption in tracer tests is that both the carrier fluid and the radiotracer flow in a similar pattern, which is the basis of the current model.

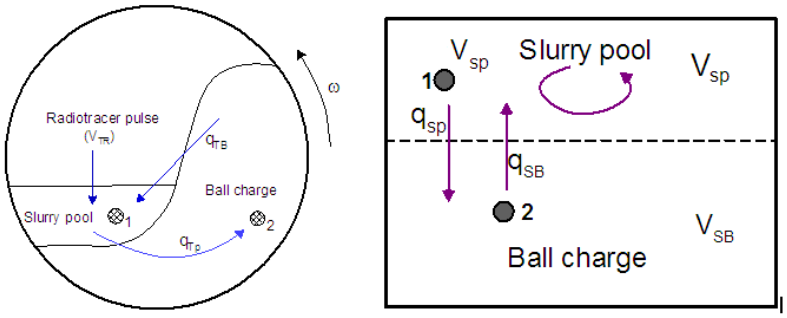

(a) (b)

Figure 6.10: (a) Physical model illustrating the flow path of the radiotracer inside the mill (b) an equivalent model illustrating the flow of slurry.

As a criterion for adequate analysis of the data, two regions of interest (ROIs) 1 and 2 were identified representing the pool and the ball charge respectively as illustrated in Figure 6.10. The slurry transport kinetics between the pool (region 1) and the ball charge (region 2) can be defined by equation 6.5 which describes the volumetric balance of the radiotracer in the slurry pool at any time instant.

$$kV_{SP}\frac{dC_P}{dt} = q_{SB}\,C_B(t) - q_{SP}\,C_P(t) \qquad [6.5]$$

Where

$C_P(t)$: the average concentration (vol/vol) of the radiotracer at the ROI within the pool region at time t, which is proportional to the intensity of the radiations detected from the ROI.

$C_B(t)$: the average concentration (vol/vol) of the radiotracer at the ROI within the ball charge at time t, which is proportional to the intensity of the radiations detected from ROI.

V_{SP}: the total volume of slurry in the pool (m^3)

q_{SP}: flow rate of slurry from the pool into the ball charge (m^3/s)

q_{SB}: flow rate of slurry out of the ball charge into the pool (m^3/s)

k : a proportionality constant (i.e. volume of ROI (1) = k*V_{Sp})

The decay factor for technetium, ^{99m}Tc is 2.3 x 10^{-5} s^{-1}, which is considered too small to have any significant impact on our results hence is ignored. Dividing equation 6.5 by q_{SP} yields the following expression.

$$\left(\frac{kV_{sp}}{q_{SP}}\right)\frac{dC_P}{dt} = \frac{q_{SB}}{q_{SP}}C_B(t) - C_P(t) \quad \Rightarrow \quad \frac{1}{\delta_{sp}}\frac{dC_P}{dt} = AC_B(t) - C_P(t) \quad [6.6]$$

The parameter A is the cross-flow ratio while δ_{sp} [s^{-1}] is a coefficient that indicates the rate of slurry transfer from the pool to the ball charge region. The parameter k is constant of proportionality which relates the volume of the ROI within the pool to the total volume of slurry in the pool. It is obtained as the ratio of the ROI area to the total pool area in pixel values. The values of k for cases *I*, *II* and *III* are 0.26, 0.48 and 0.45 respectively. Equation 6.6 represents the change in tracer concentration with time within the pool as recorded by the gamma camera, corresponding to the difference of scintillation intensity between the pool and ball charge region.

Due to gamma rays source intensity attenuation within the ball charge region (which vary with steel thickness and slurry saturation level), an attempt to measure $C_B(t)$ would be challenging and error laden; Instead it would be appropriate to apply radiotracer balance method (RBM) (IAEA, 1975; Tugrul and Altinsoy, 2002) which is based on the principle of conservation of radiotracer. In this case, $C_P(t)$ and $C_B(t)$ are correlated through a proportionality constant such that,

$$C_B(t) = C_o^* - \beta * C_P(t) \quad [6.7]$$

in which C_o^* represents the 'reference concentration' (vol/vol). Substituting for $C_B(t)$ in equation 6.6 and simplifying yields an expression of the form:

$$\frac{1}{\delta_{sp}}\frac{dC_P}{dt} = AC_o^* - C_P(t)\left(A\beta + 1\right) \qquad [6.8]$$

The solution to equation 6.8 for an input pulse C_o^* was obtained with initial conditions set as follows: at $t = 0$, $C_P(t) = C_o^*$, hence,

$$C_P(t) = \frac{AC_o^*}{\left(A\beta + 1\right)}\left[1 + \left(\frac{A\beta + 1}{A} - 1\right)\exp\left(-\delta_{SP}\left(A\beta + 1\right)t\right)\right] \qquad [6.9]$$

Since relative values and not absolute values of concentrations are of more interest here, equation 6.9 can be expressed in form of dimensionless pool radiotracer concentration, equation 6.10 in which $c_p^*(t) = c_p(t)/c_o^*$.

$$C_P^*(t) = \frac{A}{\left(A\beta + 1\right)}\left[1 + \left(\frac{A\beta + 1}{A} - 1\right)\exp\left(-\delta_{SP}\left(A\beta + 1\right)t\right)\right] \qquad [6.10]$$

Notice that only measurements of tracer concentration within the pool region would be sufficient to compute the values of δ_{sp}, A and β which are determined by fitting the model to the experimental data. If the mill holdup and the pool volume (V_{SP}) are known, it would be possible to determine the value of q_{SP}. In practice the approximate volume of the pool can be computed based on mill geometry and the measured slurry angles recorded by the mill instruments.

6.4.2 Model fitting

The simple model based on tracer balance is derived in section 6.4 to describe the slurry transport between the pool and ball charge. Fitting the model to experimental data presented in Figure 6.9 allows the quantitative estimation of the slurry volumetric transfer rate from the pool into the ball charge. Figure 6.11

shows how the model describes the experimental data at different slurry viscosities and mill speed. From the fitted data, the slurry radial transport coefficient defined by, was determined for the three conditions as $0.1972s^{-1}$, $0.1469s^{-1}$ and $0.2490s^{-1}$. Accordingly, it may be concluded that slurry transfer rate between the pool and the ball charge is affected to a greater extent by mill speed than slurry viscosity.

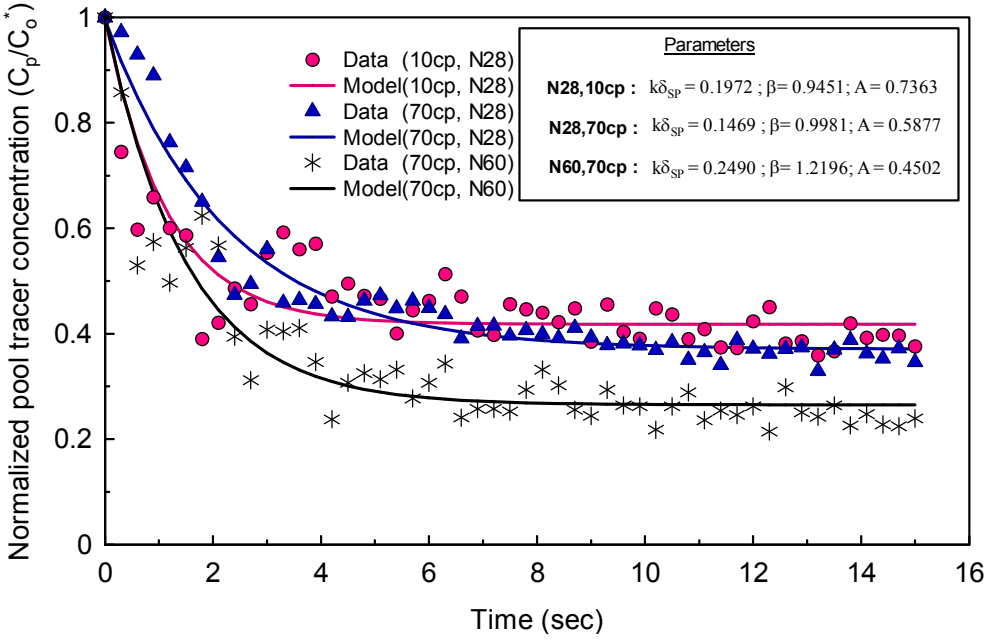

Figure 6.11: Tracer radial transport model fitted to experimental data for viscosity of 10 and 70cp at mill speeds of 28 and 60% of critical speed.

6.5 Conclusions

The work presented in this chapter demonstrates the effectiveness of a gamma camera as a non-invasive tool for probing the slurry flow behaviour inside a laboratory ball mill. Technetium-99m radioisotope tracer revealed the slurry flow path from the pool into the ball charge, its distribution map within the ball charge and the mixing time. It further gave a qualitative description of the slurry exchange rate between the pool and the ball charge for two levels of slurry viscosity and mill speed tested. The influence of both viscosity and mill speed on the slurry flow

behaviour has been clearly discernible. The slurry mixing time in the ball charge varied inversely with mill rotational speed which is consistent with literature findings. The rate of slurry flow from the pool into the ball charge has been well described by the radial transport model. The model coefficient that characterises the slurry transfer rate from the pool and ball charge displayed a strong dependence on mill speed than slurry viscosity.

The success achieved so far from the experimental work described here is a clear pointer to the fact that, more useful insight of the slurry flow behaviour in an overflow mill can be reliably acquired in a laboratory scale mill using gamma emission imaging technology. But, it is important to point out that, due to stringent procedures and other challenges related to the handling and use of radioactive material, only a few experimental tests were done.

The next chapter focuses on the analysis of slurry residence time distribution (RTD) and volumetric holdup data obtained on an industrial overflow ball mill by salt tracer tests.

CHAPTER 7

Slurry Residence Time Distribution (RTD) and Volumetric Holdup

7.1 Introduction

The slurry residence time distribution (RTD) and the volumetric holdup inside the mill are mutually dependent and both have a leading influence on milling efficiency. The residence time distribution defines the mixing regime of material inside the mill while the holdup volume influences the effectiveness of material transport to the breakage zones and the rate of breakage. Therefore, it is imperative that the optimal slurry residence time and volumetric holdup that correspond to maximum milling efficiency be well established for any given mill operating conditions. This chapter presents the studies of slurry residence time distribution and volumetric holdup in a large industrial overflow ball mill using salt as a tracer. An overview of the fundamental theory of RTD is first presented followed by a discussion of the results of RTD tests. Lastly an analysis of the slurry volumetric holdup inside the mill is given for the set of operating conditions investigated.

7.2 Fundamental theory of residence time distribution

The residence time distribution (RTD) technique has been employed successfully for decades to characterise the transport of material in a wide range of engineering processes. The concept of RTD was first proposed by MacMullin and Weber in 1935 (Fogler, 1992) for analysis of chemical reactors but later on Danckwerts (1953) developed it into a more definitive form by identifying and characterising various distribution profiles of interest. The tracer response is the method popularly used for RTD studies. Typically, measuring of RTD involves introduction of a tracer or salt at the feed and continuously or discretely monitoring the response at the discharge in terms of conductivity or concentration. If the tracer is injected as a pulse, then the fraction of tracer that remains in the system at any time (assuming constant flow rate through the mill) can be described by the distribution function *E(t)* mathematically defined as follows (Levenspiel, 1972):

$$E(t) = \frac{C(t)}{\int_0^\infty C(t)\,dt} \qquad [7.1]$$

Where *C(t)* represents the concentration of the tracer in the discharge stream as a function of time while the integral of *C(t)dt* defines the area under the curve. Interpretation of the RTD curves is based on moment analysis which provides an indication of various aspects of flow in a reactor. The zeroth moment is related to the material holdup in the system which is represented by the area under the curve. For normalized RTD data, the area under the curve is equal to unity.

$$M_0 = \int_0^\infty E(t)\,dt = 1 \qquad [7.2]$$

The first and second moment of the RTD function around the origin give the mean residence time (τ) and the variance (σ^2) respectively, where the latter is a measure of spread of the RTD curves about the mean value.

$$\tau = \int_0^\infty t\,E(t)\,dt \qquad [7.3]$$

$$\sigma^2 = \int_0^\infty (t - \tau)^2\,E(t)\,dt \qquad [7.4]$$

The shape of RTD curves depends on the combined effect of the flow behaviour and mixing performance inside the process equipment, which is usually related to the RTD function parameters i.e. mean residence time and variance. This information is important for diagnostics as well as control purposes. Specific multivariate processes such as wet ball milling require accurate knowledge of the material residence time inside the process vessel in order to effectively control and optimize the process. Studies by Kelsall *et al* (1970), Hogg (1984), Kinneberg and Herbst (1983), Austin *et al* (1984) and King (2001) have shown that residence time distribution function is a key component of the breakage behaviour model for continuous mills. The residence time distribution function describes the flow through the mill while grinding equations describe the breakage behaviour as a function of time.

In this study, salt tests have been performed on an industrial secondary ball mill at different operating conditions. The aim was first to establish the effect of changes in

key mill operating conditions such as slurry properties and volumetric ball filling on residence time distribution and the subsequent impact on milling efficiency. Secondly, to explore a possible means to estimate slurry holdup volume inside the mill based on the tracer response data.

7.3 Experimental results, analysis and discussion

7.3.1 Summary of measured data

Experimental tests were performed on an industrial mill described in chapter 3, during normal plant operation. The aim of this program was to investigate the slurry residence time distribution and holdup volume with particular attention to the effects of mill filling level and solids concentration in slurry. Table 7.1 presents experimental results obtained for twelve surveys of which six involved tracer tests. The measured residence times were obtained from the RTD data using equation 7.3. Since the mill feed was relatively fine ($d_{80} < 300\mu m$), the settling velocity of particles in the turbulent, intensely-mixed slurry pool would be very slow hence it was assumed that the liquid phase of slurry closely approximated the behaviour of the solids phase.

Table 7.1: Summary of the measured data of slurry flow rates and holdup volume

Mill Filling (%)	Slurry %Solids	In-mill S.G	τ_{mean} (mins)	Mill feed flow rate $\dot{M}$ (t/h)			Slurry flow rate (m^3/hr)	Slurry holdup (m^3)
				Solids	Water	slurry		
25	67.3	1.90	25.40	304.8	158.3	463.1	237.87	100.70
	71.4	2.02	-	331.8	130.2	462.0	229.12	-
	74.5	2.11	-	343.7	122.2	465.9	218.54	-
	75.6	2.14	29.45	330.1	111.8	441.9	206.05	101.14
30	63.5	1.81	-	361.8	177.7	539.5	297.65	-
	65.0	1.85	-	318.8	175.2	494.0	267.36	-
	73.4	2.08	27.14	336.5	126.9	463.4	220.89	99.92
	75.1	2.13	30.77	345.5	105.6	451.1	211.94	108.34
33	65.1	1.85	22.47	341.2	182.1	523.3	282.46	105.78
	67.7	1.92	-	332.9	148.4	481.3	251.35	-
	72.1	2.04	27.61	314.3	120.9	435.2	213.71	98.34
	75.6	2.14	-	321.8	98.3	420.1	195.96	-

7.3.2 Tracer response

The tracer concentration in the discharge stream, corrected for the base (zero-tracer) concentration of slurry was determined from the conductivity measurements through a simple offline calibration procedure. This involved preparation of several slurry samples to different concentrations by dissolving a known mount of tracer (between 0.3 and 1.5g) into each sample. The slurry samples were collected from the mill discharge stream prior to injection of the salt impulse. The volume of each slurry sample was determined through wet mass and dry mass analysis. The calibration equation was then obtained by mathematically relating the measured conductivity of the calibration samples to the tracer concentration. One should note that for validity of this calibration method, the calibration samples and tracer samples have to go through the same time history and that the conductivity measurement of tracer samples has to be conducted immediately after the calibration procedure. This would help to eliminate any possible errors that may arise from other ionic concentrations generated with time from continuous reactions occurring within the ore slurry.

Figures 7.1(a-c), show the tracer concentration profiles for different mill operating conditions. The effect of slurry % solids and load volume on tracer concentration distribution is easily seen in the Figures. At same level of load volume, the data indicate a relatively broader concentration spectrum and a slower convergence of the tail towards zero for the cases with higher percentage of solids in slurry. This is related to the time spend by slurry in recirculation through the ball charge (rate of slurry influx and efflux in the ball charge).

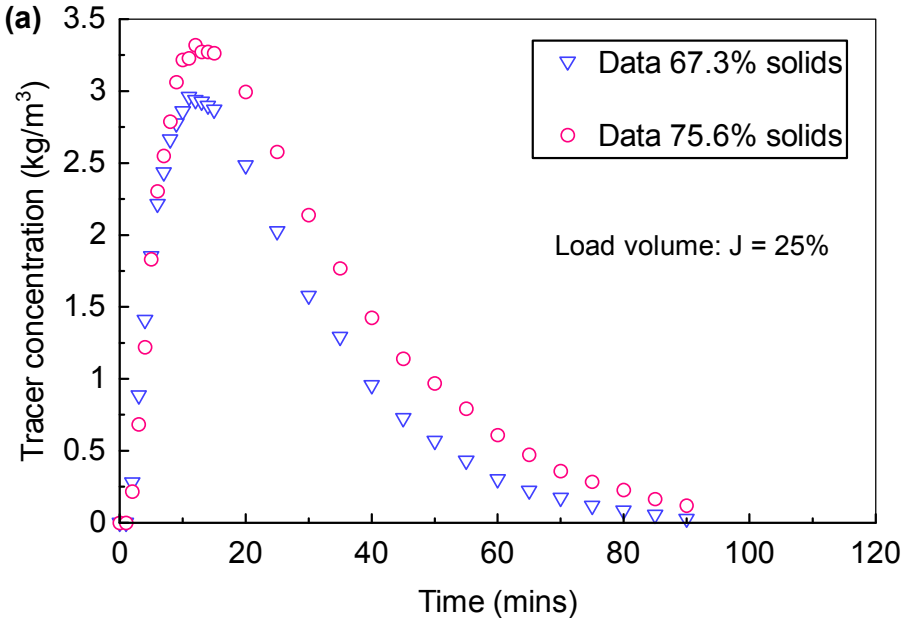

Figure 7.1(a): Distribution of the tracer concentration in the mill discharge for ball load volume of J = 25%.

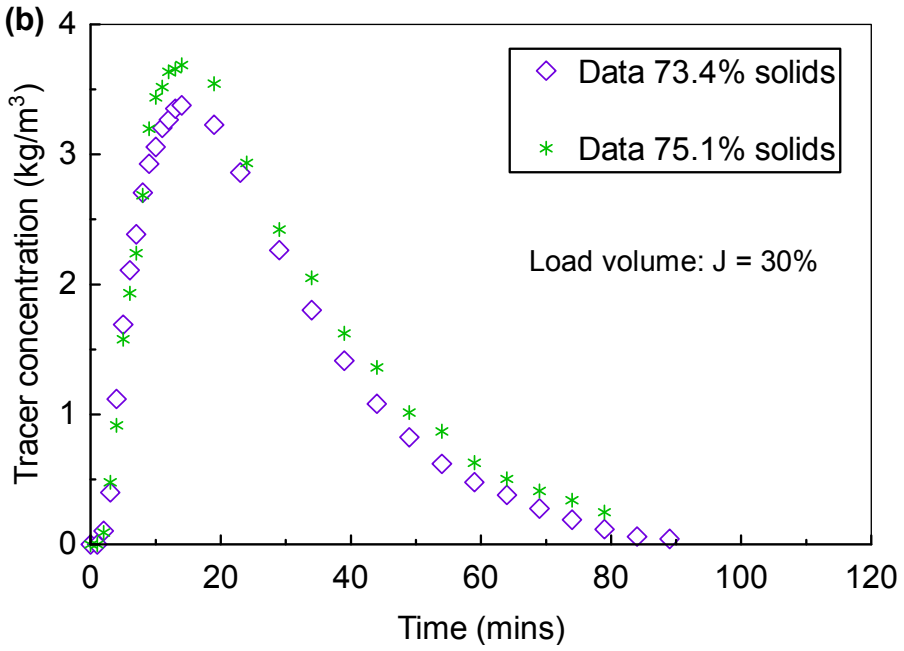

Figure 7.1(b): Distribution of the tracer concentration in the mill discharge for ball load volume of J = 30%.

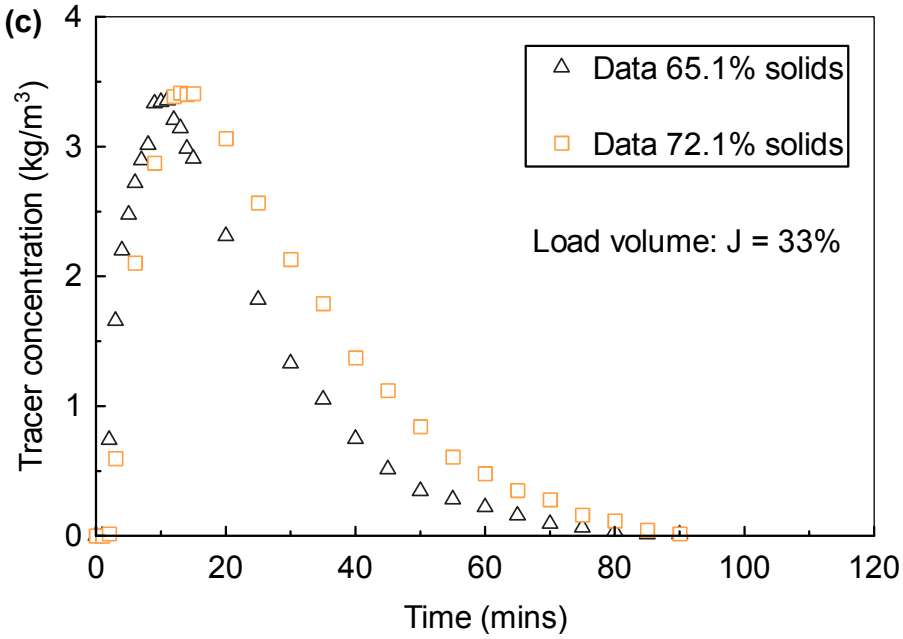

Figure 7.1(c): Distribution of the tracer concentration in the mill discharge for ball load volume of J = 33%.

7.3.3 Slurry residence time

The experimental results of the mean residence time of slurry inside the mill are summarized in Table 7.1. At same ball filling, the mean residence time shows an increasing trend with slurry % solids and load volume as depicted in the data presented in Table 7.1. This is because higher percentage of solids increases the viscosity of slurry thereby lowering its mobility. On the other hand, an increase in the ball loading from 25 to 30% and from 30 to 33% resulted in only small changes in mean residence time. The possible explanation for the observed marginal changes is that, an increase in the ball load tends to increase the slurry turnover time. It also reduces the slurry pool volume subsequently lowering the mill discharge capacity. But the combined effect of these two factors on slurry residence time is far less appreciable as compared to the effect of percentage of solids in slurry (related to slurry viscosity).

7.3.4 Feed flow rate

At steady state, the volumetric flow rate of slurry through the mill is considered to be constant. So by assuming homogeneous mixing of salt and slurry inside the mill, the mean flow rate of pulp (solids and water) through the mill can be analytically determined based on the tracer concentration profile at the mill discharge which is related to the mass balance of the tracer. The area under the concentration-time curve represents the amount of tracing material in the mill discharge stream. This can be expressed by tracer balance equation as,

$$M_t = F\int_0^{\infty} C(t)\,dt \qquad [7.5]$$

Where M_t is the mass of salt impulse (tracer) and F is the volumetric flow rate. The mass flow rate of solids ($\dot{m}_s$), ore water ($\dot{m}_l$) and pulp ($\dot{m}_p$) can be calculated using the following expressions:

$$\dot{m}_l = \rho_l \dot{Q}_l \;; \quad \dot{m}_s = \left(\frac{x_s}{100 - x_s}\right)\dot{m}_l \;; \quad \dot{m}_p = \dot{m}_l + \dot{m}_s \qquad [7.6]$$

in which the term ρ_l refers to the density of water and x_s is the weight percentage of solids in slurry. For a given level of slurry volumetric flow rate, F, the slurry hold-up mass (M_{sl}) and hold-up volume (V_{sl}) can be obtained as:

$$M_{sl} = \dot{m}_p\,\tau_{mean} \;; \quad V_{sl} = F\,\tau_{mean} \qquad [7.7]$$

Presented in Figure 7.2 is a comparison of the measured and calculated values of the slurry flow rate through the mill. A marginal variation between the measured and theoretical values of flow rates is evident. This could possibly be due to a mass balance error, attributed to unaccountable tracer losses inside the mill. The observed variation of slurry volumetric flow rate with changes in slurry solids concentration can be approximated by a linear relationship.

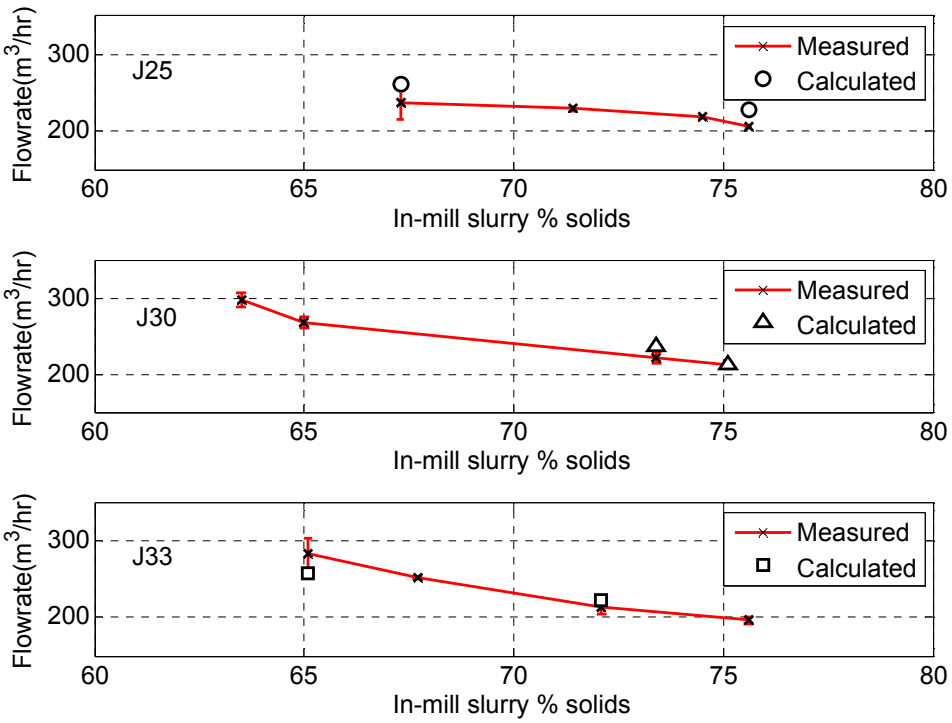

Figures 7.2: Comparison of measured and calculated values of volumetric flow of feed slurry at different levels of percent solids and ball fillings.

7.3.5 Slurry volumetric holdup

At a constant feed flow rate and solids concentration in slurry the steady state slurry holdup volume in an overflow mill should essentially be constant. But increasing the feed rate would lead to an increase in holdup volume and discharge rate due to the rise in the level of slurry above the lip of the overflow opening to accommodate the increased slurry volume inside the mill (Fuerstenau *et al*, 1986; Klimpel *et al*, 1989).

A comparison of slurry holdup volume calculated from the experimental data at low and high flow rates of water to the mill, corresponding to high and low percent solids in the feed slurry respectively reveals a noticeable variation as depicted in the results presented in Table 7.1. It is postulated that the observed trends in slurry holdup volume could be attributed to the viscosity effect on the flow behaviour of slurry and balls. Indeed, according to Smit (2000), an exponential increase in slurry viscosity at relatively high solids concentration in slurry (i.e. above 72%) significantly influences

the motion of balls inside the mill. The high viscosity would lead to a drastic increase in resistance to the flow of slurry, which subsequently impacts on load behaviour. This in effect has a predominant influence on slurry holdup volume. On the flip side, optimum solids concentration in slurry tends to boost the internal load friction which in turn suppresses ball-ball slippage thereby enhancing the lift action in the load. This in effect dilates the ball charge (higher voids volume), allowing more slurry to be entrained into the voids of the ball charge and consequently increasing the slurry holdup volume. It must however be stressed that if solids concentration is too high, load expansion is likely to occur which would lead to loss of lift and mill power.

At the same percent solids in slurry, one would intuitively expect the dynamic slurry holdup volume to increase as the ball filling is increased since the additional balls would provide more interstitial volume to be filled with slurry as the load dilates; and that a point is reached beyond which further increase in ball filling results in a decrease in holdup volume as the volume of the pool replaced by additional balls exceeds the interstitial volume presented by the additional ball filling. This pattern could not be established in our results due to variations in slurry solids concentration.

At ball filling levels of 25 and 30% of mill volume, it was observed that with increase in solids concentration in slurry (within the range investigated), the holdup volume also increases (See Table 7.1). This could be explained in relation to the viscosity effects on load behaviour. For ball load volume of 33%, an opposite trend in the variation of holdup volume is noted. Again, this is suspected to be due to changes in load behaviour.

In light of the trends observed in the measured data an attempt was made to estimate the slurry holdup volume based on calculated mill feed rates. Figure 7.3 shows a comparison of the slurry holdup volume as estimated from the measured and calculated feed rates at different mill fillings and solids concentration in slurry. In both cases, the variation of holdup volume assumes a similar trend. The comparatively large deviation observed between the measured and calculated values at lower levels of solids concentration in slurry i.e. 65.1 and 67.3% could likely be due to measurement error in the feed rates.

One interesting observation in Figure 7.3 is the sudden change in slurry holdup volume after 72% solids. A similar trend was reported by Songfack and Rajamani (1999) who observed a drastic increase in holdup volume after 75% solids in an overflow ball mill running at 80% of critical speed. They attributed the behaviour to the exponential increase in slurry viscosity.

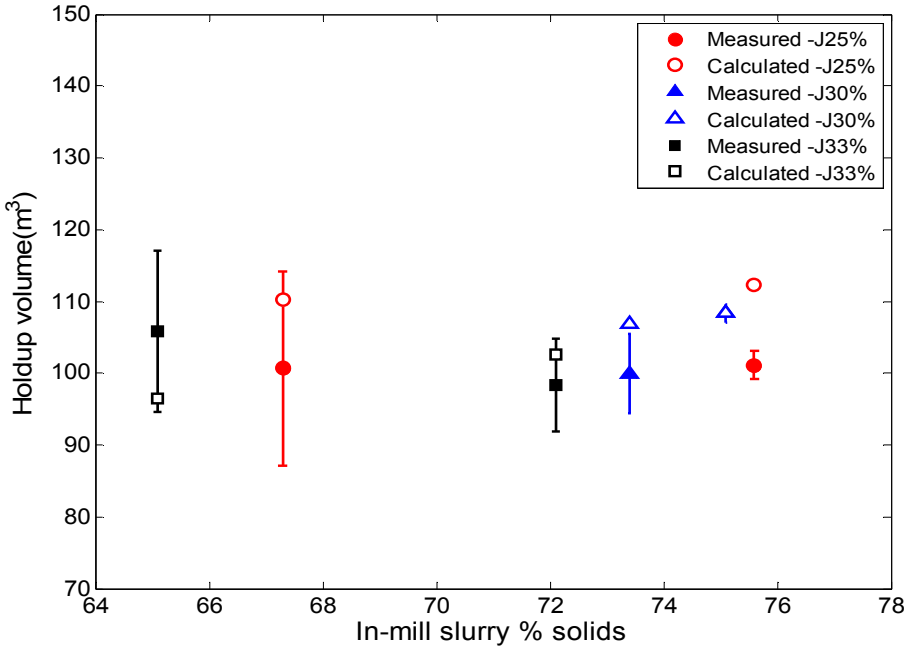

Figures 7.3: Slurry holdup volume inside the mill at different levels of percent solids and ball filling as estimated from the measured and calculated flow rate data.

Considering that mill performance is quite sensitive to the steady state slurry holdup volume, it is important that the intriguing trends in the variation of slurry holdup volume with changing ball load and slurry solids concentration discussed in the foregoing are given critical attention. Nevertheless, further exploration would be recommendable since the range of data assessed here was not sufficient to ascertain the reproducibility of the trends.

7.4 Mathematical correlations

Premised on the observed trends in the data, an effort was made to correlate the slurry holdup volume computed from equation 7.7 with the governing variables: ball load volume (J), and slurry solids concentration (x_s). The data was subjected to statistical analysis using KYPLOT software and the two independent variables passed the significance test. The regression curve that best matched the data was obtained by:

$$V_{sl} = 0.601x_s - 1.231J + 99.27 \qquad [7.8]$$

Equation 7.8 conforms to the physics of the system by which, the slurry holdup volume, $V_{sl} = f(J, x_s) + V_o$, where the functional term accounts for the second order effects of J and x_s on unsteady state holdup volume, V_o. The negative coefficient of J indicates an inverse relation between slurry holdup volume and load volume. Figure 7.4 shows the goodness of fit of equation 7.8 to the data with mean relative error of 0.9%. The observed deviations are suspected to have emanated from the tracer balance error in equation 7.5.

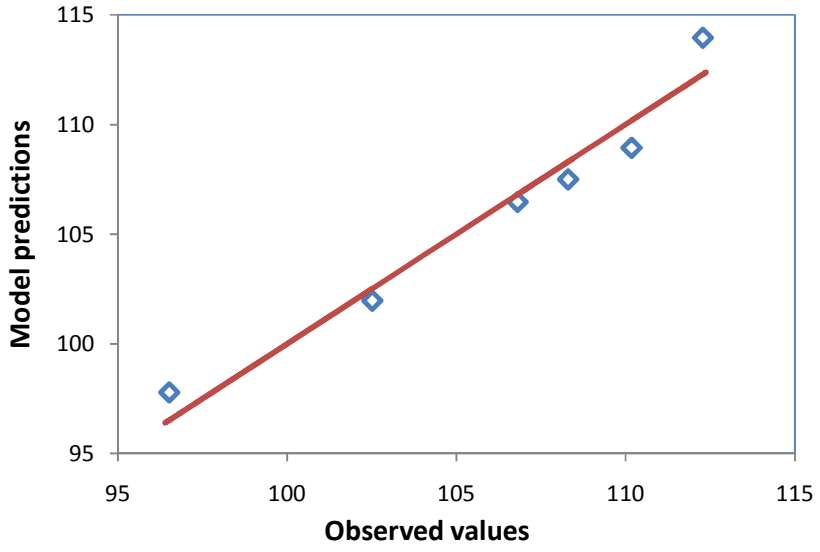

Figure 7.4: Plot of observed versus model predictions of slurry holdup volume

7.5 Conclusions

The residence time distribution (RTD) and holdup volume of an industrial overflow ball mill were successfully studied for different conditions of slurry solids concentration and ball load volume. The effects of the slurry solids concentration and the ball load volume on the mean residence time of slurry were clearly depicted in the results. Further, it was possible to estimate the slurry flow rate through the mill using RTD data and the calculated values compared reasonably with the measured ones within the limits of experimental error. Equally, the slurry volumetric holdup inside the mill was estimated on the basis of the measured slurry feed rates and residence times. The effects of slurry solids concentration on slurry volumetric holdup were evaluated and it was learnt that viscosity effects become dominant when the solids concentration exceeds 72%, impacting on the volumetric holdup. However, this remains simply speculative since no duplicate results were obtained to ascertain the reproducibility of the trend. Finally, the slurry volumetric holdup was correlated with slurry solids concentration and ball load volume yielding plausible results.

The data presented in this chapter has been modelled in Chapter 8 to provide estimates of the slurry RTD and holdup volume inside the mill for different conditions of slurry concentration and ball load volume.

CHAPTER 8

Modelling Slurry RTD and Volumetric Holdup as a Function of Solids Concentration and Ball Load Volume

8.1 Introduction

Mathematical models are often utilised to approximate complex physical phenomena in process devices. Rather than 'build and test', models can be developed to produce accurate emulation of the existing systems and through simulation, prior insights into the behaviour of the real systems can be made available. Also, the complex interactions within the system can be explored and evaluated at the lowest cost. Changes can then be made to the system to realise high efficiency and throughput. In this chapter, two models are presented; the first one describes the in-mill slurry residence time distribution (RTD) while the second describes the slurry volumetric holdup. The RTD model is derived using the concept of serial stirred mixers with a dead time component to depict the true RTD characteristics inside the mill. The volumetric holdup model on the other hand is derived from the idealised dynamic load profile defined by the media and slurry angular positions. The model takes into account mill geometry, load volume and slurry concentration.

8.2 Modelling slurry RTD

8.2.1 Background

RTD models serve as a useful means of studying the flow patterns and mixing characteristics of continuous flow reactors. The methods used by previous researchers (Austin *et al*, 1983; King, 2001; Van Nierop and Moys, 2002) to model the RTD of rotary mills include (a) Serial stirred interactive tanks with and without recycle, where the number of tanks is large enough to give the same response measured at the outlet of the continuous reactor and (b) axial dispersed flow model in which the flow of fluid elements is likened to molecular diffusion characterized by the diffusion coefficient. Both approaches provide adequate description of the flow and mixing process in general. However, with regard to multivariate nature of the milling process, no quantitative relationship is given between model parameters and various important mill operating variables. Hence one of the objectives of this chapter is to develop a model that accurately describes the residence time distribution (RTD) of slurry inside the mill as function of two important mill variables - slurry concentration and load volume.

8.2.2 RTD model

8.2.2.1 Model structure and derivation

Residence time distribution functions for ball mills can be adequately described by perfectly mixed segments (King, 2001). Therefore the derivation of the RTD model proposed in this study is based on this fundamental structure. The model consists of two small perfect mixers with mean residence times, τ_s in series with a large perfect mixer with mean residence time τ_l plus a dead time τ_d, as physically described by Figure 8.1. The dead time is included to account for non-ideal flow delays due to system dynamics.

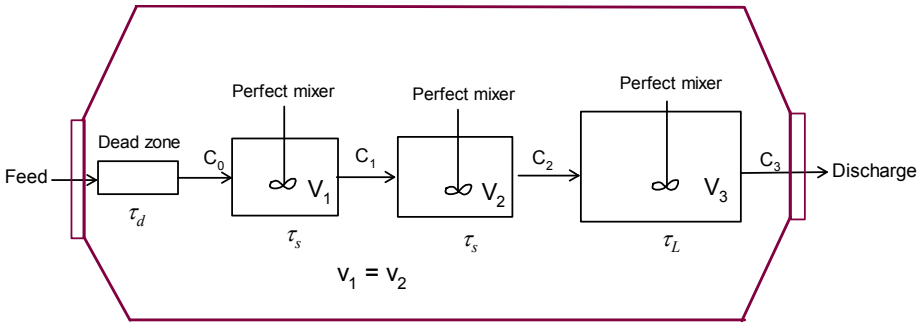

Figure 8.1: Schematic representation of the proposed RTD model

8.2.2.2 System dynamics

The mass balance around the 3 mixers assuming constant flow through the mill is given by,

$$V_i \frac{dC_i}{dt} = \dot{Q}(C_{i-1} - C_i) \quad \Rightarrow \quad \tau_i \frac{dC_i}{dt} = C_{i-1} - C_i \;\; ; \;\; i = 1, 2, 3 \qquad [8.1]$$

The dynamics for the dead zone can be described by the Dirac plug flow function $E_d(t) = \delta(t - \tau_d)$. The differential equations have to be solved to obtain the RTD function E(t). The concept of transfer function (Hopkins *et al*, 1969; Lima and Hodouin, 2005; Plugatyr and Svishchev, 2008) is applied in which the equations are

transformed from time domain to Laplace s-domain. Basically, the transfer function is defined as the ratio of the transformed time domain response and input functions. In the present case the measured response y(t) at the slurry discharge is related to the impulse input x(t) as illustrated by the transfer function diagram, Figure 8.2.

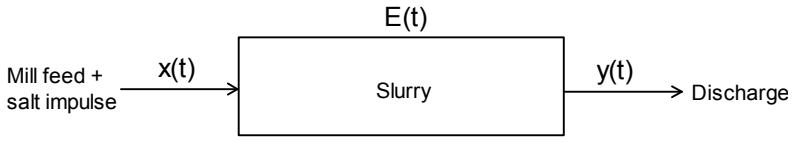

Figure 8.2: Representation of the slurry transfer function in time domain

The Laplace transform of the residence time distribution function *E(t)* yields the process transfer function, G(s) as:

$$L[E(t)] \Rightarrow G(s) = \frac{y(s)}{x(s)} = G_d(s).\,G_s(s).G_m(s).G_L(s) \qquad [8.2]$$

Where s is the Laplace space variable and G(s) is the overall transfer function for the 3 tanks in series plus dead time, as represented by Figure 8.3.

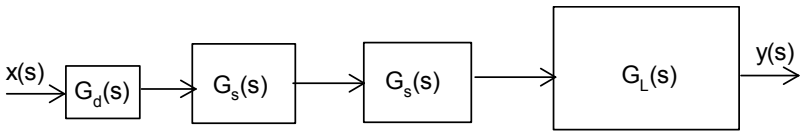

Figure 8.3: Process transfer functions for the tanks in series model

The respective transfer functions in Figure 8.3 are defined in a standard way as,

$$G_d(s) = e^{-\tau_d s};\; G_s(s) = \frac{1}{\tau_s s + 1};\; G_L(s) = \frac{1}{\tau_L s + 1} \qquad [8.3]$$

From equations 8.2 and 8.3, the overall transfer function *G(s)* becomes:

$$G(s) = \frac{e^{-\tau_d s}}{(\tau_s s + 1)^2 (\tau_L s + 1)} \qquad [8.4]$$

The inverse Laplace transform of *G(s)* gives the residence time distribution function *E(t),* which represents the RTD model, equation 8.5.

$$E(t) = L^{-1}[G(s)] = \frac{\left[-\gamma - \left(\frac{\tau_l}{\tau_l - \tau_s}\right)\right]\exp(-\gamma) + \left(\frac{\tau_l}{\tau_l - \tau_s}\right)\exp(-\alpha)}{(\tau_l - \tau_s)} \qquad [8.5]$$

$$\text{Where,} \quad \alpha = \frac{(t - \tau_d)}{\tau_l}; \quad \gamma = \frac{(t - \tau_d)}{\tau_s}$$

The overall mean residence time is sum of the individual residence times for the mixers and the dead time, estimated by fitting the model to experimental data. The model parameters are estimated by least-square criterion, by minimizing equation 8.6, using a MATLAB built-in optimization function, LSQNONLIN, which is generally used to solve non-linear least squares problems as well as nonlinear data fitting problems. Details of MATLAB optimization functions can be reviewed in Mathworks online documentation (http://www.mathworks.com/support/tech-notes)

$$e_{rr} = \sum_{i=1}^{N} \left(E(t)_{\exp} - E(t)_{\mathrm{mod}}\right)^2 \qquad [8.6]$$

where, $E(t)_{exp}$ and $E(t)_{mod}$ represent the measured and estimated values of RTD function respectively while *N* is the sample space.

8.2.3 Model fitting to experimental data

Figures 8.4 (a-c) show comparisons of experimental and predicted RTD curves over the range of conditions investigated. It can be seen that the model described the slurry residence time distribution adequately. The values of the model parameters that yielded the best fits are presented in Table 8.1 together with experimental conditions. A comparison of the measured and model values of mean residence times reveals a close match as shown in the tabulated results, Table 8.2. It is noteworthy that since the level of slurry concentration was varied between the test runs, it was not possible to distinctly assess the effect of load volume on mean residence time.

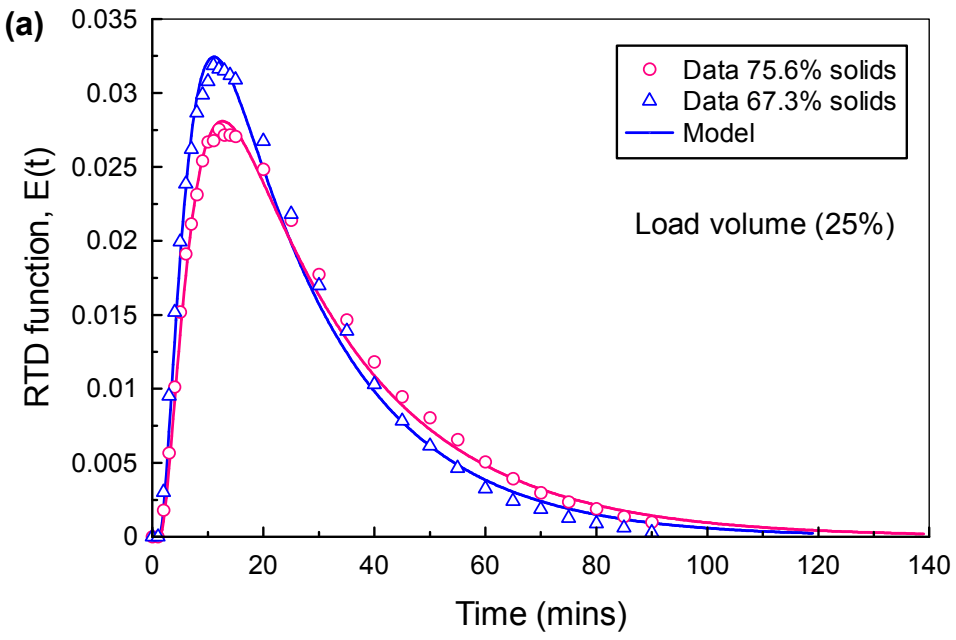

Figure 8.4(a): Comparison of experimental and predicted RTD curves for ball load volume of, J = 25%.

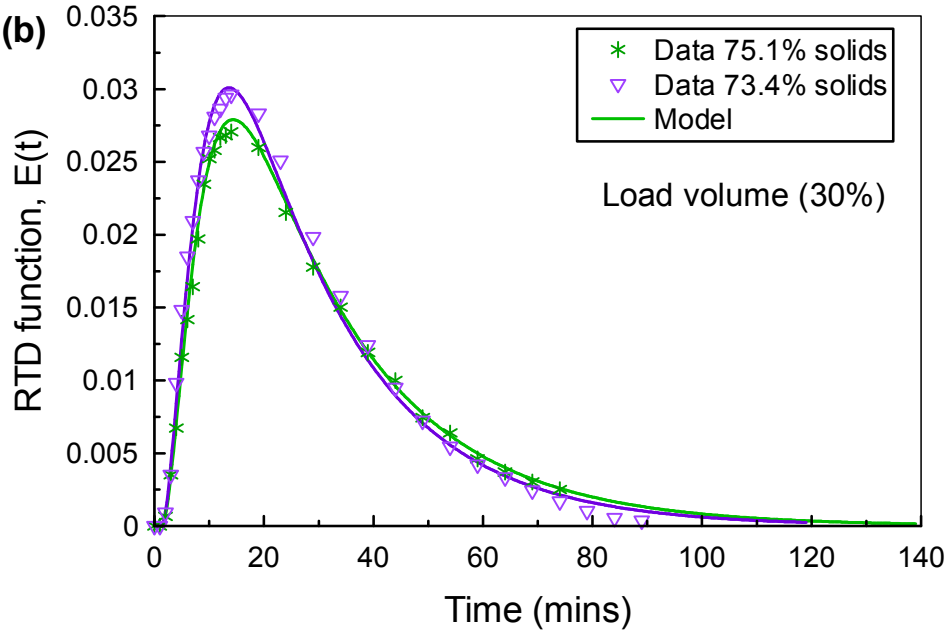

Figure 8.4(b): Comparison of experimental and predicted RTD curves for ball load volume of, J = 30%.

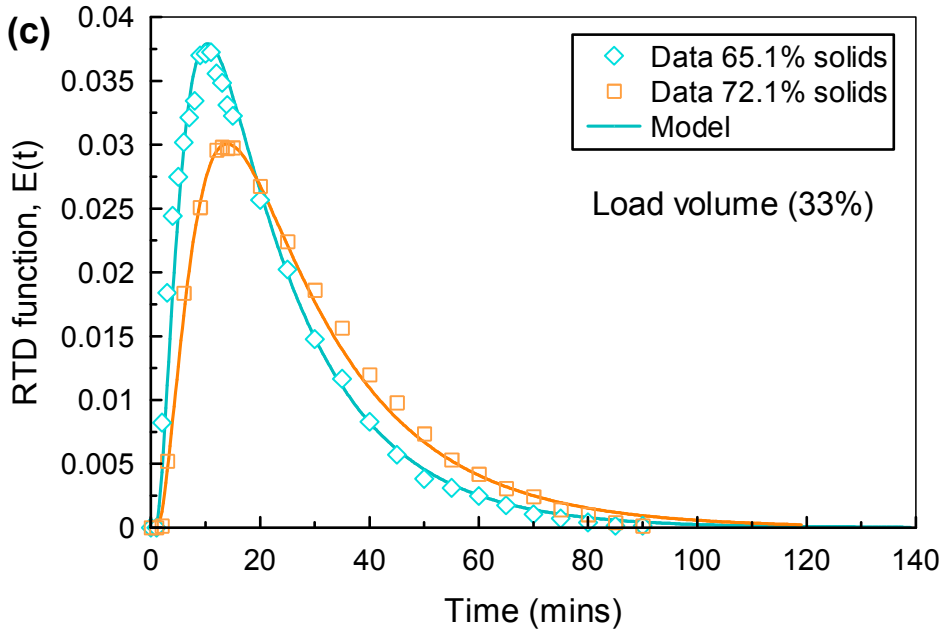

Figure 8.4(c): Comparison of experimental and predicted RTD curves ball load volume of, J = 33%.

Table 8.1: Summary of the experimental conditions and values of the parameters in the residence time distribution model

Feed flow (F) m^3/min	Load volume (%)	% Solids	τ_L	τ_s	τ_d	τ (mins)
3.96	25	67.3	20.63	2.965	1.18	27.74
3.43	25	75.6	24.31	3.154	1.22	31.84
3.68	30	73.4	21.93	3.105	1.12	29.26
3.53	30	75.1	23.95	3.214	1.2	31.58
4.71	33	65.1	16.93	2.694	0.79	23.11
3.56	33	72.1	22.08	2.919	1.06	28.98

Table 8.2: Comparison of experimental and model values of the mean residence time for different conditions of ball load volume and slurry concentration

Load volume (%)	Slurry % solids	τ(mins) Experimental	τ (mins) Model	R. error (%)
25	67.3	25.40	27.74	9.2
	75.6	29.45	31.84	8.1
30	73.4	27.14	29.26	7.8
	75.1	30.67	31.58	2.9
33	65.1	22.47	23.11	2.8
	72.1	27.61	28.98	4.9

8.2.4 Model fit quality assessment using F-statistics

It was considered expedient to statistically evaluate the fit quality of the Tanks-in-series model to the RTD data. A one way ANOVA using the F-distribution was employed to assess if the variability within and between the data for the two treatments are significantly different. In the analysis, all the twelve data sets, six each for the model and experimental were considered i.e. 2 treatments and 12 observations. The F-statistics was computed from the data and the value obtained was compared to the critical (table) value at 5% significance level. The null hypothesis is that the variances within the samples for the two treatments (experimental and model) are equal. Thus, if the F-statistics < F-table, then the model would be considered to have good fit quality to the RTD data.

The results of the F-statistics are presented in Table 8.3 where k is the number of treatments and n is the total number of observations. Note that the degrees of freedom (df) refer to the dimensions of the domain of a vector subspace holding a sample of n-independent observations while the sum of squares (SS) is the summation of the squares of the variance, which is divided into two components: between samples and within samples.

Table 8.3: Assessment of the fit quality of RTD model to experimental data using ANOVA at 5% significance level (α = 0.05)

Source of Variance	**Sum of squares** (SS)	**Degree of Freedom** (df)	**Mean square** MS = SS/df	**F-Statistics** $F = MSB/MSE$
Between samples (Explained)	SSB = 1.0083E-07	(k-1) = 1	$MSB = \frac{SSB}{k-1}$ = 1.0083E-07	$F = \frac{MSB}{MSE}$ = 0.0321
Within samples (Unexplained)	SSE = 3.1438E-05	(n-k) = 10	$MSE = \frac{SSE}{n-k}$ = 3.1438E-06	$F_{critical}$ (table) = 4.9646

Clearly the value of F-statistics is substantially lower than the table value and on the basis of this, it can be admitted that the variances between the model and experimental RTD data are not significantly different. Further the F- statistics < F-table which signifies a good fit of the model to the data.

8.2.5 Correlations

Based on the observed trends in the data presented in Tables 8.1 and 8.2, an attempt was made to correlate the mean residence time (τ) with the governing variables: Ball load volume (J), slurry concentration (x_s) and feed flow rate (F). Before regression analysis, the data was first standardized by unit variance scaling so that all the

variables have a standard deviation of one. Variance scaling allows the analysis to be based on correlations and not covariance as is the case with centering. In this case the standardized value of J would be given by $\hat{J} = J / \sigma_J$. Note that standardization leads to a corresponding change in the scale of the regression coefficients and standard errors but no change is expected in the statistical significance.

The regression analysis was performed using KYPLOT software and the fit curve that best matched the data was obtained by equation 8.7, with mean relative error ($\bar{\varepsilon}_r$) of 1.7% and 98% of variance explained. Notice that equation 8.7 complies with the physics of the system by which $\tau = V / F + \varepsilon$ where V and F represent the slurry holdup volume inside the mill and the feed flow rate respectively while ε accounts for the second order effects of J and x_s on residence time.

$$\tau = 0.278\hat{x}_s - 0.072\hat{J} + 40.501/\hat{F} \qquad [8.7]$$

A close inspection of the standardized regression coefficients in equation 8.7 reveals the dominant effect of feed flow rate on slurry residence time, which is expected. But comparing the relative impacts of ball load volume and slurry concentration as indicated by the regression coefficients, it is clear that the latter has a stronger effect on residence time. This result reinforces the findings by other researchers (Kelsall *et al*, 1970; Hogg, 1984; Songfack and Rajamani, 1999) that at constant feed flow rate the effects of slurry properties play a dominant role in defining the mass transport inside the mill.

Using τ values from equation 8.5, the correlations for the RTD function parameters (τ_L, τ_S, τ_d) were also obtained and the resultant equations are given as follows:

$$\left.\begin{array}{lll} (a) & \tau_L = 0.841\tau - 2.531 : & R^2 = 0.99;\ \bar{\varepsilon}_{rel} = 0.55\% \\ (b) & \tau_s = 0.057\tau + 1.377 : & R^2 = 0.90;\ \bar{\varepsilon}_{rel} = 1.45\% \\ (c) & \tau_d = 0.046\tau - 0.222 : & R^2 = 0.83;\ \bar{\varepsilon}_{rel} = 4.14\% \end{array}\right\} \qquad [8.8]$$

The values of the empirical coefficients were determined from regression analysis. Note that equations 8.8, provide a simple means to predict the RTD function *E(t)* without necessarily having to perform tracer tests providing the values of measurable variables, J, x_s and F are known. The form of these equations easily allows for normalization by τ_L into dimensionless form that may allow for scaling to other mills.

Presented in Figure 8.5a is a comparison of the experimental values of residence time, τ versus equation 8.7 values estimated by regression and equation 8.5 values, illustrating the 'goodness of fit'. Notice that equation 8.5 tends to over-predict the residence time, a trend suspected to be related to the extended tails of the RTD curves. Figures 8.5(b-d) on the other hand show the comparisons of the empirical estimations of the parameters, τ_L, τ_S and τ_d using equation 8.8 versus equation 8.5 predictions. Notice that the highest mean relative error ($\bar{\varepsilon}_r = 4.14\%$) is displayed in the values of dead time (τ_d); however, its contribution to the mean residence time is small due to typically low values of dead time.

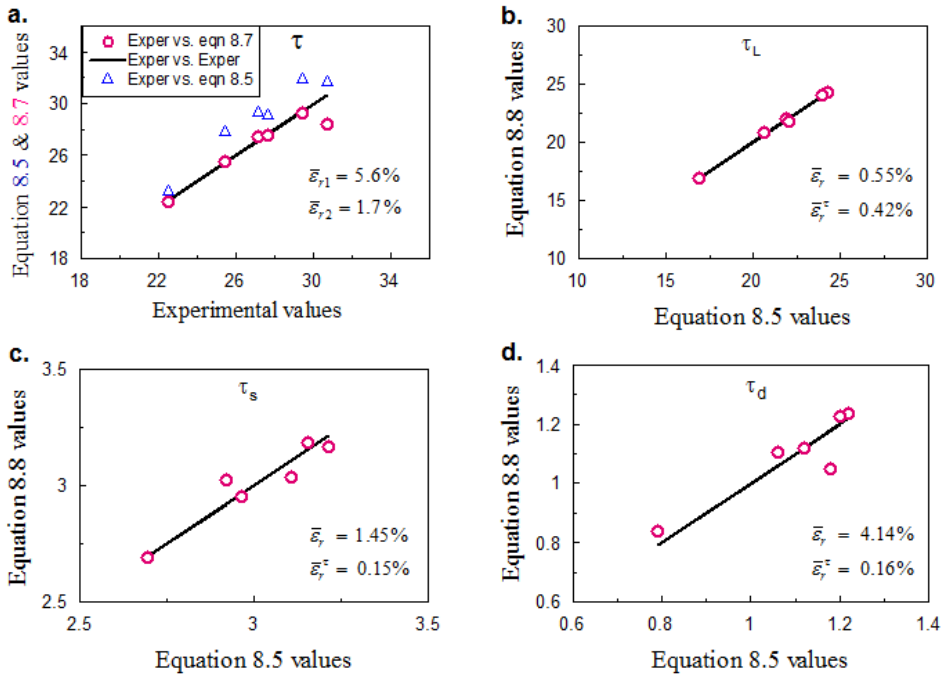

Figures 8.5: (a) Experimental values of residence time versus predictions by equations 8.5 and 8.7, **(b-d)** Empirical values obtained by equation 8.8 versus equation 8.5 predictions.

8.2.6 Conclusions

The residence time distribution (RTD) of slurry in a large ball mill has been studied under different conditions of slurry concentration, ball load volume and feed rate based on tracer response data. Trends in the results revealed that mean residence time increases as slurry concentration is increased but decreases with increase in feed flow rate. The effect of ball load volume could not be clearly delineated owing to the nature of experimental design. The experimental RTD data was modelled using three perfect mixers (two small and one large) in series with dead time and the model adequately described the experimental data. The estimated model parameters compared well with those obtained by empirical correlations. The mean residence time (τ) correlated linearly with slurry concentration and ball load volume but inversely with feed flow rate. The correlation equation fitted fairly well to the experimental values of τ with mean relative error of 1.7% and 98% of variance

explained. Slurry concentration showed a greater influence than ball load volume on mean residence time as indicated by the values of the standardized correlation coefficients. Therefore it is admissible that the model proposed here can reliably account for the combined effects of load volume and slurry concentration on the mill RTD and subsequently the grinding behaviour. For now the model is only valid for the mill investigated but with availability of data, it can be reproduced elsewhere.

8.3 Modelling of slurry volumetric holdup

8.3.1 Background

The sensitivity of slurry volumetric holdup to the performance of wet tumbling mills is well established in literature (Abouzeid and Fuerstenau, 1980; Hogg, 1982, Rogovin, 1987; Nasr-El-Din *et al*, 1992; Songfack and Rajamani, 1999). For instance, a mill overly filled with slurry (high holdup volume) would cushion the media impacts thereby lowering ore breakage rate whereas a mill depleted of slurry would experience direct ball impacts causing wear and breakage of balls. Hence, it is important that an optimum slurry holdup level is maintained during mill operation to maximise energy efficiency at desired rate of output. This is only achievable if there is an effective means to estimate slurry holdup volume inside the mill as a function of key operating conditions.

Until now, estimation of slurry holdup volume inside the mill has popularly been accomplished based on residence time distribution (RTD) studies (Kelsall *et al*, 1969; Abouzeid *et al*, 1974; Gardner *et at*, 1982; Afacan *et al*, 1990). This owes to the convenience and reliability associated with the technique. However, the technique suffers one major limitation in that measurements have to be done offline. This criterion might lead to delayed or untimely intervention by the operator where undesirable holdup conditions are detected. Thus, it is desirable to have a technique for real-time on-line monitoring of in-mill slurry holdup volume and its variation.

Methods for on-line estimation of slurry holdup volume presented in literature are largely based on information about the load weight obtained from load cells or strain

transducers mounted underneath the mill. The assumption here is that the dynamic ball load and in-mill slurry density are kept constant which is a clear uncertainty. Indeed this explains why many combinations of balls and slurry could have the same weight but comprising different proportions of these components. To address this challenge, the slurry holdup volume may be inferred from measurable mill variables such as relative positions of media and pulp, mill filling level and the relevant mill geometric parameters. This information would be fed to a process model which returns a close estimation of the slurry holdup volume inside the mill.

The positions of balls and slurry inside the mill can be measured as a function of key mill operating variables using direct sensors installed through the mill shell. Examples of direct sensors for load position measurement that have been reported in literature include (i) Conductivity probes (Moys, 1985; Vermeulen *et al*, 1985; Moys and Montini, 1987; Moys *et al*, 1996) (ii) Force probes (Skorupa and Moys, 1993); Van Nierop, 2001; Tano *et al*, 2005) (iii) Proximity sensors (Kiangi and Moys, 2006) and (iv) SENSOMAG® (Clermont *et al*, 2008).

Direct interaction of the sensors with the load provides fairly realistic and reliable information of the load dynamics inside the mill which can be mathematically related to the slurry holdup volume and linked to the mill monitoring system. Hence, our aim here is to develop a simple but reliable semi-empirical model for on-line estimation of slurry volumetric holdup inside the mill at different levels of slurry concentration and load volume based on load position signals as detected by the on-line ball and pulp sensors

8.3.2 Model structure and derivation

8.3.2.1 Physical and mathematical descriptions

To allow for mathematical analysis to be performed on the dynamic load, the dynamic shape of the load inside an overflow ball mill can be approximated to a profile shown in Figure 8.6 in which R_M is the mill radius inside liners and R_T is the radius of the discharge opening.

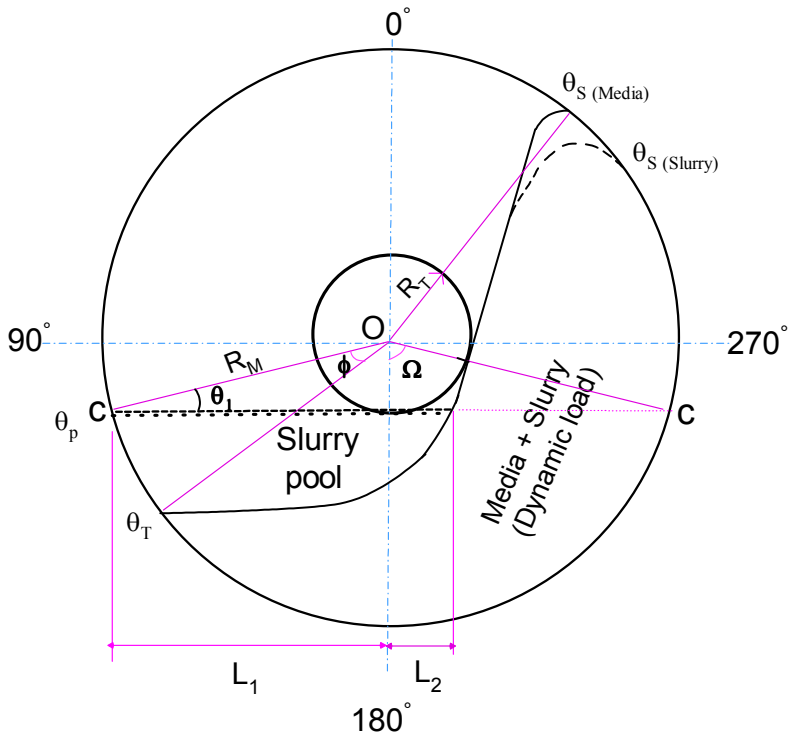

Figure 8.6: Representation of important dynamic load angles in an overflow mill.

From Figure 8.6, the angle subtended by the slurry pool (ϕ) is the difference between the media toe angle and the slurry pool angle (i.e. $\phi = \theta_T - \theta_P$). The length of the chord *C* - *C* equates to the minimum overflow filling (J_o) where the mill operates with minimum discharge of slurry. This is evaluated based on the size of the discharge trunnion and the geometry of the stationary ball charge. J_o is subtended at the mill centre by an angle (ψ_S), which is referred to as static media angle. The values of ψ_S at various levels of *J* can be obtained using an empirical relation as $\psi_S = 4.142J^{0.415}$ (see Appendix E). Alternatively, the static media angle can be estimated from a simple relationship involving the number of lifting bars around the mill circumference that are visible when the mill is stationary. The static media angle would be proportional to the number of invisible lifting bars covered by the media charge.

$$\psi_S = 2\pi(1 - n_L/n_T) \qquad [8.9]$$

where, n_L is the number of visible lifting bars and n_T is the total number of lifting bars around the mill circumference. Other load angles $\theta_1$and Ω depicted in Figure 8.6 can be obtained through geometric relations in the form,

$$\theta_1 = (\pi - \psi_S)/2 \quad ; \qquad \Omega = \pi/2 - \theta_1 \qquad [8.10]$$

Our industrial data indicates that the average level of slurry necessary to give overflow is much higher than that necessary to fill the mill to the overflow level at rest. Hence, the angle θ_1 is at maximum when the slurry level is just at the lip of the overflow opening. It reduces with increase in slurry level and becomes zero when the slurry level reaches the centre of the overflow opening.

From the geometry of Figure 8.6, the length of the cord representing the pool free surface (i.e. from the mill shell to the free surface of the ball charge) is the sum of L_1 and L_2 which is denoted as L_c. The values of L_1 and L_2 can be evaluated geometrically while L_2 can be determined through a correlation with ball loading, J and mill radius, R_M as follows:

$$L_1 = \sqrt{R_M^{\,2} - R_T^{\,2}} \quad ; \qquad L_2 \approx (0.711 - 1.404J)R_M \qquad [8.11]$$

$$L_c = \left\{\sqrt{R_M^{\,2} - R_T^{\,2}} + (0.711 - 1.404J)R_M\right\} \qquad [8.12]$$

The values of the coefficients of R_M and J in equation 8.11 were established by regression analysis using DEM simulation data (for details see Appendix E).

8.3.2.2 Determining slurry volume within the ball charge

Generally it would be assumed that, when the load is fully saturated with slurry (optimum slurry loading), the media and slurry shoulder angles should coincide; in this case $\theta_{S(media)} = \theta_{S(slurry)}$. Under this condition, the total volume of slurry within the ball charge can be calculated as follows:

$$V_{S(load)} = \varepsilon_B K_B J V_{mill} \quad [8.13]$$

Where V_{mill} *is* the volume of the mill inside liners, ε_B is the static porosity in the ball charge, taken as 0.4 while K_B is a correction factor that is related to the degree of load dilation. The general assumption here is that the cataracting media hold insignificant volume of slurry with them. So where the media flow regime is predominantly cascading, the parameter K_B can be equated to the ratio of the static and dynamic media angles. Equation 8.13 may however result in minor errors considering the effects of gravity, cohesive forces and load porosity on slurry flow at the load shoulder position. On the basis of this argument, it would be prudent to introduce some modifications as follows:

$$V_{S(load)} = \varepsilon_B K_B J V_{mill} \frac{\theta_{S(slurry)}}{\theta_{S(media)}} \quad [8.14]$$

Where $\theta_{S(media)}$ and $\theta_{S(slurry)}$ refer to the shoulder angles (degrees) of the media and slurry respectively while J is the fractional filling of the mill with ball load.

8.3.2.3 Determining the volume of slurry pool

The volume of slurry in the pool could be geometrically estimated from the media toe angle and slurry pool angle both of which are measurable parameters. But in view of the undefinitive nature of the pool profile at the interface with the ball charge, it would be worthwhile to consider some simplifying assumptions in order to allow for mathematical analysis. Based on the pool geometry in Figure 8.6, it is assumed that:

(i) The profile of the interfacial surface between the pool and the ball charge approximates to a half-parabolic arc and that the length of the arc would vary with pool volume.

(ii) The depth of the pool is defined by an arc that constitutes the outer boundary of the pool with the mill shell and which subtends an angle ϕ at the mill centre.

Under normal operating conditions, the slurry toe angle would remain almost constant as the mill rotates. Therefore, the value of L_1 (see Figure 8.6) is constant corresponding to the minimum overflow filling (J_o) while L_2 would increase with a decrease in the level of media filling. The volume of slurry in the pool can thus be obtained using an expression which is derived from the equation for calculating the area of a parabolic segment (NCEES, 2008). The angle ϕ in equation 8.15 is presented in radians. Note that the parameter K_p is introduced here as a geometric correction factor.

$$V_{S(pool)} = K_p V_{mill} \frac{L_c}{\pi R_M} Sin\phi = K_p V_{mill} \frac{\left((0.711\text{-}1.404J)R_M + \sqrt{R_M^2 + R_T^2}\right) Sin\phi}{\pi R_M} \quad \text{…….. [8.15]}$$

8.3.2.4 Total slurry holdup volume

The total volume of slurry in the mill ($V_{S(mill)}$) is given as the sum of the slurry volumes in the pool and within the load, equations 8.14 and 8.15, that is:

$$V_{S(mill)} = \varepsilon_B J K_B V_{mill} \frac{\theta_{S(slurry)}}{\theta_{S(media)}} + K_P V_{mill} \frac{\left((0.711-1.404J)R_M + \sqrt{R_M^2 + R_T^2}\right) Sin\phi}{\pi R_M} \quad \text{…….. [8.16]}$$

The only parameters to be measured in equation 8.16 are the media and slurry angles. The constants K_p and K_B are determined empirically by fitting the model to experimental data.

8.3.3 Model calibration

8.3.3.1 Media and slurry position data

The data presented in Table 8.4 represents the mean values of the media and slurry position recorded by the on-line media and slurry sensors during the 12 sampling surveys. It depicts the variation of ball and slurry positions inside the mill as the slurry concentration and load volume changes. Using this data the geometric parameters defined in equation 8.16 can be evaluated.

Table 8.4: Summary of the load position data recorded by SENSOMAG sensors

Ball load volume (%)	Slurry solids (%)	Slurry toe angle (%)	Slurry shoulder angle (^{0})	Ball toe angle (^{0})	Ball shoulder angle (^{0})
25	75.6	98.0	301.8	131.2	294.9
	71.4	97.8	302.8	132.7	295.5
	74.5	98.1	301.9	131.1	295.4
	67.3	97.4	303.7	133.3	296.0
30	75.1	97.0	307.1	126.2	301.6
	73.4	97.1	308.0	127.7	301.4
	65.0	97.1	309.0	128.8	301.5
	63.5	96.8	310.0	129.8	302.2
33	67.7	97.8	310.5	126.5	306.0
	65.1	97.4	310.8	127.0	305.8
	72.1	97.8	308.8	125.2	305.4
	75.6	98.1	307.1	123.8	305.3

8.3.3.2 Model fitting to data

Figure 8.7 shows the plot of measured versus fitted volumetric holdup, which illustrates the accuracy of the model derived here. The values of the model parameters that yielded the best fit to the data are given in Table 8.5. Currently, no other correlation exists in literature for mill holdup volume based on media and slurry position data to the best knowledge of the author; hence no comparison is given here regarding prediction capacity of equation 8.16 over others.

Table 8.5: Values of K_B and K_P parameters in the holdup model that gave the best fit to the data

Load volume (%)	Slurry % solids	K_B	K_P
25	67.3	1.068	0.658
	75.6	1.244	
30	73.4	0.938	0.734
	75.1	1.006	
33	65.1	0.686	0.791
	72.1	0.844	

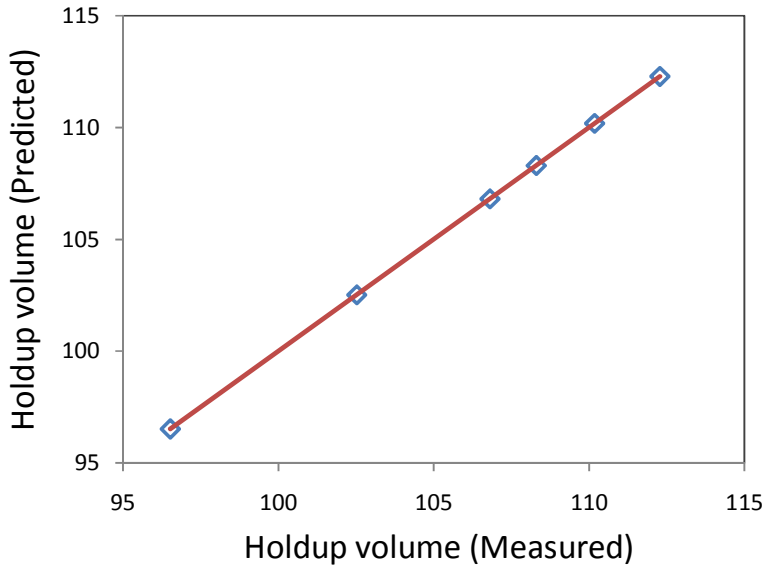

Figure 8.7: Measured versus fitted values of slurry holdup volume

Based on the data presented in Table 8.5, simple mathematical correlations were developed in the form:

$$K_B = 0.019\,x_s - 0.043J + 0.828 \;; \qquad K_p = 1.188 - 13.31/J \qquad [8.17]$$

Where x_s is the weight fraction of solids in slurry and J is the fraction of the mill filled with ball charge. A regression method was applied to estimate the values of the

empirical coefficients. Figures 8.8 (a, b) show how the values obtained from equations 8.17 compare with the data. A little disparity is evident in the predictions of K_p and K_B which could be attributed to some errors in the measured data.

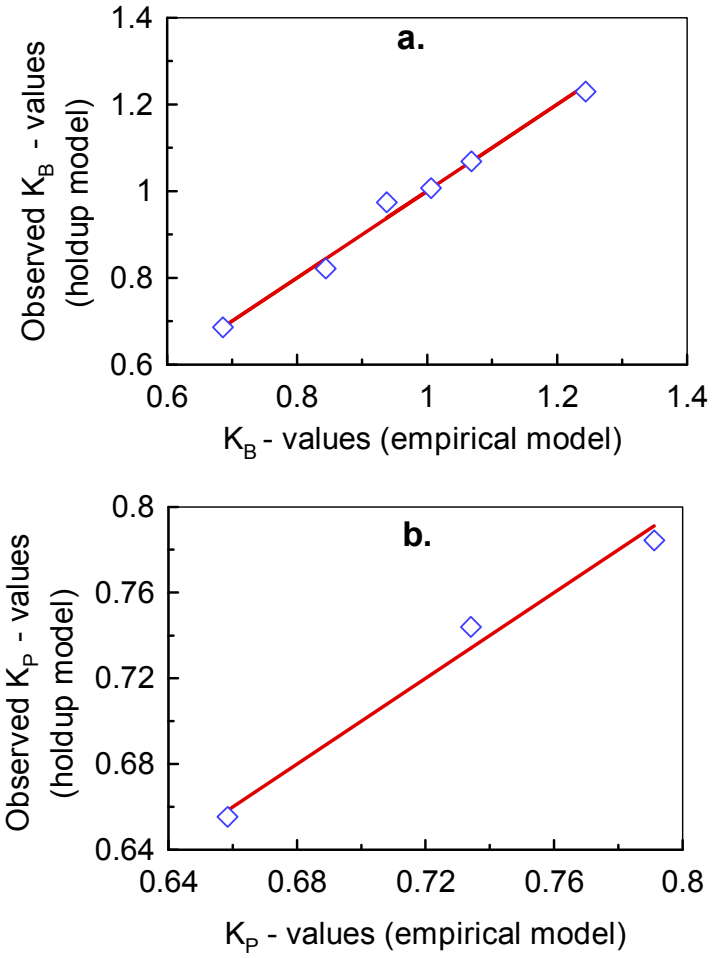

Figure 8.8(a, b): Comparison of the observed and fitted values of K_p and K_B

Presented in Figure 8.9 is the variation of holdup volume with slurry concentration and load volume. Although the feed rates were slightly varied (within 20% margin) to achieve the required solids concentration level, the holdup volume clearly appears to be greater at higher slurry concentrations (because of viscosity effects) and lower level of load volume which is typical of an overflow mill. This observation is

consistent with the findings by Klimpel *et al* (1989) and further backs up their conclusion that more than five-fold increase of slurry feed rate would be required in order to realize a notable change in volumetric holdup of slurry inside an overflow-discharge mill.

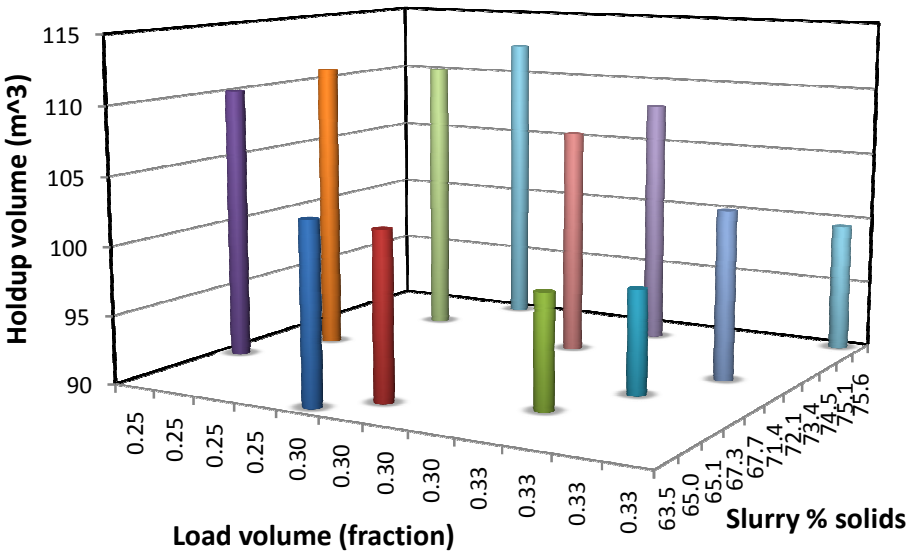

Figure 8.9: Variation of slurry volumetric holdup with load volume and percentage of solids in slurry.

Figure 8.10 shows the partitioning of slurry volumetric holdup between the pool and the ball charge regions as estimated from equation 8.15. At higher slurry concentration, the slurry holdup volume appears to be equally apportioned between the pool and the ball charge. However, with decrease in slurry concentration, the volume fraction of the slurry holdup that constitutes the pool tends to increase steadily. The possible reason for this trend could be that the load experiences a relatively reduced lift action and less expansion at lower levels slurry concentration which results in less voids volume available for slurry entrainment. The bulk of the slurry will thus remain in the pool.

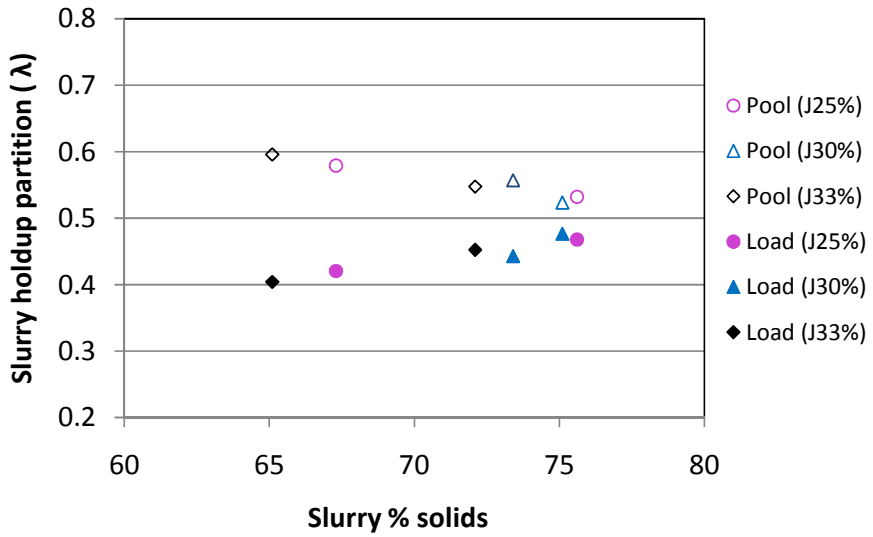

Figure 8.10: Partition of slurry holdup between the pool and ball load regions at different levels of slurry concentration and load volume

8.3.4 Conclusions

As part of the efforts to effectively control and optimize wet ball milling processes, a simple model has been developed that can predict the slurry holdup volume inside the mill as a function of ball load volume and slurry solids concentration. The model incorporates empirical coefficients to relate slurry holdup volume to load angles and mill geometry as the ball filling and slurry solids concentration change. The model adequately describes the trends in experimental data and hence it could be linked to the mill control system and utilised for continuous monitoring of the variation in slurry holdup volume inside the mill. This would provide operators with further information of mill behaviour leading to better and timely control actions which subsequently enhances mill performance.

CHAPTER 9

Characterizing Slurry Hydrodynamic Transport by an Improved Mixing-Cell Model

9.1 Introduction

The mixing cell models that have previously been applied in process design of ball mills do not sufficiently describe the slurry flow behaviour in overflow mills. They fail to provide a mechanism for characteristic exchange of slurry between the pool and the ball charge. Only by realistically accounting for effects of both axial mixing and radial convection processes as well as possible short-circuit flows on the main flow of slurry can accurate modelling of slurry transport in overflow mills be achieved.

Under normal operating conditions, the slurry in an overflow ball mill is distributed into two distinct regions as follows: a fraction of the slurry forms a pool at the toe of the ball bed while the rest is retained in the ball charge. However, there is a continuous mass exchange of slurry between the pool and the ball charge regions governed by the mill speed, load volume, slurry properties and the liner profile. Also a strong possibility exists that within the pool, there is continuous recirculation and back-mixing of slurry. Within the ball charge, the slurry flow pattern is defined by the motion of the balls and the mill drum. These complicated boundaries within which slurry flow takes place makes it practically difficult to characterise the hydrodynamic transport of slurry based on standard fluid flow equations. The goal of this chapter is develop an improved mixing cell model and apply it to examine and characterise slurry hydrodynamic transport in a large overflow ball mill with particular attention to the effects of two important mill operational variables: slurry concentration and load volume. The study serves as an initial step towards providing information that may help improve the accuracy of slurry flow models in overflow mill simulators. This would subsequently lead to better designs and performance optimisation of overflow ball mills.

9.2 Improved mixing-cell model

9.2.1 Model structure and derivation

Figure 9.1a is a schematic illustration of the dynamic profile of the pool and the ball charge in an overflow ball mill while Figure 9.1b is a block diagram describing the

associated flow patterns. This structure forms a fundamental basis upon which the improved mixing cell model will be derived. This modelling approach has been previously applied by other researchers to study mixing in continuous flow systems such as rotary kilns and dryers. Cholette and Cloutier (1959) were among the early researchers to model the behavior of a continuous flow reactor using a series of mixers consisting of back-mix regions and inert dead zones with a bypass stream. Other researchers who have used this modeling technique include (Wen and Chung, 1965; Levisch *et al*, 1967; Duchesne *et al*, 1996). To our best knowledge no work has been reported in relation to ball mills. The derivation of the improved mixing cell model envisaged in this paper shall be based on the following fundamental assumptions:

- The tracer is introduced into the mill as a pulse and flows in a similar pattern with slurry
- Non-flowing zone actively exchanges material with adjacent flowing zone.
- The mill operates at steady state conditions
- A portion of the feed slurry may simply short-circuit (bypass) to the outlet

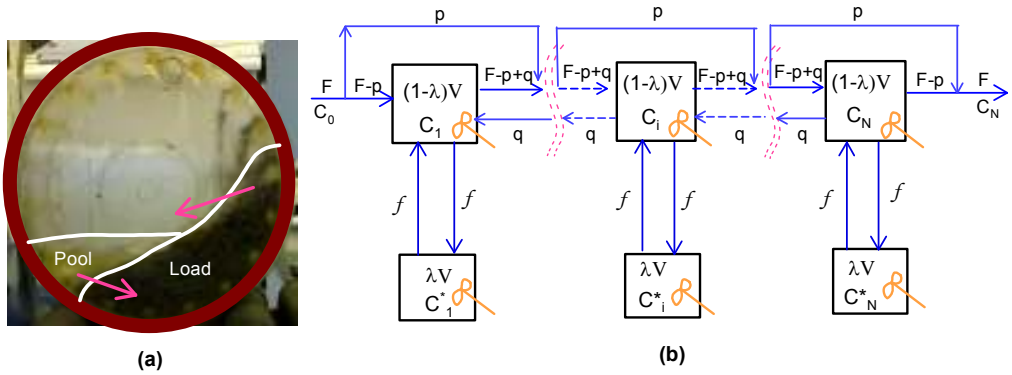

Figure 9.1: Physical representation of the improved mixing cell model

In Figure 9.1b, the parameters *f* and *q* represent the rate of slurry exchange between the flowing and stagnant zones and the rate of recirculation between adjacent flowing zones respectively while *p* is the short-circuit flow. Hence, unlike the earlier models,

the non-flowing zone is not inert but contributes to the mixing in the cell. The total volume of slurry in a single cell is denoted by V and a part of this slurry volume equal to λV is within the ball charge (stagnant zone i.e. no axial transport) while the remaining volume equal to $(1-\lambda)V$ is in the pool (flowing zone). If the total slurry volumetric holdup inside the mill is known, then the parameter λ is obtained as,

$$\lambda = 1 - \frac{Volume\ of\ slurry\ pool}{Total\ slurry\ volumetric\ holdup} \qquad [9.1]$$

The total slurry volumetric holdup inside the mill is dependent on various operating factors key among which are the mill speed, load volume and slurry properties. In the present case the slurry volumetric holdup is computed from the measured feed flow rate and the mean residence time while slurry pool volume has been estimated geometrically based on the dynamic profile of the slurry pool as obtained by discrete element method (DEM) simulation. It is the product of mill length and pool cross-sectional area where the latter is calculated using the Simpson's rule. The fundamental assumption here is that no significant variations occur in the depth of the slurry pool along the mill length between the feed and the discharge ends. The subsequent values of λ are presented later in Table 9.1. The material balance in Figure 9.1 for both flowing and stagnant zones is given by

Cell 1:

$$V(1-\lambda)\frac{dc_1}{dt} + (F-p+q+f)c_1 = (F-p)c_o + qc_2 + fc_1^* \qquad [9.2]$$

$$\lambda V\frac{dc_1^*}{dt} + fc_1^* = fc_1 \qquad [9.3]$$

Cell i = 2 to N-1:

$$V(1-\lambda)\frac{dc_i}{dt} + (F-p+2q+f)c_i = (F-p+q)c_{i-1} + qc_{i+1} + fc_i^* \qquad [9.4]$$

$$\lambda V\frac{dc_i^*}{dt} + fc_i^* = fc_i \qquad [9.5]$$

Cell N:

$$V(1-\lambda)\frac{dc_N}{dt} + (F-p+q+f)c_N = (F-p+q)c_{N-1} + fc_N^* \quad [9.6]$$

$$\lambda V\frac{dc_N^*}{dt} + fc_N^* = fc_N \quad [9.7]$$

The following notation is introduced to represent the flow coefficients.

$$\alpha = \frac{q}{V};\quad \gamma = \frac{f}{V};\quad \delta_{L-P} \Rightarrow \frac{f}{\lambda V} = \frac{\gamma}{\lambda};\quad \delta_{P-L} = \frac{\gamma}{1-\lambda};\quad \kappa = \frac{p}{F} \quad [9.8]$$

Now using the above designations, equations (9.2 – 9.7) can be rewritten as follows:

Cell 1:

$$\frac{dc_1}{dt} + \left(\frac{1-\kappa}{\bar{\tau}(1-\lambda)} + \frac{\alpha+\gamma}{(1-\lambda)}\right)c_1 = \frac{(1-\kappa)c_o}{\bar{\tau}(1-\lambda)} + \frac{\alpha}{(1-\lambda)}c_2 + \frac{\gamma}{(1-\lambda)}c_1^* \quad [9.9]$$

$$\frac{dc_1^*}{dt} + \frac{\gamma}{\lambda}c_1^* = \frac{\gamma}{\lambda}c_1 \quad [9.10]$$

Cell i = 2 to N-1:

$$\frac{dc_i}{dt} + \left(\frac{1-\kappa}{\bar{\tau}(1-\lambda)} + \frac{2\alpha+\gamma}{(1-\lambda)}\right)c_i = \left(\frac{1-\kappa}{\bar{\tau}(1-\lambda)} + \frac{\alpha}{(1-\lambda)}\right)c_{i-1} + \frac{\alpha}{(1-\lambda)}c_{i+1} + \frac{\gamma}{(1-\lambda)}c_i^*$$

..... [9.11]

$$\frac{dc_i^*}{dt} + \frac{\gamma}{\lambda}c_i^* = \frac{\gamma}{\lambda}c_i \quad [9.12]$$

Cell N:

$$\frac{dc_N}{dt} + \left(\frac{1-\kappa}{\bar{\tau}(1-\lambda)} + \frac{\alpha+\gamma}{(1-\lambda)}\right)c_N = \left(\frac{1-\kappa}{\bar{\tau}(1-\lambda)} + \frac{\alpha}{(1-\lambda)}\right)c_{N-1} + \frac{\gamma}{(1-\lambda)}c_N^* \quad [9.13]$$

$$\frac{dc_N^*}{dt} + \frac{\gamma}{\lambda}c_N^* = \frac{\gamma}{\lambda}c_N \quad [9.14]$$

The parameters γ, α, κ, $\delta_{L\text{-}P}$ and $\delta_{P\text{-}L}$ are flow coefficients defined in equation 9.8 while λ represents the fraction of cell volume that constitutes a stagnant zone, which in practice corresponds to the fraction of slurry holdup volume within the ball charge. For instance, where $\lambda = 0.5$, the slurry holdup volume within the ball charge equals the pool volume, hence $\delta_{L\text{-}P} = \delta_{P\text{-}L}$. The mean residence time ($\bar{T}$) of slurry inside the mill is the sum of the mean residence times ($\bar{\tau}$) in N individual cells expressed in the form:

$$\bar{T} \Rightarrow \sum_{i=1}^{N} \bar{\tau}_i = \sum_{i=1}^{N} \left(\frac{\lambda V + (1-\lambda)V}{F} \right) = \frac{NV}{F} \qquad [9.15]$$

while the axial back-mixing coefficient (β) is expressed as:

$$\beta \Rightarrow \frac{q}{F - p + q} = \frac{\alpha \bar{\tau}}{1 - \kappa\bar{\tau} + \alpha \bar{\tau}} \qquad [9.16]$$

In order to establish the values of the model parameters, a serial solution to the mass balance differential equations (9.9 - 9.14) should be obtained. The analytical solution to this set of equations in time domain becomes complicated for N > 5. Therefore in this study a numerical solution was sought and the fourth order Runge-Kutta method was employed in SIMULINK. The initial conditions were that at $t = 0$, $dc_i/dt = 0$, $C_o = M/F\Delta t$, where M is the mass of tracer impulse, F is the mill feed rate and Δt is a small time step that simulates an impulse input.

9.2.2 Determining the number of mixing cells

The optimum number of mixing cells was established through a non-linear regression routine that minimizes the sum of squares of the errors (SSE) between the experimental and predicted exit concentrations as:

$$\int_0^{\infty} \left(C^{\exp}(t) - C^{pred}(t) \right)^2 dt \qquad [9.17]$$

Where *C(t)* is the exit tracer concentration at time *t*. It is worth noting that only one experimental data set having the highest residence time was utilised in the calibration. As depicted in Figure 9.2, the objective function decreases with increase in number of cells up to 12 cells then the trend begins to plateau. Thus, the choice of N = 12 is considered to be optimal in terms of accuracy and computational time.

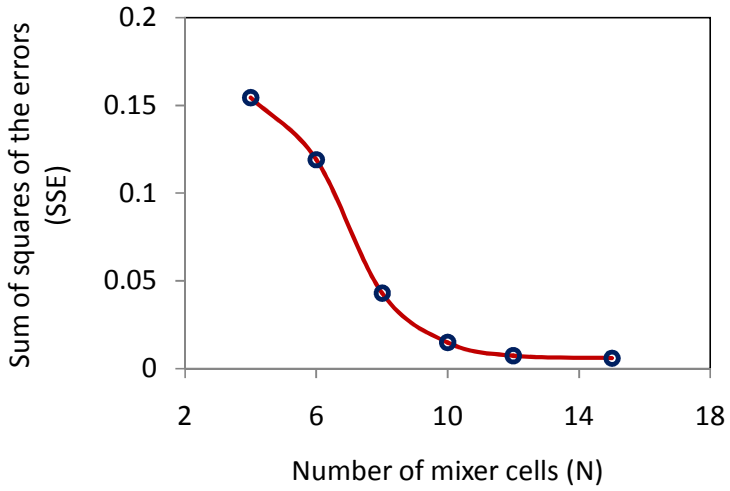

Figure 9.2: Evolution of SSE with respect to number of mixing cells

9.2.3 Sensitivity analysis of model parameters

Sensitivity analysis helps to identify parameters which exert the most influence on model results. Such knowledge is important for determining parameters for which it is important to have more accurate values. Several methods of sensitivity analysis exist that are employed in various modelling situations. The simplified form of the Smirnov test statistics (Hamby, 1994; Drews, *et al,* 2003) was adopted in the current analysis to assess the sensitivity of the parameters, κ, α, γ and λ on the model accuracy**.** In this approach the model was run with parameter variation in a defined domain of plus and minus 35% of the reference value, where the reference value here refer to the average of the maximum and minimum values that define the domain bounds. Note that the choice of domain bounds of each parameter was guided by our laboratory experience. The Monte Carlo method was used to generate 6 random sets

of parameter values uniformly distributed within the defined domain to serve as sample points. Each parameter step change was performed separately while the other parameters were kept constant and the deviation of the response from that of the reference parameters combination was analysed. The mean residual deviation (RD) was evaluated for each parameter as a characteristic of the response. The objective function values for *m* perturbations and *n* observations (data points) were obtained by

$$RD = \frac{1}{m}\sum_{j=1}^{m} RD_j \qquad where\ by, \qquad RD_j = \frac{1}{n}\sum_{i=1}^{n}\left| \left(1 - \frac{c_p(i)}{c_r(i)} \right) \right| \qquad [9.18]$$

in which $c_r(i)$ are the observed values of tracer concentration that correspond to the reference parameters combination while $c_p(i)$ are the perturbed values of tracer concentration for each parameter combination tested. The results of the analysis are presented in Figure 9.3 for $m = 6$ and $n = 30$. The parameters α and κ have less impact on the model accuracy compared to other two parameters. Therefore the choice of limits of γ and λ during model fitting to experimental data needs to be performed judiciously.

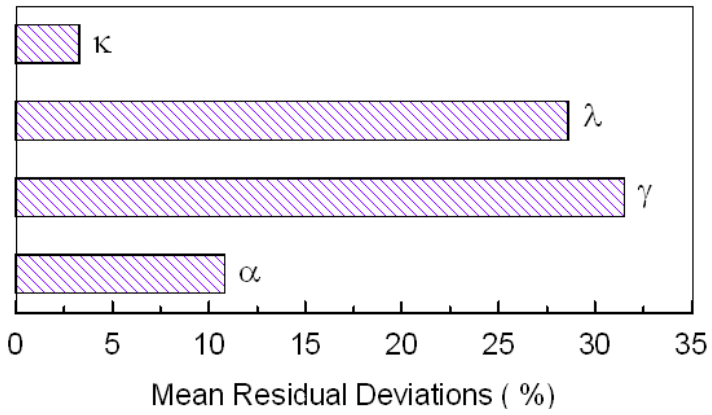

Figure 9.3: The plot of sensitivity coefficients indicating the sensitivity of individual parameters to the fit quality of the RTD curve.

9.3 Model fitting and parameter estimation

9.3.1 Model fitting to RTD data

Figures 9.4a-c show the comparison between predicted and experimental RTD curves over the range of conditions investigated, using the improved mixing cell model discussed in section 9.2. It can be seen that the RTD data was well fitted by the model. By inspecting the spread of the RTD curves, one can quickly notice that the shape of the curves remains essentially similar which may be interpreted to mean that the mill exhibited a similar state of mixing at all test conditions. The optimum values of the model parameters estimated from the fits are summarized in Table 9.1. Notice that at 65.1 and 67.3% solids the model predicts the existence of short-circuit flows. However, in relation to the total internal flow, the predicted short-circuit flows (< 1.5% of feed flow) are too small to have any visible effect on the RTD curves; on that account it can be silenced in the model which leaves only two parameters to be estimated. At higher solids concentration in slurry (>72% wt), the model predicts non-existence of short-circuit implying that every bit of feed slurry circulates through the ball charge before exiting the mill.

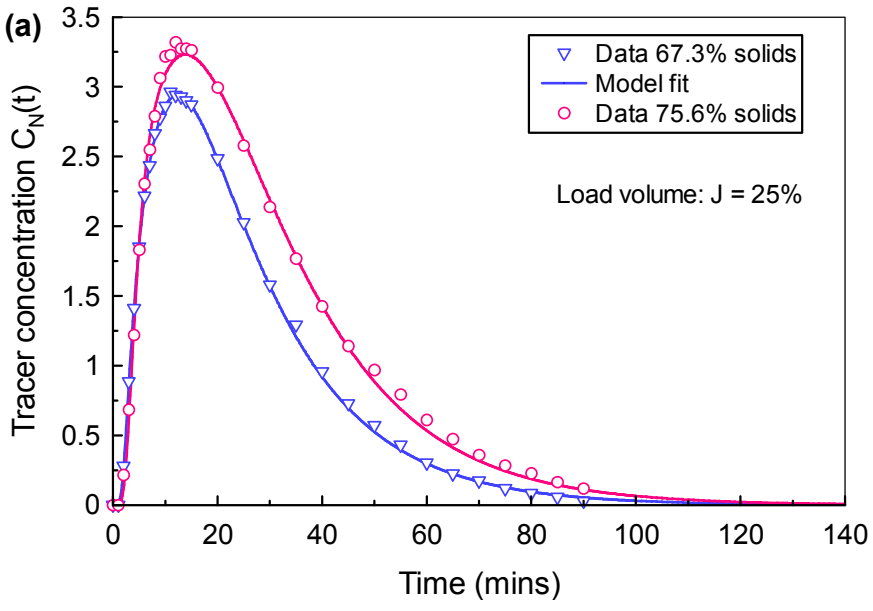

Figure 9.4 (a): Comparison of experimental and predicted RTD curves for ball load volume of J = 25%.

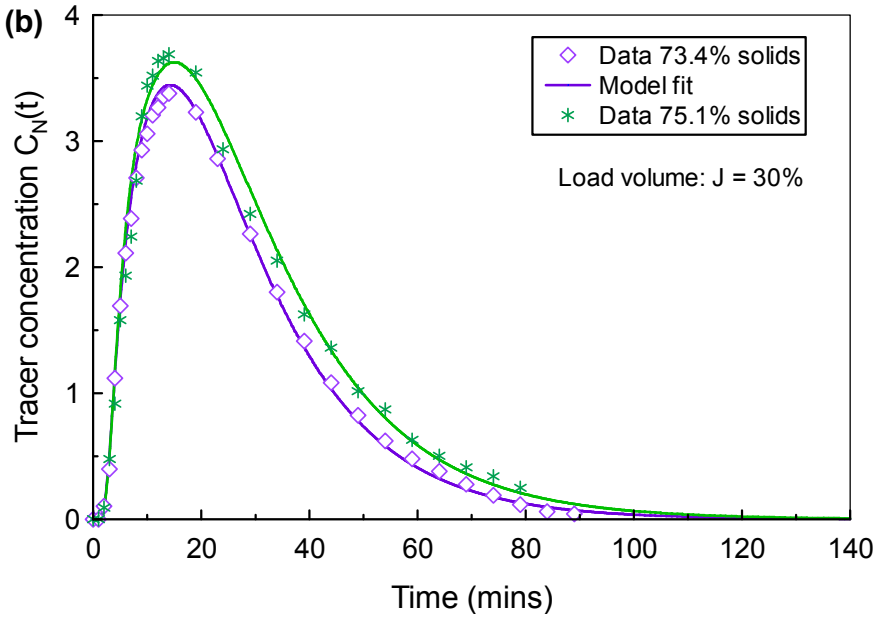

Figure 9.4 (b): Comparison of experimental and predicted RTD curves for ball load volume of J = 30%.

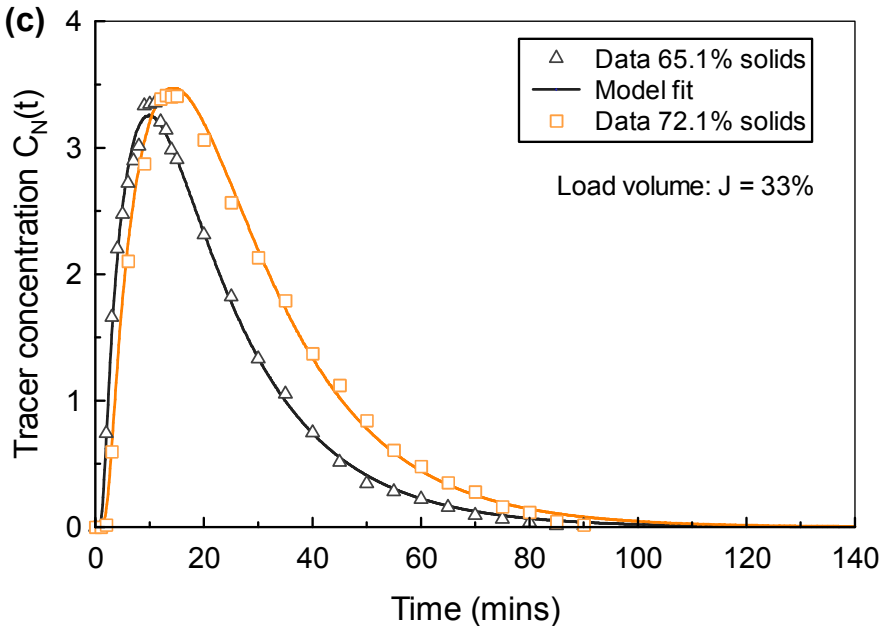

Figure 9.4 (c): Comparison of experimental and predicted RTD curves for ball load volume of J = 33%.

Table 9.1: Mill operational conditions and estimated parameters in the improved mixing-cell model.

Load volume (%)	Wt. (vol.) % Solids	(λ)	(α) min^{-1}	(γ) min^{-1}	(κ)	SSE
Pre-determined variables			Estimated model parameters			
25	67.3 (37.7)	0.4209	1.5810	0.1888	0.0122	0.0119
25	75.6 (47.7)	0.4679	0.9520	0.156	0	0.0124
30	73.4 (44.8)	0.4429	0.9865	0.1441	0	0.0289
30	75.1 (47.0)	0.4766	0.8483	0.1252	0	0.0103
33	65.1 (35.4)	0.4041	2.3381	0.2432	0.0146	0.0149
33	72.1 (43.2)	0.4524	1.1124	0.1647	0	0.0122

9.3.2 Slurry radial exchange and back-mixing

Figure 9.5 shows the effect of load volume and slurry concentration on slurry exchange rate coefficients. From the trends in the data, it can be deduced that high slurry concentration tends to suppress slurry efflux from the ball charge. Equally, as slurry concentration is increased, the disparity in the rate of slurry efflux and influx in the ball charge (indicated by parameters $\delta_{L\text{-}P}$ and $\delta_{P\text{-}L}$) becomes less distinctive This trend can be interpreted that the slurry holdup volume is getting to a more or less equal partitioning between the pool and ball charge regions. At steady state the volumetric slurry flow per unit time into and out of the pool should be constant and equal which satisfies the law of conservation of mass. Hence if $\lambda < 0.5$, it implies that $\delta_{L\text{-}P} > \delta_{P\text{-}L}$ and this is supported by the results presented in Figure 9.5. Equally, if $\lambda > 0.5$, it follows that $\delta_{L\text{-}P} < \delta_{P\text{-}L}$. So by monitoring the profile of $\delta_{L\text{-}P}$, it would be possible to detect any instance of slurry build-up inside the mill, an event that may result in load expansion and the mill will then “go off the grind”. The effect of load volume could not be clearly deduced here owing to the nature of the experimental design. It should be recognized that industrial experiments are generally expensive and labour intensive.

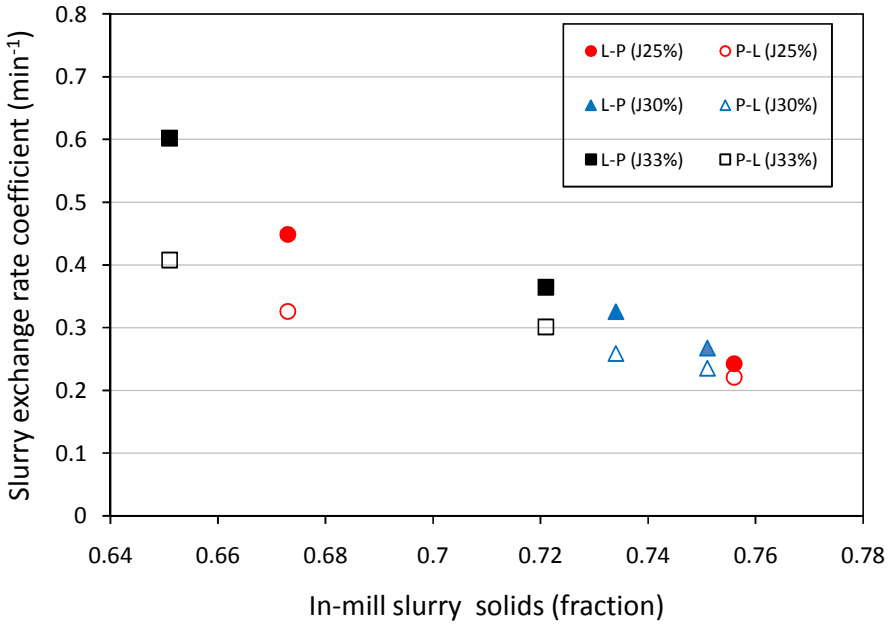

Figure 9.5: Effect of load volume and slurry concentration on exchange coefficients

Figure 9.6 shows the effect of load volume and slurry concentration on the extent of back-mixing. The dependence of back-mixing coefficient on slurry concentration and load volume is clearly evident. By inspection of the results, it appears that at the same load volume, the back-mixing increases as the slurry concentration decreases which suggests that less dense slurry inside the mill would tend to promote axial mixing. Indeed the slurry with lower solids concentration exhibits higher mobility and enhanced ability to circulate (Makokha and Moys, 2009). From Figure 9.6, all the values of back-mixing coefficient (β) lie between 0.68 and 0.82, which points towards a well mixed state attainable at $\beta = 1$. This result is consistent with the observation by Napier-Munn *et al,* (1996) who reckoned that for large diameter mills, the load tends towards perfect mixing. Earlier on, Kelly and Spottiswood (1982) were emphatic that ball mills show the behaviour between perfect mixing and plug flow.

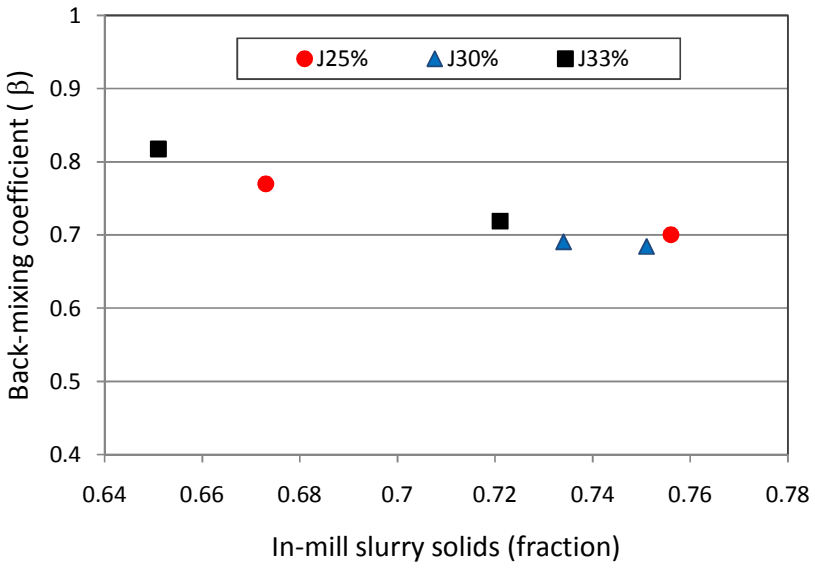

Figure 9.6: Effect of load volume and slurry concentration on the axial back-mixing coefficient

Generally, it is preferred to operate secondary ball mills (finish grinding) towards plug flow mode to achieve a narrow size distribution of mill product for better flotation recovery as opposed to a wide product size distribution that is characteristic of a well mixed mill. But it is noteworthy to mention that operating the mill towards plug flow mode would result in variations of mill properties in the flow direction which may pose control challenges. Hence a compromise would be to run the mill between the two limiting cases of plug flow and prefect mixing.

9.4 Correlations

9.4.1 Slurry radial exchange rate coefficient

Based on the trends observed in the data presented in Figure 9.5, the slurry radial exchange rate coefficient was correlated with load volume and slurry solids concentration by equation 19.9a. The standardized version of this equation is also presented (equation 19.9b). Standardization was achieved by unit variance scaling in order to give equal weight to each data value.

$$\delta_{L\text{-}P} = -0.8236 + 0.6883J + 0.4197/x_v \quad [9.19a]$$

$$\hat{\delta}_{L\text{-}P} = -6.1897 + 0.1870\hat{J} + 62.731/\hat{x}_v \quad [9.19b]$$

The variable J is the load volume (fraction) and x_v is the slurry solids concentration (volume fraction). The values of the empirical coefficients were determined from regression analysis implemented in Excel 2007. The positive coefficients of J and x_v imply that the in-mill slurry volumetric exchange would increase as J is increased but decrease with increase in x_v. The magnitude of the standardized coefficient of x_v is notably higher than that of J, which suggests that slurry concentration has a relatively stronger effect on slurry exchange rate than load volume.

Figure 9.7 presents a comparison of the empirical estimations of the slurry exchange coefficient ($\delta_{L\text{-}P}$) and the improved mixing cell model predictions illustrating the goodness of fit. The fit has a mean relative error of 3.13%. Figure 9.8 is a surface plot showing the variation of $\delta_{L\text{-}P}$ with slurry concentration and load volume.

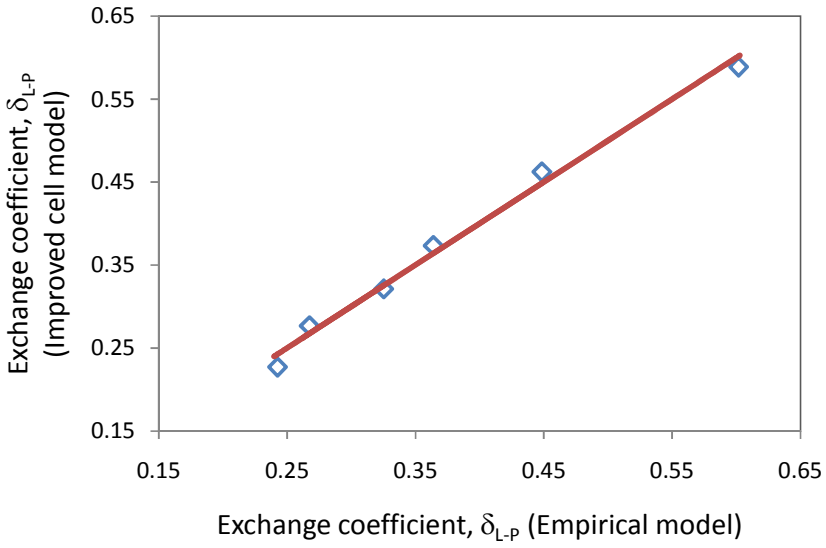

Figure 9.7: Empirical model values vs. improved mixing-cell model values of slurry exchange coefficient

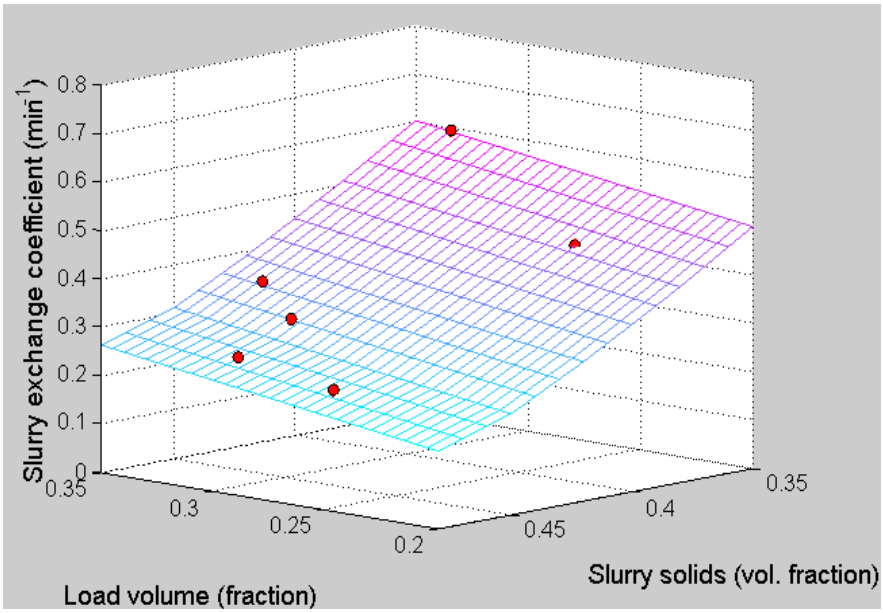

Figure 9.8: Surface plot of the variation of slurry exchange coefficient with load volume and slurry concentration.

9.4.2 Axial back-mixing coefficient

An attempt was made to correlate axial back-mixing coefficient with slurry concentration and load volume and the relation given by equation 9.20a was achieved. Equation 9.20b is the standardized version of equation 9.20a.

$$\beta = 0.3039 + 0.0042/J + 0.1735/x_v \qquad [9.20a]$$

$$\hat{\beta} = 5.7735 + 2.1189/\hat{J} + 65.538/\hat{x}_v \qquad [9.20b]$$

The values of empirical coefficients were obtained in a similar way to equations 9.19 using regression techniques implemented in Excel 2007. Equations 9.20 suggest that back-mixing decreases with increase in load volume which conforms to the findings by Sherritt *et al*, (2003). A marked difference in the magnitudes of the standardized coefficients of J and x_v is clearly evident which depicts the relative influence of load volume and slurry concentration on back-mixing process.

In order to assess the accuracy of the empirical equation for back-mixing coefficient, a plot of improved cell model values versus empirical values is shown in Figure 9.9. The fit has a mean relative error of 1.26%. The variation of back-mixing coefficient with slurry concentration and load volume is presented by a surface plot, Figure 9.10.

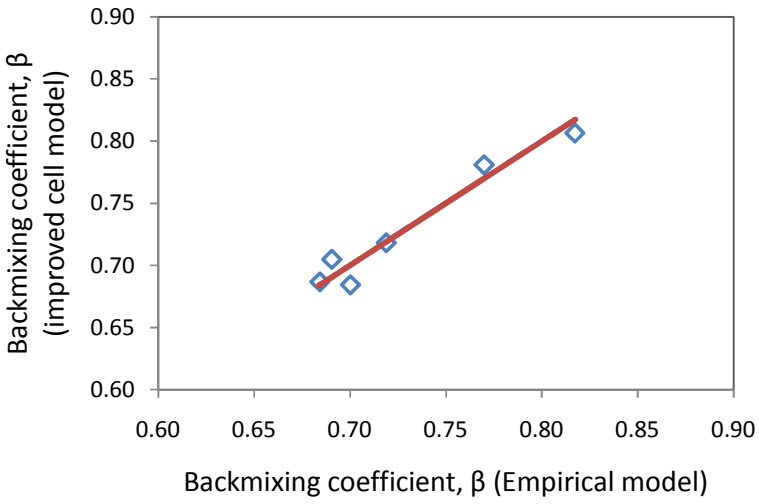

Figure 9.9: Empirical values vs. model values of back-mixing coefficient

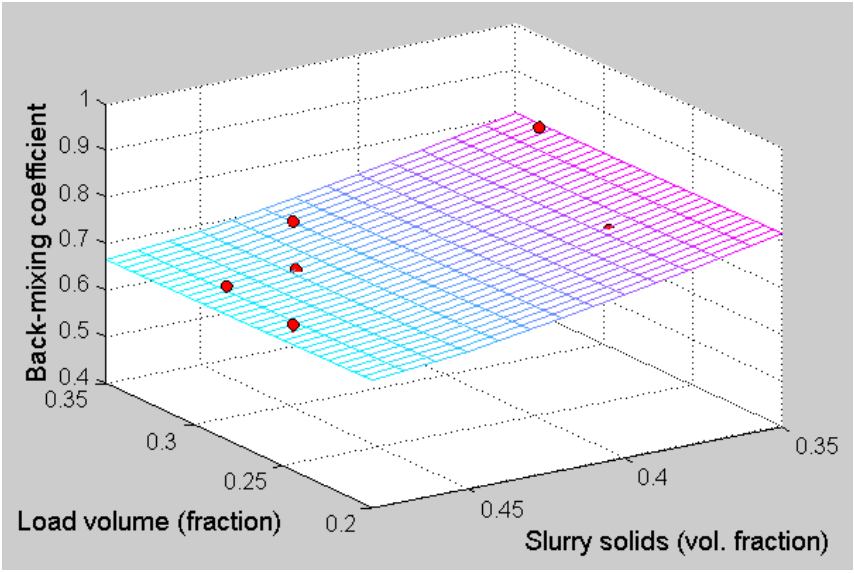

Figure 9.10: Surface plot of the variation of back-mixing coefficient with load volume and slurry concentration.

9.4.3 Axial dispersion coefficient

Axial dispersion coefficient is a parameter that is generally used to describe the axial mixing process. In axial mixing, particles or fluid elements are considered to flow in a direction perpendicular to the plane of circulation. The motion of particles/fluid elements is defined by the 1-dimensional diffusion equation (Levenspiel, 1972) as,

$$\frac{\partial C}{\partial t} = D_x \frac{\partial^2 C}{\partial x^2} - u_x \frac{\partial C}{\partial x} \qquad [9.21]$$

in which D_x is the axial dispersion coefficient, C is the concentration while $x = 0$ at inlet and $x = L$ at exit of the reactor. The key assumption of this model is that the concentration of particles/fluid elements is uniform in each cross section of the reactor i.e. is only a function of time and axial position.

Dean (1963) and Levich *et al*, (1967) have shown that for a cell model with a large number of cells and for sufficiently long porous medium described by the dispersion equation, the tracer response at the exit as a function of time would yield the same qualitative results. Other authors (Zhang *et al*, 2005; Steiner, *et al*, 1988) have pointed out the equivalence of the axial dispersion model with the mixing cells model under limiting cases in multistage columns. Work presented by Cho and Austin (2002) on ball mills also indicates qualitative equivalence between various RTD models. In view of these consistent observations, a correlation must exist between the parameters in the axial dispersion model and the cell model. An attempt has been made in this study to correlate the axial dispersion coefficient, D_x with the back-mixing coefficient with a view to providing an alternative equation for estimation of D_x in steady flow systems.

Considering a tracing element flowing through a mixing cell at mean velocity u, after pulse injection of unit quantity at $t = 0$; If the tracer migration in the axial direction approximates diffusion in an infinite 1-dimensional medium, then the distribution of the tracer displacement in the axial direction is related to the axial dispersion

coefficient in the form of equation 9.21. Several approximate solutions to equation 9.21 under different boundary conditions are found in literature. The analytical solution for open-open boundaries was published by Levenspiel (1972) which is reproduced here in dimensional form as equation 9.22 while the solution for closed-closed boundaries is presented in the work by Xu *et al* (1991), which is stated here as equation 9.23 in non-dimensional form. The two solutions were evaluated by Xu and Finch (1991) in flotation column studies and it was found that for vessel dispersion number, N_d less than 0.25 and interstitial flow below 1 cm/s, both solutions were adequate.

$$C(x,T) = \frac{1}{\sqrt{(4\pi D_x T)}} \exp\left(-\frac{\left(L-u\overline{T}\right)^2}{4D_x T}\right) \qquad [9.22]$$

$$E(\theta) = 4N_d \exp\left(\frac{1}{2N_d}\right)\sum_{n=1}^{\infty}\frac{2(-1)^{n+1}\lambda_n^2 N_d}{4\lambda_n^2 N_d^2 + 4N_d + 1}\exp\left(-\frac{\left(1+4\lambda_n^2 N_d^2\right)}{4N_d}\right) \qquad [9.23]$$

In which $u = L/T$ is the mean velocity of the fluid particles (m/s), L is the length of the medium (m), $T = N\tau$ is the residence time of a random fluid particle at the exit of mixer N and the parameter D_x represents the axial dispersion coefficient (m^2/s).

For a rotary system consisting of a flowing and a stagnant zone characterized by continuous radial exchange of material between the two zones as found in overflow ball mills, the effect of lateral convection process on the axial dispersion cannot be ignored. In this case, the residence time of a random particle in mixing cell i (where i = 1 to N) would be dependent on the volume of the stagnant zone as well as the exchange rate between the flowing and stagnant zone. From the central limit theorem of probability statistics (Peebles, 2001) , if the time taken by a random particle to exit N cells is T, and where N is sufficiently large, then dispersion of T follows a normal distribution given by,

$$C(N,T) = \frac{1}{\sqrt{(2\pi N\sigma_\tau^2)}} \exp\left(-\frac{\left(T-N\overline{\tau}\right)^2}{2N\sigma_\tau^2}\right) \qquad [9.24]$$

Where σ_τ^2 is the variance of the residence time τ about its mean value; T is the time taken by an arbitrary fluid element to reach the exit of mixer N and $\bar{\tau}$ is the mean residence time of the fluid elements in a single mixing cell. One can clearly notice the qualitative coincidence of equations 9.22 and 9.24. By relating the corresponding model parameters in the numerators of the exponential terms of the two equations, an expression for dispersion coefficient, D_x is obtained as,

$$\sigma_\tau^2 = \frac{2}{N}\left(\frac{L}{u^3}\right)D_x \qquad [9.25]$$

Also σ_τ^2 can be defined by the following equation derived from moment analysis, with details given in the paper by Levich *et al* (op cit).

$$\sigma_\tau^2 = \bar{\tau}^2 + \frac{2(1-\lambda)^2\alpha}{\gamma} \qquad [9.26]$$

By equating equations 9.25 and 9.26 then substituting for α with equation 9.16 (assuming no bypass flows) and rearranging the terms yields a correlation equation for the effective axial dispersion coefficient, D_x which is hereafter denoted as D_e.

$$D_e = \frac{L^2}{2N^2\bar{\tau}}\left[1 + \left(\frac{\beta}{1-\beta}\right)\frac{(1-\lambda)^2}{\gamma\bar{\tau}^3}\right] \qquad [9.27]$$

It is easily noticeable that equation 9.27 accounts for the dispersion due to mixing in the flowing zone as well as the dispersion associated with the radial exchange of fluid particles between the flowing and stagnant zones. The equation alludes to the fact that increased back-mixing would boost the axial mixing process. On the other hand increased slurry load within the ball charge (indicated by λ) would lower the effective axial dispersion coefficient owing to reduced pool volume. Equally a higher rate of cross flow (indicated by γ) would tend to slow down the effective axial dispersion process. Table 9.2 shows the values of the effective axial dispersion coefficient computed from equation 9.27 for six mill conditions tested. Estimated

values of the vessel dispersion number, ( ) are also presented. N_d varies between 0.05 and 0.08, which is comparable to the values found by Van Nierop and Moys (2002) of between 0.03 and 0.34 for a 6m long and 4.3m diameter grate discharge mill; but much lower than those presented by Austin *et al* (1983) of 0.5 and 0.3 for laboratory (0.3m diameter) and pilot (0.91m diameter) ball mills respectively.

Table 9.2: Values of effective axial dispersion coefficient and vessel dispersion number derived from correlation equation, 9.27

Load volume (%)	Slurry % solids	D_e (m^2/s)	N_d	95% confidence interval D_e (m^2/s)
25	67.3	0.0041	0.07	0.0039 – 0.0043
	75.6	0.0030	0.06	0.0028 – 0.0031
30	73.4	0.0033	0.06	0.0032 – 0.0035
	75.1	0.0027	0.05	0.0026 – 0.0029
33	65.1	0.0057	0.08	0.0054 – 0.0060
	72.1	0.0032	0.06	0.0030 – 0.0034

The variation of effective axial dispersion coefficient (D_e) with changes in slurry solids concentration has been graphically shown in Figure 9.11. The relation has been approximated by a linear trend with 87% of the variance explained.

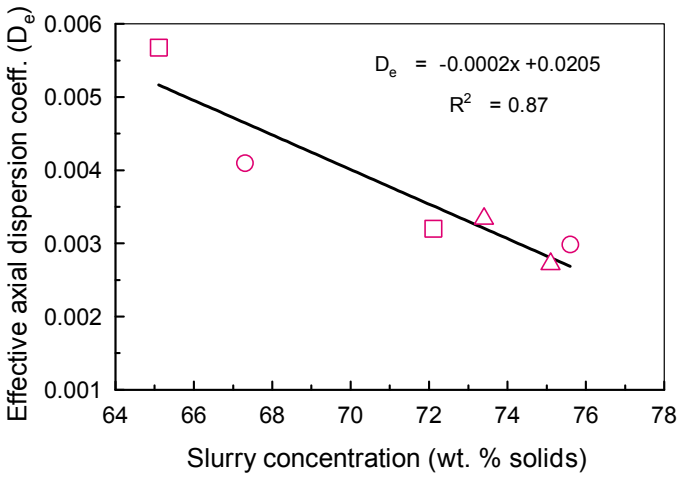

Figure 9.11: Variation of effective axial dispersion coefficient (D_e) with changes in slurry solids concentration at mill speed of 75% of critical (~ 12 rpm).

9.5 Conclusions

From the results obtained, it is undoubted that the slurry transport dynamics in an overflow ball mill can be reliably predicted using the improved cell model. The model has displayed an adequate fit to the experimental data. Using this model, it has been possible to quantitatively assess the effect of two important mill operating variables: load volume and slurry solids concentration, on in-mill slurry transport behaviour. Two flow parameters denoted as β and $\delta_{L\text{-}P}$ which respectively describe the rate of axial back-mixing and radial exchange of slurry between the pool and the ball charge have been evaluated in the model. The parameters correlate well with slurry concentration and load volume, where β displays an inverse relationship with both variables while $\delta_{L\text{-}P}$ varies linearly with load volume but inversely with slurry solids concentration. The standardized correlation coefficients indicate that the parameters β and $\delta_{L\text{-}P}$ are both influenced to a greater extent by slurry concentration than load volume. Also, it was possible to correlate β with the axial dispersion coefficient, yielding an inverse proportionality. Further, the model predicts the possible existence of short-circuit flows at low levels of slurry solids concentration.

All these observations constitute critical information whose accuracy and availability would empower mill operators and process engineers to take correct and timely actions with regard to mill control. Failure to tune the mill appropriately to achieve desirable slurry flow may result in poor milling performance and corresponding high energy expenditure.

CHAPTER10

Conclusions and Recommendations

10.1 Introduction

This thesis is a contribution to the improvement of methods for monitoring, control and optimisation of wet ball mills. The major results and observations arising from the studies undertaken for this thesis are summarised in this chapter. Also presented here are the overall conclusions and the suggestions for future research work.

10.2 Summary of main findings

Researchers and industrialists generally agree that better understanding of mill internal dynamics could be the key to accurate design, effective monitoring and better control of grinding mills, which subsequently lead to optimal mill performance. Apparently, to date not all is well-understood regarding the dynamics of media and slurry inside the mill and particularly in overflow-discharge ball mills.

Substantial progress has been made in this thesis towards generating further information on the effects of ball load volume and slurry concentration on mill internal behaviour and hence the overall performance of the mill. Experimental investigations were performed at both laboratory and industrial levels where invaluable data was successfully collected and analysed. Useful insights were acquired which are fundamental to the enhancement of milling efficiency.

It was possible to measure the load dynamic position inside the mill using media and slurry sensors on both the laboratory mill and the industrial mill. The sensors were mounted through the mill shell to achieve direct contact with the load. The data obtained was analysed both qualitatively and quantitatively firstly to assess any emerging trends in mill load behaviour, associated with changes in mill operating conditions and secondly to characterise these changes in terms of the features extracted from the sensor response data. This could make available new possibilities for effective control of the milling process. Further the mill specific energy consumption (kWh/ton of product) was determined for specific ball loadings and slurry concentration. However, these were determined under batch conditions. For the conditions tested, it was found that the optimum mill specific energy

consumption (kWh/ton of product) correspond to a specific ball loading and slurry solids concentration. For the cases with slurry concentration of 60, 65 and 70 wt. % solids, the respective levels of ball loading that corresponded to the optimum kWh/ton of product were 32, 28 and 26% of total mill volume.

It has been demonstrated that the use of statistical multivariate modelling techniques in combination with direct load sensors is a promising approach for monitoring and characterising changes in mill internal operating conditions. Two multivariate models; (i) PLS (ii) RBF-PLS, have been built and applied to predict the variation of in-mill slurry density and ball load volume based on the characteristic features extracted from the load (media and slurry) sensor data. The models were tested against both the laboratory and the industrial data and in both cases the modelled and measured data compared well albeit the hybrid RBF-PLS model gave marginally better prediction accuracies. This is attributed to the ability of hybrid RBF-PLS model to capture any non-linearity in the relations between the variables. The good prediction performance achieved is indicative of the ability of multivariate modelling as a reliable means for on-line mill monitoring and hence it can be applied effectively in mill control system. Also, it points to the available possibility to utilise the characteristic features contained in load behaviour parameters to predict changes in mill operational conditions for purpose of optimising the mill performance.

Poor knowledge of slurry hydrodynamic transport inside the mill has been recognised for decades as one of the major bottlenecks in trying to improve the efficiency of wet overflow ball mills. Our investigations of slurry transport behaviour using a gamma emission imaging technique revealed the slurry flow path from the pool into the ball charge, its distribution map and mixing rate within the ball charge. It further gave a qualitative description of the slurry exchange rate between the pool and the ball charge. The influence of both viscosity and mill rotational speed on the slurry flow behaviour was clearly noticeable. An attempt was made to quantify the rate of slurry flow from the pool into the ball charge by tracer balance method but the results were inconclusive due to gamma ray intensity attenuation by the steel ball charge, which introduces a significant error in the tracer balance.

RTD studies were performed on an industrial overflow ball mill at different conditions of slurry solids concentration and ball load volume. The RTD data was adequately described by a model described by King (2001), comprising one large and two small mixers in series with dead time. Using this model, it was possible to assess the effect of two important mill operating variables: solids concentration and ball load volume, on slurry residence time distribution. Trends in the model results revealed that mean residence time increases as slurry concentration is increased but decreases with increase in feed flow rate. However, the effect of ball load volume could not be clearly delineated owing to the nature of the experimental design. On the other hand, correlation equations were developed that provided fairly accurate estimates of the mean residence time. Once accurately validated, the equations may offer an alternative means to estimate the mean residence time without having to perform tracer tests provided that information of slurry concentration and ball load volume is known. This would save on time and eliminate the costs associated with the process of tracer tests.

Further, an improved mixing-cell model has been developed and applied to characterise the in-mill slurry hydrodynamic transport based on the measured RTD data. The model is able to account for the effects of non-ideal flow processes such as back-mixing, radial exchange and short-circuit flows which have often been ignored in most existing mill models leading to incorrect prediction of in-mill slurry transport behaviour and subsequently inaccurate mill simulation. The model displayed an adequate fit to the experimental data. The effects of slurry concentration and ball load volume on the model parameters were evaluated yielding important information that is critical to achieving effective control of the milling process.

Finally, using the measured slurry feed rates and residence times the slurry volumetric holdup inside the mill was estimated. The effects of solids concentration on slurry volumetric holdup were assessed and it was observed that for cases of slurry solids concentration above 72 mass %, viscosity effects strongly set in, impacting on the volumetric holdup. A simple model was developed that can predict the slurry holdup volume inside the mill as a function of ball load volume and slurry concentration. The model fitted trends in the experimental data well and hence it

could be linked to the mill control system and utilised for continuous monitoring of the variation of in-mill slurry holdup volume. This would provide operators with further information of mill behaviour leading to better and timely control actions which subsequently enhances mill performance.

In summary, the findings of this thesis are indicative of the benefits possible to the mineral processing plants by having clear and comprehensive information of in-mill dynamic behaviour.

10.3 Overall conclusions

The primary objective of the research work undertaken for this thesis is to utilise both experimental and mathematical techniques to advance information and understanding of the dynamic behaviour of media and slurry inside an overflow-discharge ball mill and explore possibilities to transform this knowledge into a valuable tool that would aid mill operators and process engineers in timely decision making with regard to mill control and performance optimisation. The data collected in this project though quite useful, remains valid only to the mills investigated. However, it is hoped that the project has given some impetus for further research, and where the analysis is inconclusive, provokes further thinking for improvements.

10.4 Suggestions for Future Work

It has been shown that the use of direct load sensors in combination with multivariate models may serve to provide inferential estimates of in-mill slurry density and ball load volume. The next step would be to perform rigorous tests of the method against more historical data acquired on the industrial mill investigated. However, in order to reach better accuracy in model predictions of in-mill slurry density, more information that contains features related to slurry properties should be extracted from the industrial load sensor signals. This may require installation of a conductivity probe on the SENSOMAG system to capture a more realistic conductivity profile of slurry.

Also, while it has been demonstrated clearly that the improved mixing-cell model can be used for modelling slurry hydrodynamic transport in an overflow mill, there is need for gathering more data to justify whether the incorporation of this model in the overall mill breakage model would result in worthwhile improvement in the accuracy of milling simulations. A positive result would enhance the confidence required to extend the model to other mills

APPENDIX A

Calibration Data

A.1 Torque Calibration Data

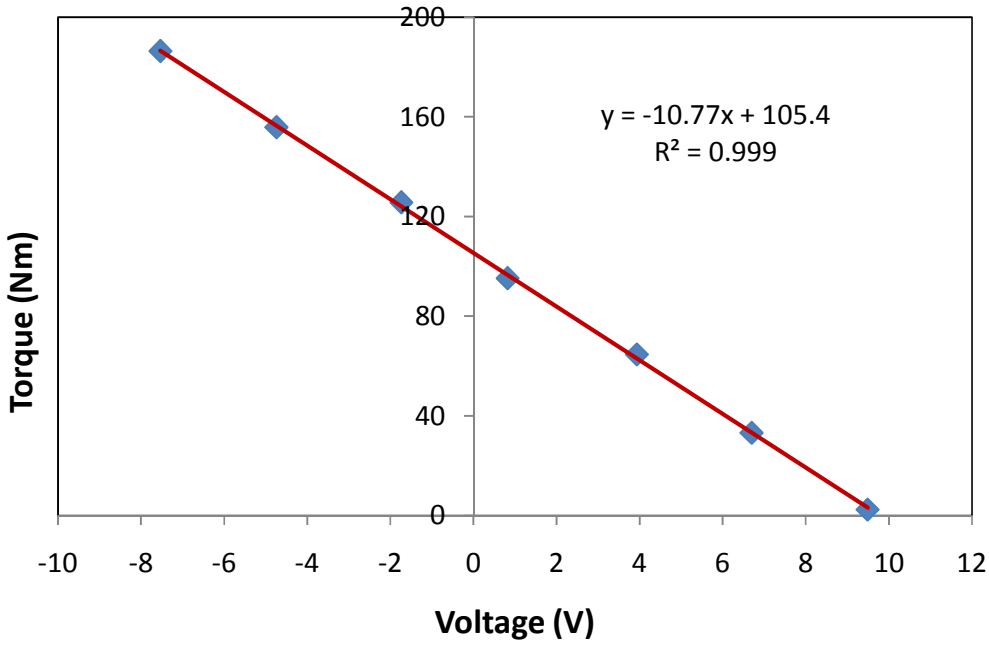

Figure A.1: Torque Calibration chart (N= 40% of critical speed)

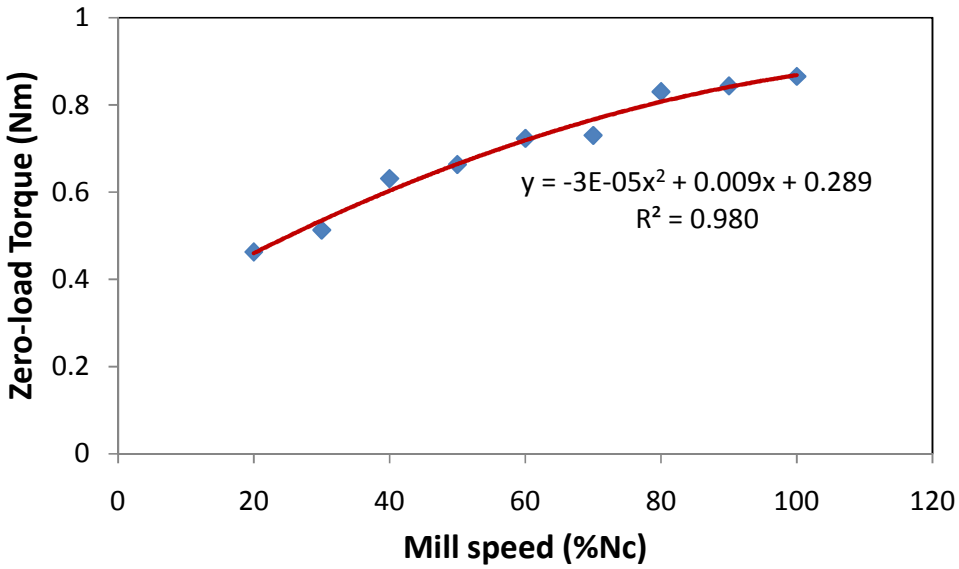

Figure A.2: Torque Calibration chart (Zero-load)

A.2 Speed Calibration Data

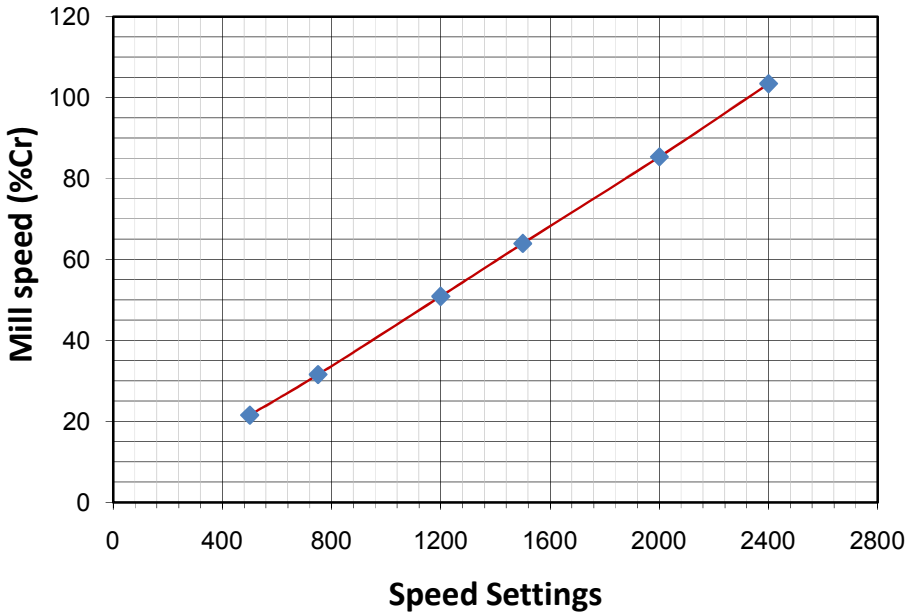

Figure A.3: Speed Calibration chart at, J = 20% (%Critical vs Speed settings)

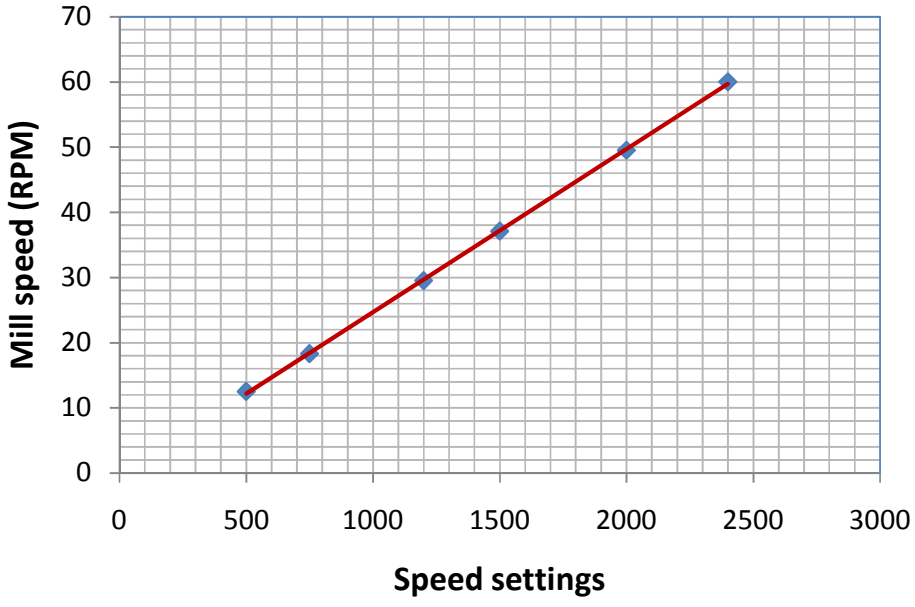

Figure A.4: Speed Calibration chart at, J = 20% (RPM vs Speed settings)

A.3 Salt conductivity –concentration calibration data

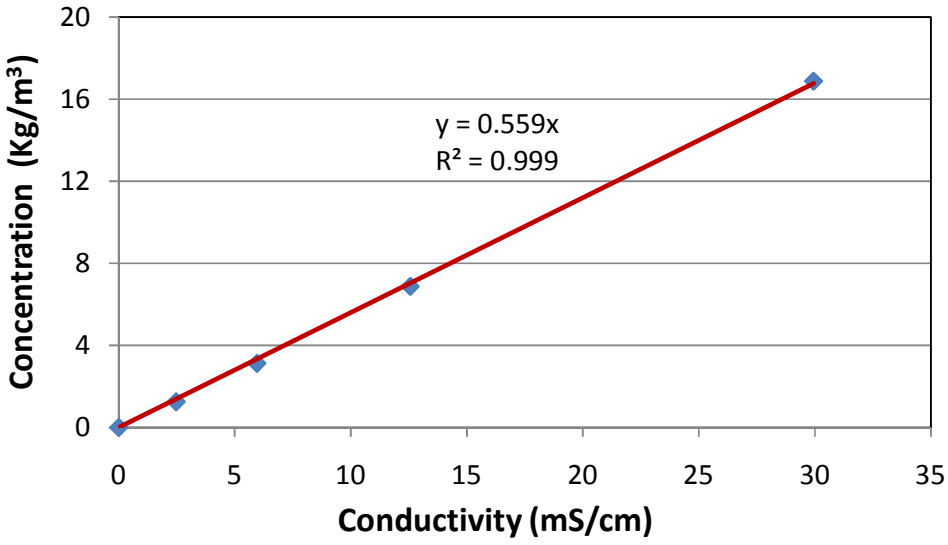

Figure A.5: Conductivity-Concentration calibration (J =25%, 67.3% solids)

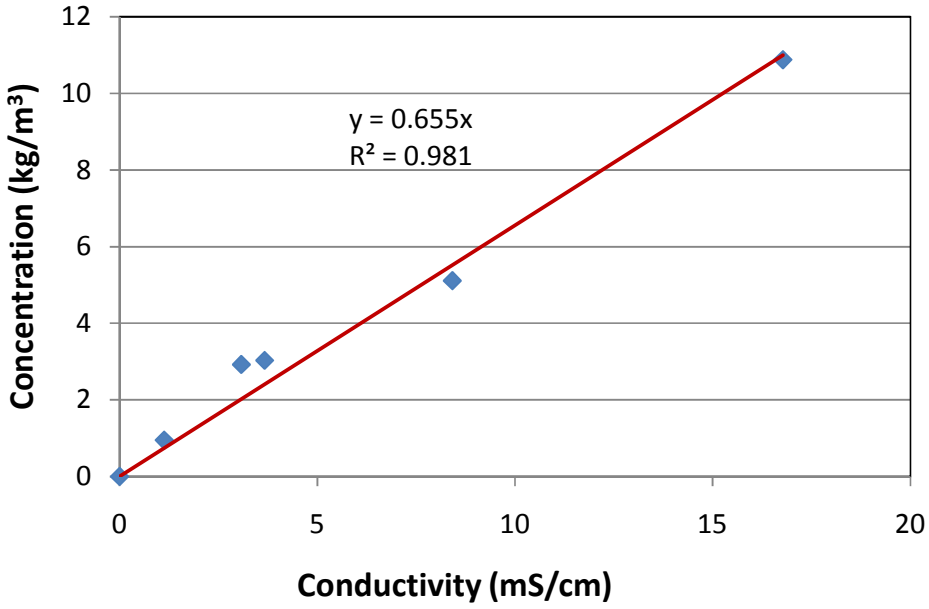

Figure A.6: Conductivity-Concentration calibration (J =30%, 75.1% solids)

APPENDIX B

Laboratory Mill Data

B.1 Experimental mill power draws data

Table B.1 Mill power draws

	J20		J25		J30		J35	
%Solids	Power (W)	stdev	Power (W)	stdev	Power (W)	stdev	Power (W)	stdev
50	479.52	5.13	564.14	0.5	641.72	4.9	702.85	2.02
60	488.69	5.44	577.24	3.8	650.8	3.41	709.59	8.49
65	494.47	3.63	582.22	9.48	655.16	4.05	695.43	7.7
70	482.28	3.48	573.26	5.36	625.48	3.4	650.55	8.32

B.2 Experimental load position data

Table B.2. Media shoulder angle (deg)

	J20		J25		J30		J35	
%Solids	Media shoulder	stdev	Media shoulder	stdev	Media shoulder	stdev	Media shoulder	stdev
50	298.56	5.84	308.75	5.8	316.44	3.44	317.73	2.92
60	307.8	5.4	310.23	2.01	316.93	2.49	318.8	1.30
65	312.29	3.31	313	3.06	319.4	3.18	324.77	6.19
70	313.08	3.82	314.79	3.53	320.5	2.88	329.83	6.18

Table B.3. Media toe angle (deg)

	J20		J25		J30		J35	
%Solids	Media toe	stdev	Media toe	stdev	Media toe	stdev	Medial toe	stdev
50	144.68	4.49	142.5	4.27	140.6	7.83	138.04	3.97
60	145.08	6.12	142.71	4.01	141.5	5.82	140.5	4.55
65	146.18	5.49	142.95	4.73	142.29	5.00	139.59	4.41
70	143.26	5.9	142.00	4.34	141.28	4.59	135.92	4.39

Table B.4. Slurry shoulder angle (deg)

	J20		J25		J30		J35	
%Solids	Slurry shoulder	stdev	Slurry shoulder	stdev	Slurry shoulder	stdev	Slurry shoulder	stdev
50	288.79	8.63	300.11	5.38	303.94	2.28	304.73	3.65
60	292.21	4.91	301.32	2.86	304.4	9.18	305.28	5.92
65	296.53	3.2	303	3.54	305.06	2.79	308.64	8.25
70	296.08	3.21	304.67	3.15	306.64	2.72	310.09	6.92

Table B.5. Slurry toe angle (deg)

	J20		J25		J30		J35	
%Solids	Slurry toe	stdev	Slurry toe	stdev	Slurry toe	stdev	Slurry toe	stdev
50	119.43	4.53	122.5	4.69	125.37	4.02	126.68	2.99
60	121.81	2.86	123.36	4.73	126.11	3.13	128.73	4.58
65	123.8	3.66	123.92	4.34	125.26	4.1	128.12	4.24
70	118.95	5.12	120.93	4.91	124.36	1.99	125.00	1.22

Table B.6. Pool angle (deg)

	J20		J25		J30		J35	
%Solids	Pool angle	stdev	Pool angle	stdev	Pool angle	stdev	Pool angle	stdev
50	31.25	2.4	25.00	2.24	20.23	2.96	16.36	1.74
60	29.27	3.06	23.35	2.19	19.39	2.24	15.77	2.78
65	28.38	2.75	23.03	2.27	18.03	2.28	15.47	2.41
70	24.31	2.94	20.07	2.31	17.92	1.65	12.25	1.40

B.3 Experimental batch milling data

Table B.7. Batch milling data for the case of 50% solids in slurry

50% Solids	Screen Size (µm)	Mass % Retained				Cumulative % passing			
		J20	J25	J30	J35	J20	J25	J30	J35
	850	0.19	0.13	0.10	0.21	99.86	99.89	99.90	99.78
	600	0.70	0.63	0.38	0.72	99.30	99.68	99.62	99.02
	425	1.08	1.01	0.47	0.89	98.22	97.81	99.16	97.48
	300	2.59	2.07	1.03	2.09	95.62	95.08	98.12	94.21
	212	6.93	9.50	3.06	4.61	88.69	85.70	93.15	86.38
	150	18.91	12.07	10.53	12.70	69.77	73.78	77.76	68.12
	106	25.92	29.07	22.62	21.16	43.83	45.08	53.83	43.30
	75	20.70	22.49	25.32	24.19	23.11	22.88	31.05	23.14
	53	10.74	12.97	15.32	13.85	12.36	10.08	17.37	12.49
	38	4.70	4.20	10.15	10.04	7.66	5.94	8.82	6.21
	Pan	7.54	5.87	11.01	9.54				

Table B.8. Batch milling data for the case of 60% solids in slurry

60% Solids	Screen Size (µm)	Mass % Retained				Cumulative % passing			
		J20	J25	J30	J35	J20	J25	J30	J35
	850	0.27	0.23	0.16	0.27	99.89	99.88	99.84	99.72
	600	0.81	0.75	0.57	1.11	99.18	99.08	99.43	98.89
	425	1.15	1.14	0.98	1.30	98.04	97.72	98.45	97.58
	300	2.98	2.33	2.69	2.82	95.05	94.42	95.76	94.74
	212	8.01	7.70	6.62	6.07	87.04	86.45	89.13	88.64
	150	20.30	20.14	16.96	15.15	66.71	66.66	72.14	73.42
	106	25.53	26.25	24.79	23.47	41.14	40.87	47.30	49.82
	75	19.61	20.34	21.66	22.44	21.50	20.88	25.61	27.27
	53	10.48	13.73	10.73	14.32	11.00	7.39	14.86	12.87
	38	5.14	3.30	7.36	5.83	5.85	4.15	7.49	7.01
	Pan	5.73	4.10	7.48	6.97				

Table B.9. Batch milling data for the case of 65% solids in slurry

65% Solids	Screen Size (µm)	Mass % Retained				Cumulative % passing			
		J20	J25	J30	J35	J20	J25	J30	J35
	850	0.45	0.33	0.21	0.40	99.85	99.87	99.78	99.60
	600	0.87	0.83	0.77	1.22	99.13	99.08	99.02	98.78
	425	1.26	1.12	1.34	1.75	97.86	97.76	97.48	97.02
	300	3.35	2.97	3.75	3.97	94.50	94.59	94.21	93.03
	212	9.32	8.41	9.07	9.13	85.15	86.20	86.38	83.86
	150	21.86	20.10	19.85	18.61	63.23	66.17	68.12	65.16
	106	25.36	25.62	24.84	23.41	37.79	40.63	43.30	41.63
	75	18.06	19.69	19.47	18.82	19.67	21.01	23.14	22.72
	53	8.18	12.51	9.82	10.88	11.47	8.54	12.49	11.78
	38	6.93	3.53	5.56	4.47	4.52	5.02	6.21	7.29
	Pan	4.35	4.90	5.32	7.26				

Table B.10. Batch milling data for the case of 70% solids in slurry

70% Solids	Screen Size (µm)	Mass % Retained				Cumulative % passing			
		J20	J25	J30	J35	J20	J25	J30	J35
	850	0.71	0.49	0.37	0.51	99.59	99.49	99.33	99.49
	600	1.12	1.13	0.96	1.45	98.87	98.84	99.03	98.55
	425	1.73	1.54	1.57	2.00	97.14	97.26	97.45	96.55
	300	4.61	3.95	3.94	4.75	92.51	93.22	93.49	91.80
	212	11.48	9.67	9.24	10.34	80.99	83.31	84.21	81.46
	150	23.34	20.86	19.88	20.54	57.58	61.93	64.24	60.92
	106	24.31	23.61	24.07	23.40	33.19	37.73	40.06	37.51
	75	16.42	17.05	18.57	18.00	16.72	20.25	21.41	19.51
	53	7.93	9.47	9.47	9.15	8.76	10.54	11.89	10.36
	38	3.82	2.91	6.50	5.99	4.92	7.56	5.36	4.37
	Pan	4.50	6.88	5.34	4.37				

Table B.11: Size distribution of the feed material used in the laboratory experiments

Size (µm)	Cum. % passing	Size (µm)	Cum. % passing
38	2.62	212	58.75
53	4.77	300	76.76
75	9.33	425	91.42
106	19.57	600	97.11
150	37.09	850	99.89

APPENDIX C

Industrial Mill Data

C.1 Tracer response data

Table C.1. Summary of tracer response data for J = 25% and 67.3% solids

Time (t) (Mins)	Abs. Conductivity (mS/cm)	C(abs) - C(base) (mS/cm)	Concentration (kg/m^3)	E(t)	t E(t)
0	6.96	0	0	0	0
1	6.96	0	0	0	0
2	7.46	0.5	0.27985	0.0030248	0.0060495
3	8.54	1.58	0.884326	0.0095582	0.0286746
4	9.48	2.52	1.410444	0.0152447	0.060979
5	10.27	3.31	1.852607	0.0200239	0.1001193
6	10.92	3.96	2.216412	0.023956	0.1437362
7	11.31	4.35	2.434695	0.0263153	0.1842074
8	11.72	4.76	2.664172	0.0287956	0.2303651
9	11.92	4.96	2.776112	0.0300055	0.2700498
10	12.07	5.11	2.860067	0.030913	0.3091296
11	12.25	5.29	2.960813	0.0320019	0.3520206
12	12.21	5.25	2.938425	0.0317599	0.3811187
13	12.19	5.23	2.927231	0.0316389	0.4113057
14	12.14	5.18	2.899246	0.0313364	0.4387099
15	12.09	5.13	2.871261	0.0310339	0.4655092
20	11.4	4.44	2.485068	0.0268598	0.5371958
25	10.58	3.62	2.026114	0.0218992	0.54748
30	9.78	2.82	1.578354	0.0170596	0.5117879
35	9.27	2.31	1.292907	0.0139744	0.4891023
40	8.67	1.71	0.957087	0.0103446	0.413786
45	8.26	1.3	0.72761	0.0078644	0.3538959
50	7.98	1.02	0.570894	0.0061705	0.3085246
55	7.73	0.77	0.430969	0.0046581	0.2561964
60	7.5	0.54	0.302238	0.0032667	0.1960039
65	7.36	0.4	0.22388	0.0024198	0.1572871
70	7.27	0.31	0.173507	0.0018753	0.1312742
75	7.17	0.21	0.117537	0.0012704	0.0952797
80	7.11	0.15	0.083955	0.0009074	0.072594
85	7.06	0.1	0.05597	0.000605	0.0514208
90	7.01	0.05	0.027985	0.0003025	0.0272228

Table C.2. Summary of tracer response data for J = 25% and 75.6% solids

Time (t) (Mins)	Abs. Conductivity (mS/cm)	C(abs) - C(base) (mS/cm)	Concentration (kg/m^3)	E(t)	t E(t)
0	7.34	0	0	0	0
1	7.34	0	0	0	0
2	7.72	0.38	0.216752	0.001801	0.0036029
3	8.54	1.2	0.68448	0.005689	0.0170665
4	9.48	2.14	1.220656	0.010145	0.0405803
5	10.55	3.21	1.830984	0.015218	0.0760881
6	11.38	4.04	2.304416	0.019152	0.1149144
7	11.81	4.47	2.549688	0.021191	0.1483362
8	12.23	4.89	2.789256	0.023182	0.1854559
9	12.71	5.37	3.063048	0.025458	0.2291176
10	12.98	5.64	3.217056	0.026738	0.267375
11	13	5.66	3.228464	0.026832	0.2951555
12	13.16	5.82	3.319728	0.027591	0.3310899
13	13.08	5.74	3.274096	0.027212	0.3537504
14	13.08	5.74	3.274096	0.027212	0.380962
15	13.06	5.72	3.262688	0.027117	0.4067513
20	12.59	5.25	2.9946	0.024889	0.4977726
25	11.86	4.52	2.578208	0.021428	0.5356981
30	11.09	3.75	2.139	0.017778	0.5333278
35	10.44	3.1	1.76824	0.014696	0.514365
40	9.84	2.5	1.426	0.011852	0.4740691
45	9.34	2	1.1408	0.009481	0.4266622
50	9.04	1.7	0.96968	0.008059	0.4029588
55	8.73	1.39	0.792856	0.00659	0.3624259
60	8.41	1.07	0.610328	0.005073	0.3043524
65	8.17	0.83	0.473432	0.003935	0.2557603
70	7.97	0.63	0.359352	0.002987	0.2090645
75	7.84	0.5	0.2852	0.00237	0.1777759
80	7.74	0.4	0.22816	0.001896	0.1517021
85	7.63	0.29	0.165416	0.001375	0.116858
90	7.55	0.21	0.119784	0.000996	0.0895991

Table C.3. Summary of tracer response data for J = 30% and 73.4% solids

Time (t) (Mins)	Abs. Conductivity (mS/cm)	C(abs) - C(base) (mS/cm)	Concentration (kg/m^3)	E(t)	t E(t)
0	6.33	0	0	0	0
1	6.33	0	0	0	0
2	6.5	0.17	0.10455	0.000916	0.001833
3	6.98	0.65	0.39975	0.003504	0.010512
4	8.15	1.82	1.1193	0.009812	0.039246
5	9.08	2.75	1.69125	0.014825	0.074126
6	9.76	3.43	2.10945	0.018491	0.110946
7	10.21	3.88	2.3862	0.020917	0.146418
8	10.73	4.4	2.706	0.02372	0.189762
9	11.09	4.76	2.9274	0.025661	0.230948
10	11.3	4.97	3.05655	0.026793	0.26793
11	11.54	5.21	3.20415	0.028087	0.308956
12	11.64	5.31	3.26565	0.028626	0.343512
13	11.78	5.45	3.35175	0.029381	0.381949
14	11.82	5.49	3.37635	0.029596	0.414349
19	11.58	5.25	3.22875	0.028303	0.537748
23	10.98	4.65	2.85975	0.025068	0.576563
29	10.01	3.68	2.2632	0.019839	0.575323
34	9.26	2.93	1.80195	0.015795	0.537047
39	8.63	2.3	1.4145	0.012399	0.483569
44	8.09	1.76	1.0824	0.009488	0.417475
49	7.67	1.34	0.8241	0.007224	0.35397
54	7.34	1.01	0.62115	0.005445	0.294023
59	7.11	0.78	0.4797	0.004205	0.248092
64	6.95	0.62	0.3813	0.003342	0.213913
69	6.78	0.45	0.27675	0.002426	0.167389
74	6.64	0.31	0.19065	0.001671	0.123668
79	6.52	0.19	0.11685	0.001024	0.080918
84	6.43	0.1	0.0615	0.000539	0.045284
89	6.4	0.07	0.04305	0.000377	0.033586

Table C.4. Summary of tracer response data for J = 30% and 75.1% solids

Time (t) (Mins)	Abs. Conductivity (mS/cm)	C(abs) - C(base) (mS/cm)	Concentration (kg/m^3)	E(t)	t E(t)
0	6.42	0	0	0	0
1	6.42	0	0	0	0
2	6.56	0.14	0.0917	0.0006864	0.0013728
3	7.15	0.73	0.47815	0.003579	0.0107369
4	7.82	1.4	0.917	0.0068638	0.0274551
5	8.83	2.41	1.57855	0.0118155	0.0590775
6	9.37	2.95	1.93225	0.0144629	0.0867777
7	9.84	3.42	2.2401	0.0167672	0.1173705
8	10.52	4.1	2.6855	0.020101	0.1608084
9	11.3	4.88	3.1964	0.0239251	0.2153263
10	11.67	5.25	3.43875	0.0257391	0.2573915
11	11.79	5.37	3.51735	0.0263275	0.2896022
12	11.97	5.55	3.63525	0.02721	0.3265195
13	12	5.58	3.6549	0.027357	0.3556415
14	12.05	5.63	3.68765	0.0276022	0.3864304
19	11.83	5.41	3.54355	0.0265236	0.503948
24	10.9	4.48	2.9344	0.0219641	0.5271377
29	10.12	3.7	2.4235	0.01814	0.5260591
34	9.55	3.13	2.05015	0.0153454	0.5217448
39	8.9	2.48	1.6244	0.0121587	0.4741886
44	8.5	2.08	1.3624	0.0101976	0.4486946
49	7.97	1.55	1.01525	0.0075992	0.3723597
54	7.75	1.33	0.87115	0.0065206	0.3521115
59	7.38	0.96	0.6288	0.0047066	0.2776886
64	7.19	0.77	0.50435	0.0037751	0.2416048
69	7.05	0.63	0.41265	0.0030887	0.2131201
74	6.94	0.52	0.3406	0.0025494	0.1886557
79	6.8	0.38	0.2489	0.001863	0.1471789

Table C.5. Summary of tracer response data for J = 33% and 65.1% solids

Time (t) (Mins)	Abs. Conductivity (mS/cm)	C(abs) - C(base) (mS/cm)	Concentration (kg/m^3)	E(t)	t E(t)
0	5.34	0	0	0	0
1	5.34	0	0	0	0
2	6.61	1.27	0.74168	0.008229	0.01645801
3	8.18	2.84	1.65856	0.0184019	0.05520559
4	9.11	3.77	2.20168	0.0244278	0.09771131
5	9.58	4.24	2.47616	0.0274732	0.13736603
6	10	4.66	2.72144	0.0301946	0.18116765
7	10.3	4.96	2.89664	0.0321385	0.22496927
8	10.5	5.16	3.01344	0.0334344	0.26747498
9	11.05	5.71	3.33464	0.0369981	0.33298302
10	11.07	5.73	3.34632	0.0371277	0.37127704
11	11.09	5.75	3.358	0.0372573	0.40983025
12	10.83	5.49	3.20616	0.0355726	0.42687141
13	10.72	5.38	3.14192	0.0348599	0.4531783
14	10.45	5.11	2.98424	0.0331104	0.46354555
15	10.32	4.98	2.90832	0.0322681	0.48402086
20	9.3	3.96	2.31264	0.0256589	0.51317874
25	8.46	3.12	1.82208	0.0202161	0.50540331
30	7.62	2.28	1.33152	0.0147733	0.44319982
35	7.14	1.8	1.0512	0.0116632	0.40821036
40	6.62	1.28	0.74752	0.0082938	0.33175191
45	6.22	0.88	0.51392	0.005702	0.25658937
50	5.93	0.59	0.34456	0.0038229	0.19114612
55	5.82	0.48	0.28032	0.0031102	0.17105958
60	5.72	0.38	0.22192	0.0024622	0.14773327
65	5.61	0.27	0.15768	0.0017495	0.11371574
70	5.5	0.16	0.09344	0.0010367	0.07257073
75	5.45	0.11	0.06424	0.0007127	0.05345612
80	5.4	0.06	0.03504	0.0003888	0.03110174
85	5.36	0.02	0.01168	0.0001296	0.0110152
90	5.36	0.02	0.01168		

Table C.6. Summary of tracer response data for J = 33% and 72.1% solids

Time (t) (Mins)	Abs. Conductivity (mS/cm)	C(abs) - C(base) (mS/cm)	Concentration (kg/m^3)	E(t)	t E(t)
0	5.98	0	0	0	0
1	5.98	0	0	0	0
2	6.01	0.03	0.01674	0.0001462	0.0002924
3	7.05	1.07	0.59706	0.0052145	0.0156435
4					
5					
6					
7					
8					
9					
10					
11					
12	12.05	6.07	3.38706	0.0295813	0.3549757
13	12.1	6.12	3.41496	0.029825	0.3877247
14	12.08	6.1	3.4038	0.0297275	0.4161852
15	12.09	6.11	3.40938	0.0297762	0.4466437
20	11.47	5.49	3.06342	0.0267548	0.5350952
25	10.58	4.6	2.5668	0.0224175	0.5604367
30	9.8	3.82	2.13156	0.0186162	0.5584873
35	9.19	3.21	1.79118	0.0156435	0.5475223
40	8.44	2.46	1.37268	0.0119885	0.4795389
45	7.99	2.01	1.12158	0.0097955	0.4407956
50	7.49	1.51	0.84258	0.0073588	0.3679389
55	7.07	1.09	0.60822	0.005312	0.2921581
60	6.84	0.86	0.47988	0.0041911	0.2514655
65	6.61	0.63	0.35154	0.0030702	0.1995642
70	6.48	0.5	0.279	0.0024367	0.1705677
75	6.27	0.29	0.16182	0.0014133	0.1059956
80	6.19	0.21	0.11718	0.0010234	0.0818725
85	6.06	0.08	0.04464	0.0003899	0.0331389
90	6.01	0.03	0.01674	0.0001462	0.0131581

C.2 SENSOMAG data

Table C.7. Summary of SENSOMAG data for load position measurements

%Solids	Ball load	Slurry toe	Stdev	Slurry shoulder	Stdev	Ball toe	Stdev	Ball shoulder	Stdev
75.1%	29.85	97.01	0.312	307.11	0.599	126.23	0.346	301.61	0.253
73.4%	30.23	97.15	0.255	308.00	0.647	127.69	0.438	301.40	0.270
65.0%	30.16	97.15	0.296	308.95	0.498	128.85	0.335	301.53	0.243
63.5%	30.16	96.84	0.221	309.96	0.533	129.83	0.316	302.16	0.317
75.6%	24.50	97.98	0.285	301.81	0.593	131.21	0.331	294.94	0.276
71.4%	24.65	97.84	0.316	302.77	0.530	132.66	0.329	295.51	0.287
74.5%	24.64	98.07	0.237	301.90	0.614	131.12	0.361	295.42	0.326
67.3%	24.86	97.42	0.366	303.73	0.610	133.33	0.325	296.00	0.266
67.7%	32.90	97.81	0.285	310.48	0.704	126.51	0.331	306.05	0.367
65.1%	32.77	97.43	0.332	310.83	1.005	127.02	0.228	305.82	0.265
72.1%	32.88	97.76	0.336	308.82	1.148	125.22	0.233	305.41	0.322
75.6%	32.87	85.23	0.266	294.21	1.451	110.91	0.259	292.39	0.293

Table C.8. Summary of mill load, power draws and slurry feed rate measurements

%Solids	Ball load	Mill power	Stdev	Mill load	Stdev	Feed rate (tph)	Stdev	RSD
75.1%	29.85	8538.19	22.182	807.85	3.984	451.05	0.997	0.002
73.4%	30.23	9013.19	35.986	779.00	40.703	443.40	19.988	0.045
65.0%	30.16	9157.26	3.213	779.78	10.378	449.03	15.794	0.035
63.5%	30.16	9323.43	15.905	771.79	6.529	464.46	19.792	0.043
75.6%	24.50	7481.89	1.024	702.32	13.880	441.83	4.270	0.010
71.4%	24.65	7800.27	6.856	712.04	11.475	435.94	8.790	0.020
74.5%	24.64	7496.97	13.556	714.31	18.938	455.95	2.362	0.005
67.3%	24.86	7994.26	34.062	610.10	20.040	408.14	51.044	0.125
67.7%	32.90	9757.93	5.699	696.08	5.308	436.39	4.771	0.011
65.1%	32.77	9793.09	7.003	717.34	7.869	457.62	43.785	0.096
72.1%	32.88	9522.49	0.393	712.76	5.014	409.21	22.383	0.055
75.6%	32.87	9281.35	5.559	704.28	5.754	420.18	13.779	0.033

APPENDIX D

MATLAB Programs and SIMULINK Models

D.1 SIMULINK block diagrams for the mixing cell model

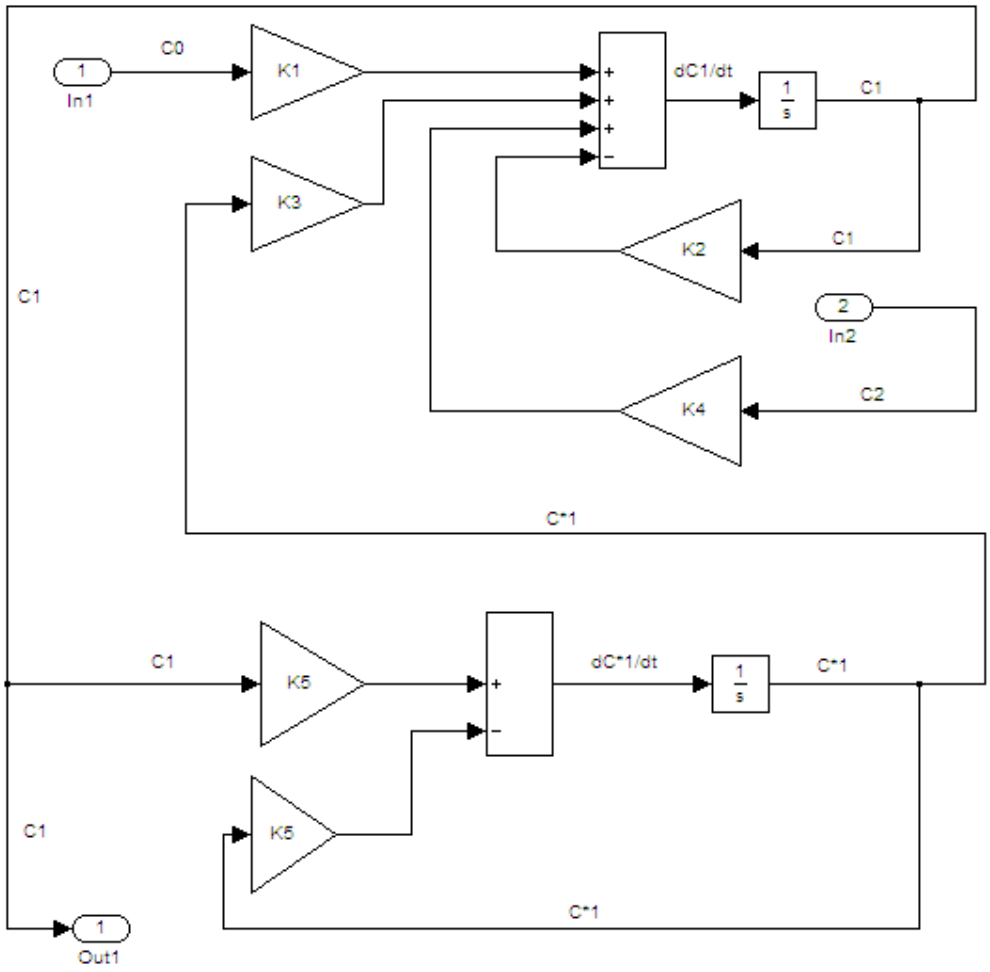

Figure D.1: SIMULINK block diagram (model) for cell 1

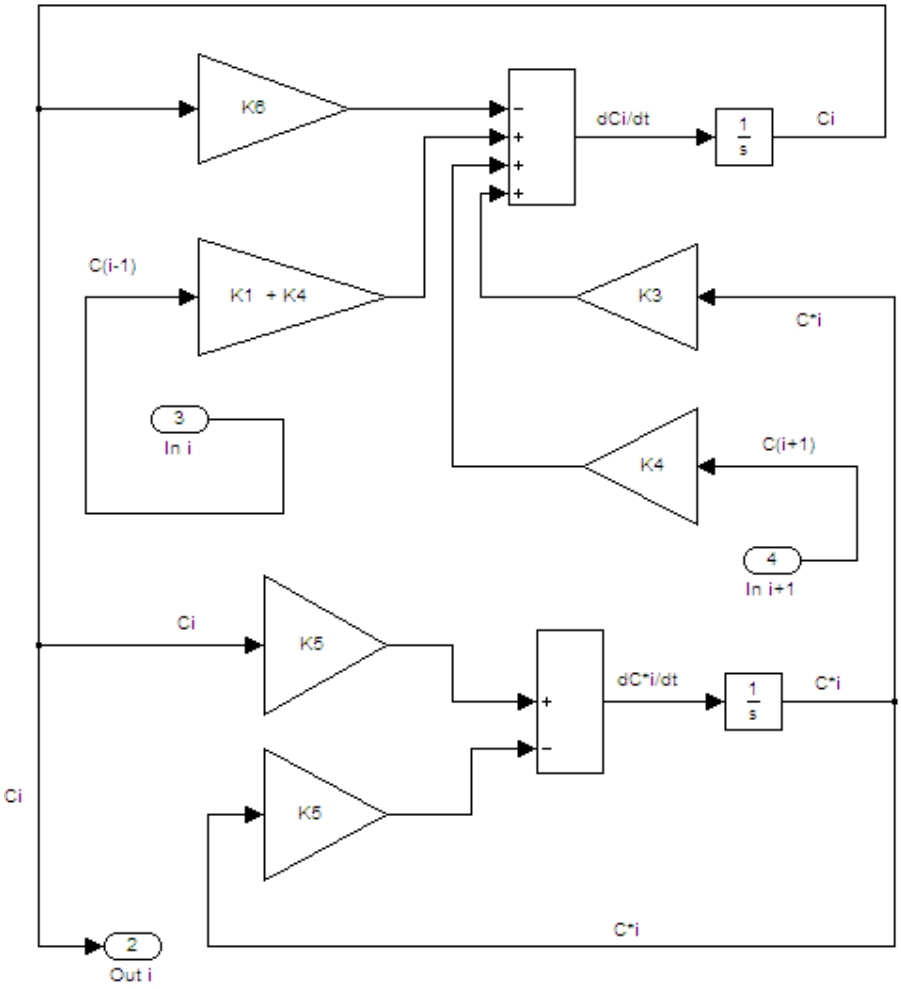

Figure D.2: SIMULINK block model for cell i

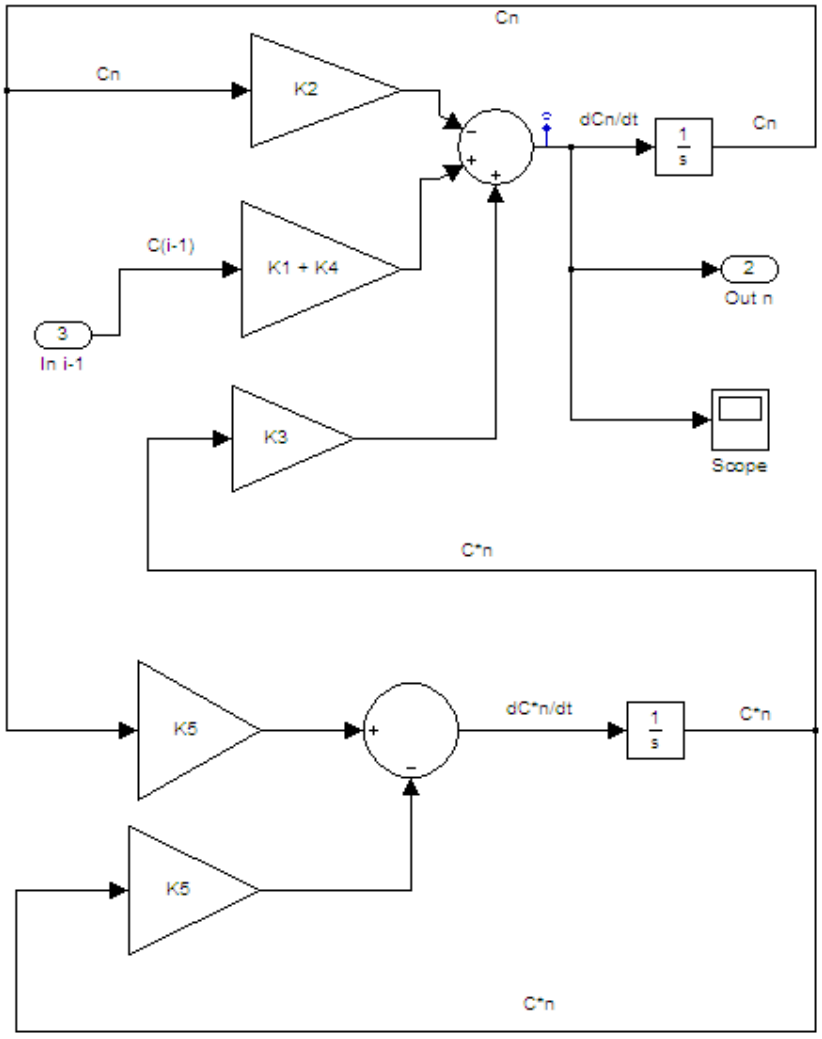

Figure D.3: SIMULINK block model for cell N

$$\left.\begin{aligned} K_1 &= \frac{(1-\kappa)}{\bar{\tau}(1-\lambda)}\ ; \qquad K_2 = \frac{(1-\kappa)}{\bar{\tau}(1-\lambda)} + \frac{\alpha+\gamma}{(1-\lambda)}\ ; \qquad K_3 = \frac{\gamma}{(1-\lambda)} \\ K_4 &= \frac{\alpha}{(1-\lambda)}\ ; \qquad K_5 = \frac{\gamma}{\lambda}\ ; \qquad K_6 = \frac{1-\kappa}{\bar{\tau}(1-\lambda)} + \frac{2\alpha+\gamma}{(1-\lambda)} \end{aligned}\right\} \quad [D.1]$$

D.2 MATLAB program to compute load positions and power draw

```
A = xlsread('file_name'); % read data file
n = A(:,1);% sample index
PP = A(:,2);% proximity probe signal data
D = A(:,3);% torque signal
CP = A(:,4); %conductivity signal
pi = 3.14;
t_sample = 0.006 % sampling rate in seconds per sample

% Determine the index matrix of the pool, toe, shoulder and marker
positions based on the set threshold voltages.

indx_t = find(PP >= 0.8 & PP <= 1.2); % Ball toe index
indx_bs = find(PP >= 1.6 & PP <= 2.0); % Ball shoulder index
indx_m = find(PP>= 4); % marker index
indx_p = find(CP >= 1.6 & CP <= 1.8); % Slurry pool index
indx_ss = find(CP>= 0.2 & CP <= 0.6); % Slurry shoulder index

% This part determines the marker position and counts revolutions

l = length(indx_m);
i = 1:l-1;
step = indx_m(i+1)-indx_m(i);
indx_step = find(step > 1); % to establish the last marker point
valid_indx_m = indx_m(indx_step); % only the last marker point

% Compute number of revolutions

revcount = valid_indx_m;% Samples indexing starts at zero
revs = length(revcount)-1;
fprintf('The number of mill revolutions %4.0f\n',revs);
n_marker = n(revcount); % based on samples index and not time index
n_toe = n(indx_t);
r = length(n_toe);
n_ball_shoulder = n(indx_bs);
```

```
s = length(n_ball_shoulder);
n_pool = n(indx_p);
w = length(n_pool);
n_slurry_shoulder = n(indx_ss);
z = length(n_slurry_shoulder);

% Compute the ball toe

theta = zeros(r,revs);
for j = 1:r
    for k = 1:revs
        if n_toe(j) > n_marker(k) & n_toe(j) < n_marker(k+1)
            theta(j,k) = ((n_toe(j)- n_marker(k))/(n_marker(k+1)...
             - n_marker(k)))*360;
        end
    end
end
valid_toe = find(theta>110 & theta<160);
toe_angle = ceil(theta(valid_toe));

% compute the ball shoulder

theta2 = zeros(s,revs);
for j = 1:s
    for k = 1:revs
        if n_ball_shoulder(j)> n_marker(k) & ...
           n_ball_shoulder(j) < n_marker(k+1)
            theta2(j,k) = ((n_ball_shoulder(j)- n_marker(k))...
            /(n_marker(k+1) - n_marker(k)))*360;
        end
    end
end
shoulder = find(theta2>240 & theta2<360);
ball_shoulder_angle = ceil(theta2(shoulder));

% Compute the slurry shoulder

theta3 = zeros(z,revs);
```

```
for j = 1:z
    for k = 1:revs
        if n_slurry_shoulder(j) > n_marker(k) & ...
           n_slurry_shoulder(j)< n_marker(k+1)
            theta3(j,k) = ((n_slurry_shoulder(j)- n_marker(k))...
            /(n_marker(k+1) - n_marker(k)))*360;
        end
    end
end

s_shoulder = find(theta3>240 & theta3<360);
slurry_shoulder_angle =ceil(theta3(s_shoulder));

% compute slurry pool angle

theta4 = zeros(w,revs);
for j = 1:w
    for k = 1:revs
        if n_pool(j) > n_marker(k) & n_pool(j) < n_marker(k+1)
            theta4(j,k) = ((n_pool(j)- n_marker(k))...
           /(n_marker(k+1) - n_marker(k)))*360;
        end
    end
end
pool = find(theta4>110 & theta4<160);
pool_angle = ceil(theta4(pool));

% Mill speed

j = 1:revs;
m = (n_marker(j+1) -n_marker(j))*t_sample; %
if m <60
    N = 60./m % mill speed in RPM
else
    N = m./60
end
N_mean = sum(N)/length(N);
```

```
%This part computes the mill torque and power

T_tot = -10.78 *D + 105.42 - T0 ; % T0 = no-load torque
T_avg = mean(T_tot)     % Average mill torque
P = ((2*pi*N_mean*T_avg)/60);    % Mill Power
P_avg = mean(P)  % Average mill power
```

D.3 MATLAB program for RBF-PLS multivariate model training and testing

```
%This program performs non-linear partial least squares regression
%(RBF-PLS) between the independent variables, X block and
%dependents, Y-block

clear
EXP_DATA = xlsread('PLS_data.xlsx','data','2:49,2:6');% read data
J = EXP_DATA(1:48,2); SG = EXP_DATA(1:48,3);PA = EXP_DATA(1:48,4);
MA = EXP_DATA(1:48,5);VV = EXP_DATA(1:48,6);
x = [PA MA VV];  y = [J SG];

% Cross validation by leave-out-one method(LOO)

N=size(x,1);
x1=x(1:N-1,:);XX1 = x(1:N,:);
y1=y(1:N-1,:);YY1 = y(1:N,:);
x2=x(N,:);
y2=y(N,:);

% normalization

xmean=mean(x1); xxmean =mean(XX1);
xstd=std(x1);   xxstd = std(XX1);
ymean=mean(y1); yymean =mean(YY1);
ystd=std(y1);    yystd=std(YY1);

%mean centred and variance scaled
```

```
X=(x1-xmean(ones(N-1,1),:))./xstd(ones(N-1,1),:);
XX=(XX1-xxmean(ones(N,1),:))./xxstd(ones(N,1),:);
Y=(y1-ymean(ones(N-1,1),:))./ystd(ones(N-1,1),:);
YY=(YY1-yymean(ones(N,1),:))./ystd(ones(N,1),:);
yt = Y; xt = X;

% Size of x and y

[rX,cX]  =  size(X);
[rY,cY]  =  size(Y);

% Allocate memory to the maximum size
n=max(cX,cY);
T=zeros(rX,n);
P=zeros(cX,n);
U=zeros(rY,n);
Q=zeros(cY,n);
B=zeros(n,n);
WW=P; k=0;
tol2 = 1e-12;
tol = 1e-10;
N_dim=2;

% iteration loop if residual is larger than specified

while norm(Y)>tol2 && k<n
    % choose the column of x has the largest square of sum as t.
    % choose the column of y has the largest square of sum as u.

    [dummy,tidx] =  max(sum(X.*X));
    [dummy,uidx] =  max(sum(Y.*Y));
    t1 = X(:,tidx);
    u = Y(:,uidx);
    t = zeros(rX,1);

    % iteration for outer modeling until convergence
```

```
while norm(t1-t) > tol
    w = X'*u/(u'*u);
    w = w/norm(w);
    t = t1;
    t1 = X*w;
    X_t = t1; Y_t = u; % INPUTS/TARGETS
    [N_t,M_dimx] = size(X_t);
    [N_t,M_dimy] = size(Y_t);

    basisfunction='gaussian';

    % Use the training data from RBF centres

    X_c=X_t;
    N_r=size(X_c,1);%number of RBF centres
    k_i=1*ones(N_r,1);%this is a prescaler for Gaussian,

   [W phi]= train_rbf(X_t,Y_t,X_c,k_i,basisfunction); % train
     uu = phi*W + k_i;
     q = Y'*uu/(uu'*uu);
     q = q/norm(q);
     u = Y*q/(q'*q);
     er = u - uu;

    % calculate weight update parameter

     [Z]=ZZ_rbf(X_c,X_t,W,k_i,basisfunction);
     for i = 1:size(X,2)
         ZZ = (Z*uu).*X(:,i);
     end
     dw = inv(ZZ'*ZZ)*(ZZ'*er);
     w = w+dw;
     w = w/norm(w);
end

t=X*w;
k=k+1;
```

```
% Update p based on t

    p=X'*t/(t'*t);
    pnorm=norm(p);
    p=p/pnorm;
   [W phi]=train_rbf(X_t,Y_t,X_c,k_i,basisfunction);%train weights
    uu = phi*W + k_i;

    % regression and residuals

    X = X - t*p';
    Y = Y - uu*q';

    % Model testing

    t2 = xt*p;
    [phi2]=pred_rbf(X_c,t2,W,k_i,basisfunction);
    uu2 = phi2*W + k_i;
    % save iteration results to outputs:
    T(:,k)=t;
    T2(:,k)=t2;
    P(:,k)=p;
    U(:,k)=uu;
    Q(:,k)=q;
    WW(:,k)=w;
    UU(:,k)= uu2;
end

%predicted values, mean centred and variance scaled

T(:,k+1:end)=[];
T2(:,k+1:end)=[];
P(:,k+1:end)=[];
UU(:,k+1:end)=[];
U(:,k+1:end)=[];
Q(:,k+1:end)=[];
WW(:,k+1:end)=[];
```

```
yp = UU*Q';
xp = T*P';
pred_y = yp.*ystd(ones(N-1,1),:)+ ymean(ones(N-1,1),:);
pred_x1 = xp.*xstd(ones(N-1,1),:)+ xmean(ones(N-1,1),:);

% Eigen decomposition

[eigvec eigval] = eig(cov([xp]));
eigval = diag(eigval);
[junk rindices] = sort(-1*eigval);
eig_vals = eigval(rindices)

% fit quality
% total sum of squares of deviations

SSX = sum(sum((x1 -xmean(ones(N,1),:)).^2));
SSY = sum(sum((y1 -ymean(ones(N,1),:)).^2));

%prediction error sum of squares (PRESS)

PRESS_Y = (yp -yt).^2;
PRESS = sum(PRESS_Y,1);
PRESS1 = PRESS(1); PRESS2 = PRESS(2);

fprintf('Sum of squares of predicted residuals:
%g\n',PRESS1,PRESS2);

SSR_X = sum((x1 - pred_x1).^2); % sum of squares of the residual
SSR_Y = sum((y1 - pred_y).^2)% sum of squares of the residual
Q1 = 1-(PRESS1/SSY)% cross-validation correlation coefficient
Q2 = 1-(PRESS2/SSY)
RY1 = 1-(SSR_Y(1)/SSY)  % Explained variance
RY2 = 1-(SSR_Y(2)/SSY)
RMSE_Y = sqrt(sum((y1-pred_y).^2)/(N)); % root mean square error
RMSE_X = sqrt(sum((x1-pred_x1).^2)/(N));

function [W phi]=train_rbf(X,Y,Xc,k_i,basisfunction)
```

```
%trains a radial basis function
if nargin<4
    k_i=1;
end
if nargin<5
    basisfunction='gaussian';
end

N_r=size(Xc,1);%number of centres
W=zeros(N_r,1);%weight matrix

[z phi]=sim_rbf(Xc,X,W,k_i,basisfunction);%simulate rbf
W=phi\(Y-k_i);%find weights

function [z phi]=sim_rbf(Xc,X_t,W,k_i,basisfunction)

%simulates a radial basis function

if nargin<4
    k_i=1;
end
if nargin<5
    basisfunction='gaussian';
end

N_r=size(Xc,1);%number of rbf centres
N_p=size(X_t,1);%number of points

if numel(k_i)==1
    k_i=k_i*ones(N_r);
end
phi=zeros(N_p,N_r);%rbf outputs
for i=1:N_r
    if k_i(i)==0
        phi(:,i)=1;
    else
        r=sqrt(sum((repmat(Xc(i,:),N_p,1)-X_t(:,:)).^2,2));
         %distance from point Xc to X_t
```

```
        sig = max(r)/(sqrt(2*N_r));
        phi(:,i)=exp((-r.^2)./(2*sig^2))
    end
end

function [phi2]=pred_rbf(Xc,t2,W,k_i,basisfunction)

if nargin<4
    k_i=1;
end

if nargin<5
    basisfunction='gaussian';
end

N_r=size(Xc,1);%number of rbf centres
N_p=size(t2,1);%number of points

if numel(k_i)==1
    k_i=k_i*ones(N_r);
end

phi2=zeros(N_p,N_r);%rbf outputs
for i=1:N_r
    if k_i(i)==0
        phi2(:,i)=1;
    else
        r=sqrt(sum((repmat(Xc(i,:),N_p,1)-t2(:,:)).^2,2));
        sig = max(r)/(sqrt(2*N_r));
        phi2(:,i)=exp((-r.^2)./(2*sig^2));
    end
end

function [Z]=ZZ_rbf(Xc,X,W,k_i,basisfunction)

if nargin<4
    k_i=1;
end
```

```
if nargin<5
    basisfunction='gaussian';
end

N_r=size(Xc,1);%number of rbf centres
N_p=size(X,1);%number of points

if numel(k_i)==1
    k_i=k_i*ones(N_r);
end

Z=zeros(N_p,N_r);%rbf outputs
for i=1:N_r
    if k_i(i)==0
        Z(:,i)=1;
    else
        r=sqrt(sum((repmat(Xc(i,:),N_p,1)-X(:,:)).^2,2));
        sig = max(r)/(sqrt(2*N_r));
        Z(:,i) = -2*r./sig^2;
    end
end
```

D.4 MATLAB program for PLS multivariate model training and testing

```
% This program performs PLS regression between the independent
%variables, X and dependents, Y as

% X = T*P' + E;
% Y = U*Q' + F = T*B*Q' + F1;
%
% Inputs:
% X     data matrix of independent variables
% Y     data matrix of dependent variables
% tol   the tolerant of convergence (defaut 1e-10)
%
% Outputs:
```

```
% T     score matrix of X
% P     loading matrix of X
% U     score matrix of Y
% Q     loading matrix of Y
% B     matrix of regression coefficient
% W     weight matrix of X
%
% Using the PLS model, for new X1, Y1 can be predicted as
% Y1 = (X1*P)*B*Q' = X1*(P*B*Q')

% Without Y provided, the function will return the principal
components as
% X = T*P' + E

clear
%read data

EXP_DATA = xlsread('PLS_data.xlsx','data','2:49,2:6');
J = EXP_DATA(1:48,2); SG = EXP_DATA(1:48,3);PA = EXP_DATA(1:48,4);
MA = EXP_DATA(1:48,5);VV = EXP_DATA(1:48,6);

x = [PA MA VV];  y = [J SG];

% Cross validation by leave-out-one method (LOO)

N=size(x,1);
x1=x(1:N-1,:);XX1 = x(1:N,:);
y1=y(1:N-1,:);YY1 = y(1:N,:);
x2=x(N,:);
y2=y(N,:);

% normalization

xmean=mean(x1); xxmean =mean(XX1);
xstd=std(x1);   xxstd = std(XX1);
ymean=mean(y1); yymean =mean(YY1);
ystd=std(y);
```

```
%mean centred and variance scaled

X=(x1-xmean(ones(N-1,1),:))./xstd(ones(N-1,1),:);
XX=(XX1-xxmean(ones(N-1,1),:))./xxstd(ones(N-1,1),:);
Y=(y1-ymean(ones(N-1,1),:))./ystd(ones(N-1,1),:);
YY=(YY1-yymean(ones(N,1),:))./ystd(ones(N,1),:);
yt = Y; yytrain = YY;
xt = X; xxtrain = XX;

% Size of x and y

[rX,cX]  =  size(X);
[rY,cY]  =  size(Y);

% Allocate memory to the maximum size

n=max(cX,cY);
T=zeros(rX,n);
P=zeros(cX,n);
U=zeros(rY,n);
Q=zeros(cY,n);
B=zeros(n,n);
W=P;   k=0;
tol2 = 1e-10;
tol = 1e-10;

% iteration loop if residual is larger than specified

while norm(Y)>tol2 && k<n

    % choose the column of x has the largest square of sum as t.
    % choose the column of y has the largest square of sum as u.

    [dummy,tidx] =  max(sum(X.*X));
    [dummy,uidx] =  max(sum(Y.*Y));
    t1 = X(:,tidx);
    u = Y(:,uidx);
    t = zeros(rX,1);
```

```
    % iteration for outer modeling until convergence

    while norm(t1-t) > tol
        w1 = X'*u/(u'*u);
        r = w1;
        w = w1/(sqrt(sum(w1.^2)));
        t = t1;
        t1 = X*w;
        q = Y'*t1/(t1'*t1);
        q = q/norm(q);
        u = Y*q/(q'*q);
    end

% update p based on t

    t=t1;
    p=X'*t/(t'*t);
    pnorm=norm(p);
    p=p/pnorm;
    t=t*pnorm;
    w=w*pnorm;

    % regression and residuals

    b = u'*t/(t'*t);
    X = X - t*p';
    Y = Y - b*t*q';

    % save iteration results to outputs:
    k=k+1;
    T(:,k)=t;
    P(:,k)=p;
    U(:,k)=u;
    Q(:,k)=q;
    W(:,k)=w;
    B(k,k)=b;
End
```

```
%predicted values, mean centred and variance scaled

yp = ((x1-xmean(ones(N,1),:))./xstd(ones(N,1),:)) * (P*B*Q');
xp = T*P';
SSX = sum(sum((x1 -xmean(ones(N-1,1),:)).^2));
SSx = sum(sum(x1.^2));
SSY = sum(sum((y1 -ymean(ones(N-1,1),:)).^2));
SSy = sum(sum(y1.^2));  % total sum of squares of deviations
pred_y1 = yp.*ystd(ones(N-1,1),:)+ ymean(ones(N-1,1),:);
pred_x1 = xp.*xstd(ones(N-1,1),:)+ xmean(ones(N-1,1),:);

%prediction error sum of squares (PRESS)

PRESS_Y = (yp - yt).^2;
PRESS = sum(PRESS_Y,1);
PRESS1 = PRESS(1); PRESS2 = PRESS(2);
fprintf('Sum of squares of predicted residuals:
%g\n',PRESS1,PRESS2);

SSR_X = sum((x1 - pred_x1).^2); % sum of squares of the residual
SSR_Y = sum((y1 - pred_y1).^2)
QY1 = 1-(PRESS1/SSY)% cross-validation correlation coefficient
QY2 = 1-(PRESS2/SSY)
RY1 = 1-(SSR_Y(1)/SSY)  % Coefficient Of determination
RY2 = 1-(SSR_Y(2)/SSY)
RMSE_Y = sqrt(sum((y1-pred_y1).^2)/(N)) % root mean square error
RMSE_X = sqrt(sum((x1-pred_x1).^2)/(N))
T(:,k+1:end)=[];
P(:,k+1:end)=[];
U(:,k+1:end)=[];
Q(:,k+1:end)=[];
W(:,k+1:end)=[];
B=B(1:k,1:k); % regression coefficients for inner relation
B_PLS = P*B*Q'; %OVERALL regression coefficient

% eigen value decomposition
```

```
[eigvec eigval] = eig(cov([xp]));
 eigval = diag(eigval);
[junk rindices] = sort(-1*eigval);
eig_vals = eigval(rindices);

% variance explained in X-block

rx1_x = eig_vals(1)/3
rx2_x = eig_vals(2)/3
rx3_x = eig_vals(3)/3

% variance explained in Y-block

[ix,jx]=size(xp);
[iy,jy]=size(yp);
rxy = corrcoef([xp,yp]); rxy_2 = rxy.*rxy;
RY= (rxy(1:jx,jx+1:jx+jy)).^2;
sum_RY = sum(RY,1);
RY1X1 = (RY(1,1)/sum_RY(1))*RY1;
RY1X2 = (RY(2,1)/sum_RY(1))*RY1;
RY1X3 = (RY(3,1)/sum_RY(1))*RY1;
RY2X1 = (RY(1,2)/sum_RY(2))*RY2;
RY2X2 = (RY(2,2)/sum_RY(2))*RY2;
RY2X3 = (RY(3,2)/sum_RY(2))*RY2;
```

APPENDIX E

Miscellaneous Calculations

E1 Calculation of static and dynamic media angles

E1.1 Introduction

Studies of media and slurry dynamic behaviour inside ore grinding mills are generally aimed at establishing the prevailing regimes of mass motion on the basis of which mills can be appropriately tuned to maximize on energy and milling efficiencies as well as reduce liner wear rate. The motion and behaviour of media and slurry inside the mill are mathematically described in terms of mill operational parameters, mill geometry and measured load angles, giving useful equations that can be used alongside mill load sensors as on-line shadows to provide inferential measurements of desired load motion and behaviour under given mill operating conditions.

E1.2 Load profile

Generally, the mill load motion and behaviour are characterised by the dynamic positions of the grinding media and slurry inside the mill. Considering the load with just sufficient slurry to fill all the interstices within the grinding media bed without creating a pool of slurry, the static and dynamic load angles, physically described in Figure E.1 can be mathematically related by an expression in the form of equation E.1, which represents the basic structure of the theoretical model envisaged in this study.

$$\psi_D = \psi_S + \varepsilon_L \qquad [E.1]$$

The model parameters ψ_D and ψ_S (in radians) represent the dynamic media angle defined by the toe and shoulder angles of the dynamic load, and the static media angle defined by the level of media filling respectively while ε_L is the qualitative description of the degree of load dilation and lift effects.

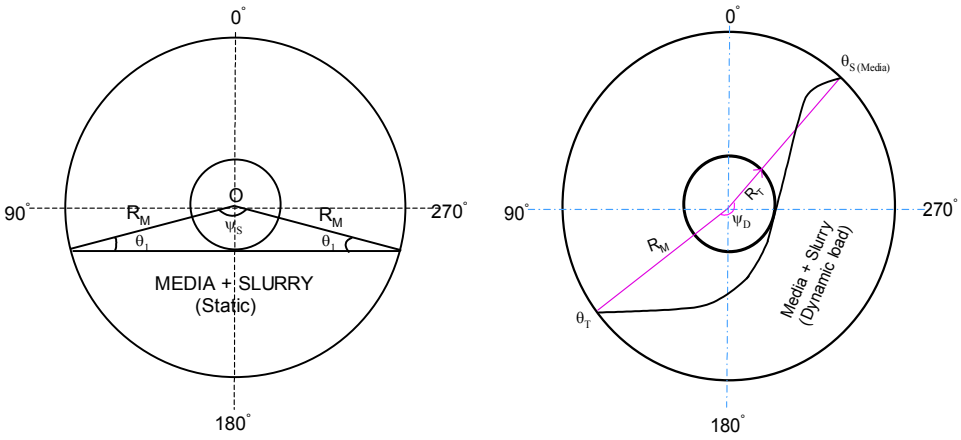

(a) **(b)**

Figure E.1: Representation of load profile and associated load angles in (a) stationary (b) dynamic mill with an overflow discharge mechanism.

E1.3 Static media angle

When the mill is stationary, the media forms a flat bed subtending an angle at the mill centre referred to as static media angle as illustrated in Figure E.1a. The size of the static media angle varies with the quantity of grinding media inside the mill and so is the angle θ_1 where the latter is at its minimum when the level of media filling is tangent to the overflow trunion.

In practice, the static media angle is utilised in estimation of the level of media filling (*J*) through a statistical relationship involving the mill radius and the load height measured vertically from the load level to the inside liner at the mill centre as demonstrated by Morrel (1993). Large errors may however be encountered with this approach at lower fill levels (<20%) notwithstanding the fact that the mill has to either grind out or be crash stopped for measurements to be taken which further renders the process cumbersome. This could be avoided through dynamic estimation of load filling which can be accomplished through a mathematical model that relates the dynamic load angles such as shoulder and toe angles with important and easily measurable mill operational and geometric parameters.

The static media angle can be estimated from the cross-sectional area of the ball charge region relative to the total cross-sectional area of the mill drum (Smit, 2000). This can be expressed mathematically as,

$$J_A = \frac{Area\ of\ the\ load\ segment\ (A_L)}{Total\ cross\,\text{sec}\,tion\ area\ of\ the\ mill\ (A_T)} \qquad [E.2]$$

Where the values of A_L and A_T are obtained from the following expressions:

$$A_L = \left(\frac{\psi_S - Sin(\psi_S)}{2}\right) R_M^2 \quad ; \quad A_T = \pi R_M{}^2 \qquad [E.3]$$

Substituting for A_T and A_L in equation E.3 and simplifying then rearranging yields an expression of the form:

$$\psi_S - Sin(\psi_S) - 2\pi J_A = 0 \qquad [E.4]$$

Equation E.4 can be solved numerically for ψ_S (in radians) and in our case a MATLAB function was applied to obtain solutions over a range of values of (J_A) spanning from 0.1 to 0.5. To overcome mathematical complexities associated with numerical computations, it was deemed appropriate to obtain an equivalent empirical expression to equation E.4 and the following equation yielded the best fit to the numerical data.

$$\psi_S = 4.142\ J^{0.415} \qquad \text{(Valid for } 0.1 \le J \le 0.5\text{)} \qquad [E.5]$$

Figure E.2 shows a comparison between the values of static media angles ψ_S as computed from equations E.4 and E.5.

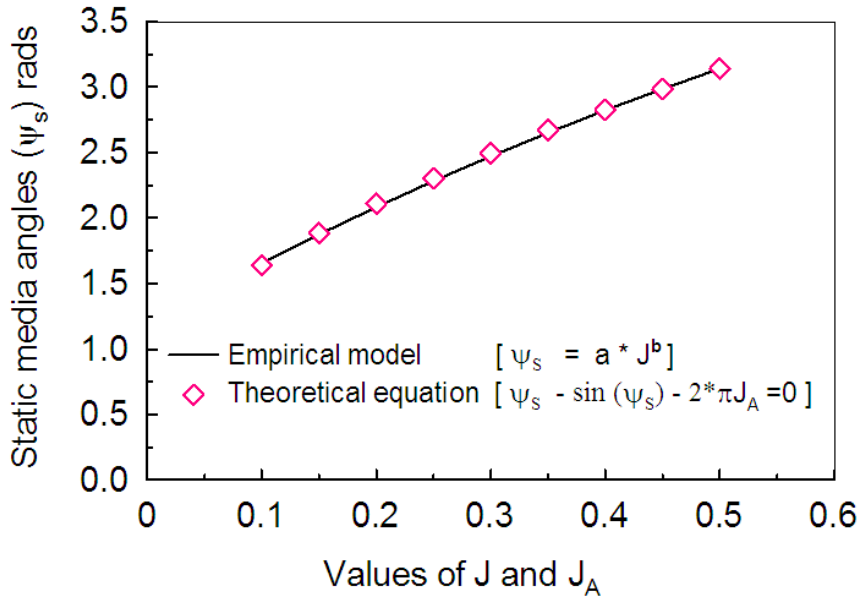

Figure E.2: Comparison of the static media angles as obtained by two equations

Alternatively, the static media angle can be estimated from a simple relationship involving the number of lifting bars around the mill circumference when the mill is stationary. The static media angle would be proportional to the number of invisible lifting bars covered by the media charge, that is:

$$\psi_S = 2\pi(1 - n_L/n_T) \qquad [E.6]$$

Where,

n_L : the number of visible lifting bars

n_T : total number of lifting bars around the mill circumference

E1.4 Dynamic media angle

The dynamic load position inside an overflow mill can be physically described as shown earlier in Figure E.1b. The dynamic media angle is the angle subtended at the mill centre by the ball charge when the mill is rotational. The angle is obtained as a difference between the shoulder and toe angles of the dynamic media which is mathematically expressed as:

$$\psi_D = \left(\theta_{S(media)} - \theta_{T(media)}\right) \quad [E.7]$$

Under normal mill operating conditions the dynamic media angle is expected to be larger than the static media angle. This is basically due to dilation of the ball charge as it gets lifted along the rotating mill drum.

Analysis of the evolution of dynamic media angle would provide an indication of the mill internal dynamics. This information might help the operator to adapt the mill accordingly so as to optimise the milling efficiency. Equally, the information would be valuable in planning for liner replacement and media replenishment.

E2 Estimating the length of the chord that defines the pool free surface

Assuming the dynamic load in an overflow mill takes the profile shown by Figure E.3, then the length of the chord defining the pool free surface would be given by,

$$L_c = L_1 + L_2 \quad [E.8]$$

Where, $L_1 = \sqrt{R_M^2 - R_T^2}$; L_2 is dependent on J and R_M

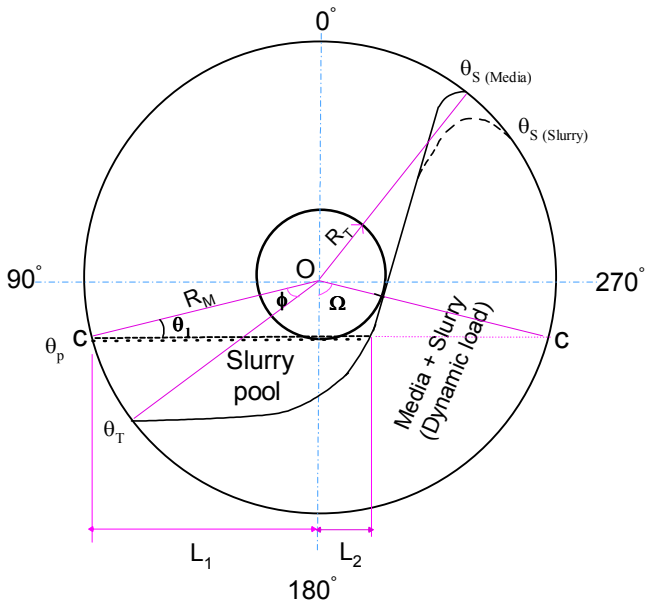

Figure E.3: Representation of important dynamic load angles in an overflow mill.

Based on the graphical data obtained by DEM simulation, presented in Figure E.4, a correlation of L_2 with J and R_M was sought. The values of R_L in Figure E.4 were measured physically in order to compute L_2 *(= R_L*sinΩ)* while the following were provided: R_M = 3.636 m, R_T = 0.84 m, Ω = 1.343 radians. The Values of L_2 obtained from measurements in Figure E.4, are presented in Table E.1 for the three levels of *J*.

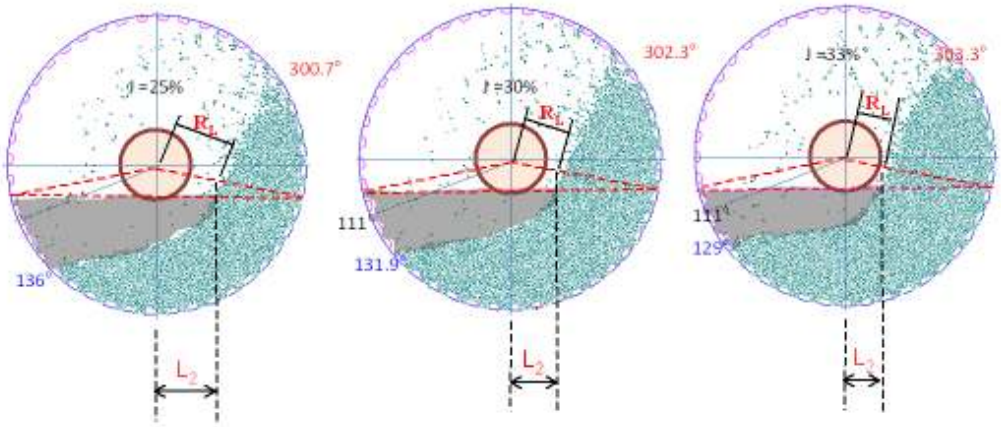

Figure E.4: DEM snap shots showing how L_2 changes with the level of ball load inside the mill.

Table E.1: DEM simulation values of L_2 for different levels of J

J (fraction)	R_L (m)	$L_2 = R_L * \sin \Omega$ (m)
0.25	1.3469	1.3093
0.30	1.0772	1.0495
0.33	0.9657	0.9408

By subjecting the data to linear regression analysis, a correlation of L_2 with J and R_M was obtained as,

[E.9]

Figure E.5 is a plot of observed values (measured) versus estimated values (calculated using equation E.9), showing the goodness of fit.

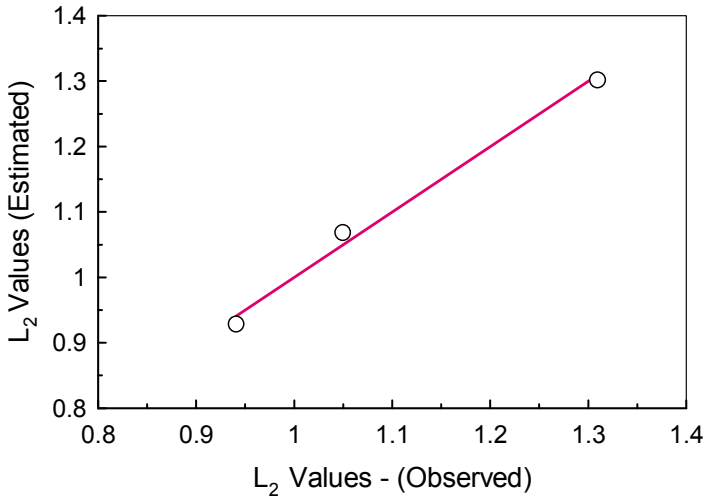

Figure E.5: Plot of observed values vs. model estimations of L_2

E3 Computation of weight updating parameter in the RBF-PLS multivariate model

The non-linear mapping by the RBF-PLS multivariate model of the scores, u and t is described in Chapter 5.

$$\hat{u} = w_o + \sum_{j=1}^{n_c} w_j . \exp\left(-\frac{\left\| c_j - t \right\|}{\sigma_j^2} \right) \qquad [E.10]$$

The input weight in the outer relation for the k^{th} variable, x_k on the input score t can be denoted as w_k . The Taylor series expansion of non-linear function, equation E.10 can be defined as,

$$u = f_{oo} + \sum_{k=1}^{m} \frac{\partial f(t)}{\partial w_k} . w_k \qquad [E.11]$$

$$where, \quad \frac{\partial f(t)}{\partial w_k} = \sum_{j=1}^{nc} w_j . \frac{\partial \left(\exp\left(-\left\| c_j - t \right\|^2 / \sigma^2 \right) \right)}{\partial w_k}$$

$$= \sum_{j=1}^{nc} w_j . \left(-2 \left\| c_j - t \right\| / \sigma^2 \right) . \exp\left(-\left\| c_j - t \right\|^2 / \sigma^2 \right) \frac{\partial \left(\left\| c_j - t \right\| \right)}{\partial w_k}$$

Since $\frac{\partial t}{\partial w_k} = x_k$, where x_k is a column vector containing the observations collected on the k^{th} input variable, the overall derivative can be written as follows:

$$\frac{\partial f(x.w)}{\partial w_k} = \sum_{j=1}^{nc} w_j . \left(-2 \left\| c_j - t \right\| / \sigma^2 \right) . \exp\left(-\left\| c_j - t \right\|^2 / \sigma^2 \right) . [\pm x_k] \qquad [E.12]$$

The final non-linear mapping function is written as,

$$u = f_{oo} + \sum_{k=1}^{m}\left(\sum_{j=1}^{nc} w_j.\left(-2\left\|c_j - t\right\|/\sigma^2\right).\exp\left(-\left\|c_j - t\right\|^2/\sigma^2\right).[\pm x_k]\right).\Delta w_k \quad [E.13]$$

The error update procedure is applied by defining a matrix $Z = [z_k]$ where each column z_k is set equal to:

$$z_k = \sum_{j=1}^{nc} w_j.\left(-2\left\|c_j - t\right\|/\sigma^2\right).\exp\left(-\left\|c_j - t\right\|^2/\sigma^2\right).[\pm x_k] \quad [E.14]$$

Now by stacking the weight updating vector Δw_k into a column vector ΔW and the Taylor series expansion can be written as,

$$u = f_{oo} + Z.\Delta W \quad [E.15]$$

The error between u and the value of RBF network model $\hat{u}$ is given by,

$$e = u - \hat{u} \Rightarrow Z.\Delta W \quad [E.16]$$

The outer input weight can be updated using the updating parameter given as,

$$\Delta W = \left(Z^T.Z\right)^{-1}.Z^T.e \quad [E.17]$$

E4 Correction for the SENSOMAG reference angle

The SENSOMAG sensor used to measure the media and slurry positions inside the industrial mill was offset from the reference probe by 1.52m, measured vertically. The details of the SENSOMAG sensor and reference probe locations are schematically illustrated in Figure E6 including the measurement details.

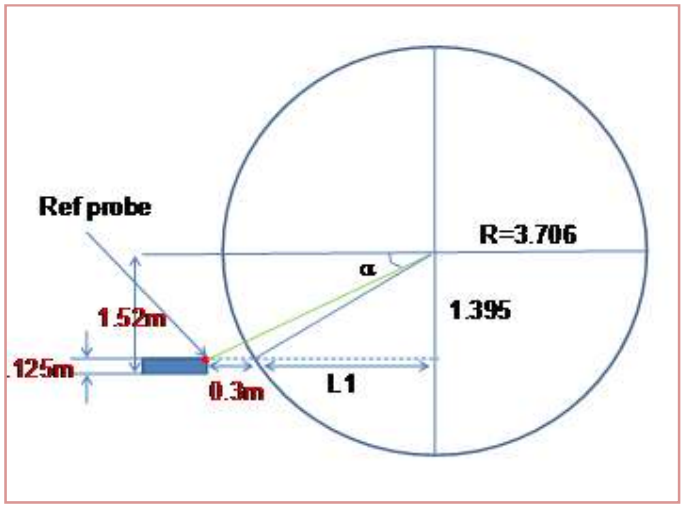

Figure E6: Schematic illustration of the SENSOMAG liner position relative to the reference position

The following parameters are given: R = 3.706m; Number of lifters, N_L = 44

The angle subtended at the mill centre by one lifter is obtained as, (360/44) = 8.2^0

While, $L_1 = \sqrt{(R^2 - 1.395^2)}$ [E.18]

Performing the geometric analysis on Figure E.6 yields the angle of displacement between the SENSOMAG sensor and reference probe as follows:

$Tan\,\alpha = 1.395 / (L_1 + 0.3)$ [E.19]

Reference angle = (90 + α) - 8.2/2 = 106.4^0

REFERENCES

Abouzeid, A.-Z.M. and Fuerstenau, D.W., (1980), Scale-up of particulate hold- up in rotary drums. *Powder Technology,* **25**: 65-70.

Afacan, A., Masliyah, J.H. and Nasr-EL-Din, H.A., (1990), Slurry holdup in a horizontal rotary drum with open-end discharge, *Powder Technology*, **63**: 179-186.

Austin, L. G., Klimpel, R. R., Luckie, P. T., (1984), *Process Engineering of Size reduction: Ball Milling*. SME/AIME, New York.

Baffi, G., Martini, E.B. and Morris, A.J., (1999a) Non-linear projection to latent structures revisited (the quadratic PLS algorithm), *Computers & Chemical Engineering*, **23**: 395-411.

Baffi, G., Martini, E.B. and Morris, A.J., (1999b), Non-linear projection to latent structures revisited (the neural network PLS algorithm), *Computers & Chemical Engineering*, **23**: 1293-1307.

Baffi, G., Martini, E.B. and Morris, A.J., (2000), Non-linear dynamic projection to latent structures modelling, *Chemometrics & Intelligent Laboratory Systems*, **52**: 5-22

Barley, R.W., Conway-Baker, J., Pascoe, D. R., Kostuch, J., McLoughlin, B. and Parker, D.J., (2004), Measurement of the motion of grinding media in a vertically stirred mill using PEPT: Part 2, *Minerals Engineering,* **17**: 1179-1187.

Behera, B., Mishra, B.K. and Murty, C.V.R., (2007), Experimental analysis of charge dynamics in tumbling mills by vibration signature techniques, *Minerals Engineering*, **20** : 84-91.

Bridge, J., Steven, A. and Heathwaite, A., (2006), Non-invasive quantitative measurement of colloid transport in mesoscale porous media using time lapse fluorescence imaging, *Environ. Sci. Technology*, **40**: 5930-5936.

Canevarolo, S.V., Melo, T.J.A., Covas, J.A. and Carneiro, O.S., (2001), Direct method for deconvoluting two residence time distribution curves, *Intern. Polym. Process.* XIV (4) 334.

Chen, S., Cowan, C.F.N. and Grant, P.M., (1991), Orthogonal least squares learning algorithm for radial basis function networks, *IEEE Transactions on Neural Networks*, **2**: 302-309.

Chibwana, C., and Moys, H.M., (2006), Radial mixing of particles in a dry batch ball mill, *Powder Technology*, **163**: 139-144.

Cho, H., and Austin, L.G., (2002), The equivalence between residence time distribution models in ball milling, *Powder Technology*, **124**: 112-118.

Cholette, A., Cloutier, L., (1959), Mixing efficiency determinations for continuous flow systems, *Can. J. Chem. Eng.*, **37**: 105-112.

Cleary, P.W., (1998), Predicting charge motion, power draw, segregation and wear in ball mills using discrete element method. *Minerals Engineering*, **11** (11): 1061-1080.

Cleary, P.W., Matt, S. and Morrison, R. (2006), Prediction of slurry transport in SAG mills using SPH fluid flow in a dynamic DEM based porous media. *Minerals Engineering,* **19**: 1517 – 1527.

Clermont, B., De Hass, B. and Hancotte, O., (2008), Real time mill management tools stabilizing your milling process, *Presented at 3rd Int. Platinum conference, SAIMM' 08*, Sun City, South Africa, October, 5-9.

Condori, P., Mainza, A., Govender, I and Powell, M.S., (2008), A mechanistic approach to modelling slurry transport in AG/SAG mills – transport through the charge. In Proc. XXIV IMPC. 23 - 27 Sep., Beijing, Vol. 2, pp 384-391.

Conway-Baker, J., Barley, R.W., Williams, R. A., Jia, X., Kostuch, J., McLoughlin, B. and Parker, D.J., (2002), Measurement of the motion of grinding media in a vertically stirred mill using PEPT: Part 1, *Minerals Engineering,* **15**: 53-59.

Danckwerts, P.V., (1953), Continuous flow systems: distribution of residence times, *Chem. Eng. Sci.*, **2** (1) 1-13.

Dayal, B.S. and McGregor, J.F., (1997), Improved PLS algorithms, *Journal of Chemometrics*, **11**: 73-85.

Din, G.U., Chughtai, I.R., Inayat, M.H., Khan, I.H., (2009), Study of axial mixing, holdup and slip velocity of dispersed phase in a pulsed sieve plate extraction column using radiotracer technique, *Int. J. Radiat. Appl. Instrum*. **67**: 1248-1253.

Dong, H. and Moys, M.H., (2003). Load behaviour and mill power, *Int. J. Mineral Processing,* **69**: 11–28.

Drews, T.O., Braatz, D. R., Alkire, C.R., (2003), Parameter sensitivity analysis of Monte Carlo Simulations of Copper Electrodeposition with multiple additives, *J. Electrochem. Soc.,* 150: C807-C812.

Duchesne, C., Thibault, J., Bazin, C., (1996), Modelling of the solids transportation within an industrial rotary dryer: A simple model, *Ind. Eng. Chem. Res*, **35**: 2334-2341

Fogler, H.S., (1992), Elements of chemical reaction engineering, Prentice-hall.

Fuerstenau, C.M. and Han, N.K., (eds.) (2003), *Principles of Mineral Processing*, SME, Colorado.

Fuerstenau, D.W. and Abouzeid, A. Z.M., (1985), Scale up of lifters in ball mills, *Int. J. Mineral Processing*, **15**: 183-192.

Fuerstenau, D.W., Abouzeid, A.-Z.M and Swaroop, S.H.R., (1986), Material transport in ball mills: Effect of discharge-end design, *Powder Technology*, **46** (2): 273-279.

Gardner, R.P., (1975), Evaluation of a radioisotope tracer method for determination of simulation parameters in open-circuit continuous ball mills, *Trans. AIME*, **258**:46

Geladi, P. and Kowalski, B.R., (1986), An example of 2-block predictive partial least squares regression with simulated data, *Analytica Chemica Acta*, **185**: 19-32.

Hamby, D.M., (1994), A review of techniques for parameter sensitivity analysis of environmental models, *Environ. Monit. Assess.,* **32**: 135-154.

Hogg, R., (1984), Mass transport models for tumbling ball mills, *Proc. Control'84, AIME*, **7:** 55-69.

Hogg, R., and Fuerstenau, D. W., (1972), Transverse mixing in rotating cylinders, *Powder Technology,* **6**: 139-148.

Hlungwani, O., Rikhotso, J., Dong, H. and Moys, H.M., (2003), Further validation of DEM modeling of milling: effects of liner profile and mill speed. *Minerals Engineering*, **16** (10): 993-998.

Hogg, R and Rogovin, Z., (1982), Mass transport in wet overflow ball mills, *Proceedings of the XIV International mineral processing congress*, Toronto.

Hopkins, M.J., Sheppard, A.J and Paul, E., (1969), The use of transfer functions in evaluating residence time distribution curves, *Chemical Engineering Science*, **24**: 1131-1137.

Huang, P., Jia, M. and Zhong, B.C., (2009), Investigation on measuring the fill level of an industrial ball mill based on the vibration characteristics of the mill shell, *Minerals Engineering*, **22**: 1200-1208.

Huang, W., Smith, C., Learner, D., Thornton, S. and Oram, A., (2002), Physical modeling of solute transport in porous media: evaluation of an imaging technique using UV excited fluorescent dye, *Water Res.*, **36**: 1843–1853.

International Atomic Energy Agency, (2008), Industrial process gamma tomography, Technical report, TECDOC series no. 1589.

International Atomic Energy Agency, (1975), Use of radiotracer techniques in industry and environmental pollution, Laboratory manual, STI/DOC/10/161.

Ivanov, O.P., Stepanov, V.E., Vokov, V.G., Volkovich, A.G., Smirnov, S.V., Danilovich, A.S., (2004), New portable gamma camera for nuclear environment and its application at rehabilitation works, *IEEE*, 1559-1562.

Jemwa, G.T. and Aldrich, C., (2006), Kernel based fault diagnosis on minerals processing plants, *Minerals Engineering*, **19**: 1149-1162.

Jonkers, G., Van der Bergen, E. and Vermount, P., (1990), Industrial applications of a gamma ray camera system: 1.Qualitative analysis, *Applied Radiation and isotopes***, 41** (10) 1023-1031.

Kantzas, A., Kelly, H., Taghi, Z., Amit, B., Ian, W., Glen, B. and Jinwen, C., (2000), Application of gamma camera imaging and SPECT system in chemical processes, *Chemical Engineering Journal*, **77**: 19-25.

Karr, C.L. and Yeager, D., (1995), Calibrating computer models of mineral processing equipment using genetic algorithms, *Minerals Engineering*, **8**: 989-998.

Kawatra, S.K. and Bakshi, A.K., (1996), On-line measurement of viscosity and determination of flow types for mineral suspensions, *Int. J. Mineral Processing,* **47**: 275-283.

Kelly, E.G., Spottiswood, D.J., (1982), Introduction to mineral processing, Wiley, N. York.

Kelsall, D.F., Reid, K.J and Restarick, C.J., (1970), Continuous grinding in a small wet ball mill, Part III: A study of distribution of residence time, *Powder Technology,* **3**: 170-178.

Kiangi**,** K K and Moys**,** M H**,** (2006), Measurement of the load behaviour in a dry pilot mill using an Inductive proximity probe. *Minerals Engineering* **19**:1348-1356.

Kiangi**,** K K and Moys**,** M H**,** (2008), Particle filling and size effects on the ball load behaviour and power in a dry pilot mill: Experimental study, *Powder Technology,* **187**:79-87.

King, R.P., (2001), Modeling & Simulation of Mineral Processing Systems, Butterworth-Heineman, Boston, USA.

Kinneberg, D,J and Herbst, J.A., (1983), A comparison of linear and non-linear models for open-circuit ball mill grinding, *Int. J. Mineral Processing,* **13:** 143-165.

Klimpel, R.R., (1982), Laboratory studies of the grinding and rheology of coal-water slurries. *Powder Technology,* **32**, pp. 267–277.

Klimpel, R.C., Austin, L.G. and Hogg,R., (1989), Mass transport of slurry and solids in a laboratory overflow ball mill, *Min. Metall. Process*, **6**: 73-78.

Kolacz, J., (1997), Measurement of mill charge in grinding ball mill circuits, *Minerals Engineering*, **10**: 1329-1338.

Kourti, T., (2005), Application of latent variable methods to process control and multivariate statistical process control in industry, *International Journal of Adaptive Control and Signal Processing*, 19: 213-246.

Lee, S., Lee, W.M., Woo, S.H., Kim, Y. and Park, J. M., (2006), Non-linear dynamic partial least squares modelling of a full biological waste water treatment plant, *Process Biochemistry*, **41:** 2050-2057.

Levenspiel, O., (1972). Chemical Reaction Engineering, 2nd ed., Wiley, New York.

Levisch, V.G., Markin, V.S., Chrismadzhev, Yu. A., (1967), On hydrodynamic mixing in a model of porous medium with stagnant zones, *Chem. Eng. Sci.*, **22**: 1357-1367.

Li, R., Meng, G., Gao, N and Xie, H., (2007), Combined use of partial least squares regression and neural network for residual life estimation of large generator stator insulation, *Measurement Science and Technology*, **18**: 2074-2082.

Liddel, K.S. and Moys M.H. (1988), The effect of mill speed and filling on the behaviour of the load in a rotary grinding mill, *J. S. Afr. Inst. Min. Metall*. **88 (2)**: 49-57.

Lima, A.L.R.P and Hodouin, D., (2005), Residence time distribution of an industrial mechanically agitated cyanidation tank. *Minerals Engineering*, **18**: 613-621.

Lindgren, F., Geladi, P. and Wold, S., (1994), Kernel-based PLS regression: Cross validation and applications to spectral data, *Journal of Chemometrics*, **8**: 377-389.

Makokha, A.B., Moys, M.H., (2009), A study of radial flow and mixing of slurry in a model overflow ball mill by gamma emission imaging, (*unpublished*).

Makokha, A.B., Moys, M.H., (2010), Towards on-line estimation of slurry volumetric holdup in a continuous overflow ball mill using direct sensors, (*internal report*).

McElroy, L., Bao, J., Yang, R.Y and Yu, A.B., (2009), A soft sensor approach to flow regime detection for milling processes, *Powder Technology*, **188**: 234-241.

McIvor, R.E., (1984). Effect of mill speed and liner configuration on ball mill performance. *Mining Engineering*, pp. 617-622.

Mellmann, J., (2001), The transverse motion of solids in rotating cylinders-forms of motion and transition behaviour, *Powder Technology*, **118**: 251-270.

Mishra, B.K and Rajamani, R.K. (1990), Motion analysis in tumbling mills by the Discrete Element Method, KONA, **8**: 92-98.

Mishra, B.K. and Rajamani, R.K., (1992), The Discrete Element Method for the simulation of ball mills. *Appl. Math. Modelling*, **16**: 598-604.

Mishra, B.K. and Rajamani, R.K., (1994), Simulation of charge motion in ball mills. Part I and Part II: *Int. J. Mineral Processing,* **40**: 171-197.

Morrell S. (1993), Prediction of power draw in wet tumbling mills, Ph.D Thesis, University of Queensland, Brisbane.

Moys, M.H. (1985). Measurement of parameters describing the dynamic behaviour of the load in a grinding mill, *Proc. Mintek 50*, Sandton, March, pp 205-219.

Moys, M.H. and Montini, A. (1987). The use of conductivity measurements in the control of grinding mills, *CIM Bulletin***, 80** (907): 52-56.

Moys, M.H., (1989), Slurry rheology- the key to further advance in grinding mill control, Proc. SAG, Vol.2, Vancouver, Canada: 713-728.

Moys, M.H., (1993), Model of mill power as affected by mill speed, load volume and liner design, *J. S. Afr. Inst. Min. Metall.*, **93** (6): 135-141.

Moys, M.H.,Van Nierop M.A., Smit, I. (1996). Progress in measuring and modelling load behaviour in pilot and industrial mills, *Minerals Engineering,* **9 (12)**: 1201-1214.

Napier-Munn, T.J., Morrel, S., Morrison, R.D., Kojovic, T., (1996), Mineral Comminution Crcuits: Their operation and optimization. JKMRC, Queensland.

Nasr-El-Din, H.A., Afacan, A., Masliyah, J.H. and Foster, J., (1992), Slurry transport in horizontal rotary drums with an end constriction, *Powder Technology*, **71**: 251-261.

National Council of Examiners for Engineering and Surveying, (2008), Fundamental Engineering Reference Handbook, 8th ed. Clemson, USA.

Nicholas, P.C., (1986), Encyclopaedia of fluid mechanics: Slurry flow technology, vol.5, Gulf Publishing, London.

Peebles, P.Z., (2001), Probability, random variables, and random signal principles, 4th ed, McGraw Hill, New York.

Perret, J., Sprasher, S., Kantzas, A., Hamilton, K. and Langford, C., (2000), Preferential solute flow in intact soil columns measured by SPECT scanning, *Soil Sci. Soc*, **64**: 469-477.

Plugatyr, A and Svishchev, M.I., (2008), Residence time distribution measurements and flow modeling in a supercritical water oxidation reactor: Application of transfer function concept, *J. Supercrit. Fluids,* **44**: 31-39.

Powell, M.S., (1991), Effect of liner design on the motion of the outer grinding elements in a rotary mill, *Int. J. Mineral Processing,* **31:** 163-193.

Powell, M.S. and Vermeulen, L.A., (1994), Influence of liner design on the rate of Production of fines in a rotary mill. *Minerals Engineering,* **7:** 169-183.

Powell, M.S. and Nurick, G.N., (1996), A study of charge motion in rotary mills, Part 2- Experimental work, *Minerals Engineering,* **9,** (3): 343-350.
Part 3- Analysis of results, *Minerals Engineering*, **9,** (4): 399-418.

Qin, S.J. and McAvoy, T.J., (1992), Non-linear PLS modelling using neural networks, *Computers and Chemical Engineering*, **16**: 379-391.

Radziszewski, P., (1999), Comparing three DEM charge motion models, *Minerals Engineering*, **12**: 1501-1520.

Rajamani, R.K. and Mishra B.K. (1996), Dynamics of ball and rock charge in SAG mills, *In Proc. SAG 1996*, Vancouver, 6-9 October, pp. 700-712.

Rogovin, Z., (1987), Possible slurry routes inside tumbling mills and hydrocyclones as deduced from an RTD model, *Powder Technology,* **52**: 179-183.

Rose, H.E. and Sullivan, R.M.E., (1958), A treatise on the internal mechanics of ball, tube and Rod mills, Chemical publishing, New York.

Sahin, F., (1997), A radial basis function approach to color image classification problem in real time industrial application, MSc Thesis, Virginia Tech. University, Blacksburg.

Sha, Y., Cao, Y.Y. and Guo, Y.G., (2006), Analysis of acoustic signals and BP neural network –based recognition of level of coal in ball mill, *Journal of Northeastern University*, **27** (12): 1319-1323.

Sherritt, R.G., Chaouki, J., Mehrotra, A.K., Behie, L.A., (2003), Axial dispersion in the 3-dimensional mixing of particles in a rotating drum reactor, *Chem. Eng. Sci.*, **58**: 401-415

Shin, S., Kim, J., Jung, S., Jin, J., (2003), The RTD measurement on a submerged bio-reactor using a radioisotope tracer and the RTD analysis, *Int. J. Contr. Auto. Syst.* **1**: 201:215.

Si, G., Cao, H., Zhang, Y. and Jia, L., (2009), Experimental investigation of load behaviour of an industrial scale tumbling mill using noise and vibration signature techniques, *Minerals Engineering*, **22**: 1289-1298.

Skorupa, J and Moys, H. M., (1993), Measurement of the radial and tangential forces exerted by the load on a liner in a ball mill as a function of load volume and mill speed, *Int. J. Miner. Process,* **37**: 239–256.

Smit, I. (2000**),** The effect of slurry viscosity and mill speed on the behavior of a rotary grinding mill, M.Sc Thesis, University of the Witwatersrand.

Songfack, P., (1996), Mass transport in wet overflow ball mills, PhD Thesis, University of Utah.

Songfack and Rajamani, (1999), Hold-up studies in a pilot scale continuous ball mill: dynamic variations due to changes in operating variables *Int. J. Miner. Process* **57***:* pp 105-123.

Stange, W., (1993), Using artificial neural networks for the control of grinding circuits, *Minerals Engineering*, **6**: 479-489.

Steiner, L., Kumar, A., Hartland, S., (1988), Determination and correlation of axial mixing parameters in agitated liquid-liquid extraction column, *Can. J. Chem. Eng*. **66**: 241-247.

Su, Z., Wang, P., Yu, X. and Lv, Z., (2008), Experimental investigation of vibration signal of an industrial tubular ball mill: monitoring and diagnosis, *Minerals Engineering,* **21**: 699-710.

Tang, J., Zhao, L., Zhou, J., Yue, H. and Chai, T., (2010a), Experimental analysis of wet mill load based on vibration signals of laboratory scale ball mill shell, *Minerals Engineering*, **23**: 720-730.

Tang, J., Zhao, L., Yu, W., Yue, H. and Chai, T., (2010b), Soft sensor modelling of ball mill load via principal component analysis and support vector machines, *Advances in Neural Network Research and Applications*, **67**: 803-810.

Tang, K. and Li, T., (2003), Comparison of differential partial least squares method in quantitative structure – activity relationships, *Analytica Chimica Acta*, **476**: 85-92.

Tangsathitkulchai, C., (1989), Slurry density effects on ball milling in a laboratory ball mill, *Powder Technology*, **59**: 285-293.

Tano, K.T., Bertil, I.P. and Anders, S., (2005), On-line lifter deflection measurements showing resistance effects in grinding mills, *Minerals Engineering*, **18**: 1077-1085.

Tinsley, H.E.A. and Brown, S.D., (2000), *Handbook of applied multivariate statistics and mathematical modelling*. AP Publishers, San Diego.

Tugrul, A.B., and Altinsoy, N., (2002), Anew modification of the radiotracer balance method for open channel flow measurement, *Flow Meas. Instrum.*, **12**: 341-344.

Van Nierop, M.A. and Moys, M.H., (1998), Premature centrifuging, oscillation and axial mixing of an industrial grinding mill load, *Minerals Engineering*, **11** (5): 437-445.

Van Nierop, M.A. (2001), Chracterisation of the load behaviour in an industrial grinding mill, Ph.D Thesis, University of the Witwatersrand.

Van Nierop and Moys (2002), Axial mixing of slurry in an autogenous grinding mill, *Int. J. Miner. Process*, **65**:151-164.

Vermeulen, L.A., Ohslen de Fine, M.J. and Schakowski, F., (1985), Continuous monitoring of information from the inside of a rotary mill. *Proc. Mintek 50 Conference,* ed. L.F. Haughton, Mintek, 949-952.

Wan, C. and Harrington, P.B., (1999), Self-configuring radial basis function neural networks for chemical pattern recognition, *Journal of Chemical Information and Modelling*, **39**: 1049-1056.

Watson, J.L., (1985), An analysis of mill grinding noise, *Powder Technology*, **44** (1): 83 – 89.

White, H.A., (1905), The theory of the tube mill, *J. Chem., Mett & Min. Soc. S. Afr*., 220 -305.

Wilson, D.J.H. and Irwin, G.W., (1997), Nonlinear PLS modelling using radial basis functions, *In Proceedings of American Control Conference, Albuquerque, 4-6 June*, pp3275-3276.

Wen, C.Y., and Chung, S.F., (1965), Dynamic response equations for various reactor models, *Can. J. Chem. Eng.*, **43**: 101-109.

Wold, S., Kettaneh-Wold, N and Skagerberg, B., (1989), Non-linear PLS modelling, *Chemometrics & Int. Laboratory Systems*, **7**: 53-65.

Wold, S., Sjostrom, M. and Eriksson, L., (2001), PLS-regression: a basic tool of chemometrics, *Chemometrics & Intelligent Laboratory System*, **58**: 109-130.

Xing, Z.H., (2004), Supervision and control of ball mill level indication realized by audio frequency signals, *Jiangsu Electrical Engineering*, **23** (4): 55-56.

Xu, M., Finch, J.A., and Laplante, A.R., (1991), Numerical solution to axial dispersion model in flotation column studies, *Can. Metall. Quart*., **30**: 71-77.

Xu, M., and Finch, J.A., (1991), The axial dispersion model in flotation column studies, *Minerals Engineering*, **4**: 553-562.

Zemouri, R., Gourivean, R. and Patic, P.C., (2010), Improving the prediction accuracy of recurrent neural network by a PID controller, *International Journal Systems Applications, Engineering & Development*, **2**: 19-34.

Zhang, L., Pan, Q., and Rempel, L.G., (2005), Liquid backmixing and phase holdup in a Gas-Liquid multistage agitated contactor, *Ind. Eng. Chem. Res*, **44:** 5304-5311.

Zheng, G.L. and Billings, S.A., (1996), Radial basis functions network configuration using mutual information and the orthogonal least squares algorithm, *Neural Networks*, **9**: 1619-1637.

Ziock, K. P., (1995), Gamma ray imaging spectrometry, *Science and Technology Review*, October, p14-27.

Mathworks, (2010), [Online]: Available, http://www.mathworks.com/support/tech-notes, [12 October, 2010].

Further reading

Abouzeid, A.-Z.M., Mika, T.S., Sastry, K.V.S. and Fuerstenau, D.W., (1974), The influence of operating variables on the residence time distribution for material transport in a continuous rotary drum, *Powder Technology*, **10** (6) 273-288.

Radziszewski, P and Caron, S., (2004), Towards AG/SAG/Ball mill on-line performance monitoring, *CIM Bulletin*, **97** (18): 112-11.